Analysis of Large Deformation Offshore Geotechnical Problems in Soft Clay

by

Zhandos Y. Orazalin

Bachelor's Degree, Karaganda State Technical University (2008)
Master of Science Degree, Massachusetts Institute of Technology (2012)

Submitted to the Department of Civil and Environmental Engineering
in partial fulfillment of the requirements for the degree of

Doctor of Philosophy in Civil and Environmental Engineering

at the

MASSACHUSETTS INSTITUTE OF TECHNOLOGY

June 2017

Signature of Author ..... Signature redacted
Department of Civil and Environmental Engineering
May 17, 2017

Certified by ..... Signature redacted
Andrew J. Whittle
Edmund K. Turner Professor of Civil and Environmental Engineering
Thesis Supervisor

Accepted by ..... Signature redacted
Jesse H. Kroll
Professor of Civil and Environmental Engineering
Chair, Graduate Program Committee

Analysis of Large Deformation Offshore Geotechnical Problems in Soft Clay

by

Zhandos Y. Orazalin

Submitted to the Department of Civil and Environmental Engineering
on May 17, 2017, in partial fulfillment of the
requirements for the degree of
Doctor of Philosophy in Civil and Environmental Engineering

Abstract

Although finite element (FE) methods are well established for modeling geotechnical problems in soil masses and soil-structure interaction, most prior research on large deformation problems has been limited to simplified assumptions on drainage conditions and constitutive behavior. This thesis investigates two large deformation problems in soft clay and proposes a methodology for performing coupled flow and deformation analyses with advanced effective stress models.

The first part of the research focuses on realistic 3-D finite element analyses (using Abaqus™ Standard) of a conductor (steel pipe pile) embedded within soft marine clay subjected to large lateral deformations caused by drift/drive-off of a drilling vessel. The proposed analyses use coupled pore pressure-displacement procedures together with the MIT-E3 soil model to represent the anisotropic, non-linear and inelastic effective stress-strain-strength properties of deepwater marine sediments with input parameters derived from a series of laboratory element tests performed on reconstituted Gulf of Mexico (GoM) clay. The numerical predictions are evaluated through comparison with experimental results from centrifuge tests with a well-instrumented model conductor. The FE results accurately predict the measured bending moment distribution along the length of the conductor and the spread of plastic strains within the conductor itself. The study has also shown the effects of soil behavior on local pile-soil interactions, enabling simplified analyses using macro-elements. The FE results have been used to calibrate input parameters for BWGG framework (Gerolymos & Gazetas, 2005), the Bouc-Wen (BW) model extended by Gerolymos and Gazetas (GG), that simulates generalized hysteretic pile-soil interactions and allows for degradation in soil resistance associated with geometric non-linearities.

The second application considers the effects of partial drainage for large deformation, quasi-static piezocone penetration in clay. The proposed axisymmetric FE analysis procedure introduces automated remeshing and solution mapping technique (similar to RITSS; Hu & Randolph, 1998) within a commercial FE solver. We have analyzed

the penetration resistance for a piezocone device using two elasto-plastic soil models (MCC, MIT-E3) and the recent elasto-viscoplastic MIT-SR soil model (Yuan, 2016) over a range of steady penetration velocities. The MCC predictions are in very good agreement with laboratory measurements of tip resistance and penetration pore pressures measured in centrifuge model tests in reconstituted kaolin. The results from more advanced soil models illustrate the impacts of anisotropic, rate dependent soil behavior on penetration tests in natural clays and are within the range of empirical measurements. The proposed analyses provide a complete framework that can now be used to investigate effects of partial drainage that occurs in piezocone tests for soils (such as silts) of intermediate permeability.

Thesis Supervisor: Andrew J. Whittle
Title: Edmund K. Turner Professor of Civil and Environmental Engineering

Acknowledgments

I would like to express sincere gratitude to all people who supported me during my studies and research at MIT. I am extremely grateful to Prof. Andrew Whittle, my research advisor, for his immense support over these years and continuous guidance in becoming an independent researcher. Prof. Whittle is an extraordinary mentor who is very patient with every student, always provides highly thoughtful advice with scientific rigor and encourages thinking big. I truly respect and appreciate him.

I am infinitely thankful to Prof. Herbert Einstein, my academic advisor, Prof. John Germaine and Prof. Eduardo Kausel for their contributions and help with the work, as well as invaluable support and constant encouragement. I immensely appreciate the opportunity to know and to learn from these remarkable professors.

I would also like to acknowledge and thank Dr. Ed Clukey, Dr. Arash Zakeri, and Dr. Ryan Phillips for their support and contributions to this research.

My deep appreciation is expressed to my father, Prof. Yerbol Orazaly, and my mother, Azhimova Shara who have always been the best parents in the world for me. I would like to mention my grandfather Ermek Orazalin, who always supported and encouraged my desire for knowledge, and my beloved grandparents Sagyntai Azhimov and Saliya Azhimova.

I would like to thank all my mentors, colleagues and friends at MIT and beyond for their support and encouragement. My sincere thankfulness and appreciation goes to Prof. Oral Buyukozturk, Dr. Lucy Jen, Prof. Jerome Connor, Prof. Adil Zhakulin, Prof. Askar Zhussupbekov, Prof. John Ochsendorf, Dr. Victor Nikitovich Popov, Prof. Ruben Juanes, Pat Dixon, Sayasat Nurbek, Prof. Markus Buehler, Angela Mickunas, Azamat Abdymomunov, Dr. Petr Aleksandrovich Kropachev, Prof. Juan Pestana, Prof. Franz-Josef Ulm, Dr. George Kocur, Kris Kipp, Kiley Clapper, Andre

Dixon, Patty Glidden, Stephen Rudolph, Mira Parsons, Jeanette Marchocki, Sheila Fay, and many others.

I thank the entire MIT Kazakh Student Association, Anton Ermakov, Yixing, Vasso, Nina, Ivo, Mauro, Eva, Despina, Ali, Jialiang, Vlad, Gonzalo, Davoud, Nikos, Amer, Sherif, Antonios, Omar, Steve, Bing, Wei, Chunwei, Amy, Bruno, Brendan, MJ, Aiden, Siavash, Adil, Sagyn, Kuandyk, Gleb and the rest of my longtime friends.

Finally, I would like to thank Madina, the love of my life, for her unconditional love and support.

Contents

List of Figures

List of Tables

Chapter 1

Introduction

1.1 Problem Statement

The constantly increasing worldwide energy demand has led to offshore hydrocarbon exploration and production. The offshore oil and gas development has expanded into the water depths greater than 1000 meters since the 1990s. These deepwater environments required different considerations for reliability and the development of novel foundation systems that facilitated the mooring of floating production and exploration platforms. These advances necessitated considerable investment in offshore engineering research and the field of offshore geotechnics (Randolph and Gourvenec [2011]). Offshore geotechnical considerations are important in all aspects of planning, designing, and operating of offshore facilities. The consequences of a failure for these facilities can be severe and the costs associated with the remediation efforts are very large. Geotechnical engineers must deal not only with design concerns for offshore foundations under various loading conditions (McCarron [2011]), but also take into account the complex behavior of soils (non-linear, inelastic, anisotropic and time dependent behavior) (Mitchell et al. [2005]), uncertainties associated with geologic materials (Einstein [2003]) and the challenges related to offshore site investigations (Randolph et al. [2005]).

Deepwater oil and gas production makes an extensive use of deep foundations including large diameter piles referred to as conductors. The conductor, a large diameter

pipe, is installed deep into the seabed to provide the stable structural foundation for the oil well. These conductor pipes connected to the floating vessels are subject to large lateral loads produced by waves and winds associated with offshore storms and other factors. As a result, a geotechnical engineering problem of an offshore foundation or a conductor pipe subjected to lateral loading involves the interaction of soil and conductor. The ability to make reasonable estimates of the behavior of laterally loaded conductors is an important design consideration. Complex loading conditions and the necessity to accurately evaluate conductor-soil interaction required the further development of numerical capabilities to reliable model the lateral responses of offshore structures. The comprehensive physical model tests of laterally loaded conductors are required to evaluate the performance of conductor-soil interaction and to validate more advanced numerical modeling capabilities. Currently, most finite element analyses of laterally loaded piles or conductors focus on the lateral displacements within 0.1-0.2 of pile/conductor diameters and are often limited to the simple isotropic constitutive soil models with the total stress approach (in which the soil is modeled as a single-phase material).

The most prominent example of large deformation geotechnical problems, however, is the soil penetration problem that relates to the mechanics of penetration in porous media (with the applications ranging from penetrometers, to the performance of driven piles, and pile installation effects). The analysis of soil penetration represents a very challenging class of geotechnical problems due to the high gradients of the field variables (stresses, strains, pore pressures, etc.) around the penetrometer, the large deformations and strains in the soil, the complex constitutive behavior of soils, and the non-linear penetrometer–soil interface characteristics. The cone penetration test (CPT) is currently the most performed in-situ test during offshore geotechnical investigations (Randolph and Gourvenec [2011]). The interpretation of engineering properties of soils is based on theoretical and experimental analyses of the testing method. The reliable numerical modeling of this test will also contribute to the development of meaningful correlations between engineering properties of soils and in-situ measurements. Although there has been some modest progress in the analysis

of penetration problems using various numerical methods with mostly simple constitutive models, the reliable modeling of large deformation geotechnical problems using advanced effective stress soil models remains to be a great challenge.

The overall goal of this thesis is to study large deformation offshore geotechnical problems with advanced effective stress soil models. The current research undertakes two main tasks: 1) the development of reliable models of conductor-soil interaction under large lateral loads using realistic modeling of constitutive soil behavior and taking advantage of extensive prior research at MIT on the Gulf of Mexico (GoM) Clay; 2) the development of numerical capabilities to perform extremely large deformation analyses using advanced effective stress soil models. These capabilities are demonstrated through the analysis of large deformation offshore cone penetration in soft clay considering the partial drainage, stress history, and penetration rate effects.

The first part of this work involves the development, validation and refinement of 3D Finite Element (FE) models of conductor-soil interactions in soft clay that simulate the loading conditions associated with offshore drift/drive-off loading events (that cause large lateral loads and tension). The analyses use the advanced effective stress soil model MIT-E3 (Whittle and Kavvadas [1994]) and some simple isotropic EPP (elastic-perfectly plastic) and IHPP (isotropic hardening) soil models. The MIT-E3 soil model provides a more comprehensive framework for characterizing the non-linear, hysteretic and anisotropic stress-strain-strength properties of soft clays and is capable of achieving reasonable predictions of cyclic load response (e.g., accumulation of plastic strains) (Whittle and Kavvadas [1994]). The simulations results were validated through comparisons with the results of physical model tests carried out in a large geotechnical centrifuge facility. This study provided some useful insights into the behavior of offshore conductor subjected to large lateral loads under tension. The effects of the soil models and the elasto-plastic properties of the conductor are considered and compared. The location of the plastic hinge developed due to large bending is determined. The load-unload-reload cycle was also considered and a simplified method to represent conductor-soil interaction was proposed.

The second part of this work includes the development of numerical capabilities

to analyze extremely large deformations related to the mechanics of penetration using advanced effective stress soil models. The method is based on the automated remeshing and solution mapping technique (Hu and Randolph [1998a]). The cone penetration test (CPT) in soft clay was modeled with several soil models including the MCC (Modified Cam Clay) (Roscoe and Burland [1968]), MIT-E3 (Whittle and Kavvadas [1994]) and MIT-SR (Yuan [2016]) soil models. The predictions of cone penetration are evaluated through comparisons with the published results (Aubeny [1992], Ladd et al. [1999], Schneider et al. [2007], Ceccato et al. [2016]) that used various numerical methods (MPM, Strain Path Method) and the experimental (field and laboratory) measurements. The realistic soil behavior, effect of stress history and the considerations of partially drained conditions were taken into account in the developed Finite Element simulations of piezocone penetration. In addition, it is well-known that the undrained shear response of clays is dependent on the shear strain rate, but this is not usually considered directly in most available soil models that have been used in the previously published penetration analyses. In this study, the realistic modeling of penetration rate effects was achieved using a newly developed elasto-viscoplastic MIT-SR model capable of modeling rate-dependent behavior of clays. The methodology to perform large deformation geotechnical analyses using advanced effective stress soil models is developed, discussed and presented in this thesis.

1.2 Thesis Organization

The thesis chapters are organized in the following way:

Chapter 2 describes the background information. Initially, it presents the introduction and motivation for this research. Then, it provides an overview of existing large deformation numerical analysis methods applicable to geotechnical engineering problems. The main Finite Element Method (FEM) formulations are introduced (Lagrangian and Eulerian formulations). The most relevant large deformation general numerical analysis methods such as ALE (Arbitrary Lagrangian Eulerian), CEL

(Coupled Eulerian Lagrangian), MPM (Material Point Method) and SPH (Smoothed Particle Hydrodynamics) are briefly presented and summarized. After that, the adaptivity techniques are discussed including the so-called Remeshing and Interpolation Technique with Small Strain (RITSS) that was used as a basis for the proposed methodology. Next, offshore geotechnical conditions are described along with the previously published research on deepwater conductors under lateral loads and cone penetration problems in soft clay. The conventional analysis methods of laterally loaded piles using "p-y" curves and the overview of cone penetration basics are also covered.

Chapter 3 presents the proposed methodology for large deformation numerical analyses of geotechnical problems. The chapter starts with the description of modeling methodology for conductor-soil interaction. The initial base case 3D Finite Element Model development is described. The methodology for obtaining soil reactions and p-y curves is presented. Then, the comparison with the previously published numerical results is shown using the total stress analysis. Next, the total stress analysis methodology is compared with the effective stress analysis approach. The theoretical preliminaries and implementation details of the proposed large deformation analysis methodology are presented. Debugging strategies, validation and practical usage evaluation are also provided. Finally, the advanced effective stress constitutive soil models are described providing a brief overview of MIT-E3 and MIT-SR soil models used in the subsequent numerical simulations.

Chapter 4 provides the results of numerical simulations for conductor-soil interaction centrifuge model tests and results validation. First, the centrifuge model tests are described. The instrumentation and model properties are presented. The Resedimented Gulf of Mexico Clay (RGoM) soil samples obtained after the centrifuge tests were delivered to MIT Soil Mechanics Laboratory and tested in K_0-consolidated triaxial compression and extension undrained shear tests with appropriate repeatibility. The results of these tests are presented, and the calibration of the advanced effective stress soil model MIT-E3 associated with Average Gulf Clay (AGC) parameters set is adjusted to best fit the laboratory data. Next, the development of 3D Finite

Element Model of the test conductors subjected to the prescribed tension loads and lateral displacements is described. The assumed properties of the conductor material and used undrained shear strength profiles are explained. The analysis results are then compared to the measured data obtained from the centrifuge model tests. The discussed results include the bending moments, lateral deflection profiles, conductor rotations and the plastic strains in the conductor to determine the location of the hinge due to excessive bending. The mesh sensitivity studies are also presented.

Chapter 5 presents the simplified methods for representing conductor-soil interactions. This chapter describes the evaluation of p-y curves associated with the lateral loading of the conductor. The back-bone curves for monotonic loading are obtained for the analyses using EPP and MIT-E3 soil models. The geometric effects and other interaction considerations are discussed. A simplified model based on BWGG framework is presented. The calibration of a hysteresis (Bouc-Wen) model is shown, and the input parameters are presented for monotonic and cyclic loading conditions. A basic set of 4 input constants are needed to achieve reasonable representation of conductor-soil response in monotonic lateral loading, including softening effects associated with geometric non-linearities. The results obtained from the simplified methods are compared with the 3D Finite Element Analysis results for monotonic and cyclic loading conditions.

Chapter 6 provides the numerical analysis of cone penetration testing in soft clays. This chapter provides an overview of cone penetration testing and modeling aspects of the problem. The development of axisymmetric numerical models is described. Large deformation effective stress analyses are conducted using the proposed methodology described in Chapter 3. The results of the analyses using the three effective stress soil soil models are presented. First, the obtained results using MCC soil model considering the effects of partial drainage are compared with the most recently published work on modeling the cone penetration test using the two-phase Material Point Method (MPM). Then, the results are compared with the measured data. Next, the analyses using more realistic soil models that take into account complex soil behavior and penetration rate effects are presented considering the effect of stress history. The

MIT-E3 and MIT-SR simulation results are compared with the measured field data (Ladd et al. [1999]) and the steady state analytical solutions obtained from the Strain Path Method (Baligh and Levadoux [1986], Aubeny [1992]).

Chapter 7 summarizes the work with the main conclusions and presents the the recommendations for future research. The obtained insights and useful contributions of the work are outlined.

The summary results of the laboratory tests conducted on the samples of Resedimented Gulf of Mexico Clay are presented in the Appendix A. The numerical details and procedures for large deformation effective stress analyses using axisymmetric and 3D Finite Element models are summarized in Appendix B. Appendix C contains the relevant program source codes developed during this research.

Chapter 2

Background

This research was initially motivated by a practical offshore engineering project involving large lateral deformations of a conductor pipe in soft clay and the opportunity to validate the three-dimensional numerical predictions against measured data from a sophisticated centrifuge model test. The study was then extended to investigate large deformation penetration problems. This chapter presents the background information on the subject and a brief overview of the existing numerical analysis methods to discuss the rationale behind the proposed methodology presented in the next chapter.

2.1 Introduction and Motivation

Deepwater well drilling projects for oil and natural gas are complex endeavors with a great number of challenges and risks (Randolph et al. [2005]). The oil and gas reserves are located deep within the seabed. An offshore borehole or oil well is drilled by a floating vessel that is dynamically positioned (DP) at the site using a satellite GPS (Global Positioning System) signal. The DP system aims to automatically maintain vessel's position by means of the vessel's own propellers (thrusters) preventing it from drifting due to the wind, waves, or sea currents. The upper section of the borehole/wellbore is stabilized by a conductor, a large diameter pipe. A blowout preventer is connected to the wellhead at the top of the conductor pipe. The blowout

preventer stack comprises the LMRP (lower marine riser package) and blowout preventer (BOP) that can be used to control and monitor or seal oil and gas wells. The drilling vessel floating on the water surface is connected to the seafloor through the blowout preventer via a marine riser. This slender pipe provides a conduit to provide a temporary extension of a subsea oil well to a surface drilling facility (Figure 2-1). The riser is held under tension to maintain stability.

Due to current, wind and wave loading, or other unfavorable conditions such as failure of the DP system the vessel may drift off-station causing failure in the riser-conductor-soil system either above or below the mudline (Figure 2-1a). During emergency drift-off situations, the riser should be immediately disconnected from the conductor and the well has to be sealed within the blowout preventer. One of the main risks during deepwater drilling operations is the failure of the conductor system below the blowout preventer (Figure 2-1b). This is the most unfavorable and catastrophic situation that can lead to uncontrolled release of oil and gas from the wellbore.

Prior simulations of DP system failures (Josefsson and Dincal [2014]) have included independent analyses of the quasi-static loading conditions during the drift/drive-off process and the dynamic response of the system following parting of the riser (recoil and collapse through the water column). For deepwater conditions (1500-1800 m), the results show that the initial yield occurs in the conductor (typically at depths up to 15m below mudline) when the drilling vessel is offset at 8-10°, with mudline displacements of 3-4.6m (i.e., d/D = 3-6, for conductors with outside diameter, 0.71–0.91m). The post-parting of the riser generates large cyclic bending moments in the conductor and can cause significant permanent deviations from the vertical.

The main goal of this research is to develop and validate numerical models of conductor-soil interactions that can be integrated within a comprehensive analysis framework of the riser-wellhead system and, hence, enable oil and gas engineers to evaluate well integrity for uncontrolled drift-off or drive-off loading conditions. The work carried out during this research has involved the development, validation and refinement of 3D Finite Element (FE) models of conductor-soil interaction that represent: 1) the large deformation conditions associated with drift/drive-off load events;

and 2) the non-linear, inelastic and anisotropic constitutive behavior of marine sediments typically encountered in the Gulf of Mexico. The former is addressed by using Abaqus™ Standard solver with coupled pore pressure-stress elements and taking into account geometric non-linearity (for extreme deformations associated with penetration mechanics problems, a new procedure for remeshing and interpolation is implemented). The latter is achieved by comparing the results for a generalized effective stress soil model, MIT-E3 (Whittle and Kavvadas [1994]), which is integrated within the commercial Abaqus™ Standard Finite Element program through a User Material (UMAT) interface. Prior studies (Whittle and Sutabutr [2005]) have shown that the MIT-E3 model is capable of describing the anisotropic, non-linear and inelastic effective stress-strain-strength properties of deepwater sediments from the Gulf of Mexico (GoM).

The numerical predictions are evaluated through comparisons with data from two physical model tests performed in a 5.5m radius beam centrifuge at C-CORE (Canadian research and development corporation) within a testbed of reconstituted GoM clay. These tests measured bending strains in the model conductor pipe over an embedded depth of 60m (prototype scale) associated with simulated riser drift-off and separation events. Numerical predictions of the centrifuge tests are conducted by independently calibrating input parameters for the MIT-E3 using a suite of elemental laboratory tests (1D consolidation and undrained triaxial shear tests) on specimens of the reconstituted GoM clay[1]. Predictions of conductor-soil interaction are then based on selection of a stress history profile for the centrifuge testbed to achieve close matching with the measured undrained shear strength profile.

Substantial computational efforts are required to conduct 3D FE simulations of conductor-soil interactions for the large lateral deformations expected in drift-off events. The representation of these interactions as a component in the simulation of the overall riser-wellhead system can be accomplished more efficiently through simplified local interaction models (p-y representation). We have implemented the BWGG generalized p-y model originally developed by Gerolymos and Gazetas [2005b]

[1]The tests were performed at the MIT geotechnical laboratory using tube specimens

to describe pile-soil interactions in seismic loading events. Input parameters for the BWGG model are then calibrated from the 3D FE simulations.

The main motivation to extend the current research into the analysis of deep soil penetration was to demonstrate the developed numerical capabilities (automatic remeshing and interpolation) on a large deformation axisymmetric problem that is very important within geotechnical engineering practice. Historically, the approximate solutions methods for the analysis of this problem in saturated clays included bearing capacity, cavity expansion and the strain path methods. Previous studies have shown the limitations of the approximate cavity expansion solutions for deep penetration problems (Levadoux [1980], Baligh and Levadoux [1986]). Strain path analyses provide an approximate solution for undrained steady state penetration. However, there was a need in a more realistic solutions that could help to improve rational approaches to in-situ test interpretation (Aubeny [1992]). Large deformation FE analyses are required to introduce correct initial conditions and to simulate a displacement of at least several times of the diameter of the cone to give a realistic build up of the shaft pressure (van den Berg [1994]). These analyses must address the large gradients of solution variables (stresses, deformations, pore pressures) and to approximate the steady state of the cone tip penetration. Currently, most full finite element analysis solutions of deep penetration in clay are limited to either total stress formulations (not taking into account the pore pressures) or simple isotropic constitutive models. Even though simple soil models provide a useful insight into the mechanics of deep penetration in clays, more comprehensive constitutive soil models are required for reliable predictions of pore pressures and effective stresses during and after the test procedures. Advanced effective stress soil models including a newly developed advanced elasto-viscoplastic model capable of capturing rate effects (Yuan [2016]) are used in the current study of large deformation deep penetration problems. The proposed methodology can be readily extended to layered soil profiles and various drainage conditions.

2.2 Overview of Large Deformation Numerical Methods for Geotechnical Application

In this thesis, we focus on the continuum approach to representing the soil in numerical models. This section presents a brief description of the traditional Lagrangian and Eulerian formulations within the Finite Element Method and introduces some of the practical methods and techniques for large deformation numerical analyses with regard to the geotechnical application.

2.2.1 Displacement-Based Finite Element Method

In the traditional displacement-based finite element method formulation (also known as the Lagrangian finite element method), the material associated with the mesh remains associated with it throughout the analysis (i.e. the mesh and the material are coupled). The material moves with mesh deformations, and the material cannot flow across the boundaries of mesh elements. The nodes at the boundary of the material remain at the boundary during the analysis (Figure 2-2). The Gauss points also move with the material allowing the constitutive equations to be evaluated at the same material points. The interface between different materials and the boundary conditions are easily tracked due to a well-defined free surface of the material boundaries. For large deformations associated with soil penetration analysis, mesh distortion problems arise when the material is severely deformed . As a result, one of the main drawbacks of the conventional Lagrangian finite element method is the limitation in modeling very large deformations associated with mesh distortion.

2.2.2 Eulerian and CEL (Coupled Eulerian Lagrangian)

In Eulerian formulation, the mesh is fixed in space and material flows through the mesh. Eulerian formulation is commonly used for fluid mechanics problems and is not susceptible to mesh distortion problem due to large deformations. The Eulerian mesh is usually a simple rectangular grid of elements extended beyond the material

boundaries and creates a space in which the material is free to move and deform (Figure 2-3). Any Eulerian material that moves outside the Eulerian mesh is not considered in the simulation. Eulerian elements may be partially or completely empty of the material. It becomes challenging to track the material boundaries as the material deforms within a fixed mesh. In the Eulerian description, the mesh is decoupled from the material. This introduces numerical difficulties with history-dependent materials (such as elasto-plastic soils) as convective terms appear in the Eulerian FE formulation. Effectively, large distortions of the material are handled at the expense of the resolution in flow details (Donea et al. [2004]).

It is possible to have Eulerian and Lagrangian meshes interacting with each other within the same analysis using contact algorithms. This type of numerical analysis method is referred to as the Coupled Eulerian Lagrangian (CEL) analysis and has been implemented in the commercial finite element software Abaqus™ Explicit (SIMULIA [2016]). CEL is typically used to model the interactions between a solid body and a yielding or fluid material, such as a Lagrangian cone penetrating through Eulerian soil or an Eulerian gas inflating a Lagrangian airbag. For geotechnical engineering purposes, the CEL method has only been applied to analyze various large deformation problems in fully drained and fully undrained conditions (Qiu et al. [2011]). This method has yet to be extended to effective stress analyses with mixed deformation and pore pressure elements in Abaqus™ (SIMULIA [2016]).

2.2.3 ALE (Arbitrary Lagrangian Eulerian)

The Arbitrary Lagrangian Eulerian (ALE) is a broad class of FE formulations that combine the advantages of Lagrangian and Eulerian formulations. In the ALE approach, the nodes of the mesh can move with the material (normal Lagrangian mode) or can be held fixed (Eulerian manner), or can be moved in some arbitrarily specified way to give a continuous mesh-update capability. As a result, the pure Lagrangian and pure Eulerian formulations can be regarded as a special cases of the ALE aproach. Larger distortions of the material can be handled than would be possible in a purely Lagrangian method with more resolution than that is afforded by

a purely Eulerian approach due to the freedom in moving the computational mesh in an ALE method (Donea et al. [2004]). The convective terms enter the governing ALE equations just as in the Eulerian formulation. The treatment of these terms plays a crucial role in the numerical implementation, especially for complex path-dependent constitutive models (Savidis et al. [2008]).

There are several variations of the ALE approach depending on different advection schemes and remapping strategies including Single-Material Arbitrary Lagrangian-Eulerian (SMALE), Multi-Material Arbitrary Lagrangian-Eulerian (MMALE) and Efficient Arbitrary Lagrangian-Eulerian (EALE), etc. Nevertheless, the key idea of ALE method is that the computational mesh can move independently (arbitrarily) of the material. Therefore, the motion of the material and of the mesh must be defined. The remapping of the solution variables is performed using the basic ALE kinematic formula (Hughes et al. [1981], Nazem et al. [2006]):

$$\underline{\dot{f}} = \dot{f} + (v_i - v_i^r)\frac{\partial f}{\partial x_i} \tag{2.1}$$

where f is an arbitrary function, v_i is the material velocity, v_i^r is the mesh velocity, $\dot{f}$ denotes the time derivative of f with respect to the mesh coordinates, and $\underline{\dot{f}}$ represents the time derivative of f with respect to the material coordinates. The term $(v_i - v_i^r)$ is the convective velocity.

In the ALE method, the discretized governing equation can be written in a general form as follows (Gadala and Wang [1998], Nazem et al. [2006]):

$$\left[K_{ij}^m\right]\left\{\Delta U_j\right\} + \left[K_{ij}^r\right]\left\{\Delta U_j^r\right\} = \left\{R_i\right\} - \left\{F_i\right\} \tag{2.2}$$

where K^m is the stiffness matrix related to material displacement vector; K^r is the stiffness matrix related to the mesh displacement vector; U is the material displacement vector; U^r is the mesh displacement vector; R is the external load vector; and F is the internal force vector. The material and the mesh displacements are two unknowns at each degree of freedom. Since the mesh displacements are coupled with the material displacements, the number of equations to be solved is

doubled. Therefore, supplementary equations are required to solve the equilibrium equation.

Benson [1989] proposed a split of the ALE operator into a Lagrangian step and an Eulerian step to decouple mesh and material displacements: i) the system of governing equations is solved in the Largangian step using implicit or explicit finite element procedures; and ii) the Lagrangian mesh is then smoothed and the solution variables are remapped on the updated mesh in the Eulerian step (Figure 2-4). In the ALE method based on the operator-split technique, the number of elements and nodes are constant during the analysis and the nodal points are free to move arbitrarily. This approach can be categorized as an r-adaptive scheme (Zienkiewicz and Zhu [1991]), in which the solution variables (e.g. stresses) can be remapped from the old mesh to the new mesh using Equation 2.1 through knowledge of the convective velocities (Nazem et al. [2006]).

In general, there are three main mesh adaptivity or refinement methods referred to as h-adaptivity, p-adaptivity, r-adaptivity, and their combinations (Di et al. [2007], Zienkiewicz and Zhu [1991]):

- h-adaptivity method changes the mesh connectivity through an addition of elements (usually via dividing elements into smaller ones),
- p-adaptivity method enhances the polynomial interpolation space in high strain location regions (usually by increasing polynomial degree of elements)
- r-adaptivity method refines the mesh by relocation of nodes without changing the mesh topology (Susila and Hryciw [2003]).

In most ALE methods with adaptive meshing and operator-split ALE, a single mesh definition is used and is adapted through the smoothing of the mesh nodes. This smoothing is typically applied frequently within analysis steps, but this is only useful when a single mesh can be effective for the duration of a simulation.

2.2.4 MPM (Material Point Method)

The Material Point Method (MPM) belongs to a class of particle-based numerical methods developed to address the mesh distortion issue associated with large deformation problems by discretizing the continuum body by a number of small Lagrangian elements referred to as material points or particles. The MPM can be categorized as a mesh-free method despite the presence of a background mesh which is used to calculate gradient terms (accelerations and deformation gradient). The method is based on the particle-in-cell method (PIC) used for fluid mechanics (Harlow [1964]). Sulsky et al. [1994] extended the method into solid mechanics. Since then the Material Point Method has been applied to many large deformations problems in various fields of mechanics. Recently, multi-phase MPM formulations have been developed to take into account the soil–water interaction in saturated soils. Various geotechnical problems including slope stability, dam, riverbank failures were analyzed using these developments. For example, a two-phase MPM formulation (Al-Kafaji [2013]) was most recently applied to the study of large deformation penetration problems in saturated clay considering different drainage conditions using the isotropic Modified Cam Clay soil model (Ceccato [2015], Ceccato et al. [2016]).

In the MPM, large deformations of material are simulated by a collection of material points that move through a finite element mesh. These points carry all the solution information (density, velocity, acceleration, stress, strain, material parameter, and external loads). The two-phase continuum is discretized with a single set of material points, which carries both fluid and solid properties and deforms according to the displacement of the solid phase. The following gives a brief outline of the solution sequence for a single time step using the two-phase Material Point Method (Ceccato and Simonini [2016], Al-Kafaji [2013]):

The discretized momentum equations are written as

$$M_w \dot{w} = F_w^{ext} - F_w^{int} - F_w^{drag} \tag{2.3}$$

$$M_s\dot{v} = -\bar{M}_w\dot{w} + F^{ext} - F^{int} \tag{2.4}$$

where $\dot{w}$ and $\dot{v}$ are the fluid and soil phase accelerations, the subscripts s and w indicate the soil and water phase, respectively; no subscript indicates that the quantity belongs to the mixture.

M is the mass matrix, F^{ext} is the external force, $F^{int}$is the internal force, and F_w^{drag} is the drag force which takes into account the soil-fluid interaction. The mass balance equation provides the pore pressure increment, and the soil constitutive model gives the effective stress increment.

At the beginning of each time increment, the momentum equations for the fluid (Equation 2.3) and the mixture (Equation 2.4) are initialized by mapping the quantities from the material points to the mesh nodes according the interpolation functions (Figure 2-5(a)). The governing equations of motion are then solved (Figure 2-5(b)). Equation 2.3 is solved for the fluid acceleration at time t

$$\dot{w^t} = M_w^{t-1}\left[F_w^{ext,t} - F_w^{int,t} - F_w^{drag,t}\right] \tag{2.5}$$

Equation 2.4 is solved for the solid acceleration at time t

$$\dot{v^t} = M_s^{t-1}\left[-\bar{M}^t{}_w\dot{w^t} + F^{ext,t} - F^{int,t}\right] \tag{2.6}$$

The velocities of the material points are updated using nodal accelerations and interpolation functions:

$$w_p^{t+\Delta t} = w_p^t + \sum_{i=1}^{n_e} \Delta t N_{i,p}\dot{w^t} \tag{2.7}$$

$$v_p^{t+\Delta t} = v_p^t + \sum_{i=1}^{n_e} \Delta t N_{i,p}\dot{v^t} \tag{2.8}$$

where n_e is the number of nodes per element, $N_{i,p}$ is the interpolation function of node i evaluated at the position of material point p, and Δt is the time increment.

The nodal values are used to compute strains and stresses at the material points according to the velocity and the position (Figure 2-5(c)). The nodal velocities $w^{t+\Delta t}$ and $v^{t+\Delta t}$ are calculated from the updated material points (using momentum equations 2.3 and 2.4) and are integrated to get nodal incremental displacements $\Delta u^{t+\Delta t} = \Delta t v^{t+\Delta t}$. The fluid and solid strains at material points are calculated as

$$\Delta\varepsilon_w^{t+\Delta t} = B_p^t \Delta t w^{t+\Delta t} \tag{2.9}$$

$$\Delta\varepsilon_s^{t+\Delta t} = B_p^t \Delta t v^{t+\Delta t} \tag{2.10}$$

where B_p^t is the matrix of the derivative of the shape functions at the location of material point p. The stresses are obtained according to the constitutive relations. The pore pressure at material points is updated as:

$$p_{w,p}^{t+\Delta t} = p_{w,p}^t + \Delta t \frac{K_w}{n} \left[(1-n)\Delta\varepsilon_{vol,s}^{t+\Delta t} + n\Delta\varepsilon_{vol,w}^{t+\Delta t}\right] \tag{2.11}$$

where $\varepsilon_{vol,s}^{t+\Delta t}$ and $\varepsilon_{vol,w}^{t+\Delta t}$ are the volumetric strains of solid and fluid.

At the end of the time step, the mesh can be updated to the initial configuration or changed arbitrarily because no information is stored in it. The assignment of material points to the mesh elements is updated after the mesh adjustment (Figure 2-5(d)).

2.2.5 SPH (Smoothed Particle Hydrodynamics)

Smoothed Particle Hydrodynamics (SPH) is another numerical method that is part of the larger family of meshless (or mesh-free) methods that has become promising for geotechnical applications (Bui et al. [2008]). The SPH method was initially developed for astrophysical problems (Lucy [1977], Gingold and Monaghan [1977]), but later was extended to a large number of other fields and applications gaining considerable theoretical support from various researchers (Monaghan [2012]). The smoothed particle hydrodynamics is a Lagrangian modeling scheme that allows the discretization of continuum equations by interpolating the properties directly at a

discrete collection of points distributed over the solution domain without the need to define a finite element mesh. Difficulties associated with fluid flow or solid mechanics problems involving large deformations and free surfaces are resolved in a relatively natural way because of the method's Lagrangian nature, associated with the absence of a fixed mesh.

The SPH method is based on dividing the continuum domain into a set of discrete elements, referred to as particles. These discrete particles that carry the material properties have a spatial distance, known as the smoothing length, over which their properties are smoothed by a kernel function. An evolving interpolation scheme to approximate solution variables at any point is used in the SPH method. The value of a variable at a particle can be approximated by summing the contributions from a set of neighboring particles, denoted by subscript j, for which the kernel function, W, is not zero.

$$\langle f(x) \rangle \simeq \sum_j \frac{m_j}{p_j} f_j W(|x - x_j|, h) \tag{2.12}$$

An example kernel function is shown in Figure 2-7. The smoothing length, h, determines how many particles influence the interpolation for a point of interest a (SIMULIA [2016]).

The Smoothed Particle Hydrodynamics (SPH) and Material Point Method (MPM) are promising methods for simulating large deformation problems. Ma and Zhang [2009] presented a detailed comparison between MPM and SPH methods concluding that both methods are worthwhile for the simulation of hyper-velocity impact and extreme deformation problems. The MPM is reportedly less computationally demanding compared to SPH since the time consuming neighboring search is not required. Also, the Smoothed Particle Hydrodynamic analyses are currently subject to several limitations. For example, it is known that the standard SPH method could be susceptible to a so-called tensile instability (Mehra et al. [2012]), which may occur when the material is subjected to a tensile stress state leading to an unstable clustering of SPH particles. This instability is usually related to the interpolation technique

of the standard SPH method (in contrary, the MPM is not inherently a subject to this issue). Although the SPH analyses are, in general, less accurate than conventional Lagrangian finite element analyses when the deformation is not too severe, the SPH method can be very effective for applications involving extreme deformations associated with multi-phase fluid flow (Tartakovsky et al. [2016], Pan et al. [2016]). The SPH method is available in several popular commercially available finite element analysis programs including Abaqus™, but is currently limited to total stress geotechnical analyses (SIMULIA [2016]).

2.2.6 Remeshing and Interpolation Approach

Hu and Randolph [1998a] described a practical approach for large deformation numerical analysis using conventional Lagrangian Finite Element Method with remeshing and interpolation of solution variables subsequently referred to as "Remeshing and Interpolation Technique with Small Strain" (RITSS). The concept was originally demonstrated through a total stress 2D analysis using AFENA finite element package (Carter and Balaam [1995]). The approach is based on the idea of performing remeshing and the interpolation of the solution variables into the new mesh typically every 10-20 increments in order to avoid mesh distortions associated with large deformations. This is essentially a form of the Arbitrary Lagrangian Eulerian approach using rezoning (mesh replacement) analysis and separate solution mapping. The analysis consists of a series of Lagrangian steps with an Eulerian-like phase accomplished by a separate regeneration of the finite element mesh and mapping of all the solution variables from the old mesh into the new one using various interpolation techniques, but without the ALE convection equations. The details of this technique is provided in the next Chapter 3.

The main advantage of remeshing and interpolation approach is that it is based on the conventional Lagrangian Finite Element Method, and the particular application of the method depends on the selected remeshing and interpolation scheme. This approach is available in Abaqus™ Standard as "mesh-to-mesh solution mapping" technique (SIMULIA [2016]) and can be used for two-phase soil media (i.e., effective

stress analysis with advanced soil models). The remeshing and interpolation approach has been applied to a large number of offshore geotechnical problems analyzed by the researchers associated with the Centre for Offshore Foundation Systems at University of Western Australia (Randolph et al. [2008], Hu and Randolph [1998b]). The applications include monotonic and cyclic penetration of penetrometers (Lu et al. [2004], Zhou and Randolph [2009]), penetration of spudcan foundations for mobile jack-up rigs (Hossain et al. [2005], Hossain and Randolph [2010], Yu et al. [2012]), lateral buckling of pipelines (Wang et al. [2010], Chatterjee et al. [2012]) and uplift capacity and keying of mooring anchors (Song et al. [2008], Wang et al. [2009], Tian et al. [2015]). To date, most of these analyses have been performed using relatively simple isotropic soil models.

In this thesis, the large deformation analysis of soil penetration problem with advanced effective stress models is based on the remeshing and interpolation approach and will be discussed in detail in the next chapter.

2.3 Offshore Geotechnical Conditions and Selected Problems

2.3.1 Gulf of Mexico Clay

Offshore oil and gas production is more challenging than the land-based production due to the remote and harsher environment. The ocean seafloor is highly complex due to its geological history and various conditions of sediment deposition. Environmental differences between inland and offshore conditions affect the engineering behavior of the sediments (Randolph and Gourvenec [2011], Gerwick [2007]). For instance, the low-temperature, high-pressure environment of ocean may affect the microstructure and the pore fluid of the offshore sediments. The high biogenic content of ocean sediments affects strength and compressibility of marine soils. The pore fluid properties differ in the ocean and on land. Offshore sediments are saturated with saline water. Thus, geotechnical considerations are important in all aspects of planning, designing,

and operating of offshore structures and facilities.

The Gulf of Mexico is a major source for hydrocarbon production in the United States. The major petroleum-producing areas of the United States include offshore Texas, Louisiana, Mississippi, Alabama and are located within the western and central Gulf of Mexico. Figure 2-8 presents the location and the undersea topography of the Gulf of Mexico.

Prior research at MIT has involved laboratory testing of soil samples from a series of five different sites on the continental slope of Gulf of Mexico (Figure 2-9). Based on these studies Whittle and Sutabutr [2005] defined typical properties of clays in Gulf of Mexico leading to an average set of soil properties referred to as "Average Gulf Clay". Recently, Cheon [2010] compiled a massive database of a total of 97 geotechnical investigations from 14 offshore project sites covering the past twenty years of deepwater development in the Gulf of Mexico and analyzed spatial variability in geotechnical properties for offshore foundations, Figure 2-10.

The Gulf of Mexico is an ocean basin surrounded by the North American continent. The size of the Gulf basin is approximately 1.6 million km^2 (615,000 sq. mi). The average water depths of the Gulf of Mexico are about 1500 m (~5,000 ft) with the maximum of about 4000 m (~13,000 ft). The water depths in the study area range from 900 m (3,000 ft) to 2700 m (9,000 ft). Approximately a half of the Gulf of Mexico is comprised of shallow and inter-continental shelf areas in which the water depth is shallow as shown in Figure 2-8. The continental shelf width ranges from 16 km (10 mi) off the Mississippi River to 354 km (220 mi) offshore west Florida (MMS [2000]). The continental slope and canyon area, where the most site investigations were performed, extends from the shelf edge at approximately 200 m (650 ft) water depth to a water depth of approximately 3000 m (10,000 ft). The overall gradient of the continental slope is 3 to 6 degrees. The shallow sub-surface stratigraphy within the research area is primarily interpreted as clays with minor zones containing sand seams. The soil condition is normally to slightly over-consolidated, marine clay. Typically, less than 6 m (20 ft) of Holocene sediments (less than 12,000 years old) cover much deeper Pleistocene sediments (greater than 12,000 years old). Holocene deposits are

composed of very soft, highly plastic clay having high water content. Pleistocene deposits are comprised of very soft clay at the top of the Pleistocene deposit to stiff or very stiff at depth. The upper part of soil layer in the study area (from the mudline to a depth of about 15 to 18 m (50 to 60 ft)) consists of hemipelagic sediments which were deposited by relatively high sea level and shows high variation of its soil properties (Cheon [2010], Dugan and Germaine [2008]). Thereafter, the soil layer is composed of mostly turbitites, the geologic deposits of a sediment gravity flow that distributes vast amounts of clastic sediment into the deep ocean, whose properties may vary with distance from the shoreline at low sea level (Anderson et al. [2004]).

According to Cheon [2010], there is a high water content (=>100%) layer within the upper 2.4 to 6.0 m (8 to 20 ft) of the sediments after which the water content gradually decreases to approximately 50% at 18 to 21 m (60 to 70 ft) below the mudline. Then, the water content decreases further and remains within the range of 35 to 70% as shown in the upper part of the Figure 2-12. The Gulf of Mexico sediments are classified as highly plastic clays (CH) with regard to the Unified Soil Classification System, and the plasticity chart based on the measured data is presented in Figure 2-12. The submerged unit weight for the Holocene deposits is within a range of 2.4 to 3.9 kN/m^3 (15 to 25 pcf). For the depths below the mudline up to 60 m (200 ft), the average value of the submerged unit weight is approximately 6.3 kN/m^3 (40 pcf) (Figure 2-13). The database compiled by Cheon [2010] includes the undrained shear strength data obtained using the remote vane and cone penetration tests in-situ and using conventional laboratory tests such as torvane, miniature vane, undrained unconsolidated (UU) triaxial and direct simple shear (DSS) tests. Figure 2-14 summarizes the measured undrained shear strength data versus depth[2].

The geotechnical group at MIT investigated samples from five different sites with water depths ranging from 750 to 1200 meters (2500 to 4000 feet) on the continental slope of Gulf of Mexico (Whittle and Sutabutr [2005]). Sutabutr [1999] calibrated the MIT-E3 model, an advanced effective stress soil model that will be presented in the

[2]The values of cone factors used to determine undrained shear strength from the net cone tip resistance is shown in Figure 2-15 with the average N_{kt} equal to 17.5.

next chapter, using the results of these investigations. The one-dimensional compression data from the Constant Rate of Strain (CRS) and incremental oedometer tests are presented in Figure 2-16. The shown virgin consolidation line with the determined parameters λ (compressibility) and e_0 (void ratio at reference stress) presents the average compression behavior of the Gulf of Mexico clay and corresponds to a set of input parameters referred to as "Average Gulf Clay" using MIT-E3 soil model. Figure 2-17 presents the incremental swelling strain versus stress level showing the comparison of measured one-dimensional swelling behavior of GoM clays with the "Average Gulf Clay" representation. For each of the five offshore sites, the small strain stiffness parameter (κ_0) was obtained from resonant column tests that measured maximum shear modulus, $G_{max}/\sigma'_{v0} \simeq 150 \pm 50$. Figures 2-18 and 2-19 present the measured effective stress paths and shear stress-strain responses of Gulf of Mexico clay obtained from the laboratory K_0-consolidated undrained triaxial compression and extension tests (Germaine and Ladd [1988]). The large strain friction angles from the five projects were within $\varphi'_{TC} = 25.6 \pm 1.2$, and the friction angles from the extension test were $\varphi'_{TE} = 27.8 \pm 2.3$. The extension mode of shearing was more challenging to obtain reliable friction angles due to laboratory sample necking issues (Whittle and Sutabutr [2005]). The undrained shear strength ratio in triaxial compression is within the range of $s_{uTC}/\sigma'_p = 0.22 - 0.30$ for normally consolidated case. In the extension mode, the undrained shear strength ratio is $s_{uTE}/\sigma'_p = 0.16$ measured at 5% axial strain for normally consolidated conditions. Figure 2-20 summarized the measured data from K_0-consolidated undrained Direct Simple Shear (CK_0UDSS) tests on the Gulf of Mexico clays. The undrained shear strength ratio in Direct Simple Shear mode of shearing was determined to be $s_{uDSS}/\sigma'_p = 0.233$ for normally consolidated case. The results show that the MIT-E3 soil model predictions with generic Average Gulf Clay (AGC) parameters can provide a reasonably close agreement the measured behavior of Gulf of Mexico clay from the considered deepwater sites.

2.3.2 Deepwater Conductors under Lateral Loads

The offshore conditions present a unique set of environmental conditions that dominate the methods, support, and procedures to be employed in offshore construction. The offshore piles and conductors must sustain lateral loading from storm-driven waves and wind (Figure 2-11). The emergency drift off and drive off loading scenarios (2-21) should also be assessed. The design of the piles for an offshore platform or the conductors connected to mobile offshore vessels presents complex problems of soil-structure interaction (Kausel [2010], Randolph and Gourvenec [2011]). All of the prior analyses for the riser system use simple rheological models to represent conductor-soil interactions. These models comprise non-linear springs that describe the relation between the lateral soil reaction force and horizontal displacement at a given depth below mudline (Figure 2-23). These rheological interaction models, known as p-y curves (after Reese et al. [1974] and Matlock [1970]) were developed originally to describe the response of pile foundations under lateral loads and have been calibrated empirically using results of instrumented field tests.

The widely used p-y method of analysis of laterally loaded piles consists of dividing the pile into a series of increments of equal length and solving the governing differential equation using the finite difference technique (Figure 2-22). The pile is assumed to be rigid, and the soil response is characterized as a set of discrete springs whose characteristics are represented by the selected p-y curves. The upper part of Figure 2-23 shows the idealization used in the p-y method. Figure 2-23 presents a cylindrical pile under lateral load with a thin slice of soil shown at the depth z below the ground level. When the pile is displaced laterally a distance y_1, the stress distribution around the pile changes increasing on the front side and decreasing on the back side of the pile with both normal and shearing components. The integration of the unit stresses produces the quantity p_1, known as the soil reaction which acts in the opposite direction to y_1. The dimension of soil resistance is force per unit length along the pile. The soil resistance, p is a non-linear function of the pile displacement, y at a certain discrete points.

The design curves presented in American Petroleum Institute (API) codes (API [2000]) have been largely unchanged from early versions based on the work of Matlock [1970] and are badly out of date. For example, they do not include well-established plasticity solutions for the ultimate lateral capacity of a pipe section (Randolph and Houlsby [1984]) shown in Figure 2-24. A more direct approach to consider the response of the soil may be achieved by the finite element method (FEM). An appropriate solution with the FEM requires a three-dimensional model at and near the ground surface, the consideration of non-linear geometry and proper constitutive modeling of the in situ soil.

Recent studies on conductor-soil interaction have been carried out in conjunction with the fatigue performance of conductors (Jeanjean [2009], Zakeri et al. [2015]) and have emphasized the importance of updating the conventional p-y response curves. Templeton [2009] carried out detailed 3D finite element analyses of a conductor embedded in the soil mass which is modeled as an elasto-plastic strain hardening material with input properties based on typical undrained shear strength and shear wave velocity profiles for deepwater sites in the Gulf of Mexico. The equivalent p-y curves are derived from the analyses at selected depths and found to differ substantially from the API design methods. The results are then validated through comparisons with results from a program of centrifuge model tests (Jeanjean [2009]). Although there is some discrepancy between the computed and measured response, the overall agreement is very good once differences in shear strength between the loading rates in the centrifuge and conventional lab tests are considered[3] (Figure 2-25).

The analyses by Templeton [2009] use conventional small strain finite element analyses (using Abaqus™ finite element analysis program) and the final validation of p-y curves focuses on response of the conductor for deformations up to 0.1 - 0.2D (Figure 2-25). It is well known that geometric non-linearities affect significantly the pile/conductor soil response close to the mudline, through the processes of post-holing (progressive separation along the interface) and mounding. Figure 2-26 shows

[3]A rate of loading correction (25% in undrained shear strength) is applied to achieve matching between analyses based on properties from lab tests and results from the centrifuge model tests.

an interesting photo of clay surface deformations in one of the prior centrifuge tests. The photo shows clearly the depression behind the pile (with a series of circumferential cracks) and the mounding ahead of the pile. For the large deformations involved in drive-off load events, these geometric non-linearities may extend to depth of more than 5 diameters (4.6 m or 15ft) and play a critical role in computing reaction forces.

In this thesis, the initial conductor-soil interaction analyses will follow the similar methodology presented by Templeton [2009], and will be extended to the large deformation effective stress analyses using advanced soil models capable of modeling anisotropic and complex soil behavior. The effect of axial tension and conductor properties will be evaluated. The full methodology developed during this research is described in the next chapter.

2.3.3 Cone Penetration in Soft Clay

The cone penetration test (CPT) is one of the common in-situ tests used in offshore geotechnical site investigations. Figure 2-27 shows the visual and schematic view of the standard pone probe used in the offshore cone penetration tests. A steel 60 degrees cone with the diameter of 3.6 cm and with the in-built measuring devices is pushed into the soft soil at a constant penetration rate, $v = 2\,cm/s$. The soil characteristics are then inferred from the monitored tip resistance, sleeve friction, and pore pressure measurements. The interpretation of engineering properties of soils is based on theoretical analyses and empirical interpretation methods (Levadoux [1980], Baligh and Levadoux [1986], Aubeny [1992], Whittle et al. [2001]). The reliable numerical modeling of this test could greatly contribute to the development of much reliable correlations between engineering properties of various soils and in-situ measurements. Most of the existing empirical and theoretical correlations are based on fully drained or fully undrained conditions assuming a simplified model of soil behavior. The analysis in partially drained conditions using realistic numerical modeling of soil behavior remains to be a challenging task.

The most recent work on numerical modeling of piezocone penetration test under variable drainage conditions was conducted by Ceccato et al. [2016] using the

two-phase Material Point Method (Al-Kafaji [2013]) with an effective stress isotropic Modified Cam Clay soil model. Figure 2-28 shows a 20 degree slice MPM model used in the numerical analysis. The cone is slightly rounded in order to avoid numerical problems associated with a discontinuous edge at the cone base. All other dimensions are reportedly correspond to those of a standard penetrometer with the diameter of 0.036 m (3.6 cm). The penetrometer is modeled as a rigid body that moves downward at a prescribed velocity of 2 cm/s applied at the nodes of the structure. The displacements are constrained in normal direction at the lateral mesh surfaces, and the bottom mesh if fully fixed. The radial boundaries of the slice are impermeable while the bottom and outside boundaries are permeable. The MPM method is used to perform large deformation penetration analysis. The soil-structure interaction is modeled with an MPM-specific algorithm. An external vertical stress of 50 kPa is applied on the top surface of the soil simulating an initial position of the cone at about 5 m depth assuming a submerged soil unit weight of 10 kN/m^3. The material weight is neglected, and the initial stresses are constant with depth with the zero initial excess pore pressures. The soil is represented as a normally consolidated Kaolin using the Modified Cam Clay (assuming von Mises yield criteria) soil model (Roscoe and Burland [1968]) with a coefficient of earth pressure, $K_0 = 0.68$. The effect of drainage conditions is investigated by changing the hydraulic conductivity of the soil at a fixed penetration rate.

The normalized penetration rate is defined as

$$V = \frac{vD}{c_v} \tag{2.13}$$

where v is penetration rate, D is cone diameter, and $c_v$is soil vertical consolidation coefficient.

Ceccato et al. [2016] assume a constant "reference value" of the consolidation coefficient which is proportional to the in-situ vertical effective stress (σ'_{v0}) as proposed by Schneider et al. [2007]:

$$c_v = \frac{k(1+e_0)\sigma'_{v0}}{\lambda\gamma_w} \tag{2.14}$$

where k is permeability, λ is virgin compression index, e_0 is void ratio, γ_w is unit weight of water, and σ'_{v0} is initial vertical effective stress.

Figure 2-29 presents the computed tip stress over the normalized cone displacement in case of smooth contact for undrained, partially drained (with V=1.2 and V=12.0) and drained conditions. The steady-state tip stress is reached withing 5D and 7D penetration displacements.

In undrained conditions, the net tip resistance ($q_c - \sigma_{v0}$) is proportional to the undrained shear strength (s_u) through a cone factor ($N_c = \frac{q_{c,net}}{s_u}$). The cone factor obtained from MPM analysis performed by Ceccato et al. [2016] is 9.6 assuming a smooth cone interface. This value is in a good agreement with other published numerical studies by various researchers such as Teh and Houlsby (1991), Van den Berg (1994), Yu (200), Lu et al. (2004), Beuth (2012), and Qiu (2014) considering similar conditions (rigidity index, cone roughness, soil model, etc.). Figure 2-30 summarized the comparison of published results of cone factor as a function of cone roughness (Ceccato [2015]). Ceccato [2015] reports that the estimated cone factor for smooth cone is in very good agreement with previous studies, but there is an overestimation of the cone factor for increasing cone roughness. Moreover, in contrast with theoretical expectations, the cone factor from her analysis seems to be in a non-linear relationship with the interface roughness. Ceccato [2015] explains that this maybe caused by the contact formulation she was using which generates oscillations and an overestimation of the contact forces when bodies with very different compressibility are involved. Ceccato [2015] states that future developments are needed to investigate this issue.

Assuming the undrained penetration as a reference condition, the normalized resistance and the normalized pore pressure is defined as

$$\frac{q_{c,net}}{q_{c,ref}} = \frac{q_c - \sigma_{v0}}{q_{c,undrained} - \sigma_{v0}} \tag{2.15}$$

$$\frac{\Delta u}{\Delta u_{ref}} = \frac{\Delta u}{\Delta u_{undrained}} \tag{2.16}$$

where $q_{c,undrained}$ is tip resistance and $\Delta u_{undrained}$ is excess pore pressure in undrained conditions.

The pore pressure parameter B_q is defined as

$$B_q = \frac{\Delta u}{q_c - \sigma_{v0}} \tag{2.17}$$

Figure 2-31 shows the variation of the normalized cone resistance, normalized pore pressure, and pore pressure parameter versus the normalized penetration rate from the MPM analyses performed by Ceccato et al. [2016].

The numerical MPM analyses with different drainage conditions were compared to the published experimented data obtained with centrifuge tests on Kaolin by Schneider et al. [2007]. Figure 2-32 shows the comparison of cone resistance between MPM results and experimental data as a function of normalized velocity. The MPM analysis uses a friction coefficient of 0.28 to compare with the experimental data. Figure 2-33 presents the effect of the normalized velocity on the pore pressure factor between numerical simulations and experimental tests. The two-phase MPM numerical analyses using Modified Cam Clay model performed by Ceccato et al. [2016] show a good agreement with the experimental data of the normalized resistance ratio for higher normalized velocities (close to the undrained conditions), but underestimates the resistance in fully drained conditions (lower normalized velocities) with regard to the measured data.

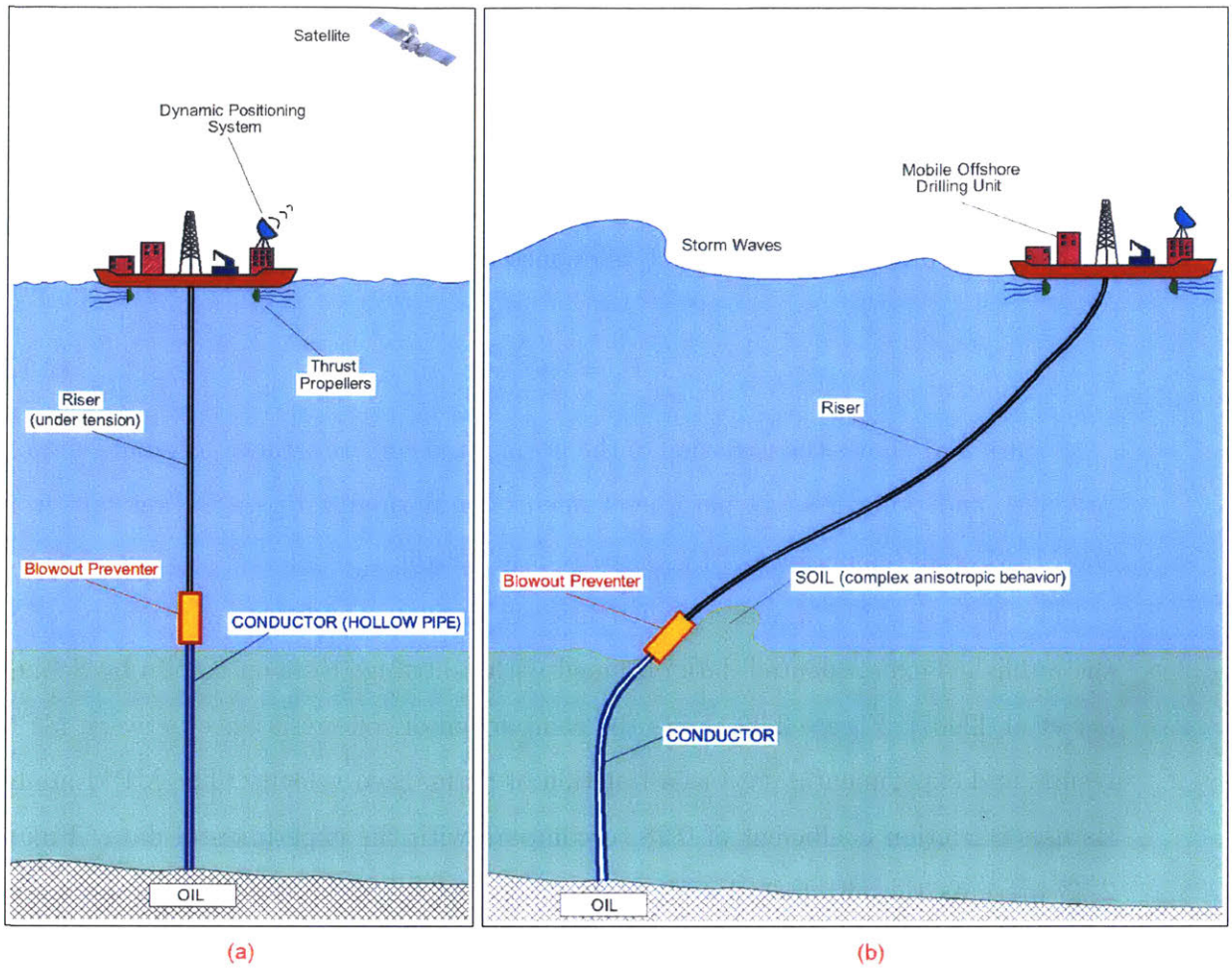

Figure 2-1: Schematic (Not to scale) of Conductor-Riser-Vessel System - Normal Operation (a) vs. Loss of Vessel Position (b)

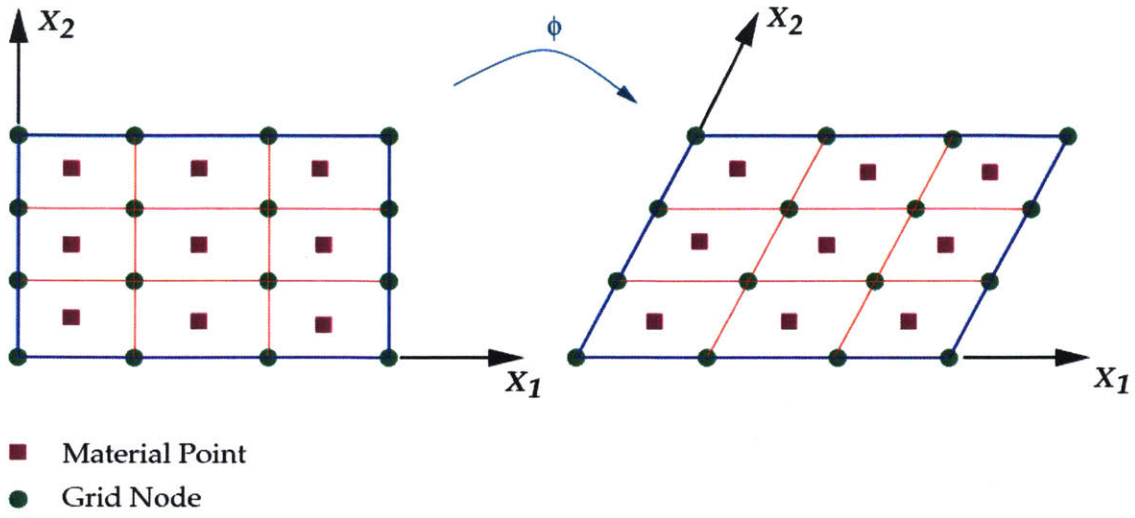

Figure 2-2: Lagrangian Approach (adapted from Banerjee)

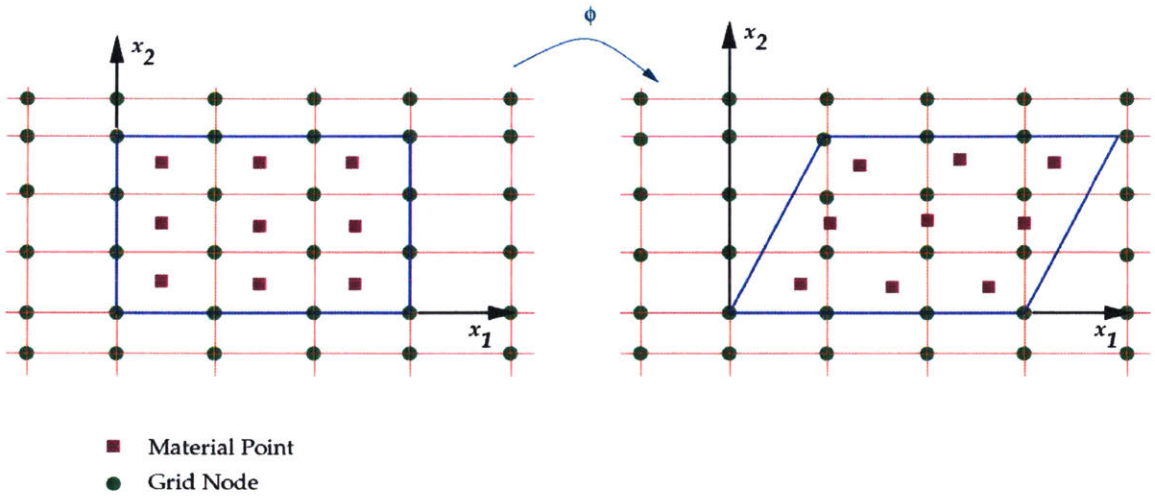

Figure 2-3: Eulerian Approach (adapted from Banerjee)

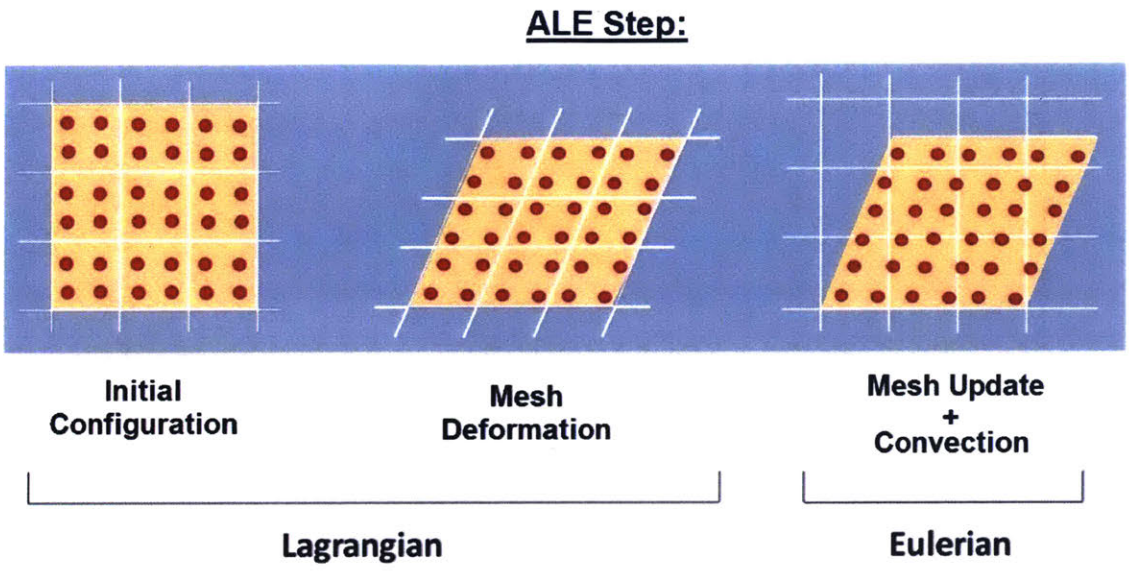

Figure 2-4: Single ALE step (adapted from Ceccato and Simonini [2016])

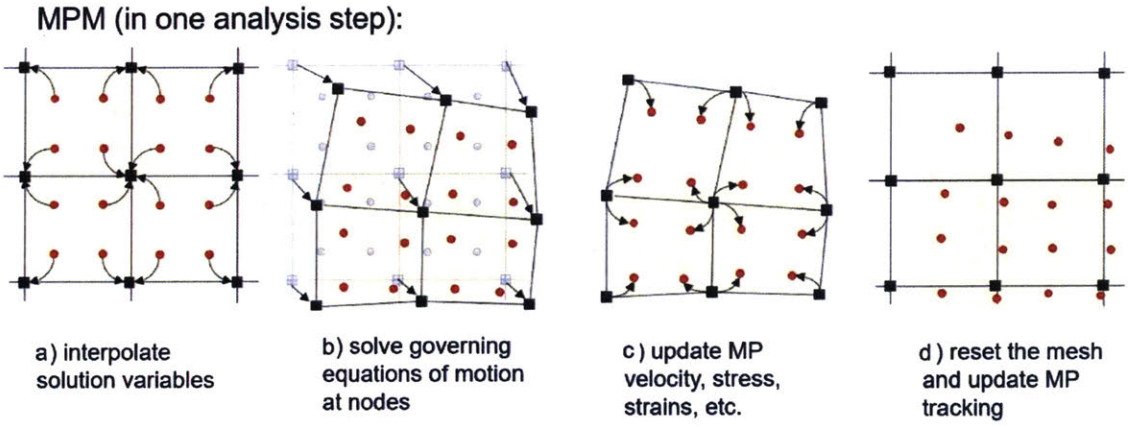

Figure 2-5: Computation scheme of MPM (Ceccato et al. [2016])

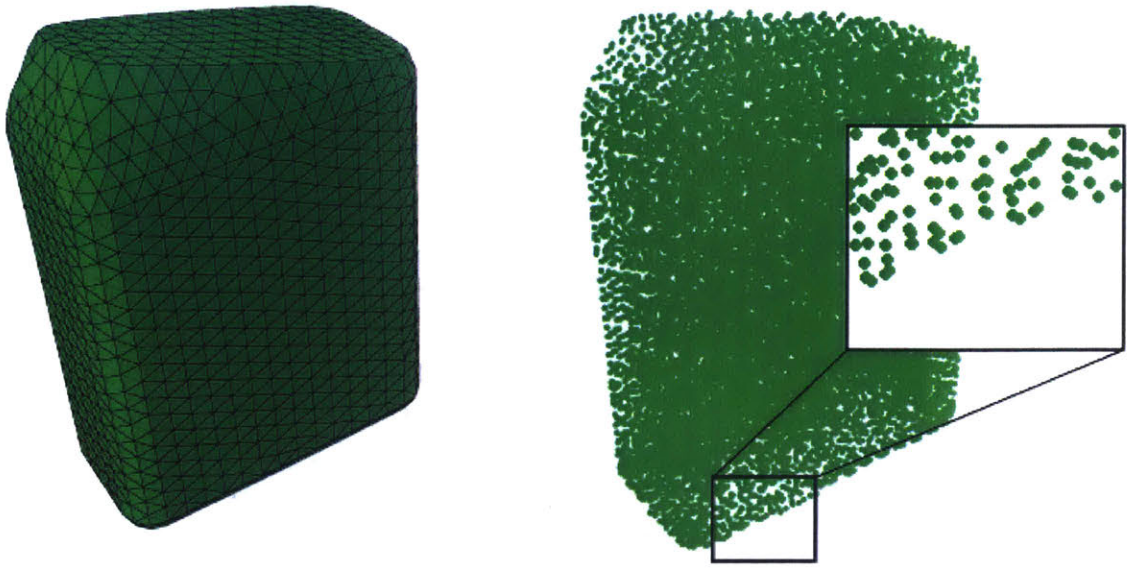

Figure 2-6: Finite element mesh and SPH particle distribution (SIMULIA [2016])

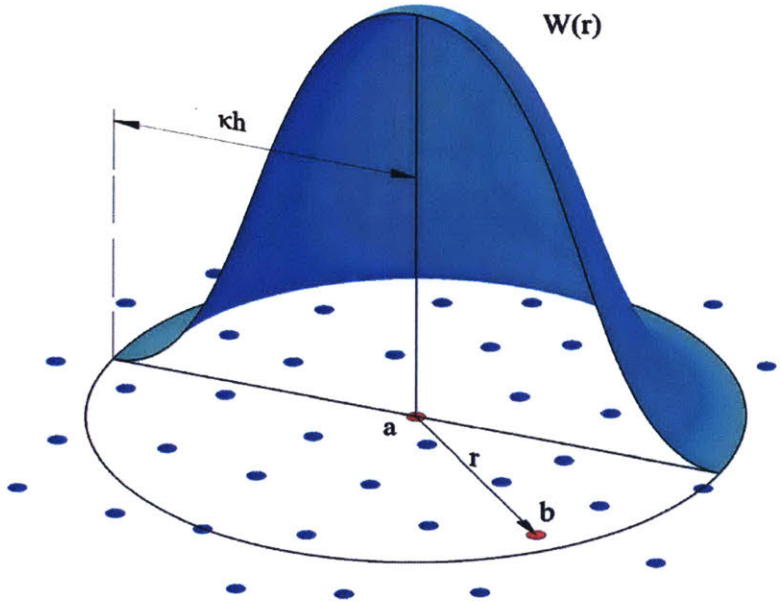

Figure 2-7: SPH Kernel function (Wang et al. [2016])

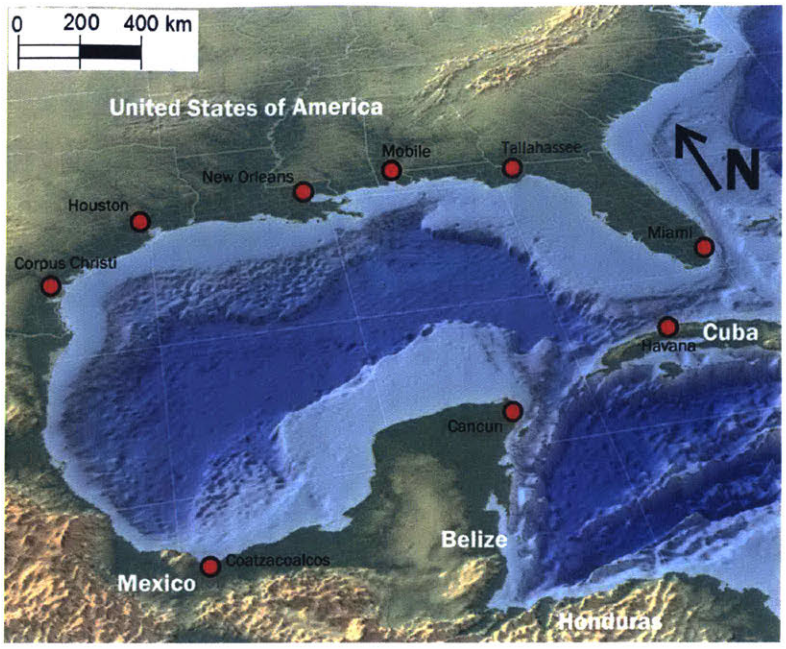

Figure 2-8: Undersea topography of the Gulf of Mexico (NOAA, Public Domain)

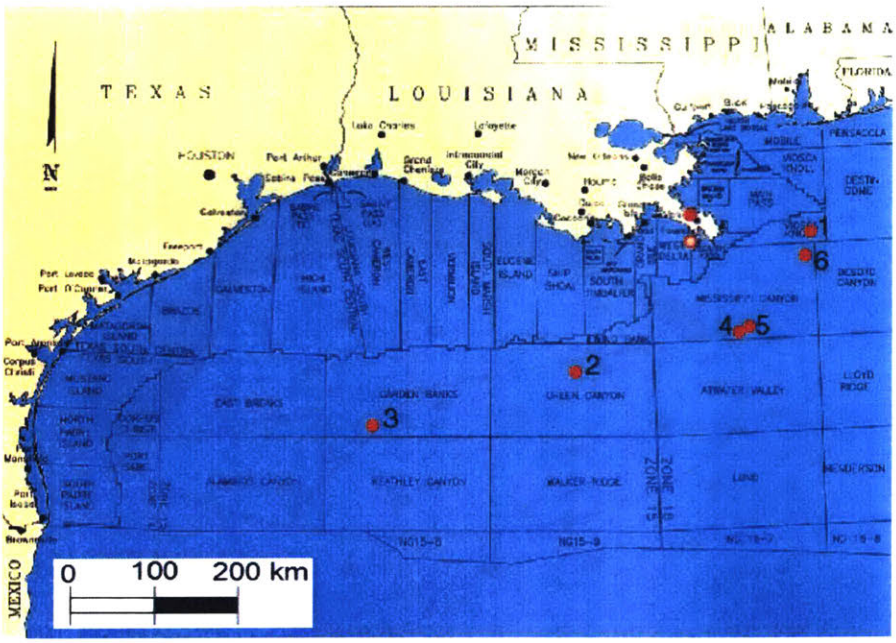

Figure 2-9: Location of deep-water sites in the Gulf of Mexico leading to an average set of soil properties referred to as "Average Gulf Clay" (Whittle and Sutabutr [2005])

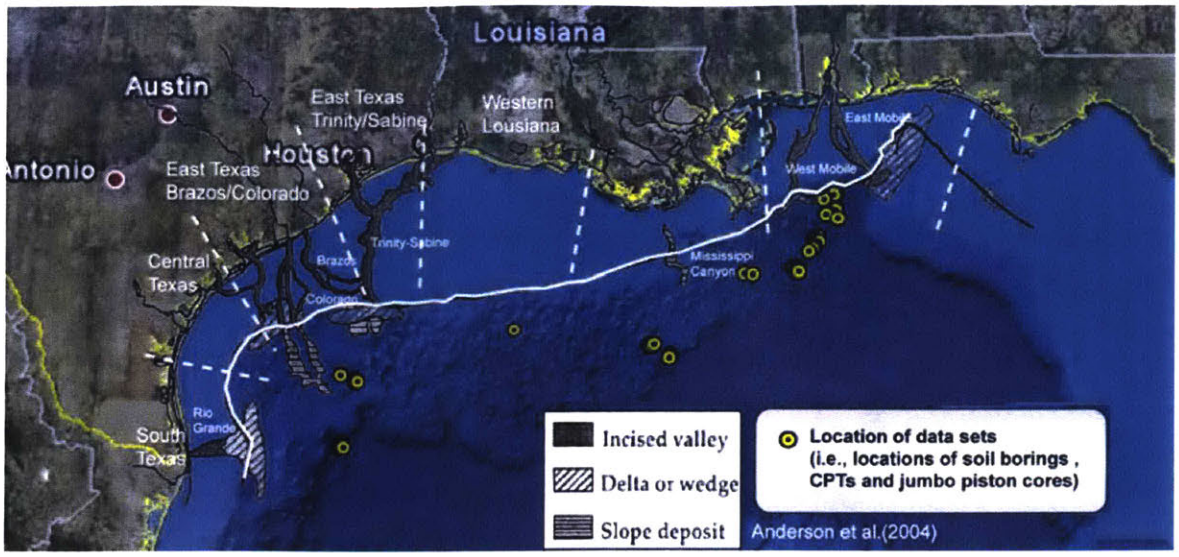

Figure 2-10: Location of Data Sets Reported by Cheon [2010]

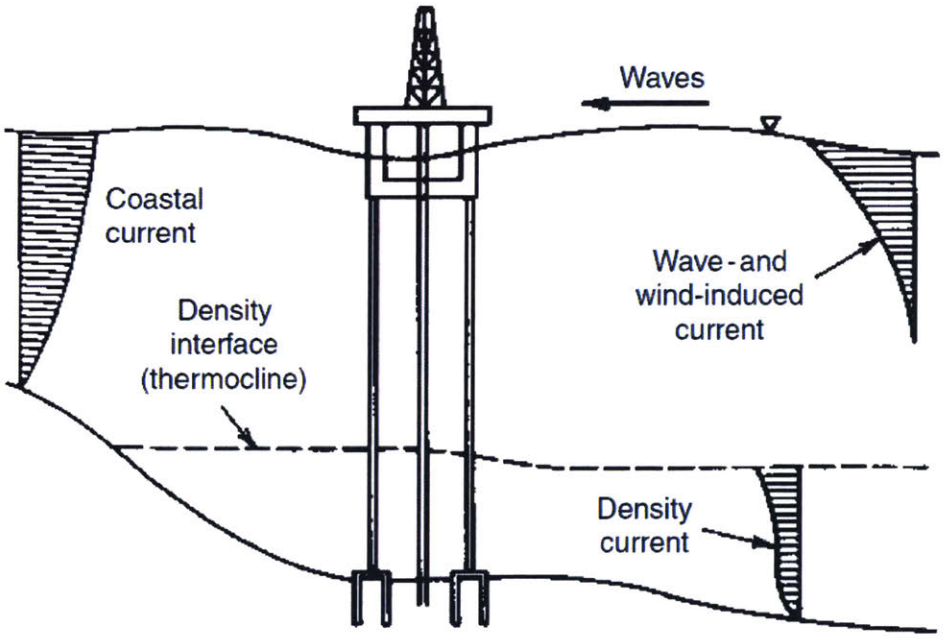

Figure 2-11: Offshore conditions, waves and deepwater currents Gerwick [2007]

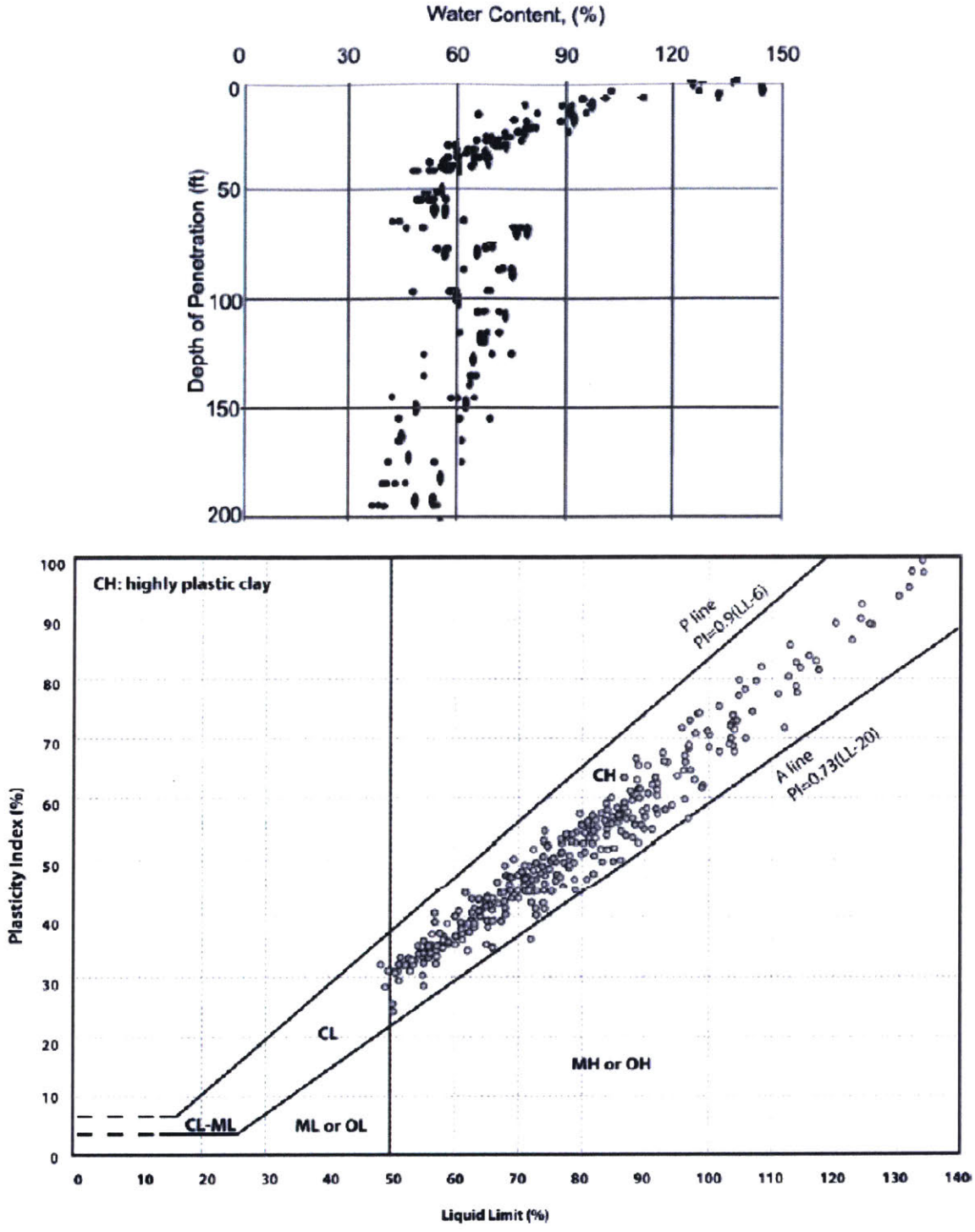

Figure 2-12: Water Content and Plasticity Chart of GoM Clay Compiled by Cheon [2010]

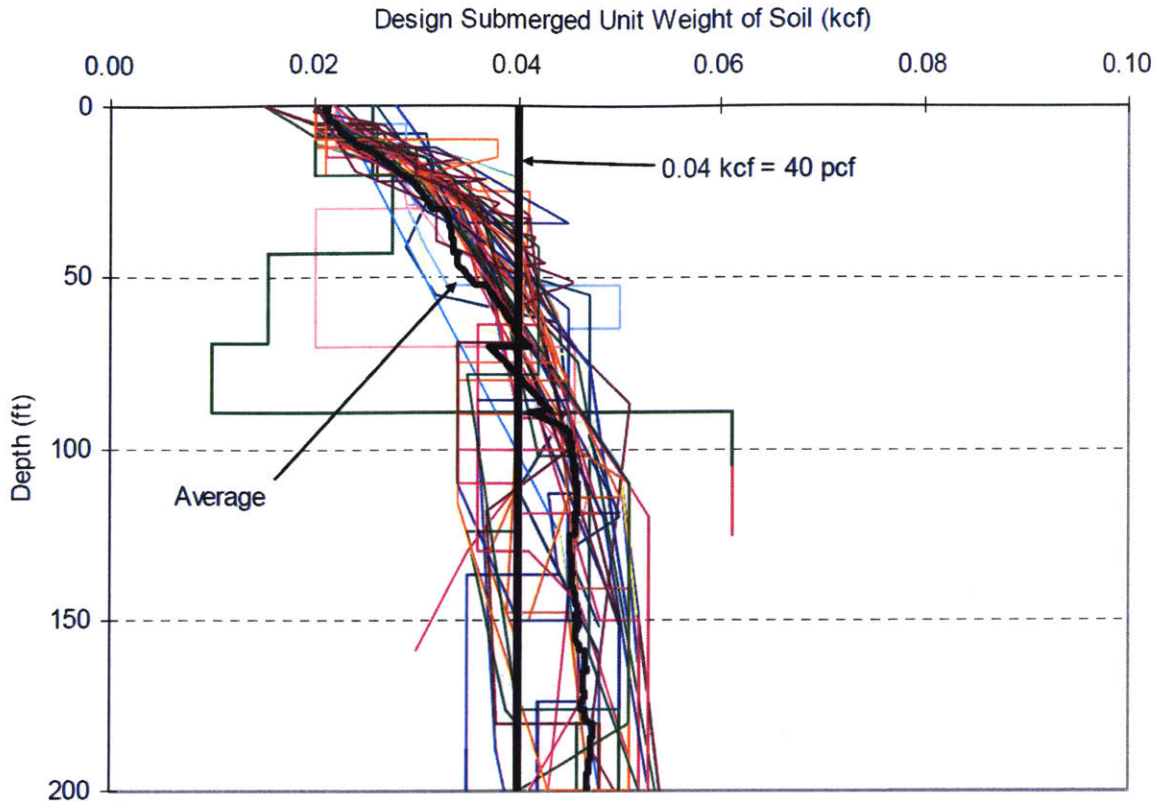

Figure 2-13: Submerged Unit Weight of Soil versus Depth of Gulf of Mexico Clay (Cheon [2010])

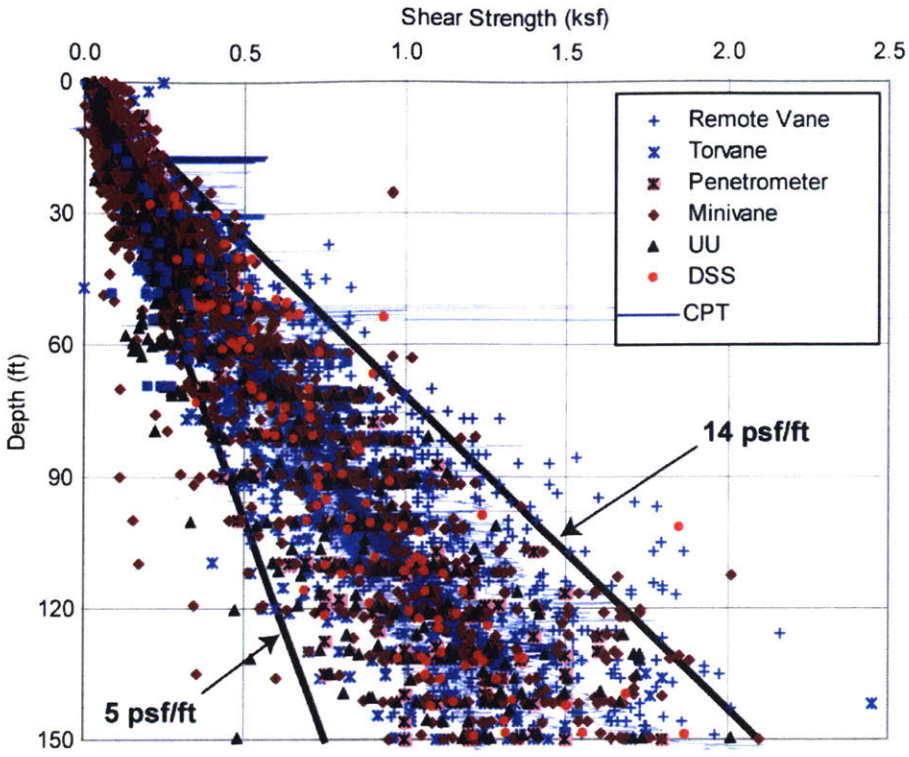

Figure 2-14: Undrained Shear Strength vs. Depth of GoM Clay Compiled by Cheon [2010]

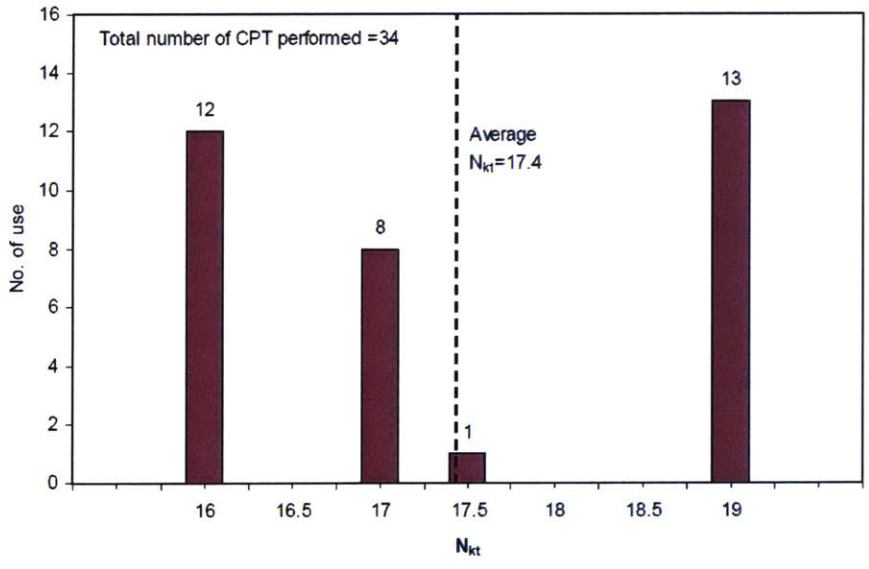

Figure 2-15: Reported Cone Factor used in Gulf of Mexico (Cheon [2010])

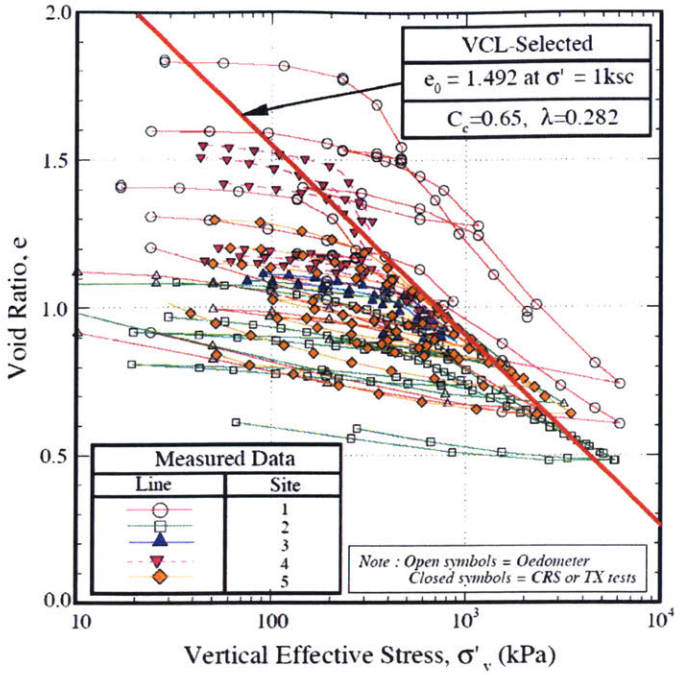

Figure 2-16: GoM Clay Compression Data (Sutabutr [1999])

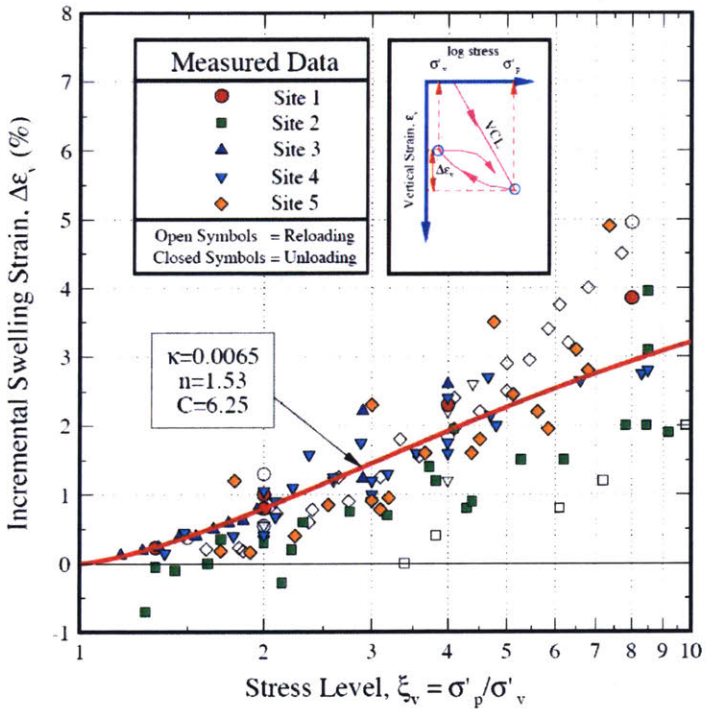

Figure 2-17: 1-D swelling behavior of GoM Clay (Sutabutr [1999])

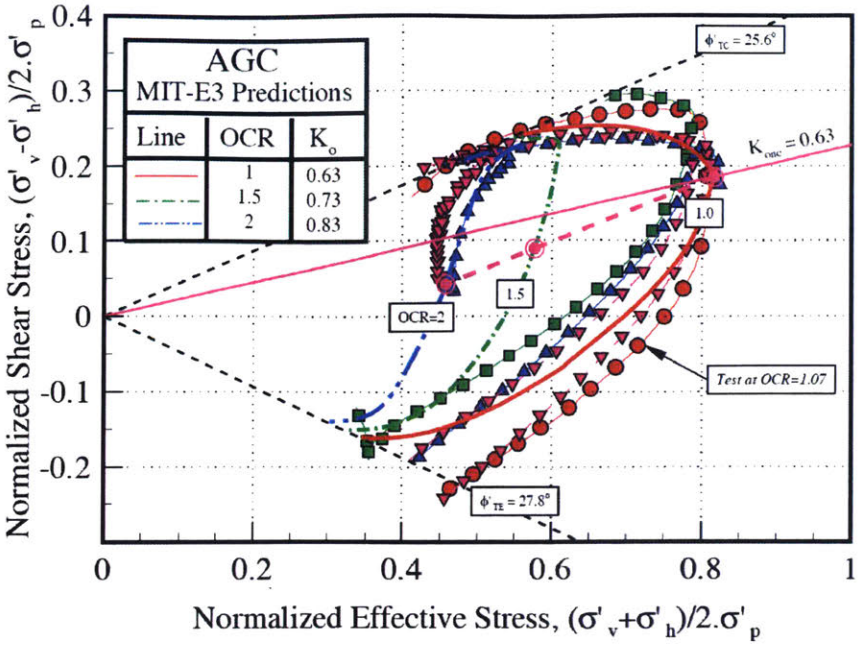

Figure 2-18: Triaxial Testing of GoM Clay - Effective Stress Paths (Sutabutr [1999])

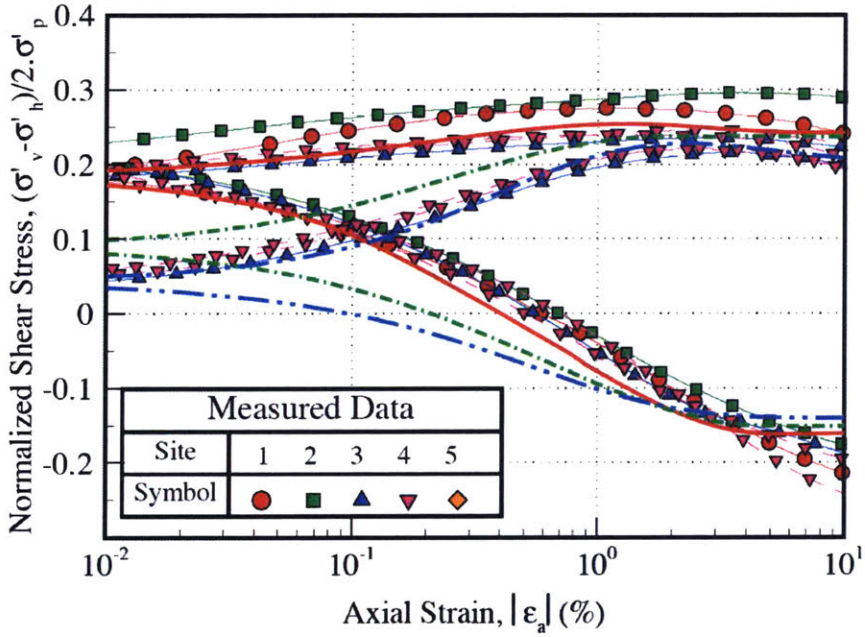

Figure 2-19: Triaxial Testing of GoM Clay - Shear stress-strain response (Sutabutr [1999])

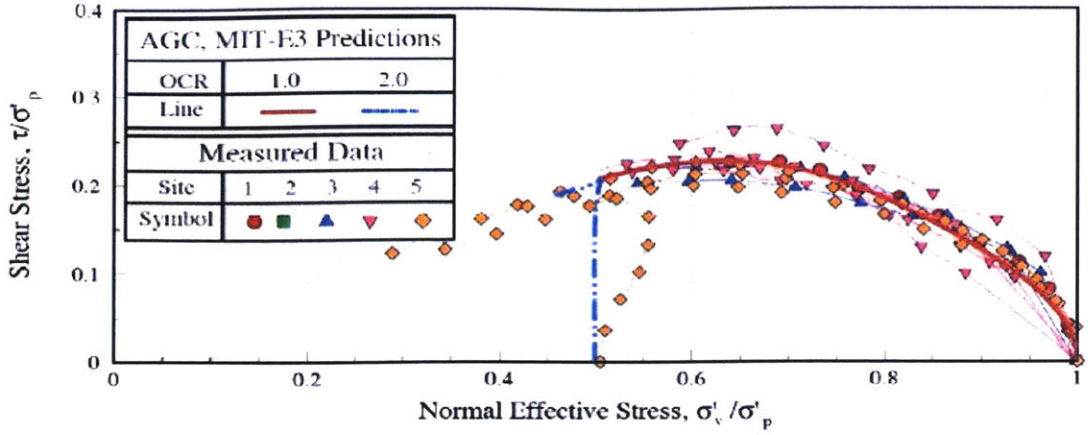

a) Effective stress paths

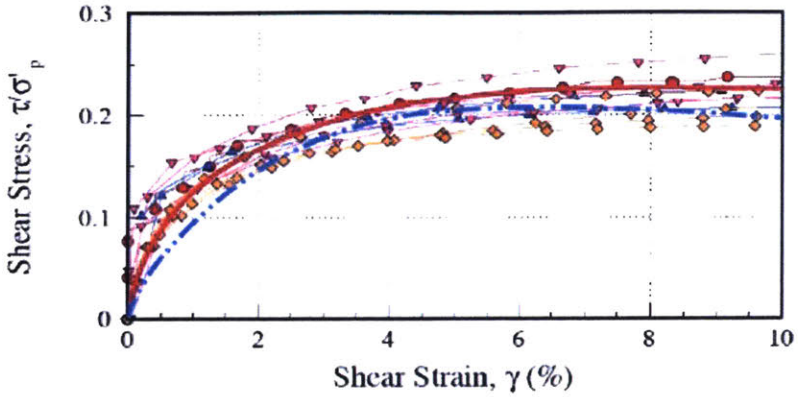

b) Shear stress-strain behavior

Figure 2-20: GoM clays in K_0-consolidated undrained direct simple shear tests (Sutabutr [1999])

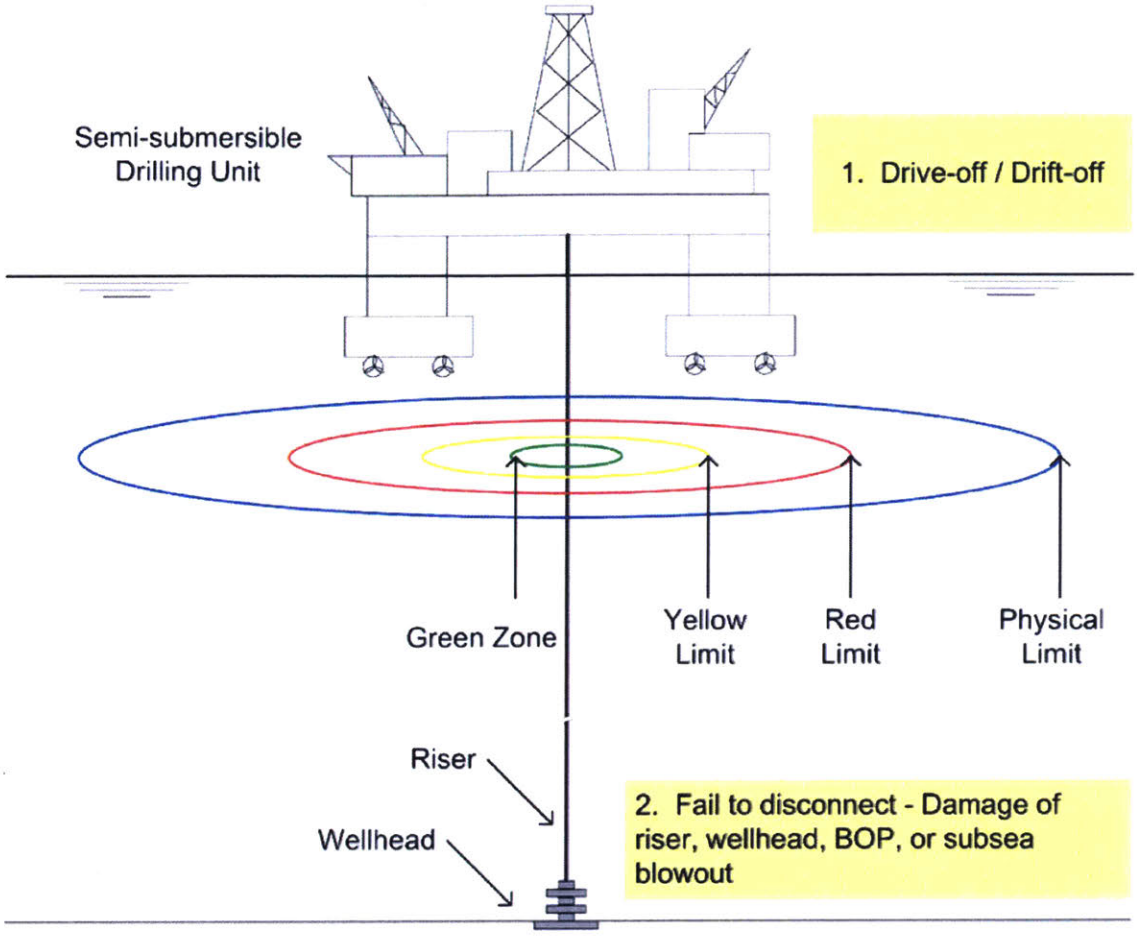

Figure 2-21: Dynamically Positioned Offshore Operation with Excursion Limits - yellow, red, physical limits are not to scale (Chen et al. [2008])

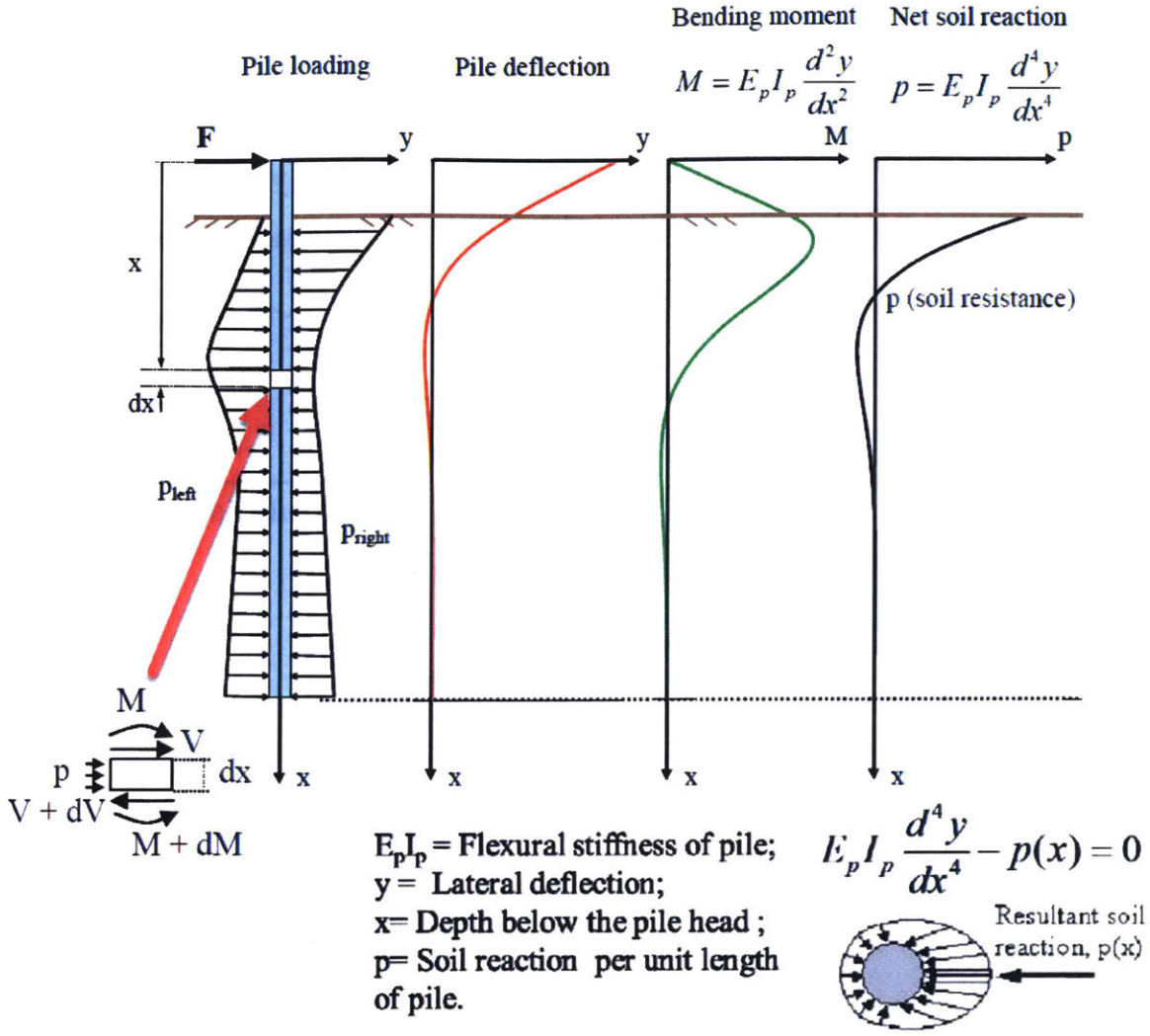

Figure 2-22: Analysis of Laterally Loaded Pile Based on Beam theory (Pando [2013])

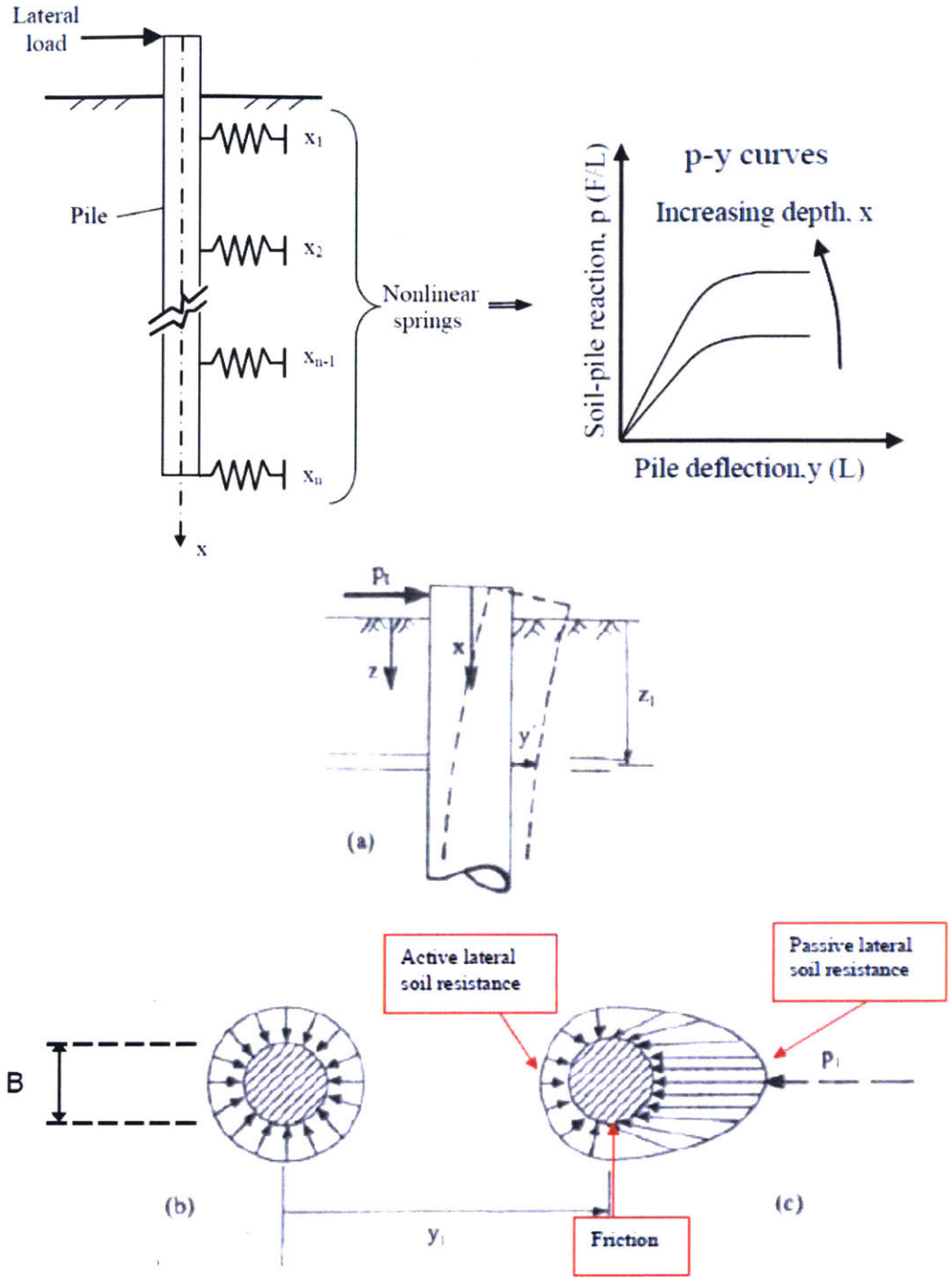

Figure 2-23: Genesis of the P-Y curves (Reese et al. [1974], Matlock [1970])

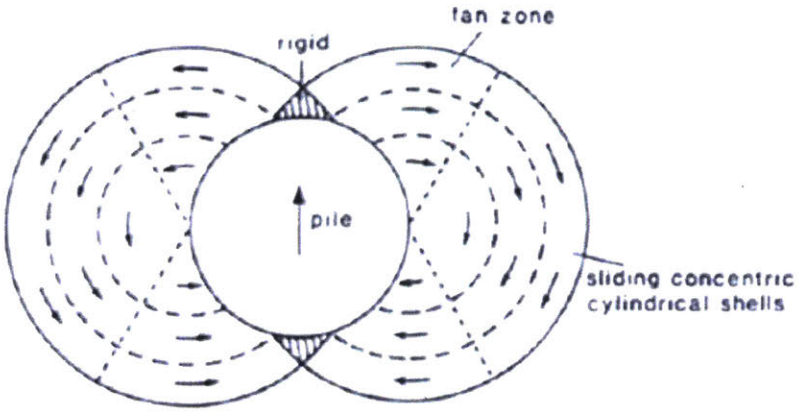

Figure 4.39 Flow mechanism for soil around laterally loaded pile

$$p_u = s_u d \left\{ \pi + 2\Delta + 4\cos\left(\frac{\pi}{4} - \frac{\Delta}{4}\right)\left(\sqrt{2} + \sin\left(\frac{\pi}{4} - \frac{\Delta}{4}\right)\right)\right\} = N_p s_u d$$

$$\sin\Delta = \frac{f_s}{s_u}$$

f_s/s_u	0.0	0.2	0.4	0.6	0.8	1.0
N_p	7.2	9.8	10.6	11.1	11.6	12.0

Figure 2-24: Plastic failure mechanism for laterally loaded conductor pile in plane strain (Houlsby & Randolph, 1984)

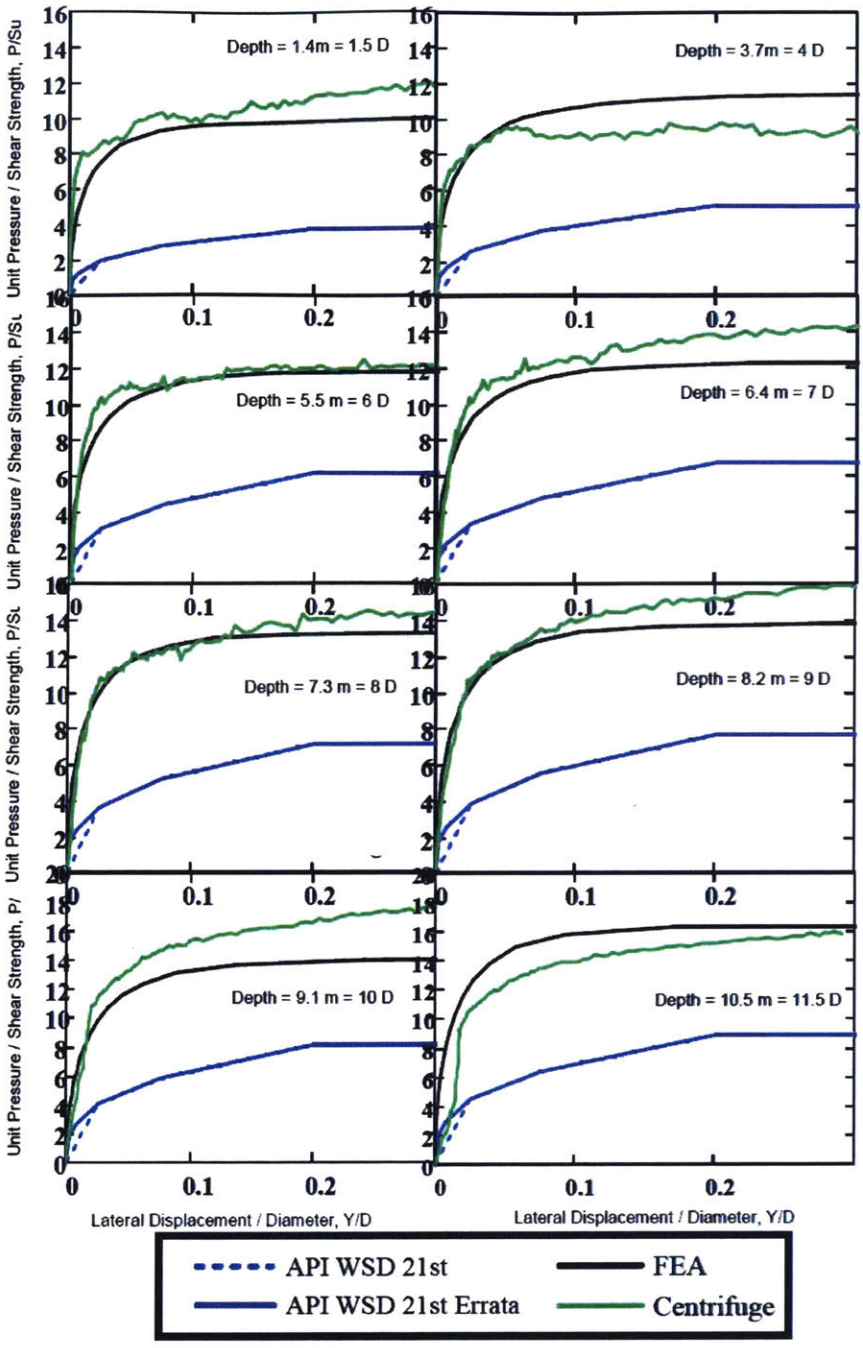

Figure 2-25: Comparison of computed p-y curves from FE models with data measured in centrifuge model tests at 8 depths (Jeanjean, 2009)

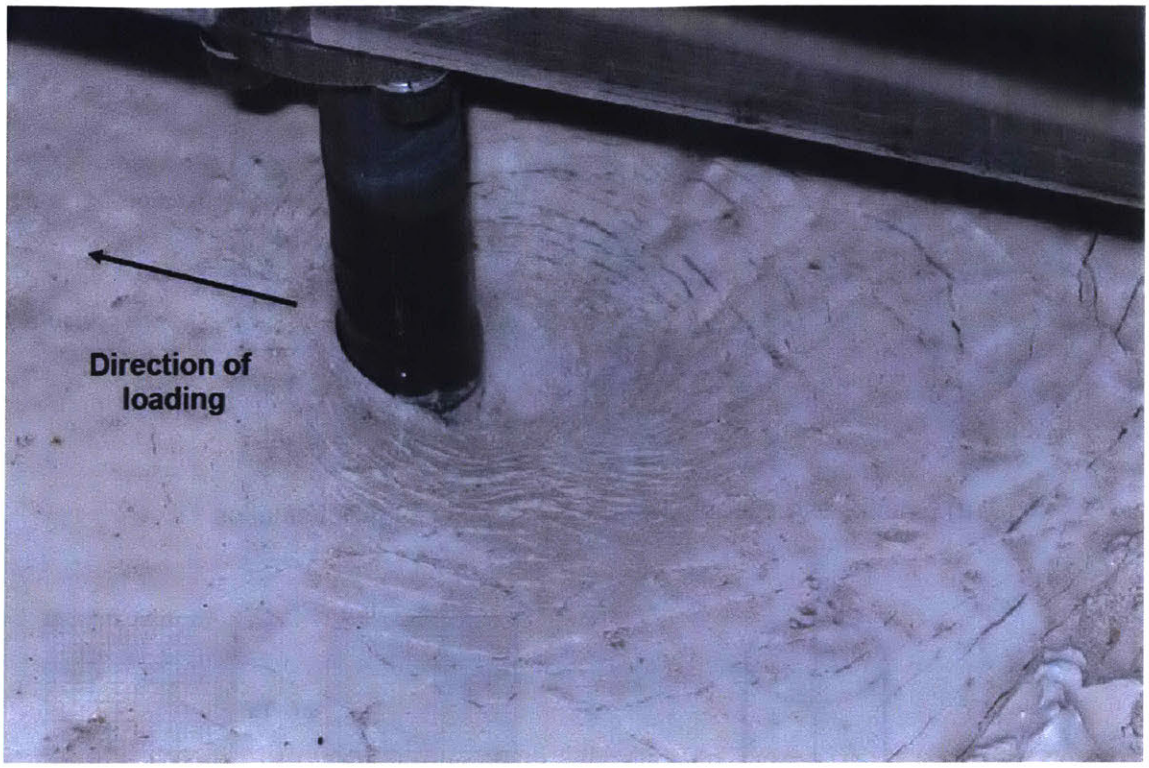

Figure 2-26: Observations of geometric non-linearities associated with surface depression (and circumferential cracking) and mounding around model pile in centrifuge model test (Jeanjean, 2009)

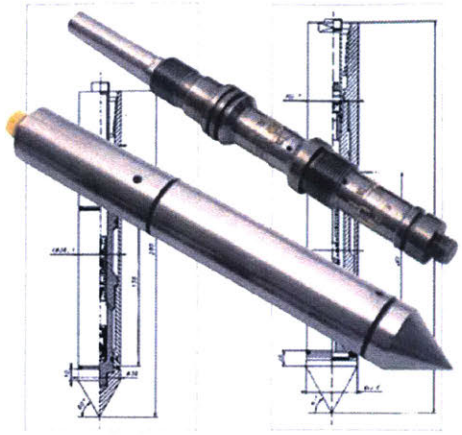

a) Exterior and interior view

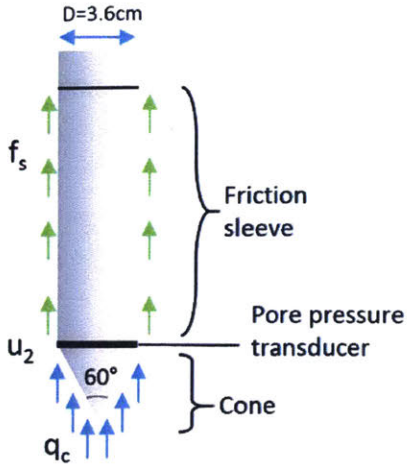

b) Schematics

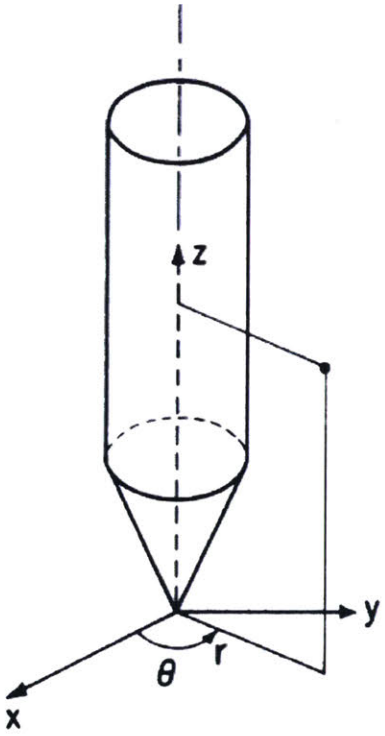

c) Cylindrical Coordinate System and Axisymmetry

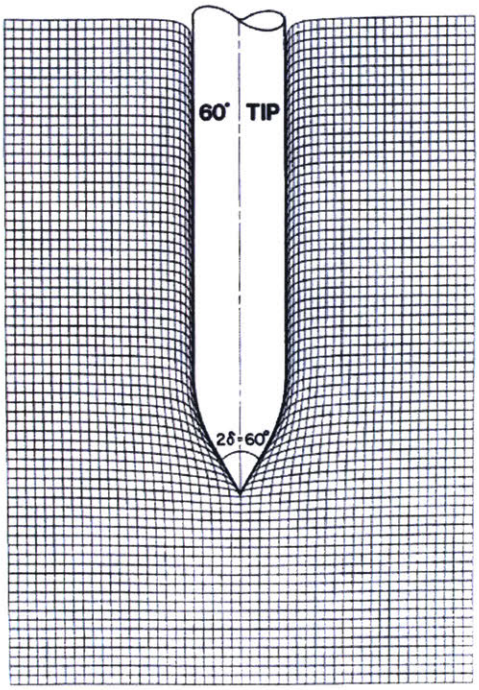

d) Steady deformations for undrained penetration in clay using the Strain Path Method

Figure 2-27: Cone Penetrometer (Aubeny [1992], Levadoux [1980], Ceccato et al. [2016])

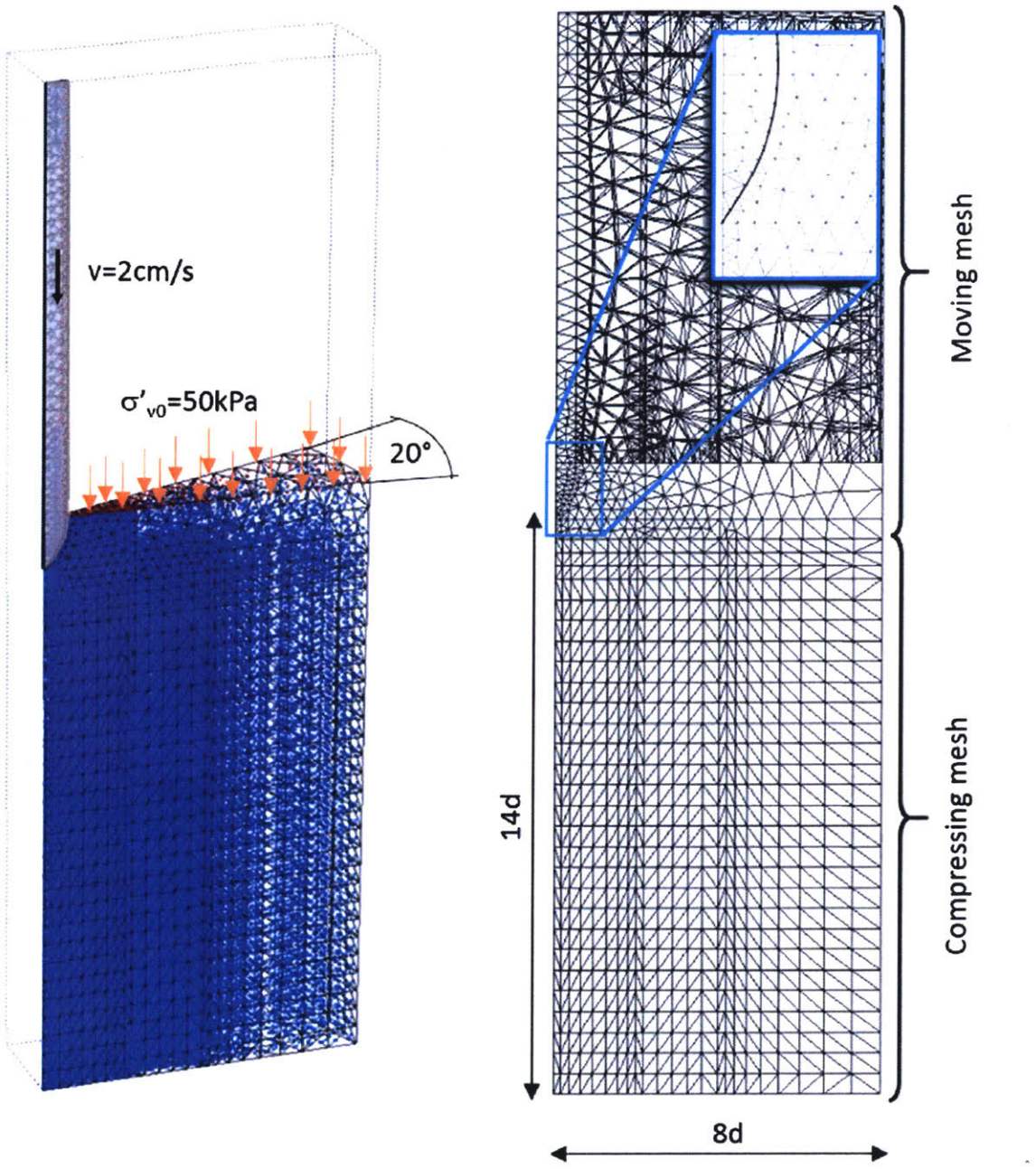

Figure 2-28: Geometry and discretization of the CPT simulation with MPM method (Ceccato et al. [2016])

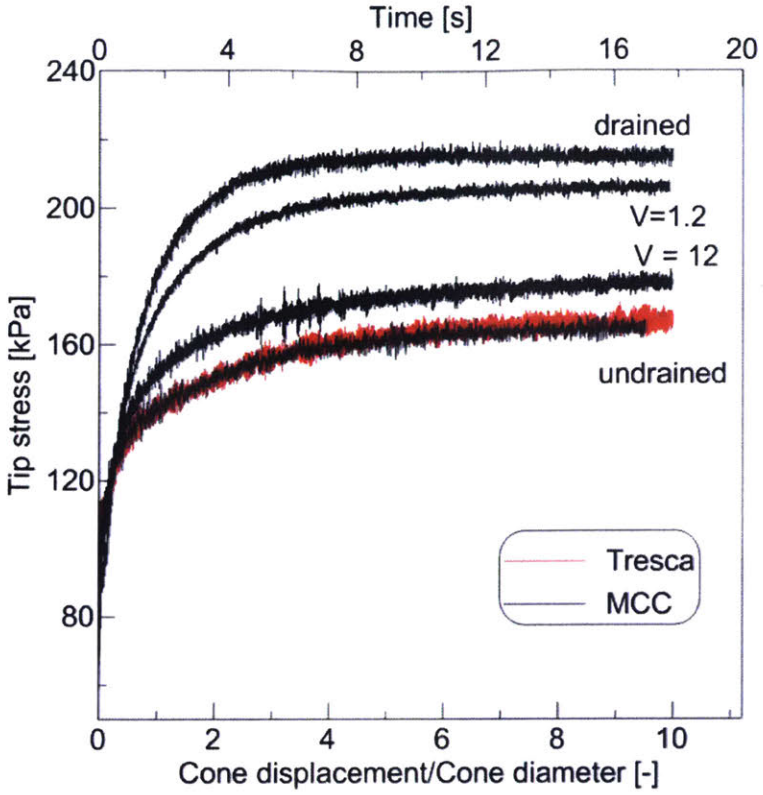

Figure 2-29: Published MPM simulation - Tip Stress over normalized penetration for different drainage conditions (Ceccato [2015])

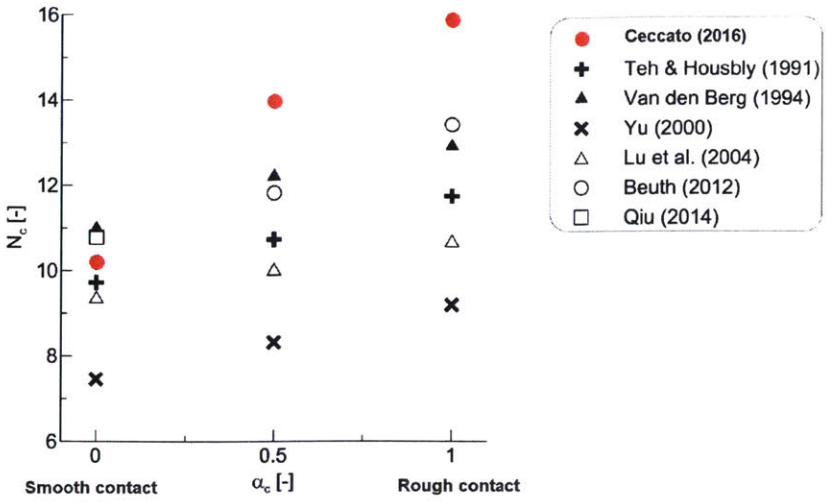

Figure 2-30: Effect of cone roughness on undrained cone factor (Ceccato [2015])

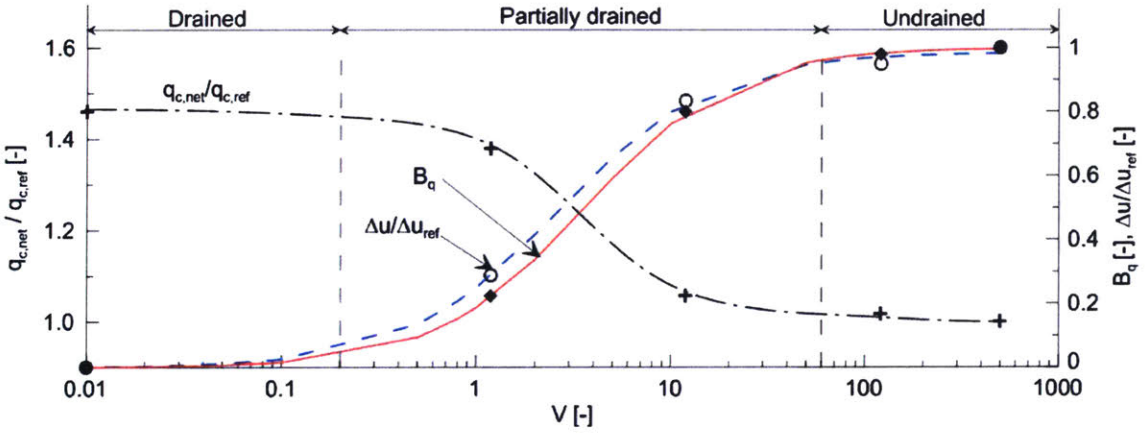

Figure 2-31: Effect of drainage conditions on cone resistance and pore pressure parameters for piezocone in Kaolin simulated using MPM method and MCC soil model (Ceccato et al. [2016])

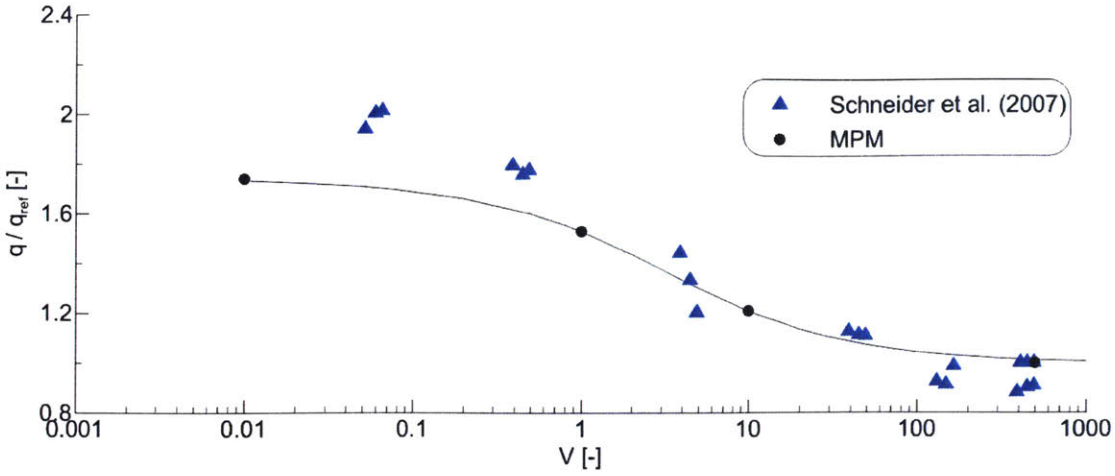

Figure 2-32: Computed (MPM, Ceccato et al. [2016]) cone resistance and measured data from centrifuge model tests (Schneider et al. [2007]) in Kaolin

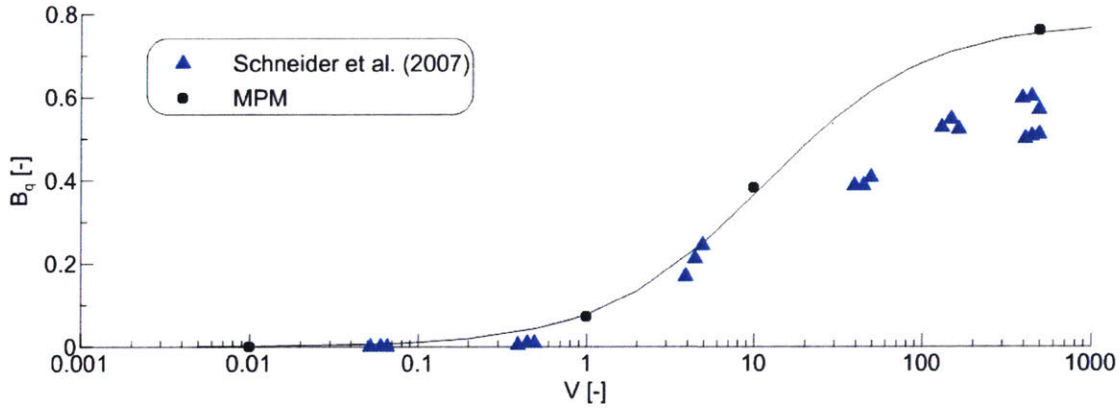

Figure 2-33: Comparison of pore pressure factor, B_q, between simulated (MPM, Ceccato et al. [2016]) and measured (Centrifuge model, Schneider et al. [2007]) piezocone tests in Kaolin

Chapter 3

Methodology

The purpose of the chapter is to describe the methodology developed for performing coupled flow and deformation analyses of the selected offshore geotechnical problems using advanced effective stress models.

3.1 Modeling of Conductor-Soil Interaction

This section describes the development of the 3D Finite Element Model of conductor-soil interaction using conventional Lagrangian Finite Element Method. This methodology is further extended to include the advanced effective stress soil model and used to perform the numerical simulation and validation of conductor-soil interaction centrifuge model tests presented in the next chapter. In this section, the methodology used for obtaining the p-y curves from the continuum-based full three-dimensional numerical models is described. The results obtained from the total and effective stress analyses using isotropic soil models are discussed.

3.1.1 3D Finite Element Model

The first step of this research was to reproduce the prior numerical results of conductor-seafloor interaction following the methodology presented by Templeton [2009]. The analyses by Templeton [2009] used conventional total stress finite ele-

ment analyses. Templeton's model used 8-noded brick isoparametric elements with linear interpolation of displacements (and reduced integration[1]). The model considered a 0.9144m diameter conductor that extended to a depth of 60m with a fixed base. The soil was modeled with an elasto-plastic, isotropic hardening model with Mises yield referred to as 'IHPP' total stress model (SIMULIA [2016]). Figure 3-1 shows the original and replicate FE models using the same element type and integration.

The conductor was modeled with the 4-node shell elements used by Templeton, Figure 3-1). The hollow steel conductor with the wall thickness of 5.08 cm was assumed to have elasto-plastic behavior with the maximum yield strength $\sigma_y = 413MPa$. A 4-node doubly curved thin shell elements with finite membrane strains were used to represent the conductor in the replicate model (Figure 3-1), while no slip was allowed at the conductor-soil interface (this is simulated using a set of tied connections between conductor-soil nodes).

The reference undrained shear strength profile was based on $\Delta s_u/\Delta z = 1.57$ kPa/m (10 psf/ft) line through the depth of the soil. The continuous undrained shear strength profile for the replicate model was discretized with 30 soil layers as shown in Figure 3-2.

Figure 3-3a shows the ratio of small strain elastic shear stiffness to undrained shear strength considered by Templeton [2009] for modeling clay behavior at deepwater sites in the Gulf of Mexico ($G_{max}[z]$ can then be extracted by combining profiles shown in Figs. 3-2, 3-3a). Figure 3-3b shows a more detailed comparison between the undrained shear-stress-strain behavior measured in a laboratory test on GoM clay[2] with simulations using the IHPP model. The model introduces a set of nested set of yield surfaces that approximate the non-linear stress-strain properties by a linear curve as shown in Figure 3-3b. The current Replicate analysis uses the same reference lab test data and achieves a similar fit to the data as reported by Templeton [2009].

Figure 3-4 compares the load-displacement behavior of the conductor at the mud-

[1]This method uses a reduced number of Gauss points for numerical integration of the element stiffness matrix. This method reduces computational costs but can potentially produce less accurate solutions.

[2]Data are from the published Holstein prospect (Templeton [2009])

line (point of load application) from the Replicate analyses with predictions reported by Templeton [2009]. The results show very good agreement for lateral displacements up to 1 m, but the Replicate model tends to underestimate the load capacity for continued deformations (by up to 7%). This small discrepancy may reflect differences in the discretization of the soil profile (Fig. 3-2) or other undocumented differences in model details. The original analyses used Abaqus™ Explicit (i.e., with explicit load steps) while the Replicate analysis was conducted with Abaqus™ Standard (i.e., implicit load steps).

3.1.2 Methodology for Obtaining p-y Curves

Interactions between the conductor and soil can be further interpreted by considering numerically-derived p-y curves, where p (kN/m) is the net soil reaction force at a selected depth and y is the local lateral displacement at that same depth. Figure 3-5 shows the "p-y" response at different depths. The soil resistance is obtained by integrating the surface tractions around the circumference of the conductor (based on stresses computed at Gauss points in the adjacent soil (e.g. as procedure reported by Fan and Long [2005])[3]. The soil resistance per unit length along the conductor is the x-component of the total stress acting on the conductor circumference. The x-component stress at a point in a soil element can be represented by traction vector, t_x, as follows:

$$t_x = \sigma_{xx} n_x + \sigma_{xy} n_y + \sigma_{xz} n_z \tag{3.1}$$

where n_x, n_y, and n_z are components of unit normal along the x-, y-, and z-directions, respectively, and are expressed as:

$$n_x = \cos\theta_x = \frac{x_g}{\sqrt{x_g^2 + y_g^2}} \tag{3.2}$$

$$n_y = \cos\theta_y = \frac{y_g}{\sqrt{x_g^2 + y_g^2}} \tag{3.3}$$

[3]Templeton [2009] does not report his procedure for obtaining p-y curves – and appears to have used a different methodology using dummy structural elements (pers. comm).

$$n_z = \cos\theta_z = 0 \tag{3.4}$$

where x_g and y_g are the coordinates of the closest Gauss points

The total lateral soil resistance, p_x(per unit length of pile) is then obtained by integration around the conductor circumference, and p_x is expressed as:

$$p_x = 2\int_0^{\pi} t_x R d\theta \tag{3.5}$$

The "p–y" relationship at a given depth is obtained by relating the soil resistances, p, to the corresponding lateral deflections, y, of the pile at that depth.

Figure 3-5 shows very good agreement between the p-y curves computed in the Replicate analysis with results reported by Templeton [2009] over the upper 10m of the conductor[4]. The overall response shows excellent agreement indicating that the current model successfully replicates the key features of the original Templeton [2009] model. The offset in z-values (depth) may reflect small differences in s_u-profile represented in the models.

It is also instructive to consider the interpretation of the peak soil resistance using analytical, plane strain plasticity solutions (Randolph and Houlsby [1984]). Figure 2-24 shows the theoretical failure mechanism for undrained shearing of a long cylindrical, pipe pile section displacing laterally within a soil mass. The limiting lateral resistance, p_u, can be expressed in terms of the local undrained shear strength, s_u, the pile diameter, d, and a bearing factor, N_p, that depends on the pile-soil interface properties. For a perfectly rough interface, $f_s/s_u = 1.0$ (comparable to the tied connection used in the current Finite Element model), $N_p = 12$.

The table in Figure 3-5 summarizes the values of N_p derived from the Replicate FE model with results reported by Templeton [2009]. The Replicate analysis shows bearing factors that increase with depth from $N_p = 8.31$ at 0.5m to $N_p = 12.0$-12.2 for $z \geq 6$m. These results suggest that the plane strain geometric simplification is

[4]It should be noted that there is a small offset in depths between the Replicate analysis and values used by Templeton [2009] in order to achieve close matching of the maximum soil resistance

appropriate for estimating lateral soil resistance below 6m, while lower values occur nearer to the ground surface due to 3D failure mechanisms. In contrast, Templeton [2009] reports values of N_p that exceed significantly the theoretical plane strain solutions (by up to 25%). While these results are feasible due to rotation of the conductor pipe, it is more likely that they reflect approximations in the s_u profile used in the original Finite Element model.

3.1.3 Total Stress Analysis

An initial 3D Finite Element model for a total stress analysis has been developed using the large displacement formulation (similar to the previously described numerical model). It includes a continuous (linear) undrained shear strength profile, tied interface connections between soil and conductor, and an elasto-plastic hollow steel conductor (D = 0.91m [36ins]) with wall thickness, t=5cm (2ins). The steel conductor is made from Grade X80 steel with initial yield strength, σ_y = 413MPa. The model simulates the upper 46m (150ft) of the conductor (and assumes a single conductor over this depth). The loads are applied at the mudline. The soil is modeled with brick elements (C3D8R - continuum stress/displacement, three-dimensional, 8-noded, reduced integration[5] finite element) and conductor is modeled with solid elements as a hollow pipe with correct geometrical dimensions.

Figure 3-6 presents the in-situ stresses and undrained shear strength profiles for different modes of shearing for typical Gulf of Mexico conditions for 'Average Gulf Clay' (AGC) presented by Whittle and Sutabutr [2005] (AGC parameters are based on studies of pile set-up from a series of deepwater projects in the Gulf of Mexico). The AGC exhibits undrained strength anisotropy such that the ratio of undrained shear strengths measured in triaxial extension and compression modes, $su_{TE}/su_{TC} \approx$ 0.6 as shown in Fig. 3-6. Figure 3-6 shows that s_{uDSS} is slightly smaller than s_{uTC}. The current Base Case model uses is s_u/σ'_{vc} = 0.25, which corresponds to a profile with s_u/z= 1.57kPa/m [10 psf/ft] (i.e., '10-pound line'). The Base Case analysis

[5]Reduced integration uses a lower-order integration to form the element stiffness and substantially reduces running time in three dimensions

introduces a linearly elastic-perfectly plastic (EPP) soil model with $G_{50}/\sigma'_{vc} = 15$ (note contrast with prior study based on G_{max}/s_u, Figure 3-2a). Figure 3-7 compares the normalized shear stress-strain behavior (τ/s_u) for the EPP model in the DSS shear mode with prior parameters for IHPP used in the Replicate analysis. Isotropic constitutive models (such as EPP and IHPP) are based on parameters selected from lab tests in Direct Simple Shear (i.e., $s_u = s_{uDSS}$).

Figure 3-8 presents the computed load-displacement response of the conductor at the mudline from the initial total stress FE model, which is loaded to a target offset and then restored to its original position. The analyses compare the effects of displacing the conductor to offsets of 1m vs. 2m (A vs. B) and the effects of plasticity in the conductor pipe (B vs. C). The results show that yielding of the conductor only becomes significant when the offset at the mudline exceeds 1m. Thereafter, yielding of the conductor reduces the lateral load resistance at a given offset and the initial model predicts a maximum lateral capacity ($P_u \approx 1675$kN, for a mudline offset greater than 1.5m). It is important to note that non-linearity in load-deformation response occurs throughout the unloading process and with significant and that a large fraction (50 – 65%) of the deformations are not recovered upon unloading to P = 0kN. Additional loads (P = -700kN to -1400 kN) are needed to restore the conductor to its original location at the mudline.

Figure 3-9 compares the deformation profiles of the conductor (with elasto-plastic properties) at the maximum offset (1m vs. 2m) and final configurations. These results show clearly the development of a plastic hinge within the conductor at z $\approx$ 14m (below mudline) and the permanent deformations within the ground when the conductor is restored to its original position at the mudline (i.e. $\delta h = 0m$).

Figure 3-10 compares the computed p-y curves from the initial FE model for loading to the same two target offsets at the mudline (maximum$\delta h = 1.0, 2.0m$). The results are consistent with the prior Replicate analyses and show a small increase in the peak soil resistance with depth with maximum values of the bearing factor, $N_p \approx 12$. The most notable new feature of these results is the significant softening in soil resistance which most clearly for loading to a large offset (2m case) for z $\geq$ 4.4m.

This behavior is clearly not related to details of the soil model (EPP) and is most likely associated with geometric non-linearities due to large rotation of the conductor pipe (which yields when the mudline offset is $\delta h \geq 1m$, Figure 3-8).

3.1.4 Effective Stress Analysis

In a total stress analysis, the soil is assumed to be a single phase material. Undrained conditions are approximated by specifying an elastic Poisson's ratio ν_u = 0.49 (to represent the incompressible response). More comprehensive models of conductor soil-interaction treat the soil mass as a two-phase continuum and allow for coupled flow and deformation within the soil mass (i.e., they can consider partial drainage due to local migration of pore water close to the conductor). These types of analyses can incorporate more comprehensive, effective stress soil models.

A new Abaqus™ model was developed for performing effective stress analysis. The soil is modeled using a coupled pore pressure-displacement 20-node brick elements with quadratic interpolation of soil displacements and linear interpolation of excess pore pressures[6]. The conductor is modeled with continuum elements (two layers of 8-noded brick isoparametric elements[7] with linear interpolation of displacements and reduced integration). This section compares the computed response for the Base Case model (single phase elements) with the behavior using an identical mesh of coupled elements simulating 'transient consolidation' . Migration of pore water within the soil skeleton is represented by D'Arcy's law with a constant hydraulic conductivity, k = 0.09 m/day. In order to replicate the prior undrained analyses, the conductor is displaced at a rate of 1m/sec with free flow boundary conditions in the far field (and at the ground surface) and no flow across the wall of the conductor.

Figures 3-11 and 3-12 compare the load-displacement response at the mudline and p-y curves from the total and effective stress analyses. The results show ex-

[6]The examples in this section use elements with reduced integration (C3D20RP) to accelerate computation time. We have also checked for numerical accuracy using full element integration.

[7]Note: The effective stress model simulates the conductor use solid elements, while the prior Base Case model used shell elements for the conductor. Soil behavior is represented using the EPP soil model with the same shear modulus as the Base Case analyses and an effective Poisson's ratio, ν'=0.3.

cellent agreement between the two analyses and hence, confirms that the coupled pore pressure-displacement elements are able to represent accurately the reference undrained response for the conductor found previously using a total stress approach.

The Modified Cam Clay (MCC) soil model (Roscoe and Burland [1968]) is calibrated for the Average Gulf Clay properties based on a series of deepwater sites in the Gulf of Mexico in the past (AGC; Whittle and Sutabutr [2005]). Table 3.1 shows the input parameters for the MCC model. Using these parameters the MCC model matches closely the s_{uTC} profile presented in Figure 3-6.

Figure 3-13 summarizes the predictions of undrained conductor response in normally consolidated AGC clay using the MCC soil model. The response is similar to results obtained using the EPP model (cf. Figure 3-12) and reflects close similarity in the undrained shear strength profiles for these two isotropic soil models. Figure 3-14 presents the effect of pore pressure dissipation around the conductor with time. The holding test is performed at $\delta h = 0.5m$ at the mudline (the lateral loads are measured while the displacements are fixed). The reduction in lateral load was around 15%.

Figure 3-15a shows the excess pore pressures computed using the MCC model around the conductor at a depth z=10 m, when the loaded is offset at $\delta h = 0.5m$ at the mudline. The undrained results show excess pore pressure ratios, $\Delta u/\sigma'_{v0}$ ranging from -0.3 to +0.9 at locations around the surface of the conductor. The high local gradients of pore water highlight the potential for partial drainage around the conductor. Figures 3-15b shows the dissipation of excess pore pressures around the conductor during the holding test (t=50 hours). Figure 3-15c shows the minimal amount of excess pore pressures at t=100 hours (close to drained conditions).

3.2 Proposed Large Deformation Analysis Procedure for Cone Penetration

As shown in Section 3.1, the conventional Lagrangian Finite Element Method can be conveniently used to analyze complex geotechnical problems using effective and to-

tal stress approaches within a practical range of deformations provided that the finite element mesh is not completely distorted. For many geotechnical problems including the cone penetration in soft clays, it is also important to take into consideration the effects of partially drained conditions (for soils of intermediate permeability (soils) or layered soil profiles) using the consolidation (coupled pore fluid diffusion/stress) analyses. Most advanced constitutive soil models are formulated in terms of the effective stresses and require coupled pore fluid-stress finite elements with a pore pressure degree of freedom. As discussed in Chapter 2, the excessive mesh distortion problem restricts the usage of the pure Lagrangian Finite Element Method to analyze problems with extremely large deformations like modeling the cone penetration tests in soft clay. Therefore, in order to analyze such problems, a suitable large-deformation analysis method is needed to overcome the issue of excessive mesh distortion. Chapter 2 presents an overview of the existing large deformation analysis methods that have been applied to geotechnical problems previously. Among the most relevant and promising methods are the Material Point Method (MPM) (Sulsky et al. [1994], Al-Kafaji [2013]) and so-called Arbitrary Lagrangian Eulerian (ALE) (Hughes et al. [1981], Savidis et al. [2008]) approach in which the Eulerian flow of the soil or soil particles through the Lagrangian mesh was introduced. Most of the published analyses use relatively simple isotropic constitutive soil models. In many cases, these large-deformation methods incorporate the "convection" of the soil relative to the mesh within the finite element governing and constitutive equations which is usually difficult to implement in complex soil models.

In this thesis, the proposed procedure for large deformation cone penetration analysis using advanced effective stress soil model is based on the principles described by Hu and Randolph [1998a] and is independently implemented for the widely-used commercially available finite element program Abaqus™. This approach comprise the conventional Lagrangian Finite Element Method with separate remeshing and solution mapping using the interpolation of all the solution variables from the old mesh into the new mesh (without the ALE convection equations). The global analysis consists of a series of conventional Largangian Finite Element analysis steps, followed

by a complete remeshing of the domain and the interpolation of the solution variables (stresses, pore pressures, state variables, etc.) from the previous mesh. The sequence of conventional Lagrangian Finite Element analysis, remeshing and interpolation is repeated until the necessary displacement is achieved. The main principle is that each remeshing step makes up a new analysis with the appropriate initial conditions (geometry, solution variables, loads and boundary conditions) that reflect the preceding sequence of analysis steps. The accuracy of the analysis depends on the success of the interpolation employed to map the solution variables (including the history-dependent state variables). The main advantage of this approach is that it can be used in the effective stress analysis with advanced soil models and doesn't require complex re-formulation of the constitutive equations. The disadvantage is that the each large deformation analysis requires a series of multiple remeshing steps that need to be tailored to a specific problem. The so-called "mesh-to-mesh solution mapping" built-in technique available in Abaqus™ Standard can be used to perform the proposed remeshing and interpolation approach. Each new step within the global large deformation analysis can be created manually using the built-in solution mapping capabilities provided by Abaqus™ Standard. However, it would be impractical to perform this manually each time since a large number of remeshing steps would be required. We find that simulation of the requires frequent remeshing at intervals $\Delta z/R = 0.1$. Therefore, automated implementation with a high degree of customization is necessary to apply this approach to various large deformation offshore problems using advanced constitutive soil models including cone penetration. This has been accomplished independently during the course of this research for both 2D and 3D conditions using Abaqus™ Standard solver with Python scripting. The implementation details will be presented in the next subsections.

3.2.1 Theoretical Preliminaries

A finite element mesh is a partition of a given domain (problem geometry) into simple subdomains with known properties, which are called elements (Figure 3-16). The whole domain must be discretized by the elements without overlapping (i.e.

tessellation), and the conditions of compatibility between the finite elements have to be satisfied. In general, two-dimensional domains can be discretized into triangular or quadrilateral elements (or their mixture). Three-dimensional domains are usually discretized with tetrahedral or hexahedral elements (although pyramids or wedges can also be employed). The finite element meshes can be generally divided into two main types such as structured and unstructured (Figure 3-17). A structured mesh has a pre-determined connectivity and is based on a fixed pattern that periodically repeats. A mesh is called unstructured if its pattern of connectivity is not periodic, and the number of elements connected to a node varies and is unpredictable. The unstructured meshes are usually used to discretize the domains with complex geometry.

A large number of mesh generation methods have been developed since 1970s, and the popular methods include Delaunay triangulation, Advancing Front meshing, Quadtree/Octree decomposition, Meccano transformation, Hybdrid methods, etc. Ho-Le [1988], Owen [1998], Frey and George [2010], Lo [2014] provide a comprehensive survey of the modern finite element mesh generation methods and discuss them in detail. In this thesis, we only consider the Delaunay triangulation (as used in the original "Remeshing and Interpolation Technique with Small Strain" approach by Hu and Randolph [1998a]) and the Advancing Front Meshing algorithm (used in the developed procedure). Both of these methods can also be used in several combinations including Advancing Front-Delaunay approach (Borouchaki et al. [2000]).

The Delaunay criterion implies that any node must not be contained within the circumscribing circle of any triangle of the mesh. Formally, for a set of points $S = \{P_k\}$, $k = 1, n$, a set of regions $\{V_k\}$ assigned to each of these points can be defined, such that any location within V_i is closer to P_i than any other of the points:

$$V_i = \{P : |P - P_i| \leq |P - P_i|, \forall j \neq i\} \tag{3.6}$$

The Delaunay triangulation is a triangulation of the convex hull of S that is a result of joining all the pairs P_iP_j sharing a common segment of the regions (Frey and George [2007]). The incremental point insertion algorithm proposed by Watson

[1981] and Bowyer [1981] is one of the general methods for computing Delaunay triangulation. It was implemented for 2D and 3D finite element mesh generation by Cavendish et al. [1985] among the first (Lo [2014]).

Hu and Randolph [1998a,b] and subsequently Wang et al. [2009], Tian et al. [2014] described the remeshing and interpolation approach referred to as RITTS (Remeshing and Interpolation Technique with Small Strain) with several application examples. The 2D mesh generation method described in the original RITTS includes mesh generation using normal offsetting and Delaunay triangulation, mesh smoothing with the Laplacian technique and the application of an external mesh density function. The mesh generation using normal offsetting produces an array of spaced nodes that are connected to form a finite element mesh using a Delaunay triangulation offsetting of the nodes at the boundaries (Johnston and Sullivan [1992]). Figure 3-18 shows the mesh produced using the Delaunay triangulation and normal offsetting of the nodes. A mesh smoothing procedure is then applied using the Laplacian technique to adjust the element shapes such that:

$$x_i = \frac{1}{2N_i}\sum_{n=1}^{N_i}(x_{nj} + x_{nl}); \qquad i = 1 \rightarrow I \tag{3.7}$$

$$y_i = \frac{1}{2N_i}\sum_{n=1}^{N_i}(y_{nj} + y_{nl}); \qquad i = 1 \rightarrow I \tag{3.8}$$

where x_i, y_i - nodal coordinates, N_i is the number of elements surrounding node i (Figure 3-20a), I is the number of nodes inside the domain.

The mesh density is controlled using a density function which can be decoupled from the mesh generation procedure. The local nodal distances are determined using an external function during mesh generation. Various density functions including linear and non-linear functions can be devised and used to prescribe mesh densities. The mesh density function, f_d, used in the original description of RITSS was assumed to be an exponential function of the distance, d, from a specified origin at (x_0, y_0):

$$f_d = Ae^{Ed} \tag{3.9}$$

where A and E are constants. The example application of the mesh density function as implemented in the original RITSS is shown in Figure 3-19.

Hu and Randolph [1998a] also described multiple planar interpolation methods. One of them is the Inverse Distance Algorithm (IDA), in which the common idea of weight average was adopted. The values of the Gauss points in the reference field are summed using an inverse distance weighting function as

$$\phi_d = \frac{\sum(w_r \phi_r)}{\sum(w_r)} \tag{3.10}$$

where w_r is a weighting function defined as

$$w_r = d^{-e} \tag{3.11}$$

where d is the distance between points, and e is an exponent that is usually taken as 3.5 (recommended value by Hu and Randolph [1998a]). It was reported that a minimum value for the distance can usually be specified.

Another method is Arbitrary Linear Interpolation (ALI), in which the element shape function was used. In this method, the solution variables for the new mesh are obtained by performing isoparametric mapping. The three nearest reference Gauss points are found that surround a given destination point. Using these old Gauss points as vertices, the field values of the new Gauss point are obtained from

$$\phi(\xi, \eta) = [1 - (\xi + \eta)]\phi_1 + \xi\phi_2 + \eta\phi_3 \tag{3.12}$$

where ξ and η are normalized local parameters (Figure 3-20b).

Several other interpolation methods used in the further iterations of the RITSS approach included the so-called unique element method (Hu and Randolph [1998a]), superconvergent patch recovery (Zienkiewicz and Zhu [1992]), recovery by equilibrium in patches (Boroomand and Zienkiewicz [1997]), etc.

Hu and Randolph [1998a] validated their early implementations of the remeshing and interpolation approach on the problems with exact analytical solutions and concluded that there is no significant drift in the accuracy of the large deformation so-

lution due to repeated remeshing. Song et al. [2008] demonstrated a good agreement between the measured data from centrifuge model tests and the large deformation total stress numerical simulations with RITSS of the vertical pullout capacity of plate anchors embedded in clay. The remeshing and interpolation technique has also been applied to a large number of offshore geotechnical problems analyzed by various researchers mostly associated with the Centre for Offshore Foundation Systems at University of Western Australia (Randolph et al. [2008], Lu et al. [2004], Wang et al. [2009], Zhou and Randolph [2009], Hossain and Randolph [2010], Tian et al. [2014], Chatterjee et al. [2012], Han et al. [2016], Ragni et al. [2017]).

In this thesis, the Advancing Front Meshing method as implemented in the popular commercial Finite Element Analysis package Abaqus™ is used to generate the finite element meshes. The Advancing Front Meshing algorithms have been developed to automatically produce 2D and 3D unstructured meshes in which the user has control of the mesh characteristics and was investigated by various researchers including Lo [1985], Peraire et al. [1987], Löhner and Parikh [1988], Möller and Hansbo [1995].

The advancing front algorithm generates the finite elements initially at the boundary and continues to generate them as it moves systematically to the interior of the domain geometry. The seeds are markers that can be placed along the edges of a geometry to specify the target mesh density. The mesh density in the interior of the region is determined by the seeds along the edges of the geometry (Figure 3-21). The finite element mesh quality can be assessed using the shape and size metrics such as shape factor, face corner angle, aspect ratio, geometric deviation factor and edge size. The shape factor criterion is usually applicable only for triangular (2D) and tetrahedral (3D) elements. For triangular and tetrahedral elements the shape factors, $\Omega_{triangle}$ and $\Omega_{tetrahedra}$, are defined as

$$\Omega_{triangle} = \frac{A_{element}}{A_{optimal}} \tag{3.13}$$

$$\Omega_{tetrahedra} = \frac{V_{element}}{V_{optimal}} \tag{3.14}$$

where $A_{element}$ is the element area, $A_{optimal}$ is the area of an equilateral triangle with the same circumradius[8] as the element, $V_{element}$ is the element volume, $A_{optimal}$ is the volume of an equilateral tetrahedron with the same circumradius as the element. The shape factor ranges from 1 (the optimal element shape) to 0 (a degenerated element). The aspect ratio is the ratio between the longest and shortest edge of an element. The face corner angle controls the angle at which two edges of elements faces meet. A measure of how much an element edge deviates from the original geometry is called the geometric deviation factor.

In large deformation geometrically nonlinear analyses, the elements may become so severely distorted that the further solution is not feasible. Therefore, a manual remeshing analysis is possible in Abaqus™ Standard using the "mesh-to-mesh solution mapping" feature. This feature allows to continue the analysis as a new problem by the interpolating the solution onto the manually regenerated mesh from the output databases generated with the old mesh, provided that the remeshing is completed before the elements become too distorted. The model must be set up all over again because the boundary conditions, loads and other model features are not carried over from the old mesh to the new mesh. Only the solution variables such as stresses, strains, pore pressures and state variables are transferred from one mesh to another.

The in-built solution mapping algorithm operates by interpolating results from nodes in the old mesh to points (either nodes or integration points) in the new mesh. This procedure assumes that the new mesh is within the boundaries of the old mesh. The algorithm has three steps. First, the solution variables in the old mesh are extrapolated from the integration points to the nodes of each element by averaging these values over all similar elements abutting each node. Second, the element in the old mesh in which the new point lies is found, and the point's location in that element is obtained. Third, the values are interpolated from the nodes of the old element to the points in the new model. All solution variables are interpolated automatically. This solution mapping algorithm introduces some diffusion in the mapped solution which scales with the solution gradient in the old mesh. An additional step is usually

[8]The radius of the circle passing through the vertices of the triangle.

included to check for equilibrium after the interpolation has been done. In Abaqus™, the stress unbalance after the interpolation can be resolved either in the first increment or linearly over the step.

3.2.2 Practical Implementation and Numerical Details

The Abaqus™ finite element package offers the scripting interface which is an extension of the popular object-oriented language, Python (SIMULIA [2016]). This interface uses the same syntax and operators required by Python (Van Rossum and Drake [2003]). The Abaqus Scripting Interface allows users to bypass the Abaqus Environment's Graphical User Interface and communicate directly with the kernel. A file containing Abaqus Scripting Interface commands (same as Python code) is called a script. Figure 3-22 illustrates how the Scripting Interface commands interact with the Abaqus/CAE (Complete Abaqus Environment) kernel.

In this thesis, the proposed large deformation analysis procedure using the remeshing and interpolation approach is independently implemented using a set of Python scripts that can be used in Abaqus Scripting Interface. The full source code of the script is presented in Appendix B. Figure 3-23 presents the general algorithm of the proposed procedure. The proposed procedure implemented in a package of scripts that can be customized though multiple variables to a specific geometry, elements, boundary conditions, target displacement, etc. First, a Finite Element Model of the desired problem is developed. Second, an initial analysis with a prescribed displacement is performed. For convenience, the model name (e.g. the file name of the model) contains a variable $N = i + 1$ added at the end, where i is the current step number. This way each model is distinguished by its file name containing the associated step number. The prescribed displacement must not cause the excessive element distortion. For example, the prescribed displacement for a cone penetration analysis was set to be 2 mm.

The first two processes (model development and initial analysis) are mostly manual. After the necessary adjustments, the rest of the process is automated using the developed scripts. When the main script is called for the first time, it checks whether

a target displacement has already been reached. If it is reached, then a set of other scripts are invoked to automatically iterate through all output databases (previously mentioned N variable represents the total number of remeshing steps) and plot the desired results automatically. For example, Force vs. Displacement combined from each remeshing step or Excess Pore Pressure evolution at a fixed point thought the entire analysis. If the target displacement if not reached, then a new model is created by invoking the following Abaqus™ Scripting Interface Command:

mdb.Model(name=*newmodel*, objectToCopy=mdb.models[*oldmodel*])

where *oldmodel* is the variable containing the name of the previous model, and *newmodel* is the variable containing the new model name in which the step number is incrementally updated $(i + 1)$. This command makes an identical copy of the initial model with a different name.

The next step, is to import the deformed mesh from the output database replacing the old part in the model associated with this mesh. The undeformed part of the model can simply be moved to the amount of prescribed displacement. Then, we check the step number because the first remeshing model must be treated differently than all other steps. In the first model, the script replaces the regular "Geostatic" step usually used for geotechnical problems with a new "Equilibrium" step for to resolve the stress unbalance after the solution mapping. A special command "*MAP Solution" is properly inserted into the description of the input file. This step is important because this command activates the in-built solution mapping algorithm implemented in Abaqus that extrapolates the solution variables from the old mesh into the new mesh when the solver is called specifying the "current" and "previous" input files. If the current model is not the first remeshing model (i.e. $i > 1$), then the "Equilibrium" step and "*MAP solution" commands are already embedded within the model.

The next step is to read the coordinates of reference mesh points and store them in the arrays and variables. The orphan mesh is converted into the geometry. The detailed explanation of this procedure is given in Appendix. In some cases the geometrical parts may contain unnecessary details such as very small faces and edges.

The Virtual Topology toolset in Abaqus™ allows the removal of these small details by combining a small face with an adjacent face or by combining a small edge with an adjacent edge. This tool is applied within the script to combine extra edges as determined from the mesh reference points. This procedure allows proper detection of the edges of the model geometry and re-create sets and surfaces associated with each part of the model. The material section is also applied to the replaced part in this step. Afterwards, the seeding is applied to the reference edges and the geometry is remeshed using the Advancing Front Meshing algorithm based on the boundary seeds. Finally, the input file is saved into the working directory and Abaqus solver is invoked to continue the analysis.

This process is repeated in the loop until the target displacement is achieved (i.e. the current step number will be equal to the target step number associated with the desired displacement).

Figures 3-24a,b illustrate the axisymmetric model of the Cone Penetration Test. The initial cone penetration model was developed using EPP and MCC soil models with a target displacement, $\frac{\Delta u_y}{R} = 10$. Figure 3-25 presents the completed large deformation Abaqus analysis using proposed procedure of the cone penetration test that consists of 60 remeshing steps. Figure 3-26 shows the first 7 remeshing steps. After the initial step, the deformed configuration is remeshed in the next step (labeled as "Remeshed" in the Figure). Figure 3-27 shows the deformed mesh.

Figure 3-28presents the geometry building based on the deformed mesh. Figure 3-29 shows the location of edges and seeding the boundaries. Figure 3-30 presents the remeshed model. Figure 3-31 shows the solution mapping example. Figure 3-32 presents the 3D example.

3.2.3 Evaluation and Validation

Figure 3-33 presents the initial cone penetration analysis using MCC soil model. Figure 3-34 shows the development of excess pore pressures around the penetration. Figure 3-35 presents the results obtained using 60 remeshing steps. Figure shows 3-36 the error associated with solution mapping. Figure 3-37 presents the comparison with

the previously published results.

3.3 Advanced Constitutive Soil Models

One of the most important aspects of the numerical analysis of geotechnical engineering problems is the selection of an appropriate constitutive model to simulate the soil behavior. Advanced constitutive models can capture many important features of real soil behavior including small strain non-linearity, anisotropic stress-strain-strength properties, rate-dependency, etc. The MIT-E3 soil model (Whittle [1987]) was developed to simulate the effective stress-strain-strength behavior of normally to moderately overconsolidated clays. It is a rate-independent advanced elasto-plastic model that has been successfully applied to the effective stress modeling of clay behavior in the Gulf of Mexico and the predictions of set-up for driven piles in soft clays (Sutabutr [1999], Whittle and Sutabutr [2005]). The model provides a comprehensive framework for characterizing the non-linear, hysteretic and anisotropic stress-strain-strength properties of soft clays and is capable of achieving qualitatively reasonable predictions of cyclic load response (Whittle et al. [1988]). The MIT-E3 model has been implemented and extensively used within popular finite element programs such as Abaqus™ and Plaxis™ through a User Material (UMAT/UDSM) interfaces (Hashash [1992], Jen [1998], Akl [2010], Corral [2013], Orazalin et al. [2015]), and is described in the next subsection. The MIT-E3 soil model is used in the numerical simulation and validation of conductor-soil interaction centrifuge model tests presented in the next chapter.

Recently, an advanced elasto-viscoplastic effective stress soil model, MIT-SR, was developed by Yuan [2016]. The new constitutive model is capable of predicting a wide range of rate-dependent characteristics of soft soils within a unified framework. The MIT-SR effective stress model is built upon previously developed advanced soil models at MIT, but it uses a novel elasto-viscoplastic framework with a physically-based representation of viscoplastic deformation. The model has been calibrated for Resedimented Boston Blue Clay (RBBC) and validated on the elemental level

against the experimental data for various strain-rates and overconsolidation ratios. Sottile [2016] implemented and validated the MIT-SR model within the finite element program Abaqus™, and analyzed the long-term performance of an embankment built on Boston Blue Clay considering rate-dependent soil behavior. In this thesis, the MIT-SR soil model is used to analyze the cone penetration test considering various rate effects and drainage conditions using the developed large deformation analysis procedure.

The MIT soil modes use a set of transformed variables (Kavvadas [1982]) for the general tensorial spaces: the effective stress space (σ', $\underset{\sim}{S}$), the strain space (ε, $\underset{\sim}{E}$), the yield surface gradient (Q, $\underset{\sim}{Q}'$), the plastic flow direction (P, $\underset{\sim}{P}'$), and the anisotropy (1, $\underset{\sim}{\beta}$). Each transformed variable involves six components that include one isotropic component (such as σ', ε, Q, P) and five deviatoric components (for example, $\underset{\sim}{S}$ that includes S_1, S_2, S_3, S_4 and S_5). These transformed variables are consistent, and their usage can substantially simplify the numerical implementations of the advanced constitutive soil models as shown in Kavvadas [1982].

This section provides a brief description of MIT-E3 and MIT-SR constitutive soil models used during this research. The full discussion and the details of the model formulations can be found in Whittle [1987], Hashash [1992], Whittle [1995] for MIT-E3 soil model and in Yuan [2016], Sottile [2016] for MIT-SR soil model. The typos that appeared in the previous descriptions of the MIT-E3 soil model (Whittle [1987], Whittle and Kavvadas [1994], Whittle [1993b], Hashash [1992], Akl [2010]) were fixed, and the main equations were checked against the implementation in the Fortran code. The list of typos in the previously published model documentation can be found in Whittle [1995].

3.3.1 MIT-E3 Soil Model

The MIT-E3 soil model formulation (Whittle and Kavvadas [1994], Whittle [1993a], Whittle et al. [1988], Whittle [1987]) is based on the incrementally, linearized theory of rate independent, elasto-plasticity. The formulation consists of three components: a) an elasto-plastic model for normally consolidated clays; b) a perfectly hysteretic

formulation and c) bounding surface plasticity. The model describes a number of important aspects of soil behavior which have been observed in laboratory tests on K_0-normally consolidated clays including: 1) anisotropic stress-strain-strength properties associated with 1-D consolidation history and subsequent straining; 2) post-peak, strain softening in undrained shear tests in certain modes of shearing on normally and lightly overconsolidated clays; 3) small-strain non-linearity following a reversal of load direction; 4) hysteretic behavior during unload-reload cycles of loading; 5) occurrence of irrecoverable plastic strains during cyclic loading and shearing of overconsolidated clays.

The yield surface used in the MIT-E3 soil model is initially oriented along the direction of consolidation and is written as:

$$f = \sum_{i=1}^{n} (S_i - \sigma' b_i)^2 - c^2 \sigma' (2\alpha' - \sigma') = 0 \tag{3.15}$$

where S_i is the deviatoric stress components using transformed variables, σ' is the mean effective stress, b_i is the components of a vector describing the orientation of the yield surface, c is the ratio of the semi-axes of the ellipsoid, $2\alpha'$ is the size of the yield surface (Figure 3-38), n is the number of independent stress components ($n = 3$ is for 2D, and $n = 5$ for 3D problems)

Failure conditions are represented by an anisotropic failure criterion:

$$h = \sum_{i=1}^{n} S_i^2 - 2\sigma' S_1 \xi_1 + \sigma'^2 (\xi_1^2 - k^2) \tag{3.16}$$

where the values of ξ_1 and k are:

$$\xi_1 = \frac{1}{2}\left(\sqrt{\frac{2}{3}}\frac{6\sin\varphi'_{TC}}{3-\sin\varphi'_{TC}} - \sqrt{\frac{2}{3}}\frac{6\sin\varphi'_{TE}}{3+\sin\varphi'_{TE}}\right) \tag{3.17}$$

$$k = \frac{1}{2}\left(\sqrt{\frac{2}{3}}\frac{6\sin\varphi'_{TC}}{3-\sin\varphi'_{TC}} + \sqrt{\frac{2}{3}}\frac{6\sin\varphi'_{TE}}{3+\sin\varphi'_{TE}}\right) \tag{3.18}$$

The MIT-E3 assumes that the orientation of the failure criterion is fully defined by the friction angles measured in triaxial compression and extension tests (φ'_{TC} and

φ'_{TE}) at large strains (typically measured ε_a =10% in undrained shear tests).

Two hardening rules to describe the changes in the size and orientation of the yield surface are assumed:

$$\dot{\alpha}' = \alpha' \varsigma \dot{\varepsilon}^p \tag{3.19}$$

$$\dot{\boldsymbol{b}}_{\boldsymbol{i}} = \Psi_0 \langle r_x \rangle \frac{1}{\alpha'} (\boldsymbol{S}_{\boldsymbol{i}} - \sigma' \boldsymbol{b}_{\boldsymbol{i}}) \dot{\varepsilon}^p \tag{3.20}$$

where ς is dimensionless function of the state variables obtained by invoking the consistency requirement ($\dot{f} = 0$), Ψ_0 is a material constant controlling the rate of rotation of the yield surface, and r_x is a scalar which describes the relative orientation of the yield surface to the critical state cone (Figure 3-38).

A non-associated flow rule is used:

$$P = 2c^2 \alpha' r_c \tag{3.21}$$

$$\boldsymbol{P}'_{\boldsymbol{i}} = c^2 x \left(\boldsymbol{Q}'_{\boldsymbol{i}} + |r_c| \, \boldsymbol{S}_{\boldsymbol{i}} \right) \tag{3.22}$$

$$x = \left(\frac{\lambda}{\lambda - \kappa}\right) \left\{ \frac{1 + 2K_{0NC}}{3(1 - K_{0NC})} - \frac{K}{2G} \left(\frac{\kappa}{\lambda}\right) \right\} \tag{3.23}$$

where x is a constant that defines the K_{0NC} condition, r_c is a scalar variable (analogous to r_x) that describes the location of the current state relative to the failure surface, K is tangential bulk modulus, 2G is tangential shear modulus, K_{0NC},λ ,κ are the material constants.

The elasto-plastic modulus, H, is defined by detailed consideration of the behavior of K_0 - normally consolidated clays.

$$H = 2c^2 \left(\frac{\kappa}{\lambda - \kappa} \right) K \left\{ \alpha' P - S_t 2c^2 \alpha' x \langle r_c \rangle \sum_{i=1}^{n} (Q_i b_i) \right\} \tag{3.24}$$

where S_t is a material constant which strongly affects the softening behavior.

For the overconsolidated soil behavior, the MIT-E3 model includes a hysteretic model and a bounding surface plasticity model. A closed symmetric hysteresis loop (Figure 3-39) is obtained using a hysteretic model formulation which is piece-wise continuous between stress reversal points (Hueckel and Nova [1979]). The load reversal point must be identified in the model formulation, and the stiffness is related to the distance between the current stress state and the reversal point. The volumetric response during unloading is described by a tangential bulk modulus as the following function:

$$K = \frac{1+e}{\kappa_0(1+\delta)}\sigma' \tag{3.25}$$

$$\delta = Cn(\log_e \xi + \omega\xi_s)^{n-1} \tag{3.26}$$

where e is the void ratio, κ_0 defines the initial unloading slope in $e - \log_e \sigma'$space, and C, n, ω are the material constants that describe the small strain non-linearity, ξ and ξ_s are dimensionless distances in stress space which relate the current stress state to the stress reversal state:

$$\xi = \begin{cases} \frac{\sigma'}{\sigma'_{rev}} & for\ \sigma' > \sigma'_{rev} \\ \frac{\sigma'_{rev}}{\sigma'} & for\ \sigma'_{rev} > \sigma' \end{cases} \tag{3.27}$$

$$\xi_s = \sqrt{\sum_{i=1}^{n}(\eta_i - \eta_i^{rev})^2} \tag{3.28}$$

$$\boldsymbol{n_i} = \frac{\boldsymbol{S_i}}{\sigma'} \tag{3.29}$$

where σ'_{rev} is the mean effective stress at the stress reversal point, η_i^{rev} is the stress ratio at the most recent stress reversal state.

In the original MIT-E3 formulation, the stiffness moduli are described relative to the most recent stress reversal point. Immediately, after stress reversal, the soil exhibits isotropic, elastic response governed by K_{max} and G_{max}. The stress reversal

point is defined from the direction of the strain rates. The definition of the load reversal point is achieved by introducing a scalar strain amplitude parameter, χ, which describes the strain history relative to the most recent stress reversal point as follows:

$$\chi = \sqrt{\sum_{i=1}^{n}(E_i - E_i^{rev})^2} \tag{3.30}$$

$$\dot{\chi} = {}^{t+\Delta t}\chi - {}^{t}\chi = \begin{cases} > 0 & \text{Continue loading} \\ \leq 0 & \text{Unloading (set stress reversal point)} \end{cases} \tag{3.31}$$

During reloading, the bounding surface model relates the plastic strains of overconsolidated clays to the plastic behavior previously defined for the normally consolidate material. A radial mapping rule is used to define a unique image point in the bounding surface. Functions are developed to relate the elasto-plastic modulus, H, and flow direction, $\boldsymbol{P}$, to the corresponding values at the current image point, H_I and $\boldsymbol{P}_I$. The MIT-E3 model introduces separate mapping rules for the elasto-plastic modulus and the flow direction which are expressed in general form:

$$\boldsymbol{P} = \boldsymbol{P}_I + \boldsymbol{P}_0 g_1 \tag{3.32}$$

$$H = H_I + H_0 g_2 \tag{3.33}$$

where $\boldsymbol{P}_0$, H_0 are the values of $\boldsymbol{P}$ and H at the first yield; and g_1, g_2 are mapping functions described by the relative position of the current stress and image stress states. A consistent set of equations is used:

$$\boldsymbol{P}_0 = -\left\{2c^2\alpha' r_c + (\boldsymbol{\eta}_I : \boldsymbol{Q'}_I)\right\} \tag{3.34}$$

$$g_1 = \left(\frac{\alpha' - \alpha'_0}{\alpha'}\right)^{\gamma} \tag{3.35}$$

$$H_0 = \frac{1}{\kappa_0}(1+e)\left\{(\alpha' - \alpha'_0)\, h|\boldsymbol{Q}_I||\boldsymbol{P}_I|\right\} \tag{3.36}$$

$$g_2 = \frac{\alpha' - \alpha'_0}{\alpha'_0 - \alpha'_{0i}} \tag{3.37}$$

where α'_{0i} is the size of the load surface at first yield and h, γ are dimensionless material constants which are established from parametric studies.

Table 3.3 presents the description of MIT-E3 model input parameters and the list of standard laboratory tests from which they can be determined. In addition, the following state variables are used in MIT-E3 soil model: effective stress tensor (σ', $\boldsymbol{S}$), the size and orientation of the bounding surface (α',$\boldsymbol{b}$), the effective stresses at the stress reversal point (σ'_{rev}, $\boldsymbol{S}_{rev}$), the strains developed since the last stress reversal state ($^{\Delta l}\varepsilon$, $^{\Delta l}\boldsymbol{E}$), the size of the load surface at first yield, α'_{0i}.

Figure 3-40 shows the predictions of undrained behavior of normally consolidated Boston Blue Clay (BBC) in triaxial compression and extension modes of shearing using simple isotropic Modified Cam Clay (MCC) and advanced MIT-E3 soil models. It can be seen that the advanced anisotropic soil model captures the real soil behavior as measured in laboratory tests (Ladd and L. [1972]) substantially better than the MCC soil model which has its well-known limitations (Kavvadas [1982]).

3.3.2 MIT-SR Soil Model

Yuan [2016] proposed a new elasto-viscoplastic model capable of overcoming the drawbacks of existing isochrone or isotache-based (Suklje [1957]) models and providing a new framework for describing a full spectrum of rate dependent behavior, including isotache-type behavior and temporary rate effects observed in 1-D consolidation tests. The MIT-SR soil model formulation assumes that the volumetric and deviatoric components of the total strain tensor are decomposed into elastic and viscoplastic contributions as follows:

$$\begin{pmatrix} \dot{\varepsilon} \\ \dot{\boldsymbol{E}} \end{pmatrix} = \begin{pmatrix} \dot{\varepsilon}^{el} + \dot{\varepsilon}^{vp} \\ \dot{\boldsymbol{E}}^{el} + \dot{\boldsymbol{E}}^{vp} \end{pmatrix} \tag{3.38}$$

where superscripts ^{el} and ^{vp} denote the elastic and viscoplastic, respectively.

Similar to prior MIT models, the generalized MIT-SR formulation incorporates a 3-D ellipsoidal loading surface (Figure 3-41) to couple the volumetric and deviatoric responses, and a conical surface to represent the critical state conditions. The MIT-SR model does not need a bounding surface to constrain stress states, and it introduces a 3-D ellipsoidal reference surface. Figure 3-42 shows the MIT-SR surfaces in the meridian plane which comprises the mean effective stress and shear stress corresponding to triaxial compression and extension conditions. The model assumes that elastic response is isotropic and the viscoplastic strain is described by a generalized flow rule. The loading surface has the following expression:

$$f = (\sigma')^2 \left\{ (\boldsymbol{\eta} - \boldsymbol{b}) : (\boldsymbol{\eta} - \boldsymbol{b}) - \zeta^2 \left(\frac{\alpha_1'}{\sigma'} - 1 \right) \left(\frac{\sigma'}{\alpha_1'} \right)^m \right\} \tag{3.39}$$

where $\sigma'$is the mean effective stress, $\boldsymbol{\eta}$is the deviatoric stress ratio ($\frac{\boldsymbol{S}}{\sigma'}$), $\boldsymbol{b}$ is a tensor describing the orientation of the surface, $\alpha_1'$is a measure of the size of the loading surface, m and $\zeta$are the material parameters that control the shape of the surface. When $m = 1$ the shape of the surface is equivalent to MIT-E3 (ellipsoidal). The parameter ζ describes the frictional characteristics of clays:

$$\zeta^2 = c^2 + \boldsymbol{b} : \boldsymbol{b} - \boldsymbol{\eta} : \boldsymbol{b} \tag{3.40}$$

$$c^2 = \frac{24 \sin^2 \phi_m'}{(3 - \sin \phi_m')^2} \tag{3.41}$$

where ϕ_m' is the material constant controlling the amplitude of the reference surface.

In MIT-SR soil model, a reference surface is introduced which is similar to the loading surface. It is defined in terms of radially mapped current stress state referred to as the image stresses (σ'^r, q^r):

$$f = (\sigma')^2 \left\{ (\boldsymbol{\eta} - \boldsymbol{b}) : (\boldsymbol{\eta} - \boldsymbol{b}) - \zeta^2 \left(\frac{\alpha'}{\sigma'^r} - 1 \right) \left(\frac{\sigma'^r}{\alpha'} \right)^m \right\} \tag{3.42}$$

where α' is a state variable representing the size of the reference surface.

The critical state condition is represented by an isotropic failure criterion, h_f, based on the generalization of Matsuoka and Nakai criterion (Panteghini and Lagioia [2014]):

$$h_f(\eta) = k^2 - \boldsymbol{\eta} : \boldsymbol{\eta} = \mathbf{0} \tag{3.43}$$

$$k^2 = k_a^2 + (3 - \frac{k_a^2}{2}) J_{3\eta} \tag{3.44}$$

$$k_a^2 = \frac{8 \sin^2 \phi'_{cs}}{3 + \sin^2 \phi'_{cs}} \tag{3.45}$$

where k is defined in terms of the third invariant of the deviatoric stress ratio, $J_{3\eta} = \det |\boldsymbol{\eta}|$, $\phi'_{cs}$is the critical state friction angle in triaxial compression measured at large strain (about 10%).

The MIT-SR model uses this plastic multiplier as an external activation source for the internal strain rate. The plastic loading condition (CL) is evaluated on the reference surface at a certain image stress as:

$$CL = (K^r Q^r \dot{\varepsilon} + 2G^r \boldsymbol{Q}'^r : \dot{\boldsymbol{E}}) \tag{3.46}$$

where $K^r$and $G^r$are the elastic bulk and shear moduli evaluated at the reference surface. $Q^r$and $\boldsymbol{Q}'^r$are the volumetric and deviatoric components of the reference surface gradient:

$$\begin{Bmatrix} Q^r \\ \boldsymbol{Q}'^r \end{Bmatrix} = \sigma'^r \begin{Bmatrix} \left[(m\zeta^2 + \boldsymbol{n} : \boldsymbol{b}) \left(1 - \frac{\alpha'}{\sigma'^r} \right) + \zeta^2 \frac{\alpha'}{\sigma'^r} \right] \left(\frac{\sigma'^r}{\alpha'} \right)^m - 2\boldsymbol{\eta} : (\boldsymbol{\eta} - \boldsymbol{b}) \\ 2(\boldsymbol{\eta} - \boldsymbol{b}) + \boldsymbol{b} \left(\frac{\alpha'}{\sigma'^r} - 1 \right) \left(\frac{\sigma'^r}{\alpha'} \right)^m \end{Bmatrix} \tag{3.47}$$

The plastic multiplier (Λ) is computed from the consistency condition ($\dot{f}^r = 0$):

$$\boldsymbol{\Lambda} = \frac{\langle CL \rangle}{H + K^r Q^r P + 2G^r \boldsymbol{Q}'^r : \boldsymbol{P}'}$$

$$H = -\frac{\partial f^r}{\partial \alpha'} \frac{\dot{\alpha}'}{\boldsymbol{\Lambda}} - \frac{\partial f^r}{\partial \boldsymbol{b}} : \frac{\dot{\boldsymbol{b}}}{\boldsymbol{\Lambda}} \tag{3.48}$$

where H is the plastic modulus containing contributions from isotropic and kinematic hardening. The detailed derivation of the plastic modulus is in Yuan [2016].

The MIT-SR model has a non-associated flow rule:

$$\begin{pmatrix} P \\ \boldsymbol{P}' \end{pmatrix} = \begin{bmatrix} (k^2 - \boldsymbol{\eta} : \boldsymbol{\eta}) \frac{\sigma'^r}{\alpha'} \\ \chi P \boldsymbol{\eta} + \frac{\zeta^2 ||\boldsymbol{\eta}||}{\alpha'} \boldsymbol{Q}'^r \end{bmatrix} \tag{3.49}$$

$$\chi = \left(\frac{\rho_c}{\rho_c - \rho_r} \right) \left[\frac{1}{3} \left(\frac{1 + 2K_{0NC}}{1 - K_{0NC}} \right) - \frac{K}{2G} \left(\frac{\rho_c}{\rho_r} \right) \right] \tag{3.50}$$

where $\rho_c$is the compressibility input parameter that controls normally consolidated behavior, ρ_r governs the small strain unloading/reloading behavior, $K_{0NC}$is the input parameter for the lateral earth pressure ratio for normally consolidated state.

The volumetric and deviatoric viscoplastic strain rate components, $\dot{\varepsilon}^{vp}$ and $\dot{\boldsymbol{E}}^{vp}$, are computed by projecting the viscoplastic multiplier ($\boldsymbol{\Lambda}^{vp}$) onto the plastic flow directions, P and $\mathbf{P}'$:

$$\begin{pmatrix} \dot{\varepsilon}^{vp} \\ \dot{\boldsymbol{E}}^{vp} \end{pmatrix} = \Lambda^{vp} \begin{pmatrix} P \\ \boldsymbol{P}' \end{pmatrix} \tag{3.51}$$

The viscoplastic multiplier represents the magnitude of viscoplastic strain rate and can be explicitly assumed as:

$$\Lambda^{vp} = R_a \cdot f(\frac{\alpha'_1}{\alpha'}) \tag{3.52}$$

$$f\left(\frac{\alpha'_1}{\alpha'}\right) = \sqrt{\frac{\alpha'_1}{\alpha'}} \exp\left(\frac{1}{2\beta_2} \left[1 - \left(\frac{\alpha'}{\alpha'_1} \right)^{\beta_2} \right] \right) \tag{3.53}$$

where β_2 is the material constant that characterizes the decrease in the predicted rate dependency and creep properties according to stress history, R_a [1/time] is a state parameter that represents the internal strain rate activated at the meso-scale due to the stimulation of historical straining.

The internal strain rate, $\dot{R}_a$, plays an important role in defining the magnitude of the viscoplastic multiplier and is described by an Activation/Decay mechanism based on concepts from "Granular Solid Hydrodynamics" (Jiang and Liu [2009]):

$$\dot{R}_a = [f_A - R_a] \cdot m_t \tag{3.54}$$

where f_A is the activation function and m_t is the transition coefficient.

The plastic multiplier concept is used to represent the activation function (f_A) :

$$f_A = \Lambda \left(\frac{\Lambda \cdot P_0}{\dot{\varepsilon}_{ref}} \right)^{-\beta} \tag{3.55}$$

$$P_0 = \left(k^2 - \boldsymbol{b} : \boldsymbol{b} \right)_{\eta=b} \tag{3.56}$$

The transient coefficient, m_t , is defined as a function of the magnitude of viscoplastic and total strains:

$$m_t = \left(\frac{\rho_c}{\rho_a} - 1 \right) \frac{||\dot{\boldsymbol{\varepsilon}}^{vp}||}{\rho_c \cdot n} + O(||\dot{\boldsymbol{\varepsilon}}||) \tag{3.57}$$

The $O(||\dot{\boldsymbol{\varepsilon}}||)$ is a sufficiently small term often assumed to be $0.1||\dot{\boldsymbol{\varepsilon}}||$ to to ensure a positive transition coefficient when $||\dot{\boldsymbol{\varepsilon}}^{vp}|| = 0$.

For unloading conditions (CL<0), it is assumed that the internal strain rate, R_a, decreases with the size of the loading surface in a power-law relation:

$$\dot{R}_a = (\beta_3 - 1) \left(\frac{\dot{\alpha}'_1}{\alpha'_1} \right) R_a \tag{3.58}$$

where β_3 is a material constant that controls the decreasing rate in R_a.

Table 3.4 presents the description of MIT-SR model 17 input parameters and the suggested calibration methods from which they can be determined. The MIT-SR soil

model has 5 continuous internal state variables ($\alpha', \boldsymbol{b}, R_a, \sigma^h, \boldsymbol{\eta}^h$), whose initial values can be estimated based in stress and strain rate history of the past consolidation process described in Yuan [2016].

Yuan [2016] calibrated the MIT-SR model for Resedimented Boston Blue Clay (RBBC) and evaluated the performance of the model in predicting the behavior of K_0-consolidated RBBC in different modes of shearing with different OCR and under various strain rates. Figure 3-43 presents the comparison of MIT-SR predictions and measured data for results of CK0UC and CK0UE tests on RBBC for various levels of OCR. Figures 3-44 and 3-45 show the examples of strain rate effects in the undrained triaxial compression and extension tests, respectively, and the comparison with the measured data (Yuan [2016], Sheahan [1991]). It can be seen that the MIT-SR soil model can capture the effects of various strain rates very well.

Table 3.1: Input parameters for Average Gulf Clay using MCC soil model (Whittle and Sutabutr [2005])

Parameter	**Average Gulf Clay (AGC)**
λ	0.282
κ	0.055
M	1.01
φ'_{TC}	25.6
2G/K	0.923
ν'	0.30
K_{0NC}	0.63
e_0 at p'=100kPa	1.492

Table 3.2: Transformed variables used in MIT soil models (Whittle and Kavvadas [1994], Yuan [2016])

Effective stress $(\sigma', \mathbf{S})$	**Stress ratio** $\boldsymbol{\eta}$	**Strain** $(\varepsilon, \mathbf{E})$	**Yield surface Gradient** $(Q, \mathbf{Q}')$	**Plastic flow direction** $(P, \mathbf{P}')$	**Anisotropy** $\mathbf{b}$
$\sigma' = \frac{(\sigma'_x + \sigma'_y + \sigma'_z)}{3}$	1	$\varepsilon = \varepsilon_x + \varepsilon_y + \varepsilon_z$	$Q_s = Q_x + Q_y + Q_z$	$P = P_x + P_y + P_z$	1
$S_1 = \frac{(2\sigma'_y - \sigma'_x - \sigma'_z)}{\sqrt{6}}$	$\eta_1 = \frac{(2\eta_y - \eta_x - \eta_z)}{\sqrt{6}}$	$E_1 = \frac{(2\varepsilon_y - \varepsilon_x - \varepsilon_z)}{\sqrt{6}}$	$Q_1 = \frac{(2Q_y - Q_x - Q_z)}{\sqrt{6}}$	$P_1 = \frac{(2P_y - P_x - P_z)}{\sqrt{6}}$	$b_1 = \frac{(2b_y - b_x - b_z)}{\sqrt{6}}$
$S_2 = \frac{(\sigma'_z - \sigma'_x)}{\sqrt{2}}$	$\eta_2 = \frac{(\eta_z - \eta_x)}{\sqrt{2}}$	$E_2 = \frac{(\varepsilon_z - \varepsilon_x)}{\sqrt{2}}$	$Q_2 = \frac{(Q_z - Q_x)}{\sqrt{2}}$	$P_2 = \frac{(P_z - P_x)}{\sqrt{2}}$	$b_2 = \frac{(b_z - b_x)}{\sqrt{2}}$
$S_3 = \sqrt{2}\sigma_{xy}$	$\eta_3 = \sqrt{2}\eta_{xy}$	$E_3 = \sqrt{2}\varepsilon_{xy}$	$Q_3 = \sqrt{2}Q_{xy}$	$P_3 = \sqrt{2}P_{xy}$	$b_3 = \sqrt{2}b_{xy}$
$S_4 = \sqrt{2}\sigma_{yz}$	$\eta_4 = \sqrt{2}\eta_{yz}$	$E_4 = \sqrt{2}\varepsilon_{yz}$	$Q_4 = \sqrt{2}Q_{yz}$	$P_4 = \sqrt{2}P_{yz}$	$b_4 = \sqrt{2}b_{yz}$
$S_5 = \sqrt{2}\sigma_{zx}$	$\eta_5 = \sqrt{2}\eta_{zx}$	$E_5 = \sqrt{2}\varepsilon_{zx}$	$Q_5 = \sqrt{2}Q_{zx}$	$P_5 = \sqrt{2}P_{zx}$	$b_5 = \sqrt{2}b_{zx}$

Table 3.3: MIT-E3 Soil Model Input Parameters (Whittle [1993b])

Test type	Parameter	Physical contribution/meaning
One-dimensional consolidation (oedometer CRS, etc.)	e_0	Reference Void Ratio on VCL
	λ	Normally Consolidated Compression
	C	Non-linear Volumetric Swelling Behavior
	n	
	h	Irrecoverable Plastic Strain
K_0-oedometer or K_0-triaxial	K_{0NC}	K_0 for virgin normally consolidated clay
	2G/K	The ratio of the tangential elastic shear modulus to the bulk modulus, which is related to the Poisson's ratio of the soil skeleton
Undained triaxial shear tests, OCR=1 (compression), OCR=1 (extension), OCR=2 (compression)	φ'_{TC}	Critical State Friction Angles in Triaxial Compression and Extension
	φ'_{TE}	
	c	Undrained Shear Strength (geometry of bounding surface)
	s_t	Amount of Post-peak Strain Softening in Undrained Triaxial Compression
	ω	Non-linearity at Small Strains in Undrained Shear
	γ	Shear Induced Pore Pressures for OC Clay
Resonant column	$\varkappa_0$	Small strain compressibility at load Reversal
Drained triaxial	Ψ_0	Rate of Evolution of Anisotropy (rotation of bounding surface)

Table 3.4: MIT-SR Soil Model Input Parameters (Yuan [2016])

Symbols	Physical Meaning	Suggested Calibration Method
ρ_c	Compressibility of NC Clay (LCC regime)	Measure from log$e$ – logσ' compression curve
C_b	Small strain elastic compressibility	Derive from high quality small strain measurement of G
D	Nonlinear volumetric and deviatoric hysteretic behavior	Measure from 1-D swelling log$e$ – logσ' curve
r		
w_s		Measure from shear stiffness degradation curve
$2G/K$	Alternative measure of Poisson's ratio at small strain	Measure from 1-D swelling stress path
K_{0NC}	Lateral earth pressure ratio in LCC region	Measure for NC clays using SHANSEP consolidation
ϕ'_{cs}	(Large strain) critical state friction angle	Measure in triaxial compression tests
ϕ'_m	Friction coefficient of loading/reference surface	Fit undrained strengths for CK_0UC on NC clays
m	Geometry of loading/reference surface	Fit tendency of softening for CK_0UC on NC clays
Ψ	Rate of evolution of anisotropy due to stress history	Fit CK_0UE behavior over strain range>5%
ρ_α	Compressibility in secondary compression	Fit 1-D secondary compression curve or inferred from reported C_α/C_c ratio
β	Rate-sensitivity of state steady of R_s	Measure from the rate-sensitivity of CRS tests
$\dot{\varepsilon}_{ref}$	Reference strain rate	Measure at the 24hr interval in IL oedometer tests ($\approx 1x10^{-7}$/sec)
β_2	Nonlinear variation of rate-dependency with stress history	Measure reduction of the post-unloading creep property with OCR in 1-D swelling
β_3	Reduction of creep rate during unloading	Measure decrease in creep rate with OCR in 1-D swelling
D_L	Dilation behavior	Fit effective stress path for CK_0UC with OCR>2

Table 3.5: Bearing Capacity Factors - Replicate Analysis vs. Templeton [2009]

Templeton (2009)		**Replicate Analysis**	
Depth, m	N_p value	Depth, m	N_p value
0.61	9.29	0.5	8.31
1.22	10.45	1.5	9.00
1.83	11.72	2.5	10.20
2.74	13.32	3.5	11.02
3.35	14.08	4.5	11.56
4.57	15.04	5.5	11.90
5.49	15.35	6.5	12.03
7.10	14.11	7.5	12.11
9.41	13.97	8.5	12.15
		9.5	12.22
		10.5	12.15
		11.5	12.04

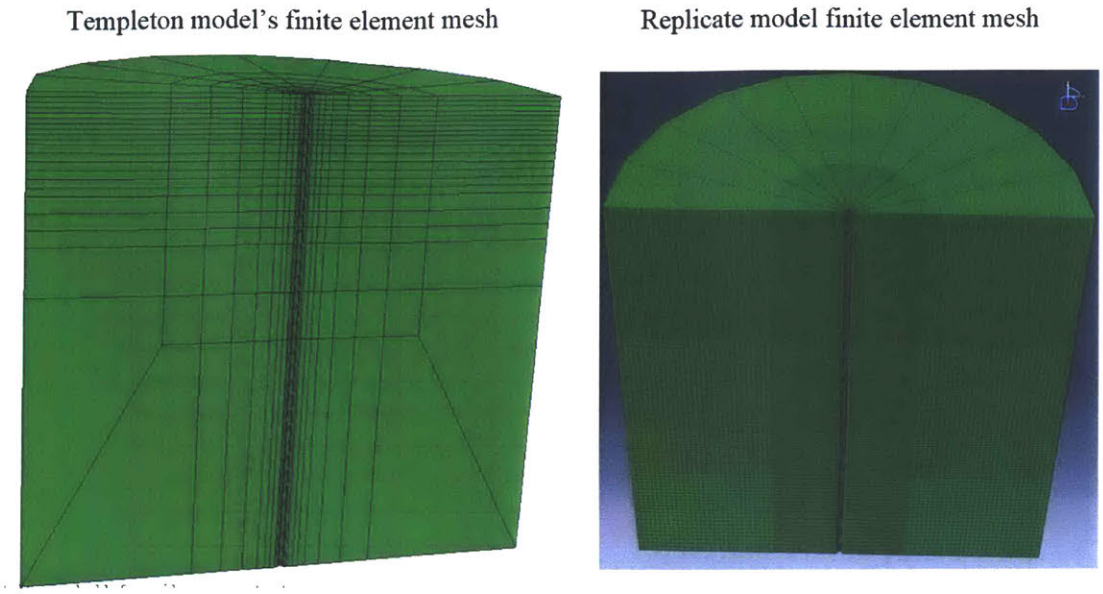

Figure 3-1: Reference Model Geometry of Replicate Analysis

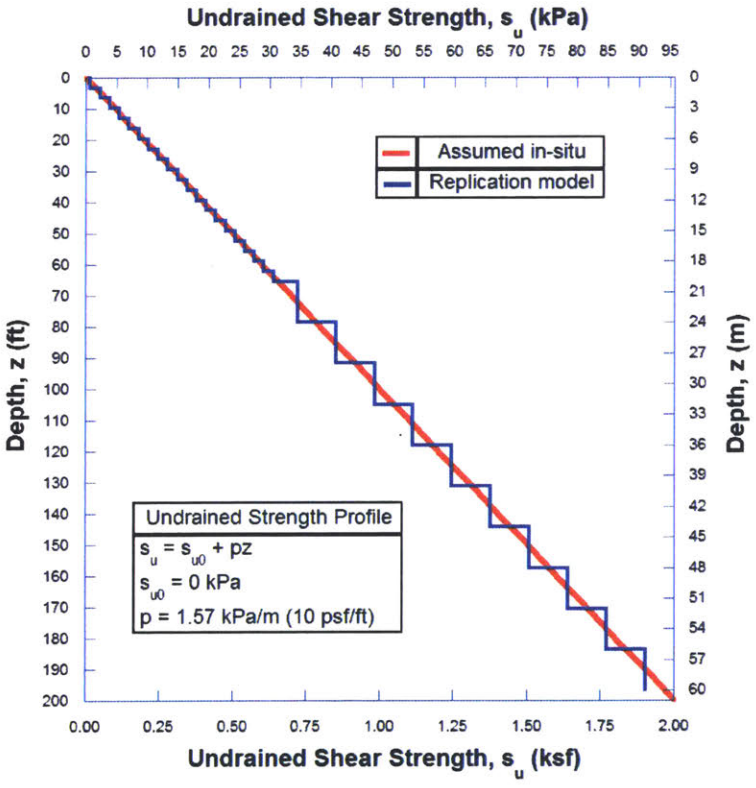

Figure 3-2: Undrained shear strength profile (Templeton, 2009)

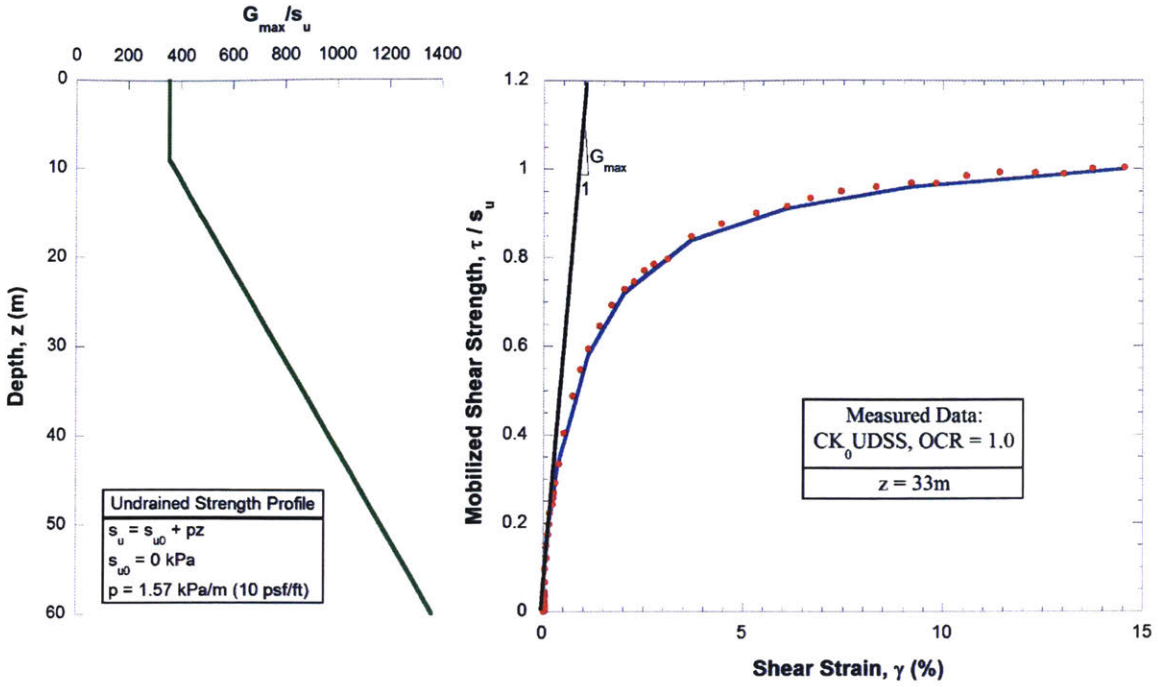

Figure 3-3: IHPP model parameters (Templeton, 2009)

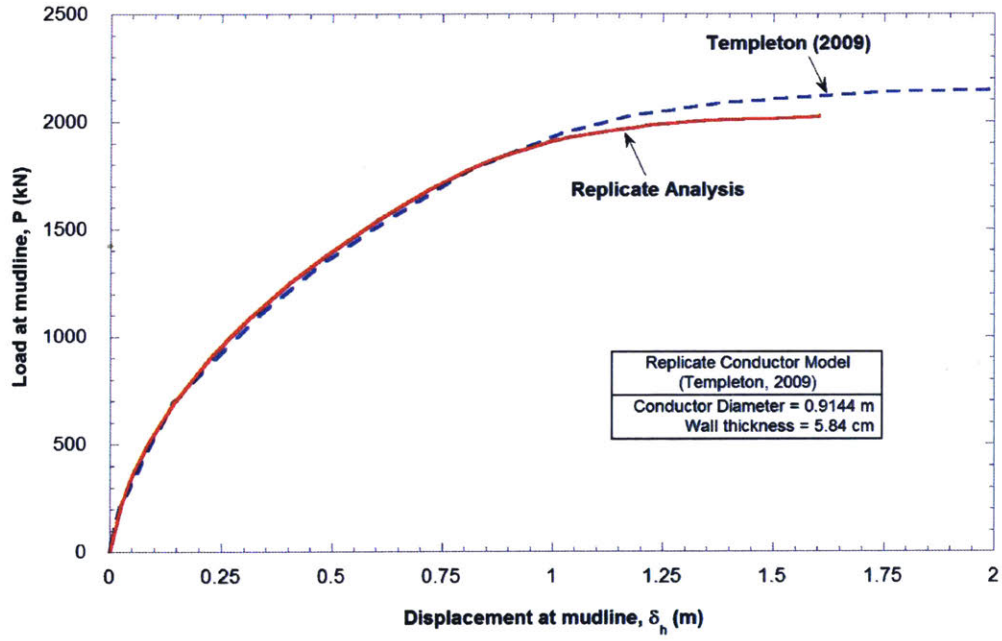

Figure 3-4: Load-displacement response of Replicate Analysis

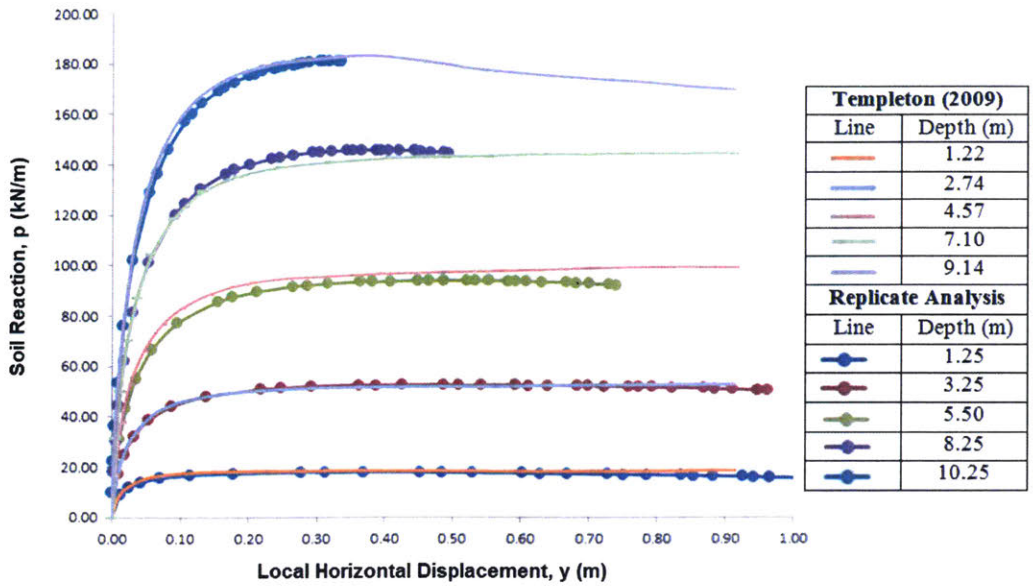

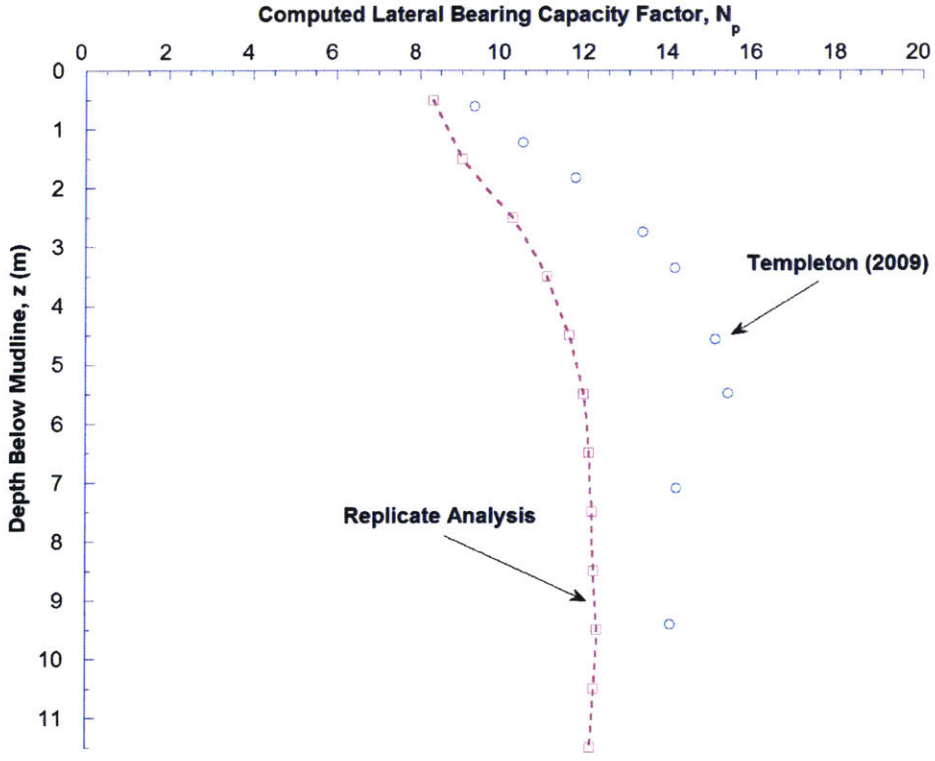

Figure 3-5: Replicate Analysis -"p-y" response

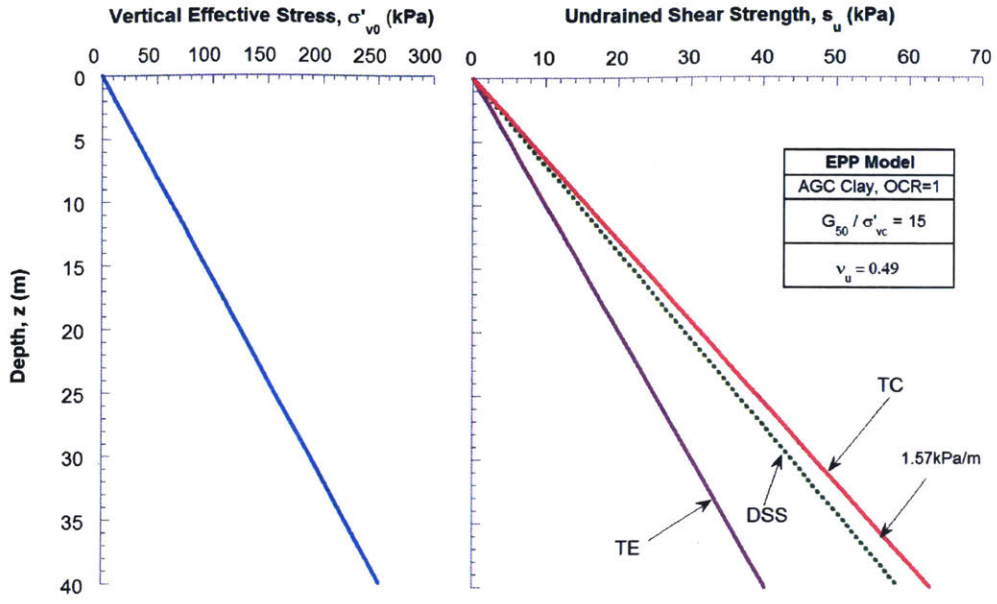

Figure 3-6: In-situ Stresses and Undrained Shear Strength Profiles for Typical Deep-water Gulf of Mexico Conditions

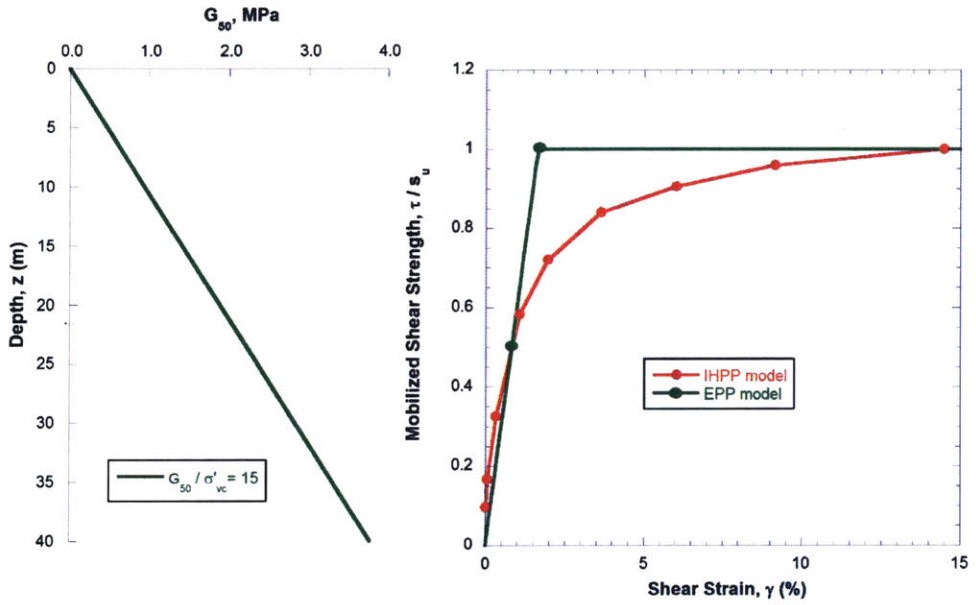

Figure 3-7: IHPP vs. EPP Soil Model Parameters for Initial Total Stress Analysis

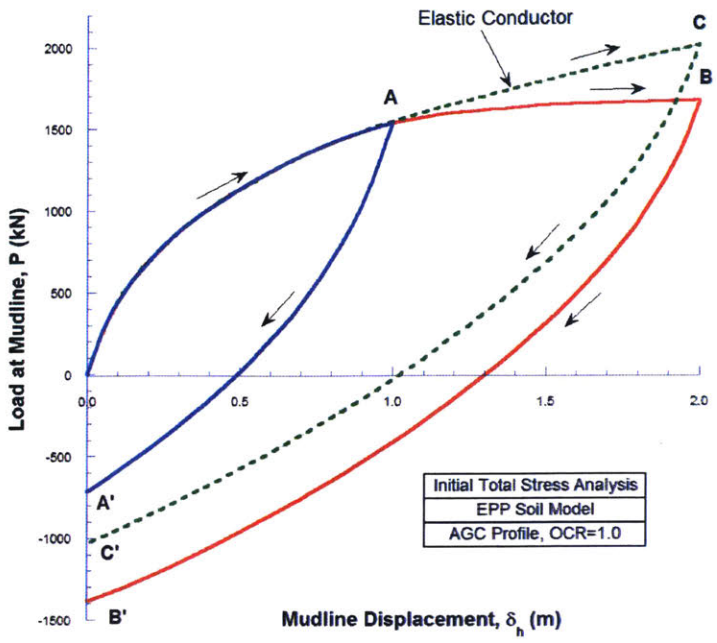

Figure 3-8: Initial Total Stress Analysis - Load-Displacements at Mudline

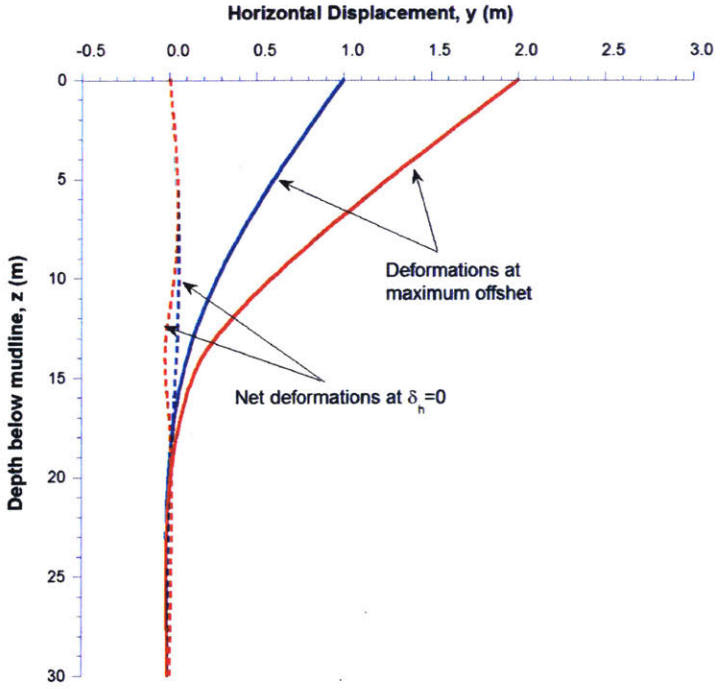

Figure 3-9: Initial Total Stress Analysis - Lateral deformation profiles of elasto-plastic conductor from Base Case analyses with max. mudline offsets 1m and 2m

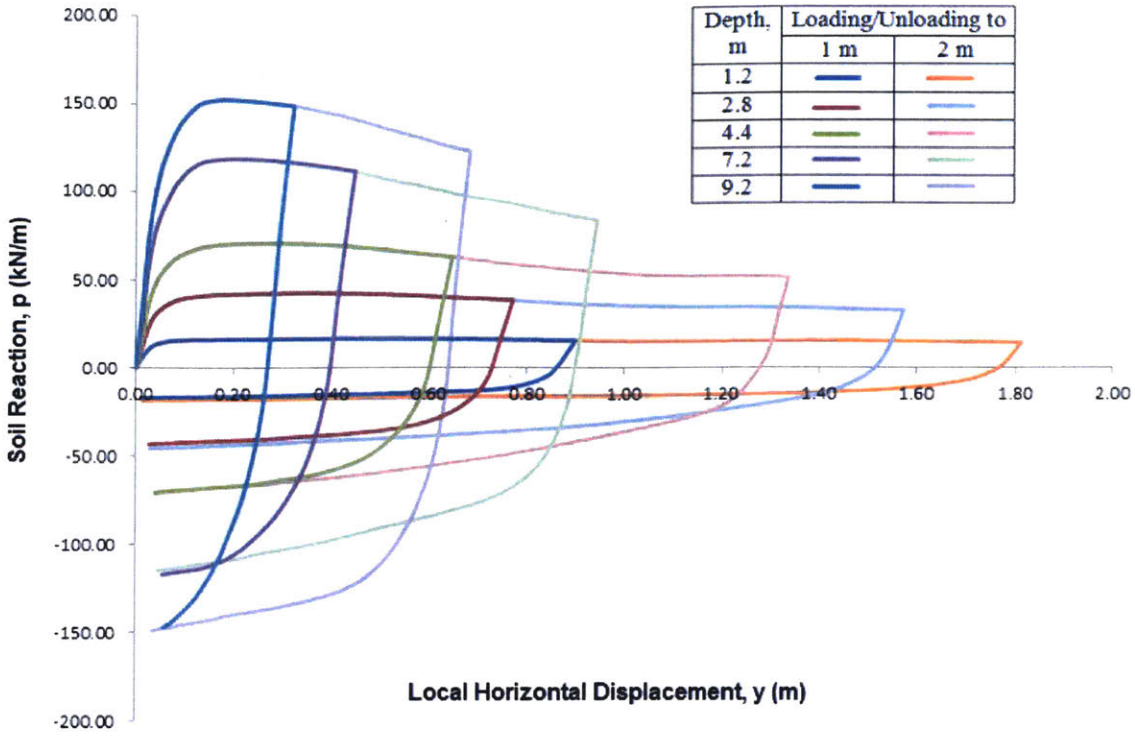

Figure 3-10: Initial Total Stress Analysis - "p-y" response

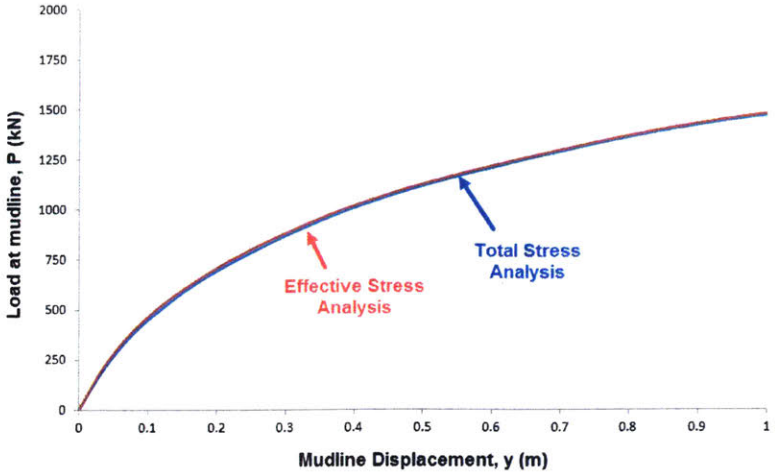

Figure 3-11: Comparison of undrained load-deformation response at mudline using coupled finite elements with initial total stress analysis results

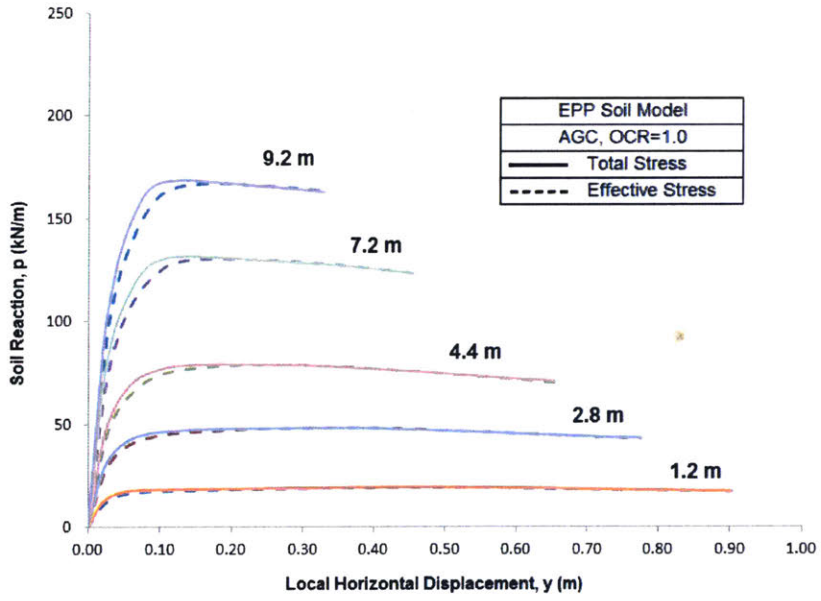

Figure 3-12: Comparison of p-y curves for undrained loading of conductor using coupled finite elements with initial total stress analysis results

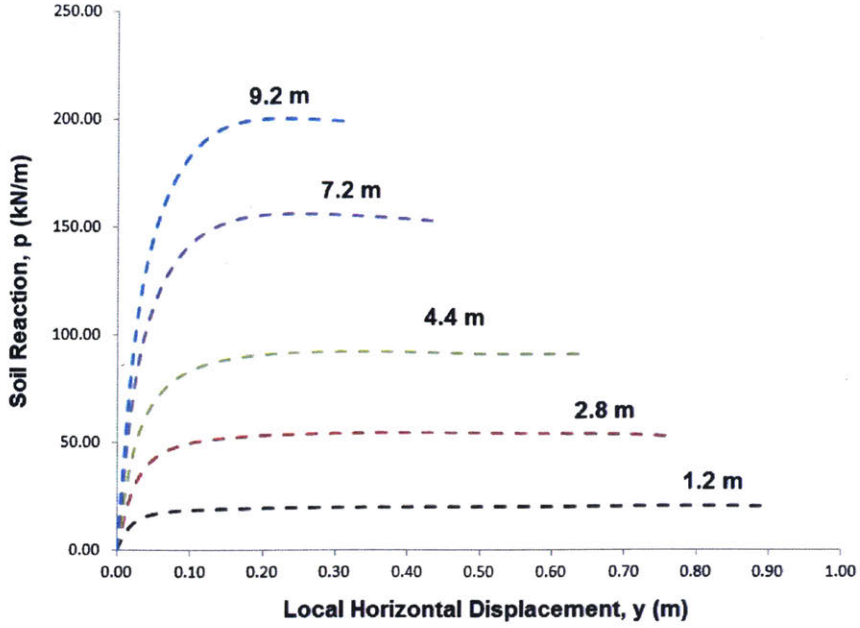

Figure 3-13: p-y interaction curves from undrained analysis using MCC soil model

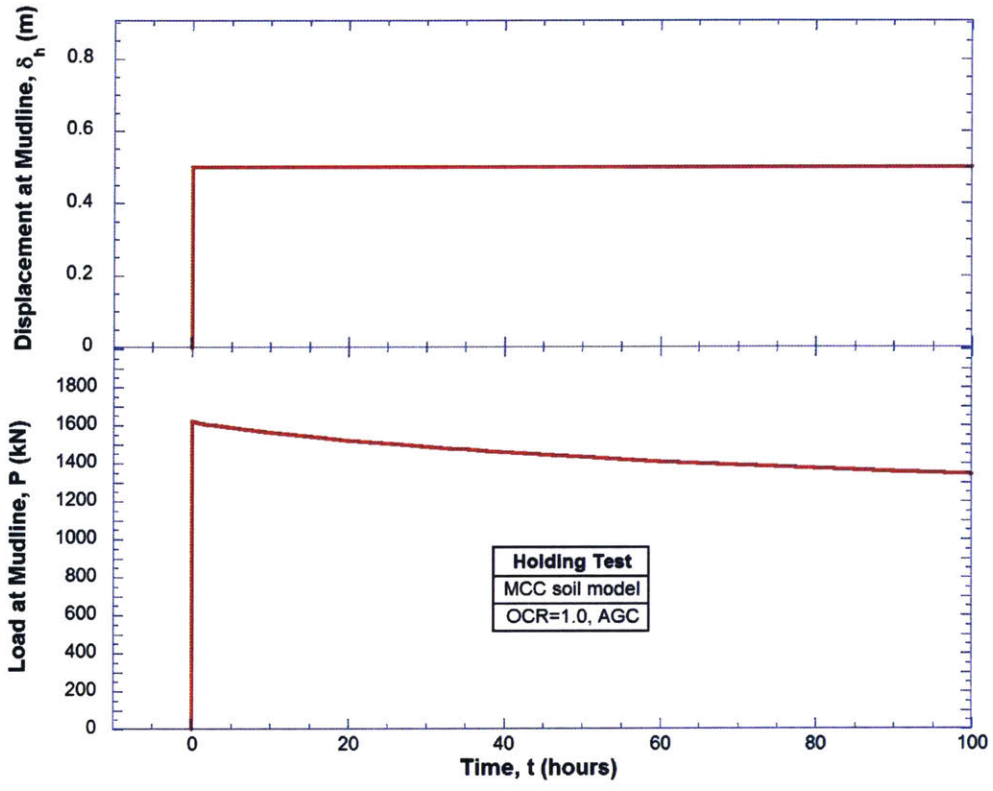

Figure 3-14: Effect of excess pore pressure dissipation in AGC (Holding Test)

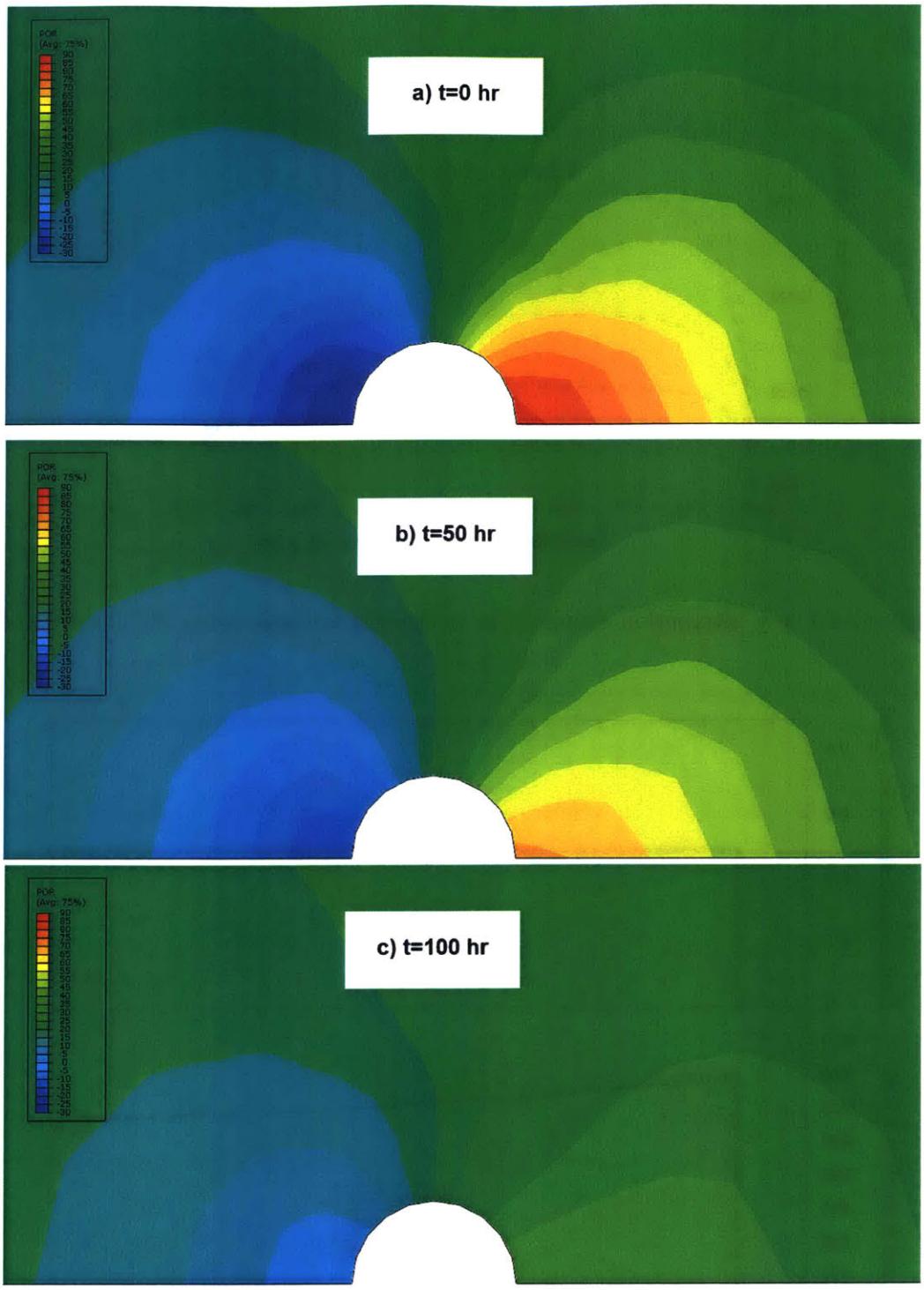

Figure 3-15: Excess pore pressures around conductor at depth of 10m, computed using MCC soil model for normally consolidated AGC at $\delta_h = 0.5m$ (Holding Test)

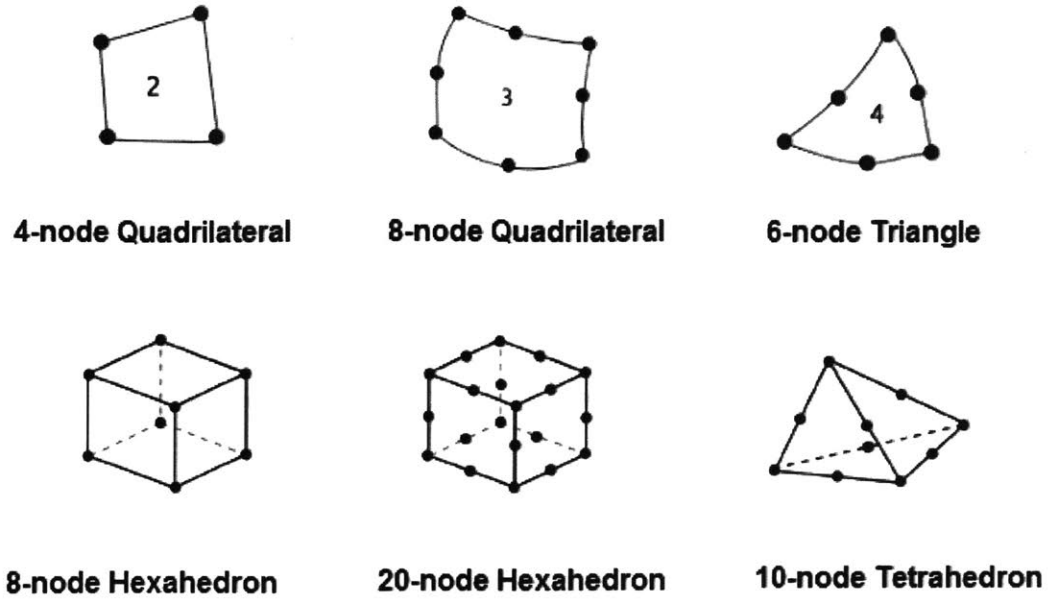

Figure 3-16: Finite Elements for 2D and 3D domains

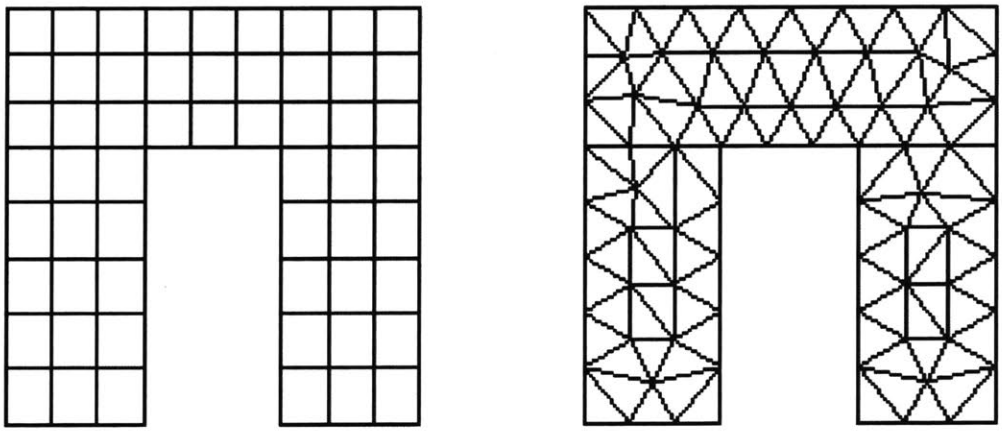

Figure 3-17: Structured Quadrilateral mesh vs. Unstructured Triangular mesh

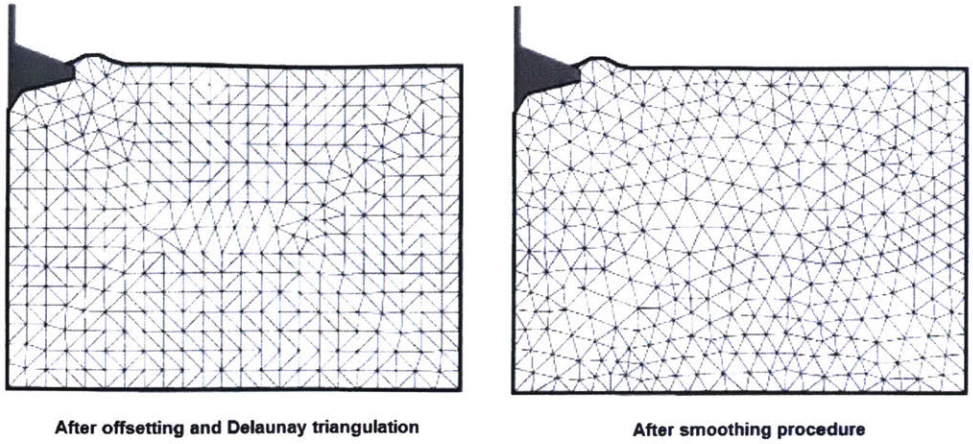

Figure 3-18: Delaunay mesh and Laplacian smoothing (Hu and Randolph [1998a])

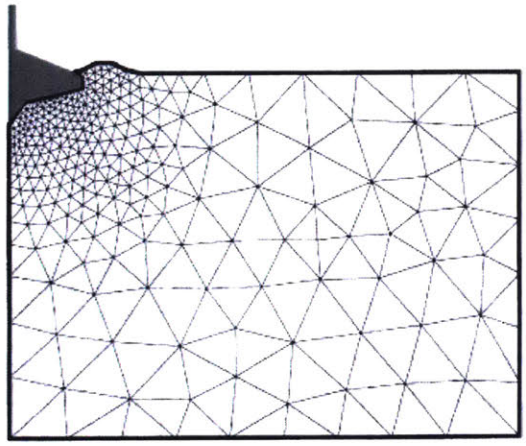

Figure 3-19: Application of mesh density function (Hu and Randolph [1998a])

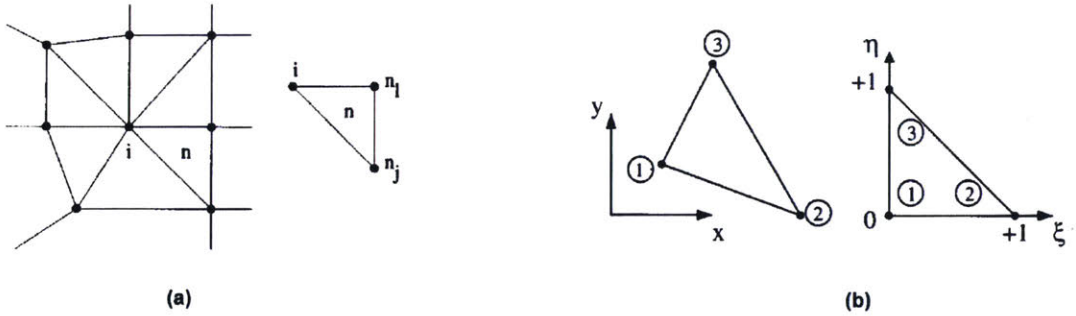

Figure 3-20: Neighboring elements and nodes numbering (Hu and Randolph [1998a])

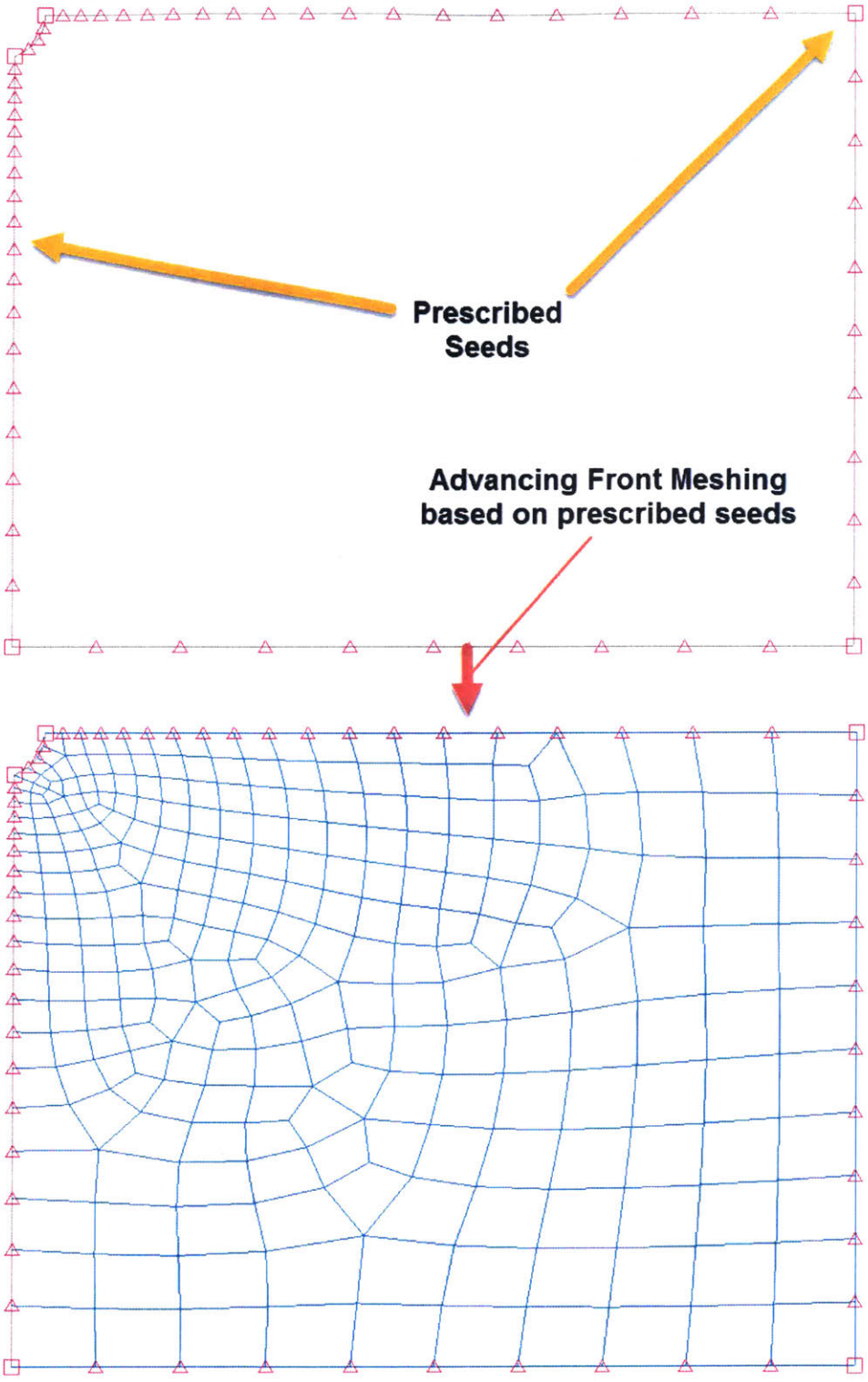

Figure 3-21: A geometry with biased seeding

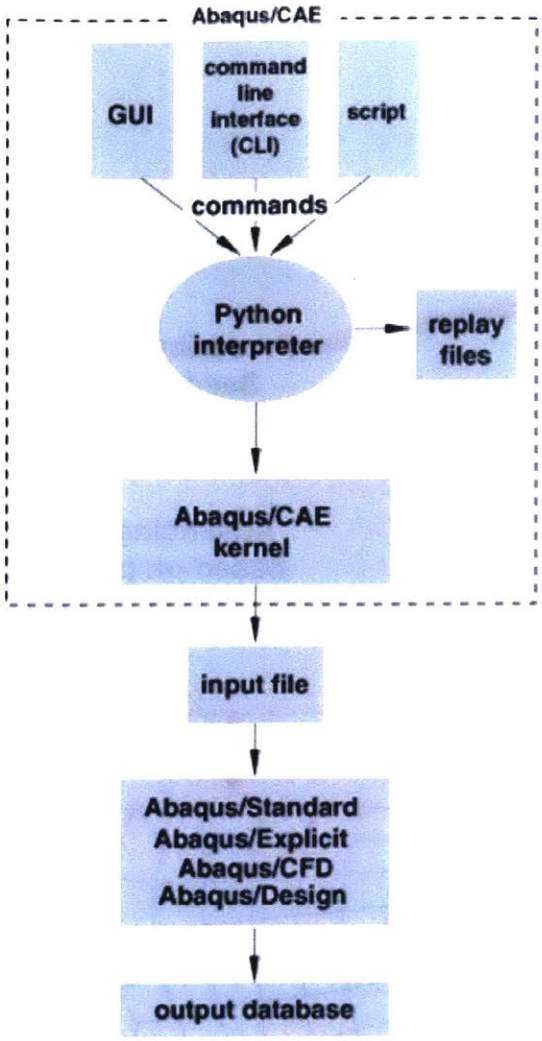

Figure 3-22: Scripting Interface commands and Abaqus™ Environment (SIMULIA [2016])

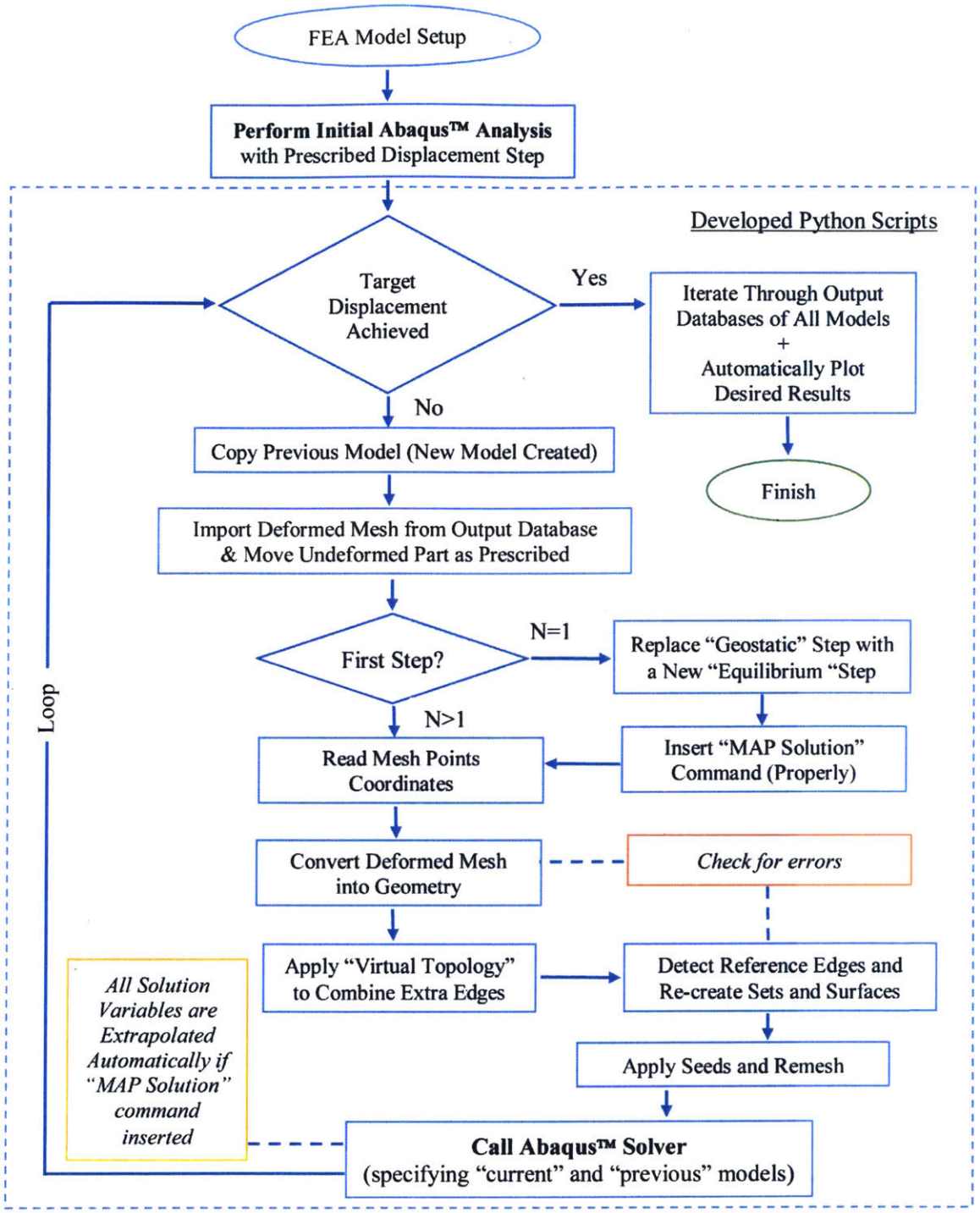

Figure 3-23: General algorithm of the proposed procedure

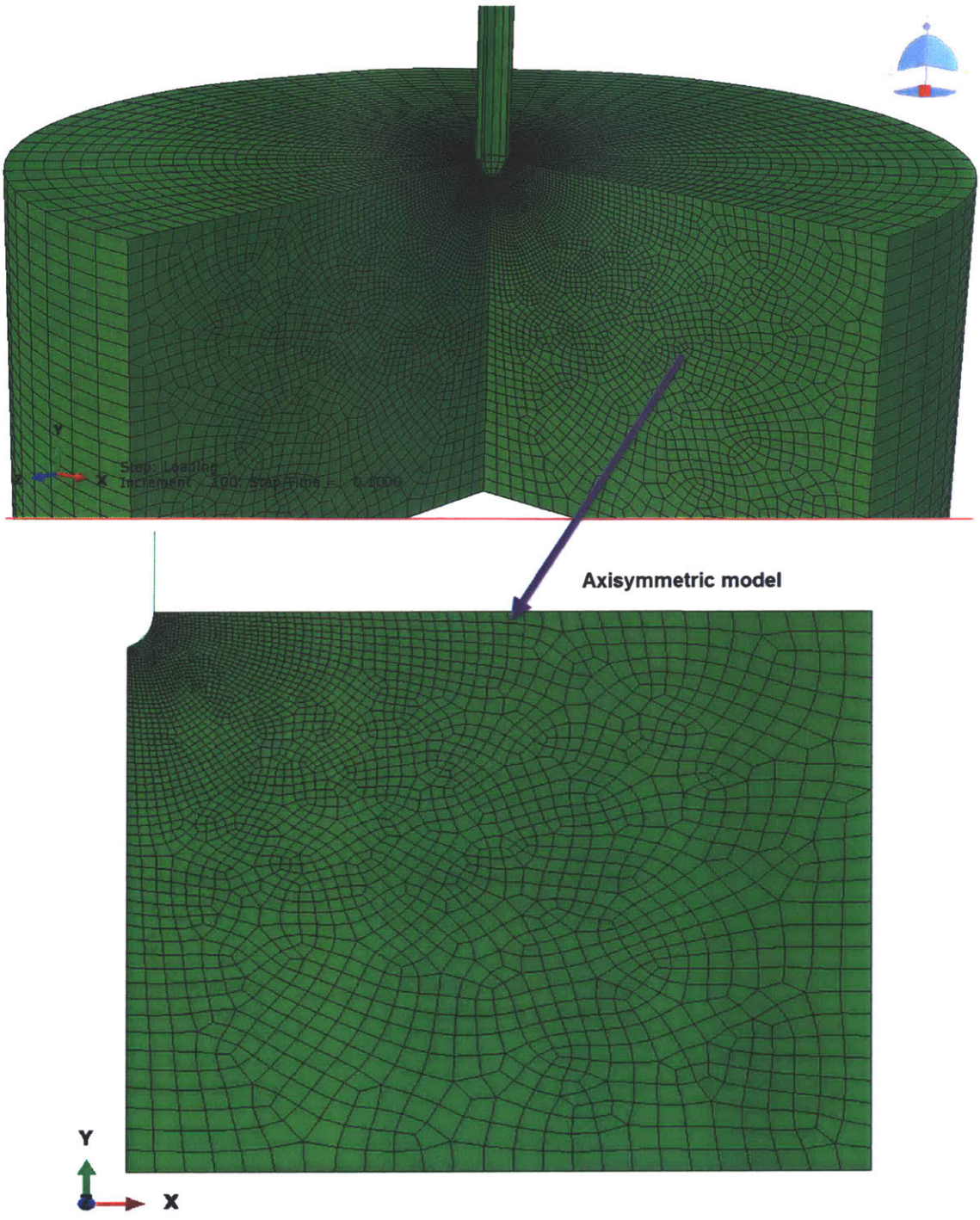

Figure 3-24: Axisymmetric model of Cone Penetration Test

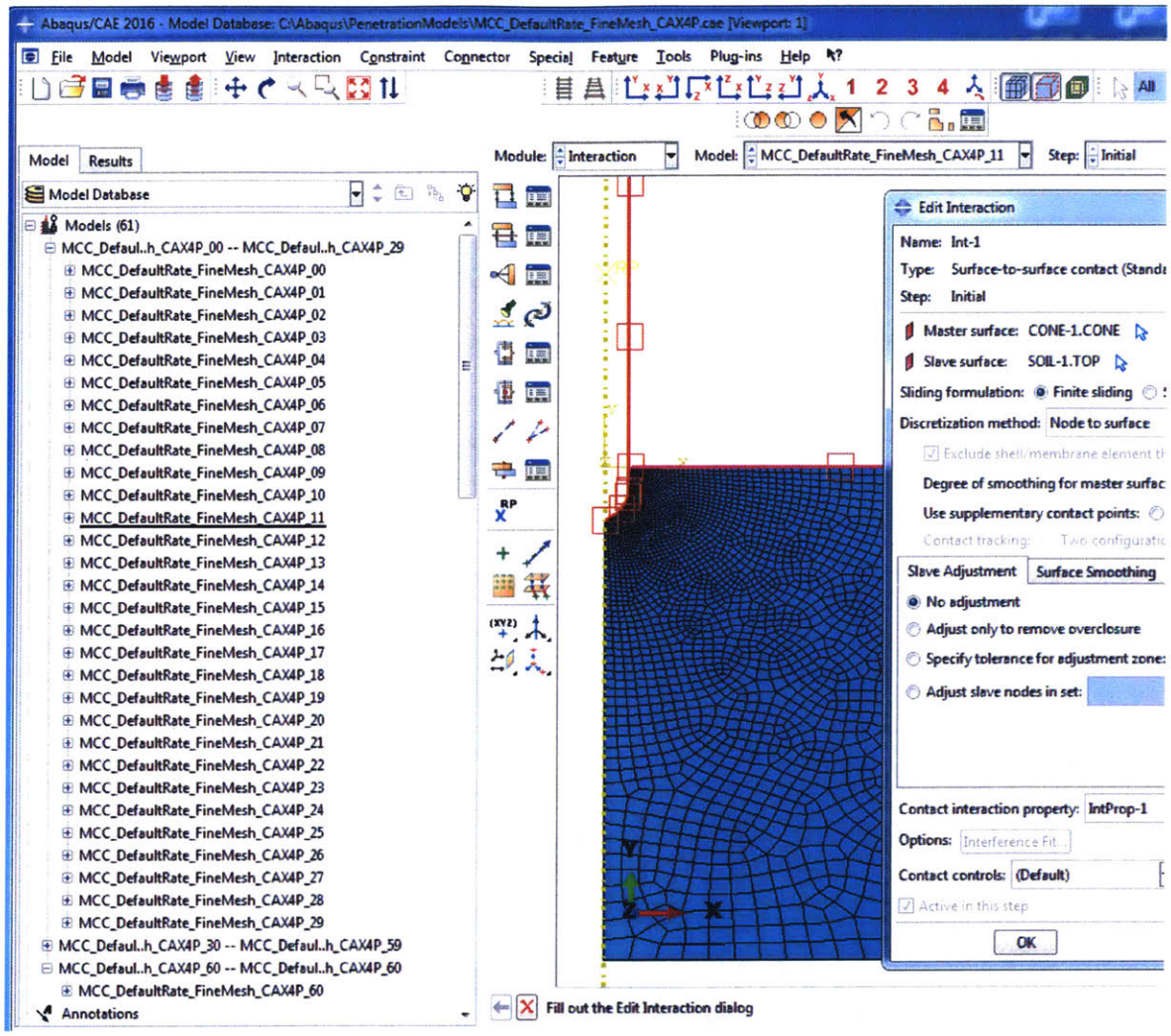

Figure 3-25: Abaqus Model with 60 Remeshing Steps and Contact Properties

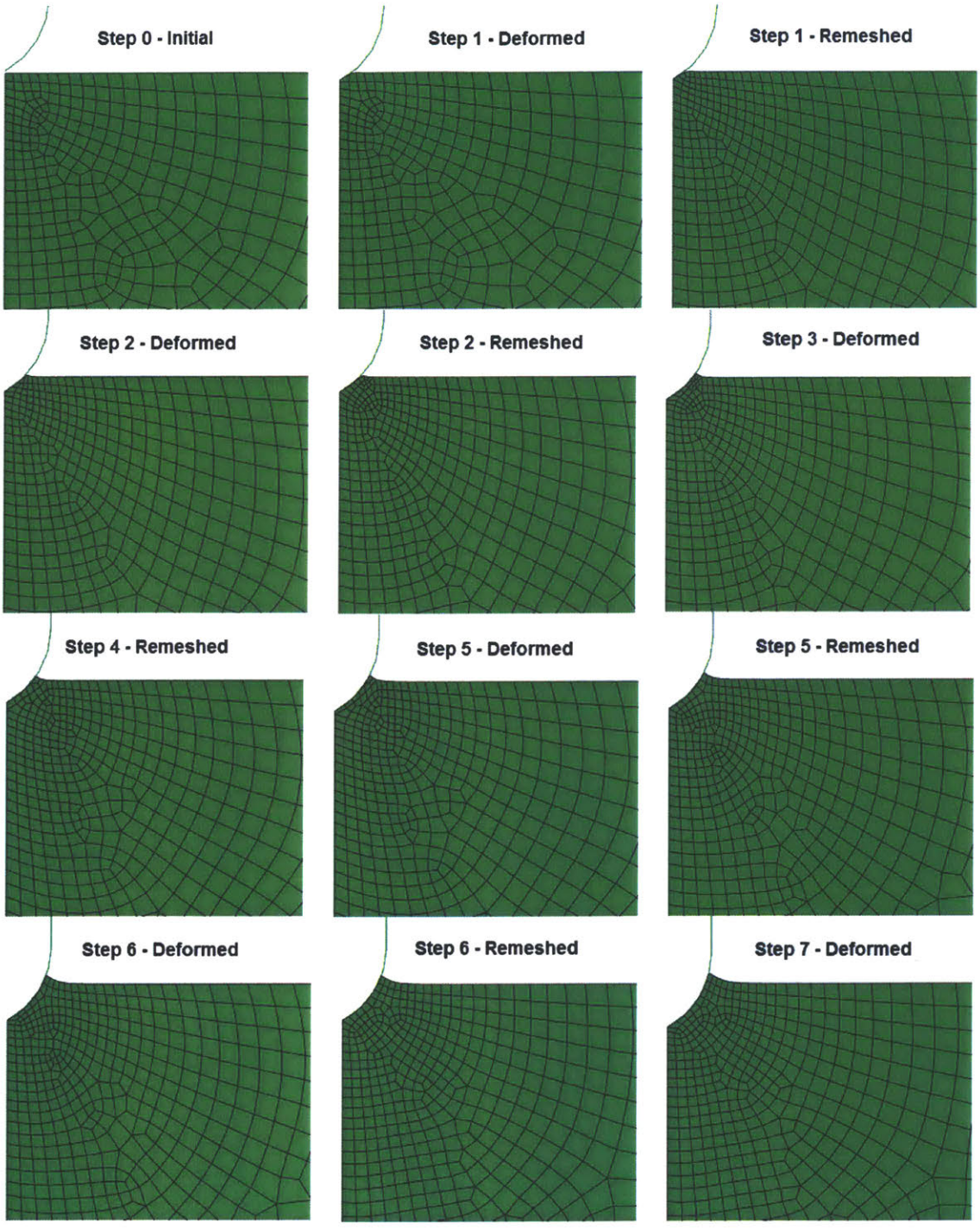

Figure 3-26: Proposed Procedure - Remeshing Example

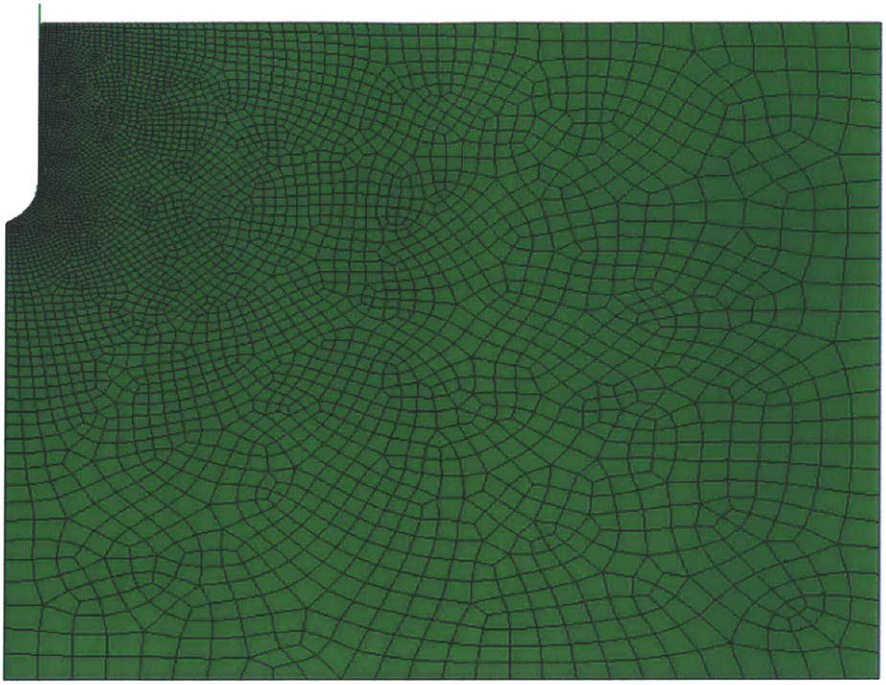

Figure 3-27: Proposed Procedure - Step 1 - Deformed Mesh

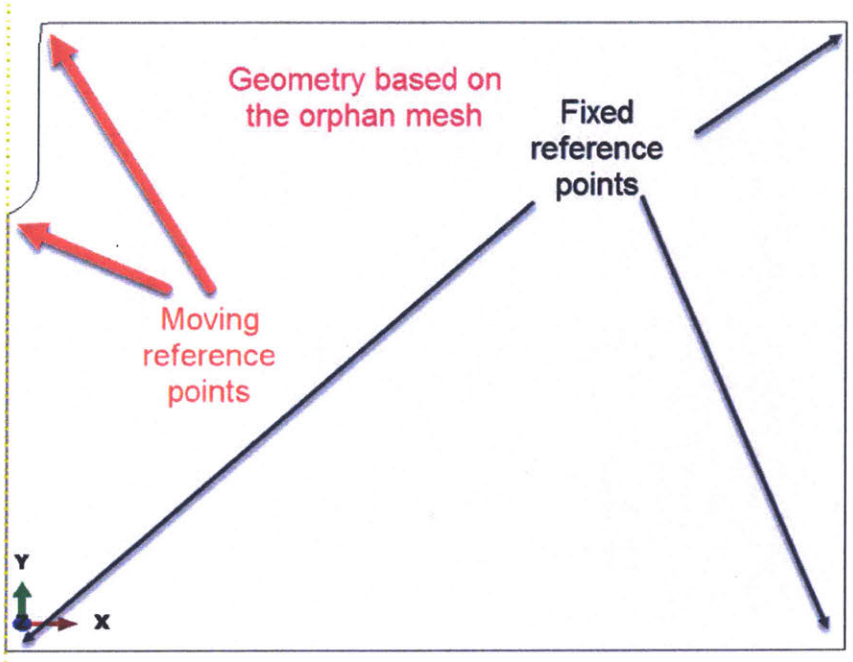

Figure 3-28: Proposed Procedure - Step 2 - Geometry

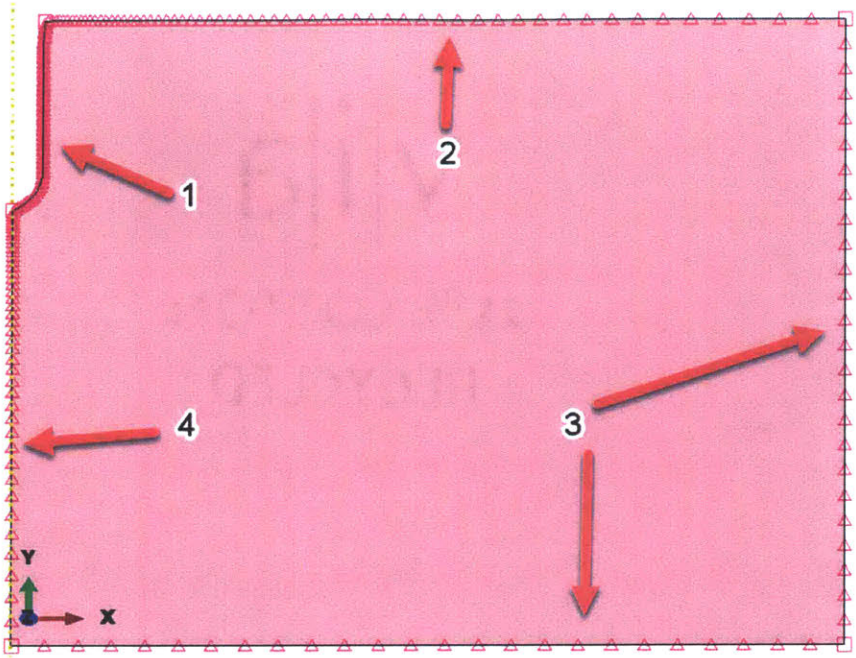

Figure 3-29: Proposed Procedure - Step 3 - Locating Edges and Seeding

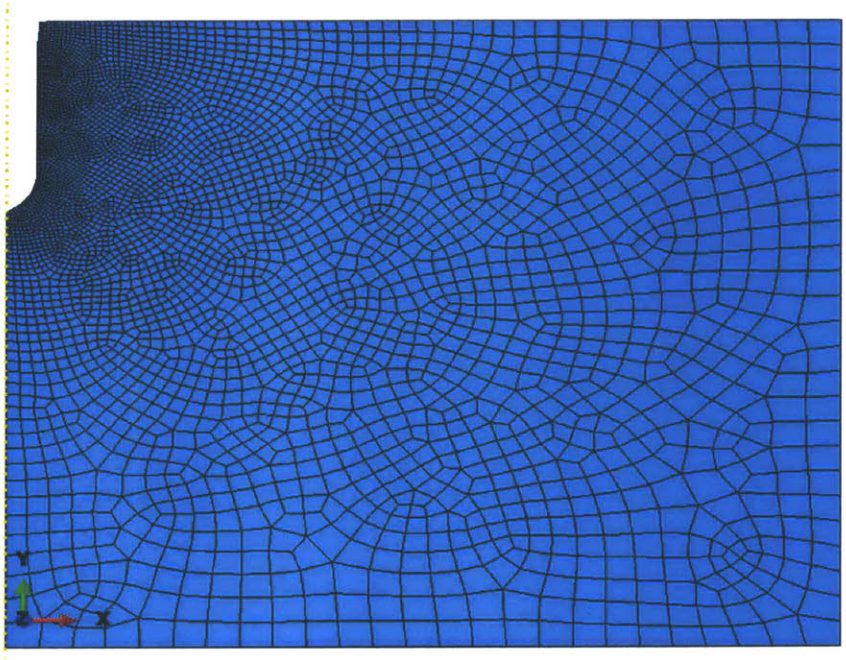

Figure 3-30: Proposed Procedure - Step 4 - Meshing

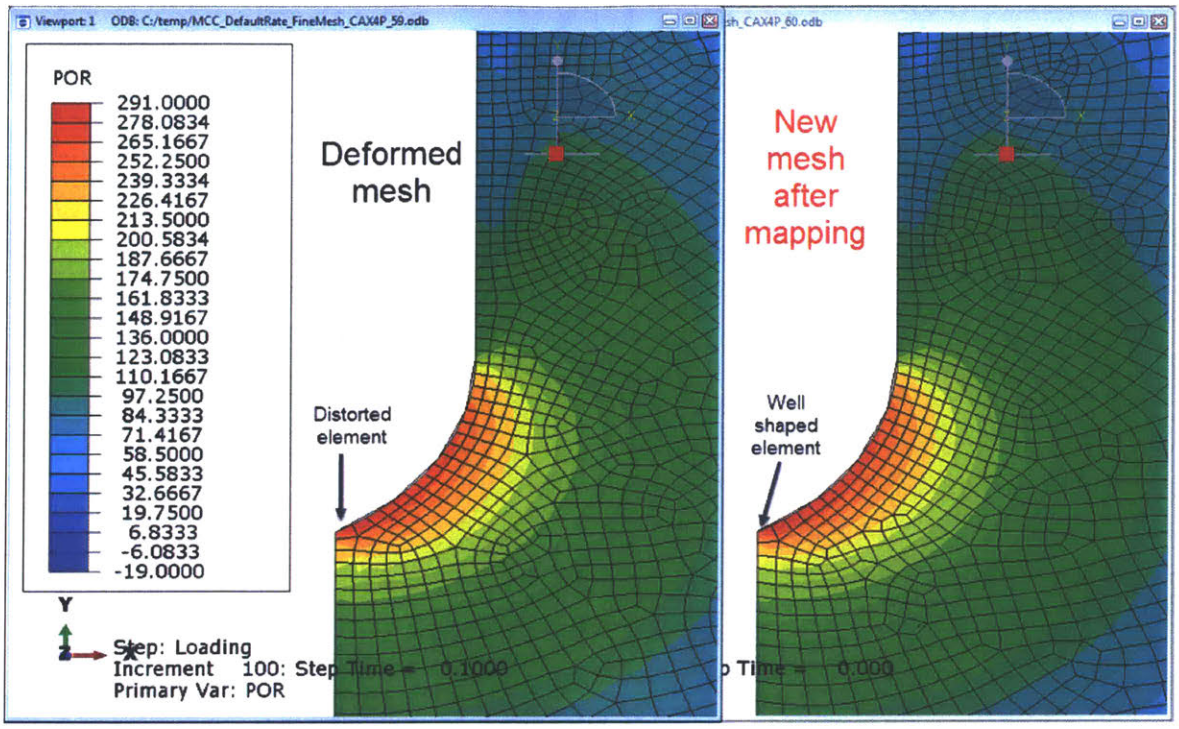

Figure 3-31: Proposed Procedure - Solution Mapping Example

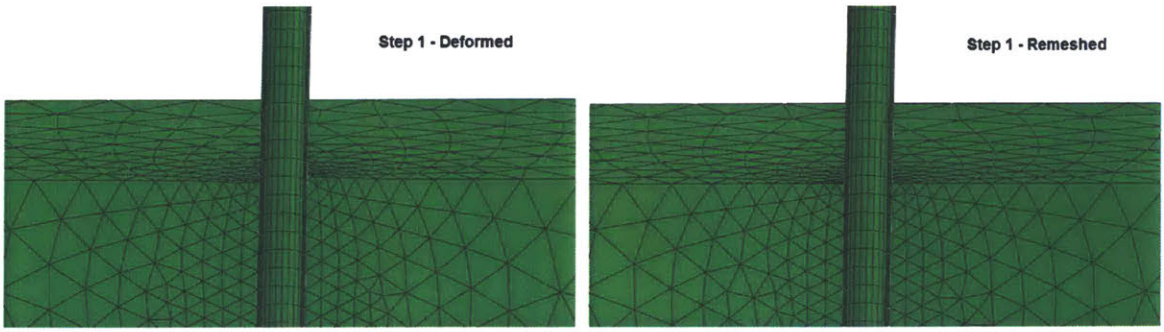

Figure 3-32: Proposed Procedure - 3D Case

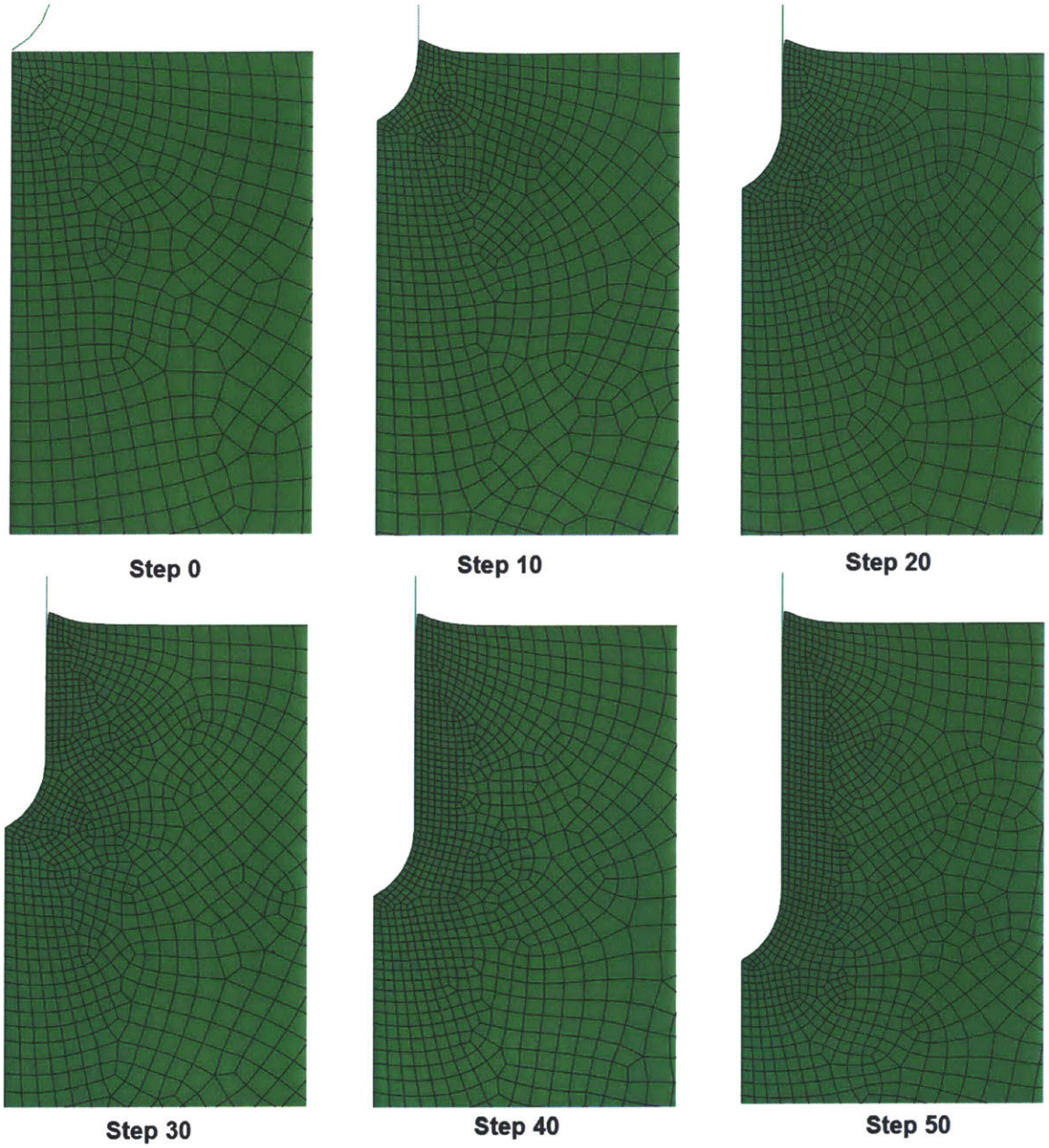

Figure 3-33: Initial Cone Penetration Analysis - Mesh

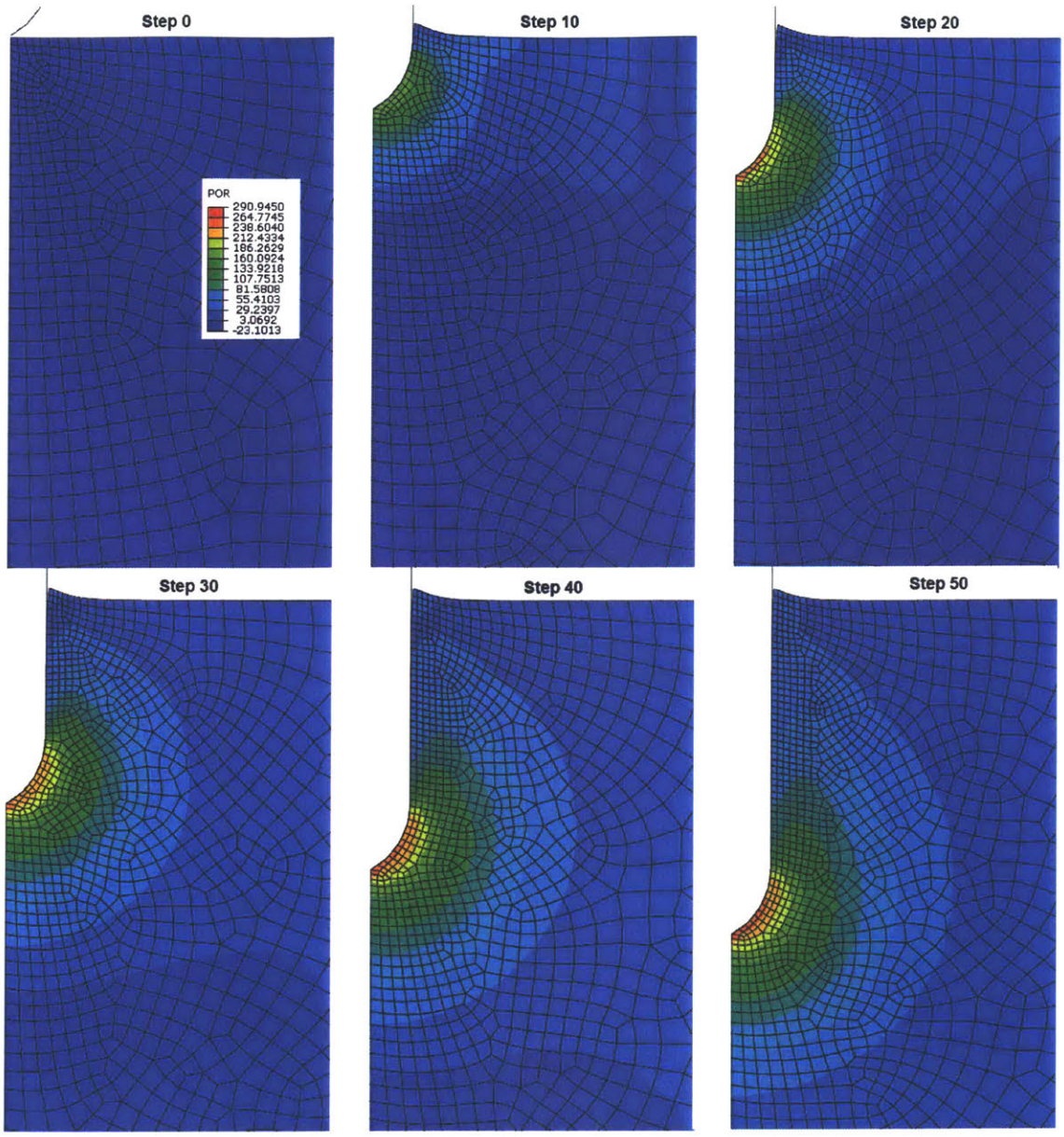

Figure 3-34: Initial Cone Penetration Analysis - Excess Pore Pressures

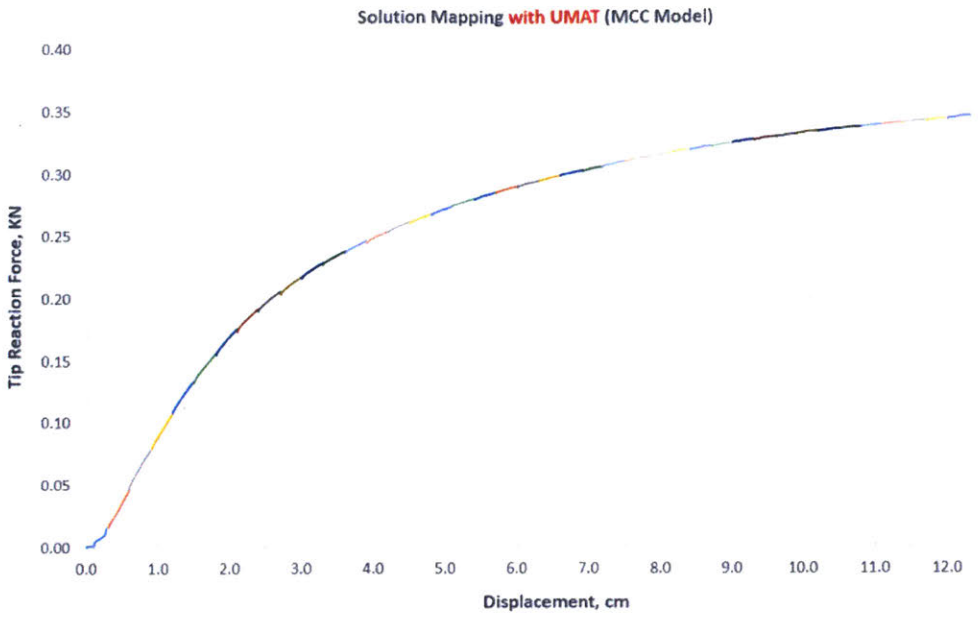

Figure 3-35: Initial Cone Penetration Analysis - Tip Reaction Force vs. Displacement

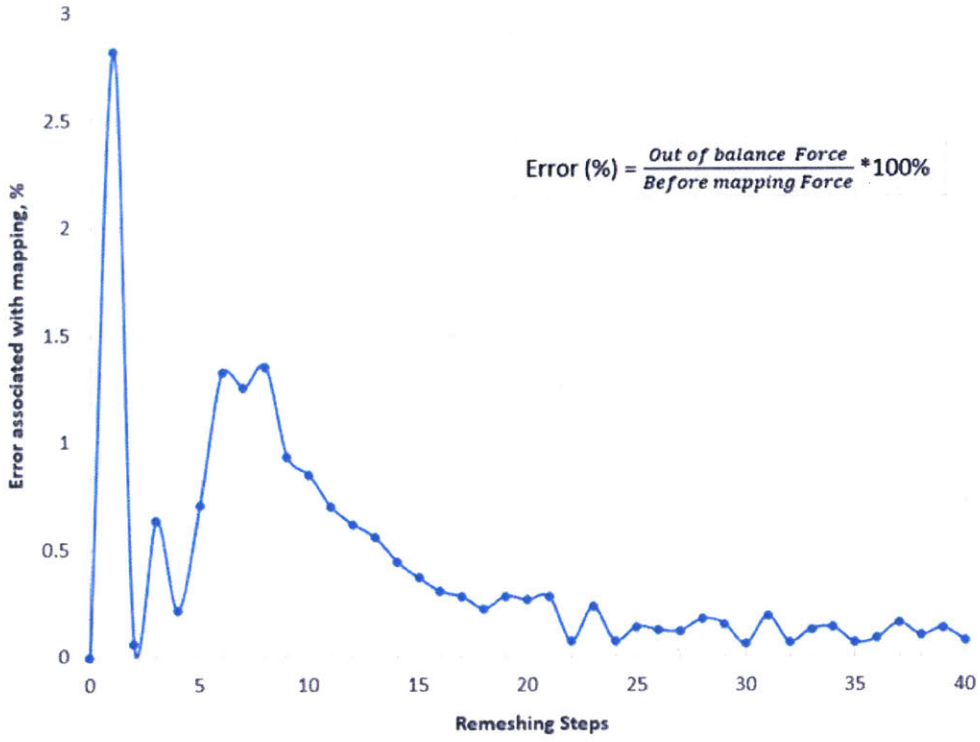

Figure 3-36: Initial Cone Penetration Analysis - Error Assessment

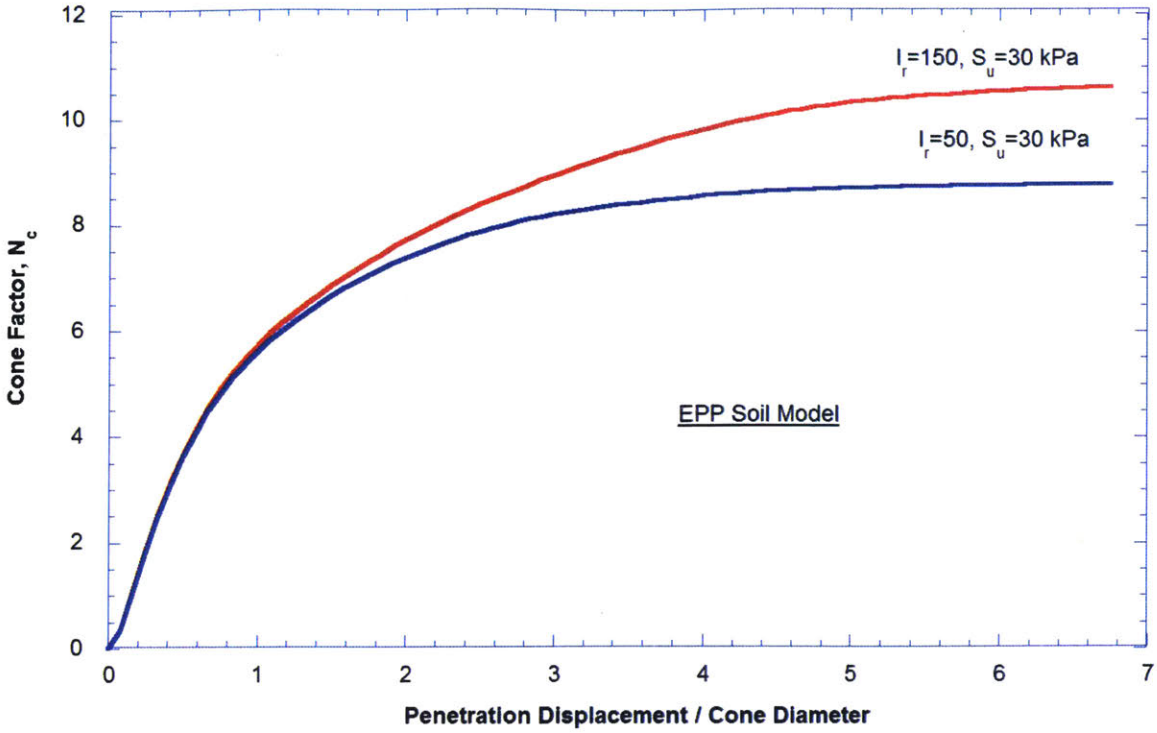

Method	Source	$N_c = (q_t - \sigma'_{v0}) / s_u$	
		I_r=50	I_r=150
Strain Path (steady state)	Baligh	8.5	10.5
Strain Path + FE	Teh & Houlsby	8.4	10.6
ALE FE	van den Berg	9.5	-
RITSS	Lu & Randolph	9.6	11.3
Proposed	Orazalin	8.8	10.6

Figure 3-37: Initial Cone Penetration Analysis - Validation

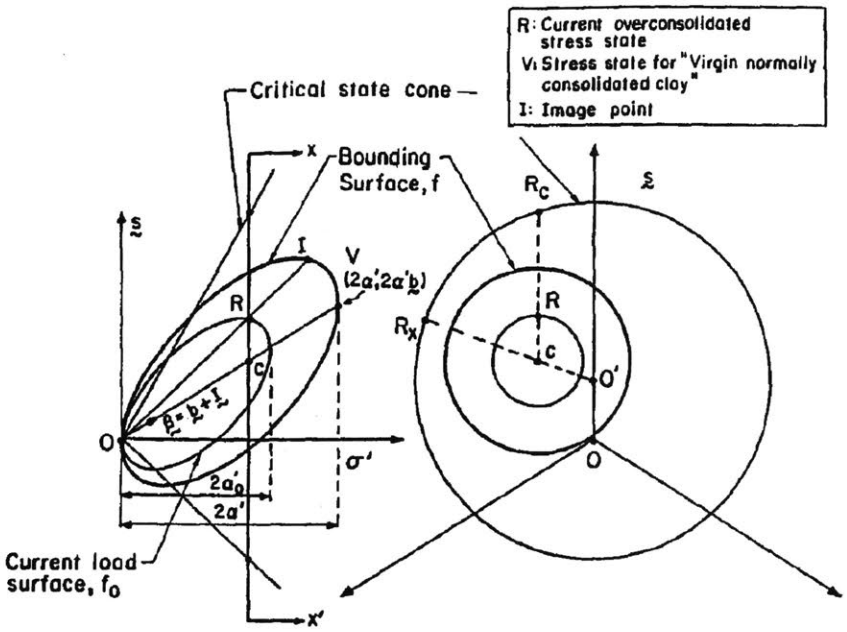

Figure 3-38: Yield, Failure, and Load Surfaces used in MIT-E3 Model (Whittle and Kavvadas [1994])

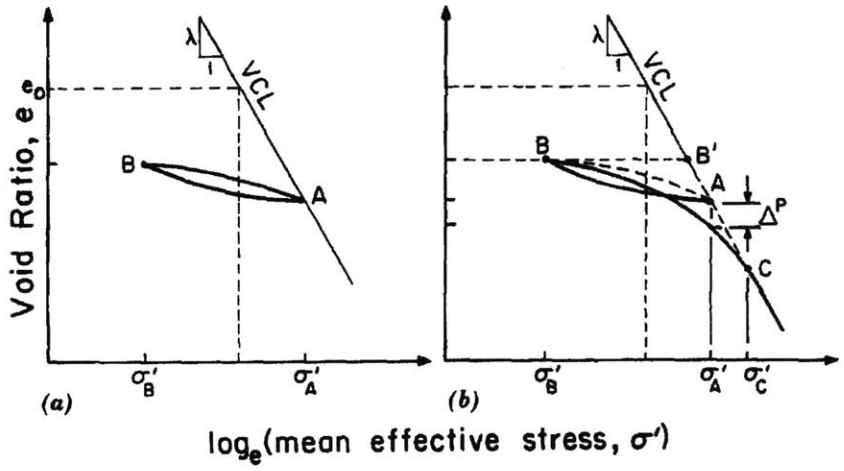

Figure 3-39: Hysteresis Model Used in MIT-E3 for Hydrostatic Compression: (a) Perfect Hysteresis; and (b) Hysteresis and Bounding Surface Plasticity (Whittle and Kavvadas [1994])

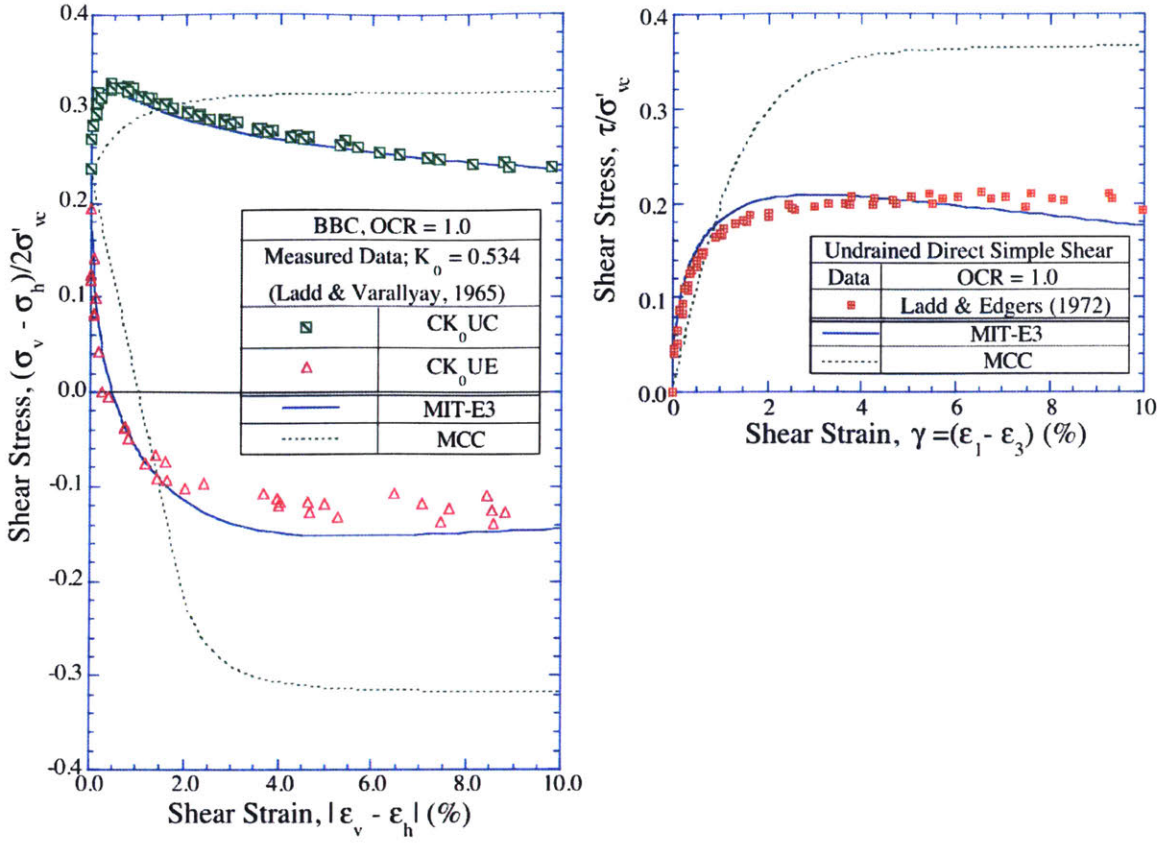

Figure 3-40: Comparison of computed and measured undrained shear behavior - MCC and MIT-E3 soil models (Whittle and Kavvadas [1994])

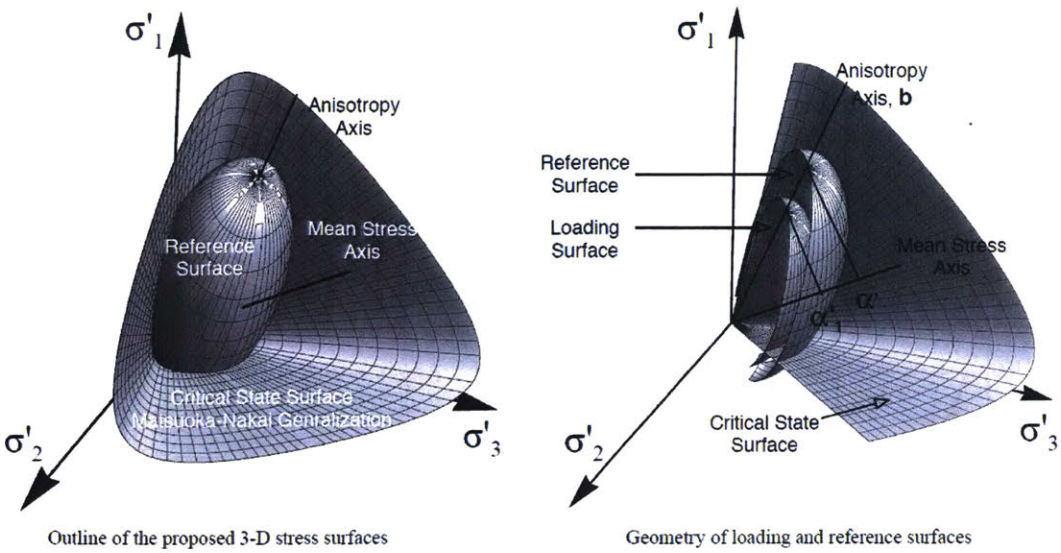

Figure 3-41: MIT-SR model surfaces in the triaxial stress space (Yuan [2016])

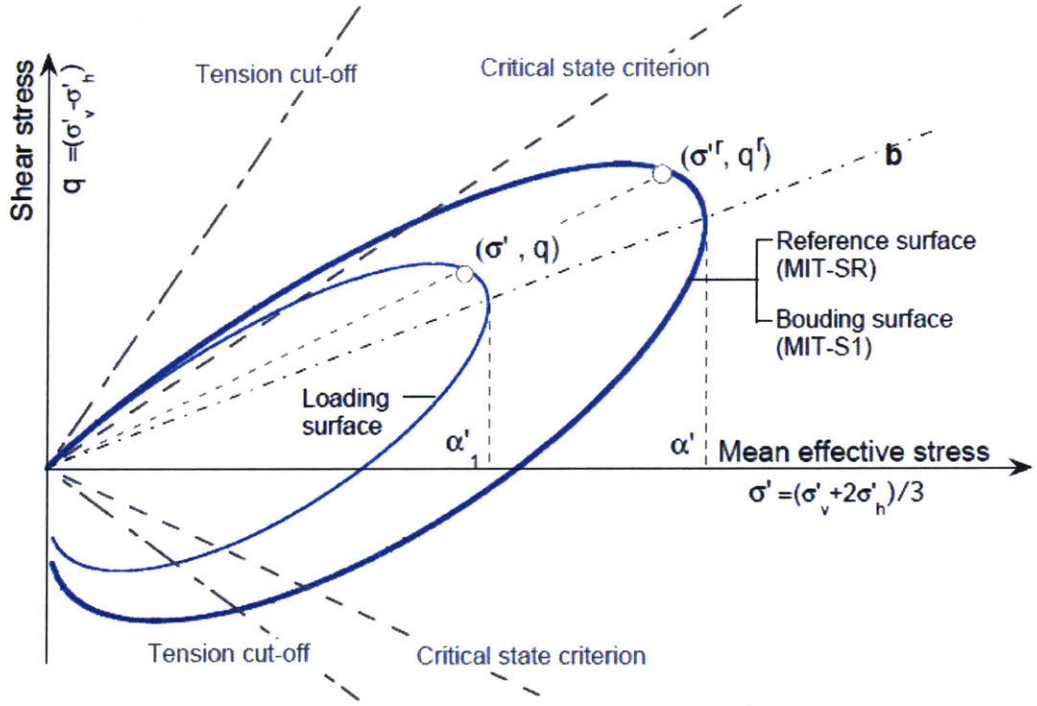

Figure 3-42: MIT-SR model surfaces in the triaxial stress space (Yuan [2016])

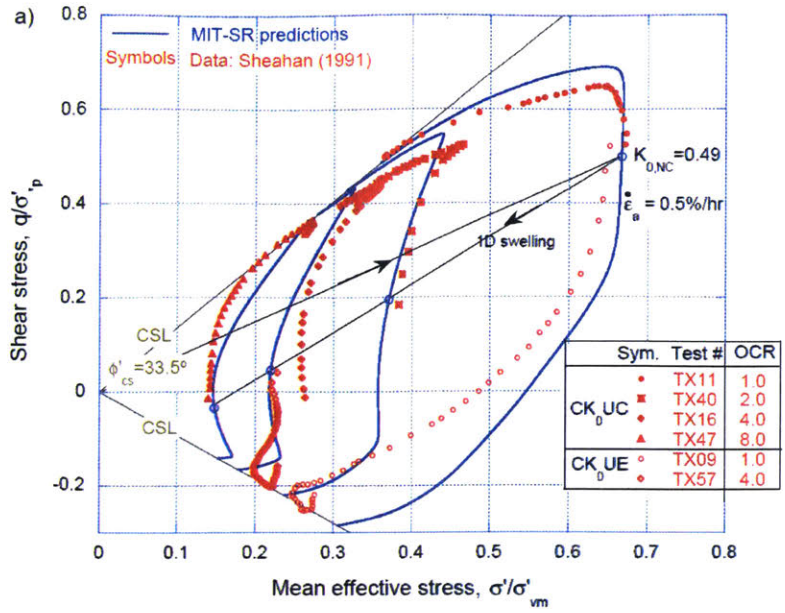

(a) Predicted and measured effective

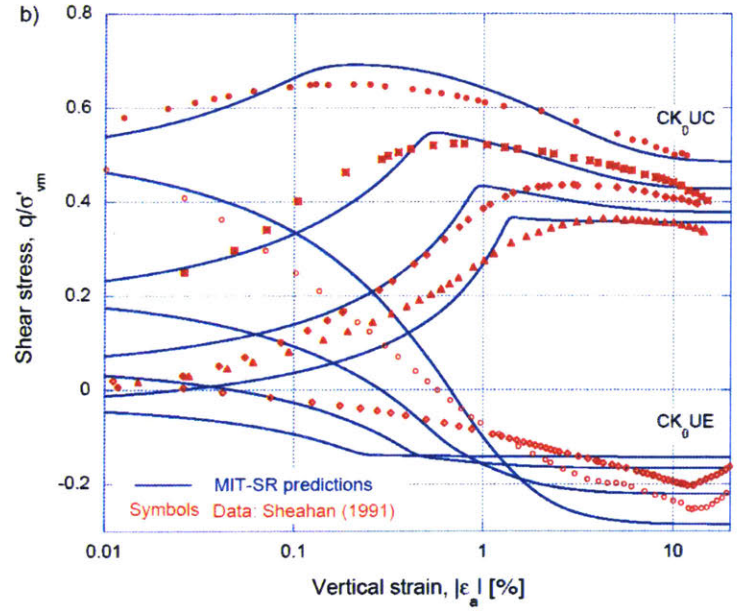

(b) Predicted and measured stress-strain path

Figure 3-43: Comparison of MIT-SR predictions and measured data for results of CK_0UC and CK_0UE tests on RBBC at a reference strain rate $\dot{\varepsilon_a} = 0.5\%/hr$ (Yuan [2016])

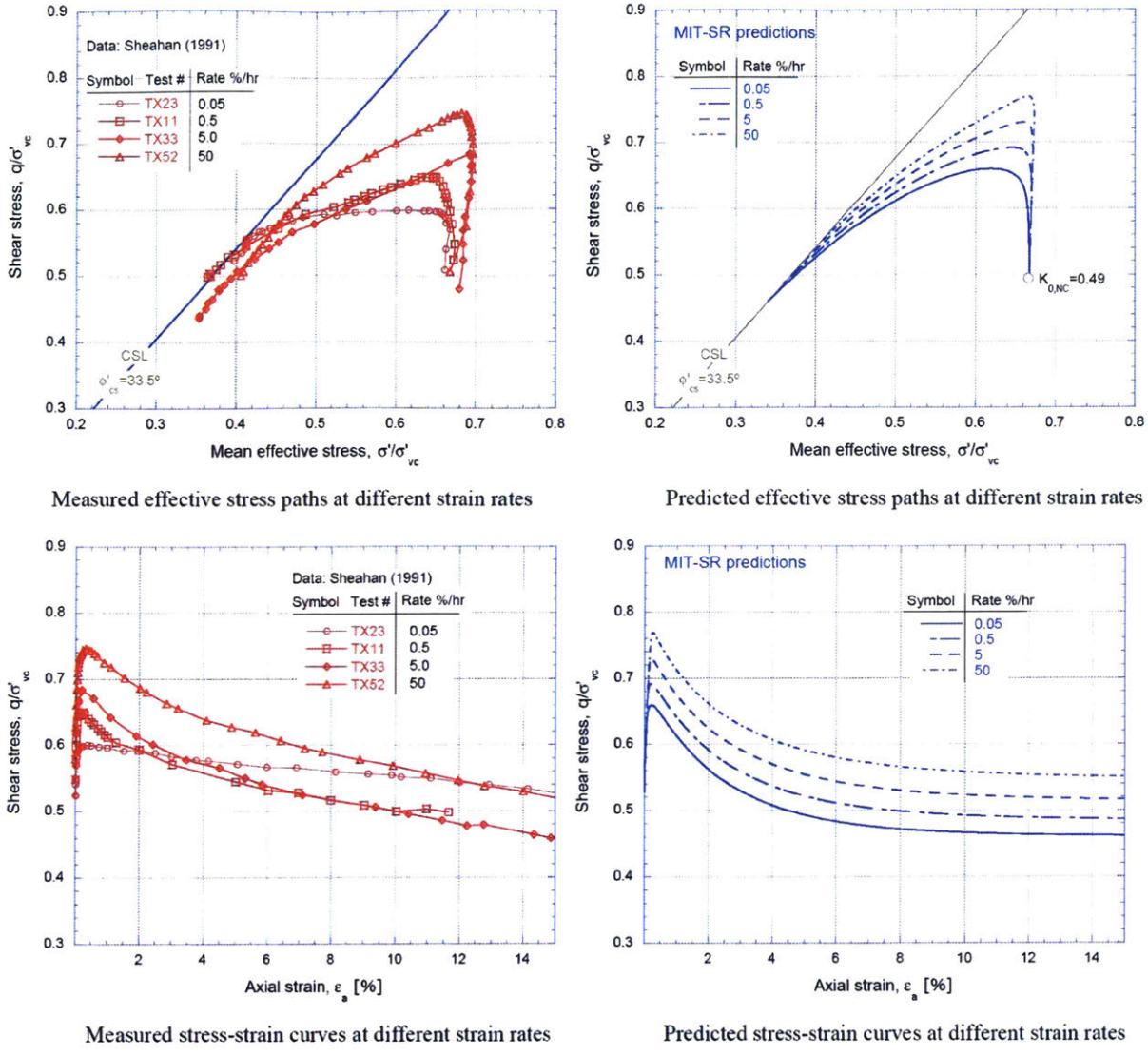

Figure 3-44: Effects of strain rate on the computed and measured undrained shear behavior of RBBC in CK_0UC tests at OCR=1 (Yuan [2016])

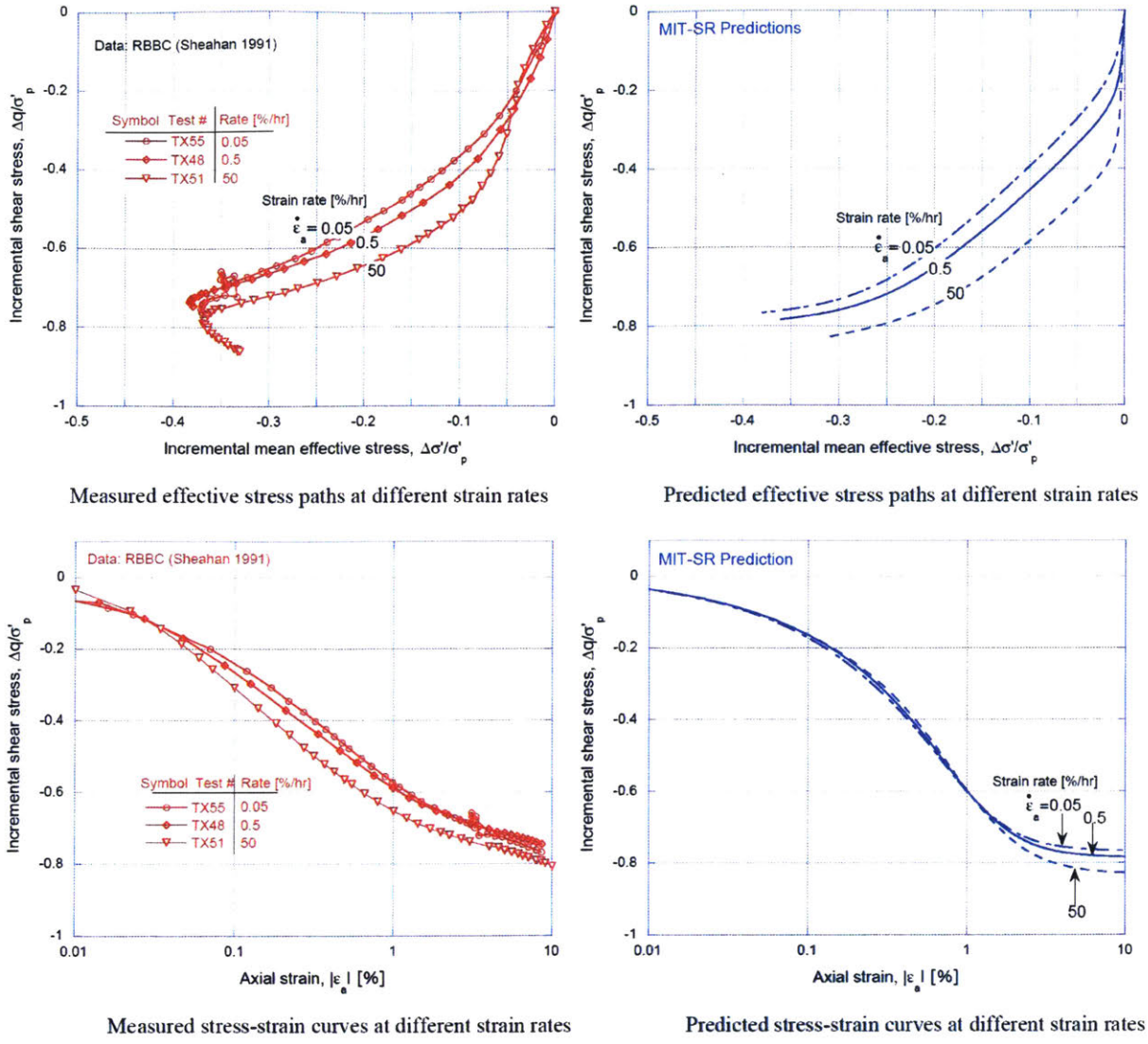

Measured effective stress paths at different strain rates

Predicted effective stress paths at different strain rates

Measured stress-strain curves at different strain rates

Predicted stress-strain curves at different strain rates

Figure 3-45: Effects of strain rate on the computed and measured undrained shear behavior of RBBC in CK_0UE tests at OCR=1 (Yuan [2016])

Chapter 4

Numerical Simulation of Conductor-Soil Interaction Centrifuge Tests and Validation

This chapter interprets the results of centrifuge physical model experiment on the performance of a conductor pipe loaded under conditions that simulate the drift-off of a deepwater drilling vessel. The experiments were performed independently at C-CORE, a Canadian research and development facility located on Memorial University Campus in St. Johns, Newfoundland (C-CORE [2014])[1]. The performed numerical analyses comprise 3D Finite Element analyses with advanced effective stress soil models that represent the behavior of GoM sediments.

4.1 Centrifuge Model Tests

The C-CORE centrifuge tests simulate the behavior of a 3ft [0.91m] diameter conductor pipe with 2.3" [58.4mm] thick steel wall embedded in high plasticity GoM (Gulf of Mexico) clay and subjected to combined push-over and axial tension loads. The model tests are performed at a gravitational acceleration of 115g, such that all linear dimensions are scaled by 1:115 relative to the prototype while maintaining

[1]The centrifuge test data were provided to MIT as part of the jointed research project

1:1 scaling of stress and strain. Figure 4-1 shows a schematic layout of the physical model test (with dimensions at prototype scale). The model simulates the upper 60m of sediments, and loading is applied through a pinned connection located 17.5m above the mudline (corresponding to the top of the Lower Marine Riser Package, LMRP). Two model conductor tests (Models 1 and 2) were performed within the same clay specimen and differ only in the mass of the simulated Blowout Preventer (BOP) and slightly in the schedule of axial load-lateral deformation (at LMRP). The test procedure simulates a quasi-static, drive-off phase corresponding to a total lateral displacement of approximately 5.8m [19.0ft] (at LMRP elevation) over a period of 93 secs followed by recoil after quick release of the load (separation of the riser from the mobile offshore drilling vessel).

In order to achieve a prescribed/target undrained shear strength profile, reconstituted GoM clay was consolidated (at 1g) using a downward hydraulic gradient over a period of more than 4 months. Two 0.35m thick intermediate sand layers (4-1) were used to control the hydraulic gradient and reduce consolidation times. Figure 4-2 shows that the sand layers are not continuous across the specimen and are absent within the exclusion zones around the conductor load paths (to minimize their impacts on the tests). After 1g consolidation the instrumented model conductors were installed from the base of the specimen through pre-augered holes. The piezometers embedded within the clay were then used to monitor in flight consolidation of the centrifuge package (these data show zero excess pore pressures after 34 hours). The resulting undrained shear strength profile of the clay is evaluated by performing a miniature T-bar test (done in flight after completion of the two model conductor tests). Following Randolph and Houlsby [1984] and Stewart and Randolph [1994], the undrained shear strength is interpreted from the T-bar penetration resistance using an average bar factor, $N_b = 10.5$. Although there is a sand exclusion zone around the T-bar, the results, the undrained shear strength profile (Figure 4-5) clearly shows that the sand layers do have a significant influence on the shear strength properties of the clay at depths below 20m. The reported undrained shear strength profile is at the upper limit of the target range defined in the test specifications.

The conductor models were manufactured to be geometrically similar to the prototype conductor and were instrumented with strain gauges to measure bending moments over the depth of the conductor. The conductor wall thickness and material type were chosen so as to best match the elastic modulus and yield moment of the prototype.

4.1.1 Instrumentation

Figure 4-3 shows photos of the instrumentation setup and model conductors inside the centrifuge test tub. Table 4.1 lists the instrumentation used in the C-CORE centrifuge test. Each of the conductor models were instrumented with 14 pairs of strain gauges installed at depths ranging from 1.66m to 47.99m below mudline (prototype scale). Each pair of strain gauges was connected in a full Wheatstone bridge circuit to enable direct calculation of the local elastic bending moments. The gauges were calibrated using a dead load cantilever beam method.

Prior to the tests, four Pore Pressure Transducers (PPTs) were used to measure the pore pressures during in-flight consolidation, while clay surface settlements were monitored using two Linear Voltage Displacement Transducers (LVDTs).

During the centrifuge test, an axial load cell was attached to the model conductor to measure the specified tension load (Fig. 4-1). Two load cells (one primary and one backup) were used to measure the lateral loads at the conductor head. The conductor head rotation was measured with the installed inclinometer. A linear displacement transducer (LDT) was used to control the displacement of the actuator while a laser was used to measure the displacements at the conductor head. The visual information was obtained from the digital cameras that allowed the monitoring of soil deformation at the surface around the conductors during the test motions.

4.1.2 Prototype and Centrifuge Model Properties

Table 4.2 presents the C-CORE centrifuge model parameters and their equivalents in the prototype scale. The linear dimensions were scaled as 1:115 relative to the

prototype while the yield strength, Young's modulus were identical for the model and prototype conductors. It was noted that heat shrink coating was added after strain gauge attachment in order to waterproof the electronics (the outside diameter of the instrumented model conductor was approximately 9mm, i.e., 1.035m at prototype scale). The tension tests were carried out by C-CORE to determine the modulus of elasticity and yield stress of the steel used in the model conductor (Figure 4-4).

4.2 Results of Centrifuge Model Tests

Figure 4-6 summarizes the bending moments reported from the 14 pairs of strain gauges in centrifuge Model 1. Figure 4-6a shows data from the full range of conductor displacements in the pushover phase (up to $\delta_h = 5.9$m at LMRP). The results suggest the yielding of the conductor ($M_y = 12$MNm, Table 4.2) occurred at $\delta_h \approx 2.0$m. The results at $\delta_h = 2.3$m show a continuous (smooth) moment distribution along the length of the conductor with 'apparent elastic' bending moment, $M_{max} = 17$MNm. Although much higher moments are reported as the pushover test progresses (up to 30MNm at $z = 16$m), C-CORE [2014] acknowledged that these data are not reliable and attribute fluctuations (local minima) in the moments to debonding of the strain gauges. According to this information, the elastic bending moments are assured to be credible for $\delta_h < 2.9$m (Fig. 4-6b).

Figure 4-7 shows that very similar results are obtained from centrifuge Model 2 (minimal added mass for LRMP). Initial yielding of the conductor occurs at $z = 6$-7m below mudline at $\delta_h < 2.0$m. Maximum elastic moments range from $M_{max} = 17 - 20$MNm (at $\delta_h = 2.6 - 3.1$m). At larger pushover deflections, the local minima in bending moments (at $z \approx 12$m) are associated with the debonding of the gauges.

Figures 4-8 and 4-9 compare the measured (elastic) bending moments and maximum moments from the two centrifuge models, respectively. The results show that the mass of the LMRP has little influence on the measured performance of the conductors. Yielding of the conductor occurs at $z = 7$-8m below mudline for $\delta_h = 1.7$m.

4.3 Laboratory Tests on GoM Clay Samples

A suite of laboratory tests (1D consolidation and undrained triaxial shear tests) on specimens of the reconstituted GoM clay were performed at the MIT geotechnical laboratory using tube specimens provided by C-CORE. Figures 4-10 and 4-11 summarize the measured 1D compression and Figure 4-12 shows the undrained triaxial (compression and extension) shear tests for K_0-normally consolidated specimens. Figure 4-10 shows the pre-test void ratio vs. depth in centrifuge model. Figure 4-11 shows compression behavior of the samples from the K_0-consolidated triaxial tests. All specimens were SHANSEP consolidated to the NC range prior to shearing.

4.4 Development of 3D Finite Element Models

This section summarizes the details of the numerical modeling procedures and parameters used in the development of 3D FE geotechnical models of conductor-soil interaction problem associated with drift/drive-off load events in the Gulf of Mexico.

4.4.1 Conductor Model Properties

Table 4.2 presents the C-CORE centrifuge model parameters and their equivalents in the prototype scale (used in the FE model). The linear dimensions were scaled as 1:115 relative to the prototype while the yield strength, Young's modulus were identical for the model and prototype conductors.

4.4.2 Finite Element Modeling

Three-dimensional Finite Element (FE) models of the physical centrifuge model tests are developed at a prototype scale using the Abaqus™ Standard finite element program. The large-displacement formulation was activated in each load step (i.e., "Nlgeom" was activated). Mesh adaptivity (mesh-to-mesh solution mapping) was not used as the maximum displacement at the load application point (LMRP $\delta_h = 6$m) was achieved before the limit of excessive element distortions was reached. The centrifuge

numerical models assume tied interface connections between the soil and conductor, the soil is modeled with brick elements (using C3D8RP elements that simulate coupled consolidation). The conductor is also represented with solid elements using the appropriate geometrical dimensions (Table 4.2).

The tension tests were carried out by C-CORE to determine the modulus of elasticity and yield stress of the steel used in the model conductor (Figure 4-4). The steel conductor was initially modeled as a linearly-elastic, perfectly plastic material with von Mises yield surface ($E = 205\,GPa$ and $f_y = 380MPa$). As a refinement of this Base Case, the isotropic hardening metal plasticity (IHPP) model was used and calibrated to tension test data performed on a coupon sample (Fig. 4-13). Figure 4-14 shows the input data (yield stress vs. plastic strain) for this metal plasticity model with isotropic hardening.

Figures 4-15 and 4-16 show the FE Models for each of the conductor models of the C-CORE centrifuge test with appropriate dimensions. The selected mesh configuration and mesh sizing is based on prior mesh sensitivity studies (Figures 4-17 and 4-18). The soil is discretized with 30,000 elements. The half-circumference around the conductor ($D = 0.9144m$) is subdivided by 10 equally sized elements. Model 1 has an added mass simulating the BOP (blowout preventer), and Model 2 is a lighter ('minimal added mass') system. The conductor is displaced horizontally at the load application point located 17.5 m above the mudline under undrained conditions . The axial tension load is prescribed for each model based on the schedule of load and displacement data shown in Figure 4-19.

4.5 Calibration of Advanced Effective Stress Model

The MIT-E3 soil model is used to describe the effective stress-strain-strength properties of the reconstituted GoM clay. A generalized effective stress soil model that describes the rate-independent behavior of normally and lightly overconsolidated clays (MIT-E3 (Whittle and Kavvadas [1994], Whittle [1993a])). This model describes a number of important aspects of soil behavior, including small strain nonlinearity and

anisotropic stress–strain–strength properties and was previously calibrated at a series of deep-water sites in the Gulf of Mexico leading to an average set of soil properties referred to as "Average Gulf Clay" (AGC; Whittle and Sutabutr [2005]). MIT-E3 was originally implemented in Abaqus™ through a User Material (UMAT) interface (Hashash [1992]).

The selection of MIT-E3 input parameters for reconstituted GoM clay (Table 4.3) has followed a standardized procedure based on a suite of laboratory tests on specimens from the centrifuge model (tests were performed at MIT and are summarized in Appendix A). Figures 4-20 and 4-21 show that the MIT-E3 model is able to simulate the 1-D consolidation behavior, as well as the shear stress-strain behavior (Fig. 4-21b) and effective stress paths (Fig. 4-21a) measured in the laboratory tests. The clay exhibits significant undrained strength anisotropy ($s_{uTC}/\sigma'_{vc} = 0.26$ vs. $s_{uTE}/\sigma'_{vc} = 0.16$ for NC clay) with minimal post-peak strain softening (typical of high plasticity clay). Figures 4-22 and 4-23 show the effects of OCR on model predictions of undrained triaxial and direct simple shear tests (at the same vertical effective consolidation stress, σ'_{vc}). The stress history has a major influence on the shear-induced pore pressures (particularly noted from effective stress paths in the compression shear mode, Fig, 4-22a, 4-23a). The initial K_0 state and undrained strength ratio, s_u/σ'_{vc}, increase with OCR. Table 4.4 shows that there is a close agreement between the engineering properties of the Reconstituted GoM clay and Average Gulf Clay (Whittle and Sutabutr [2005]).

Figure 4-5 compares the measured undrained shear strength in the centrifuge model with simulations using the MIT-E3 soil model initially assuming that the clay is normally consolidated, i.e., OCR = 1.0 (Note: the comparison uses MIT-E3 properties simulated in the DSS mode of shearing; cf. Fig. 4-22). Although the results show a good agreement over the full depth (60m at prototype scale) of the model, a closer inspection of the upper 20m, Fig. 4-23, shows that this Base Case assumption likely leads to an underestimate of the actual shear strength close to the mudline. A second Refined Case achieves better matching to the measured su profile though small adjustments of OCR.

The role of the soil model in predictions of conductor-soil interactions is evaluated by performing additional FE analyses using a much simpler isotropic, linearly Elastic-Perfectly Plastic (EPP) soil model (with Tresca yield criterion). Undrained shear strength is a direct input parameter for this model (and can be matched to the T-bar penetration data; Fig. 4-5), while the elastic shear modulus is assumed to vary linearly with depth ($G/\sigma'_{vc} = 15$).

4.6 Results of 3D Finite Element Analyses

The following sections present the results from four FE analyses for Centrifuge Model 1:

1. Base Case – MIT-E3 model, OCR = 1.0; 3.0m pushover applied at LMRP

2. Refined Case – MIT-E3 model, OCR varies to achieve better agreement with measured su profile (Fig. 4-5); 3.0m pushover applied at LMRP. Simulations have been performed using: i) EPP model of conductor response ii) IHPP (hardening model) of conductor response (Figs. 4-13, 4-14)

3. EPP Case; 6.0m pushover applied at LMRP. The undrained shear strength profile varying with depth for the EPP Case was specified in a single layer as in Figure 4-25 using field variables varying linearly with the soil depth.

Figure 4-26 summarizes the bending moments and horizontal displacements of the prototype conductor for the pushover phase of centrifuge Model 1 following the loading schedule in Figure 4-19. The bending moments are computed directly as the resultants of the stresses obtained in the FE model. The analyses show that plastic yield of the conductor initiates approximately 8m below the mudline at a reference displacement, $\delta_h = 1.7$m (at LMRP). Subsequent loading causes a small increase in the maximum moment within the conductor ($M = 14$MNm at $z \approx 10$m below mudline, vs. $M_y = 12$MNm). Figure 4-27 provides further details of yielding within the conductor by comparing the Mises stresses ($f_y = 380$MPa, Table 4.2) and equivalent plastic strain rate along the edge of the conductor. The zone of plasticity spreads from the point of initial yield upwards towards the mudline, and extends to a depth $z > 13$m for

$h = 2.3m$ (Fig. 4-27).

In the centrifuge tests, bending moments are found from the differential strains between the pairs of axial strain gauges (i.e., compressive and tensile strains, C and T in Fig. 4-29) assuming elastic bending of the conductor (with bending stiffness, EI, cf. Table 4.2). This measuring system is not able to interpret the bending moments accurately once yielding has initiated (i.e., $h \geq 1.7m$). Figure 4-29 illustrates the limitations by computing apparent elastic bending moments along the conductor based on computed axial strains at the extreme edges of the conductor. These apparent bending moments become much larger than the true moments once plastic yielding spreads through the conductor (e.g., $\delta_h = 2.3m$ in Fig. 4-29).

Figure 4-30 compares the results of the Base Case FE analysis with the bending moments reported from centrifuge Model 1, for pushover up to $\delta_h = 2.3$ (LMRP). The computed results include actual bending moments (i.e., resultants of stresses in the elasto-plastic conductor) and elastic moments based on computed axial strains at the outer edge of the conductor (cf. Fig. 4-29). The analyses are in a very good agreement with magnitude and location of the maximum moment for loading in the elastic range ($\delta_h < 1.7m$) and theoretical elastic moments also match the measured strain gauge data in the post-yield range (i.e., $\delta_h < 1.7 - 2.3m$). Closer inspection shows that the Base Case analysis tend to underestimate the moments in the upper part of the conductor ($z < 6m$) and overestimate the measured behavior below the point of maximum moment. These discrepancies are not linked to plastic behavior of the conductor but are most likely related to differences in the simulated and measured profiles of undrained shear strength and stiffness in the clay (cf. Figure 4-25).

Figure 4-31 compares the computed bending moment distributions from the Base Case and Refined Case FE analyses (for centrifuge Model 1). These two simulations differ only in the stress history profiles used in conjunction with the MIT-E3 soil model. The Refined Case matches more closely the measured undrained strength profile (from T-bar penetration data) in the upper 20m of the clay. The comparisons show that the Refined Case produces a small reduction in the depth to the point of maximum moment, increasing the bending moment near to the mudline and reducing

the moments for $z \geq 10$m relative to the Base Case.

Figure 4-32 shows direct comparisons between the Refined Case FE analysis and the measured data from centrifuge Model 1. These results show even closer agreement between the computed and measured bending moments over the upper $20-25$m of the conductor, while post-yield behavior is accurately interpreted from the apparent elastic bending moments. The differences between the Base Case and Refined FE analyses highlight the importance of simulating accurately the undrained shear strength profile for depths $z = 0$ - 20m below the mudline.

The effects of refinements in modeling the yielding of the steel conductor (using the IHPP metal plasticity model) on the computed bending moments and apparent elastic bending moments are shown in Figures 4-33 and 4-34, respectively. These results show that refinements in modeling the plasticity of the steel conductor have no effects on the bending response for $\delta_h < 0.6$m (linear elastic regime) but the computed moments are 1.4 - 7.5% lower than those for the linearly elastic perfectly plastic (EPP) conductor (Fig. 4-33), with $M_{max} = 12.85$ MNm at $\delta_h = 2.3$m. It should be noted that there is minimal effect on the deformed shape of the conductor at all stages. In contrast, the apparent elastic bending moments increase by up to 1.8 - 7.2% at $\delta_h = 1.7$m (Fig. 4-34) but converge to the EPP response as plasticity spreads within the conductor ($\delta_h \geq 2.3$m). Figure 4-35 shows that refinement in modeling of the conductor (IHPP model) generally causes a small overestimate of the measured apparent elastic moments in centrifuge Model 1.

Table 4.1: Centrifuge Test Instrumentation

Label	Instrumentation	Quantity	Measurements	Test phase
1	Strain Gauges	14	Bending moments	Main
2	Inclinometer	1	Conductor head rotation	Main
3	LDT	1	Displacements of the actuator	Main
4	Laser	1	Displacements at the conductor head	Main
5	Load Cells	4	Axial and Lateral Loads	Main
6	T-bar Penetrometer	1	Undrained Shear Strength	Post-test
7	Accelerometer	1	g-levels	Main
8	LVDTs	2	Clay settlements	Consolidation
9	Pore Pressure Transducers	4	Pore pressures	Consolidation
10	Digital Camera	1	Visual Data	All

Table 4.2: Conductor properties

Parameters	**Centrifuge Test Model (115g)**	**Prototype Scale (1g) [FE Model]**
Diameter, d	7.94 mm	0.914 m (3.0 ft.)
Wall Thickness, w	0.51 mm	5.84 cm (2.30 in.)
Length Above Mudline, m	152.0 mm	17.5 m (57.4 ft.)
Conductor Material	Stainless Steel 304 Modeled using i) Classical Metal Plasticity (EPP; von Mises yield), and ii) Hardening metal plasticity (IHPP)	
Yield Strength, f_y	380 MPa	
Young's Modulus, E	205 GPa	
Moment of Inertia, I	0.0145 m^4	
Elastic Bending Stiffness, EI	2.963x10^3 MNm^2	
Yield Moment, M_y	12.011 MNm	

Table 4.3: MIT-E3 Soil Model Input Parameters for C-CORE GoM Calibration

Description	**Parameter**	**Centrifuge GoM Clay**
Reference Void Ratio on VCL	e_0	1.492
Normally Consolidated Compression	λ	0.282
Non-linear Volumetric Swelling Behavior	C	13.0
	n	1.2
Irrecoverable Plastic Strain	h	0.3
K_0 for virgin normally consolidated clay	K_{0NC}	0.63
The ratio of the tangential elastic shear modulus to the bulk modulus, which is related to the Poisson's ratio of the soil skeleton	2G/K	0.923
Critical State Friction Angles in Triaxial Compression and Extension	φ'_{TC}	24.0
	φ'_{TE}	26.6
Undrained Shear Strength (geometry of bounding surface)	c	0.73
Amount of Post-peak Strain Softening in Undrained Triaxial Compression	s_t	2.4
Non-linearity at Small Strains in Undrained Shear	ω	0.39
Shear Induced Pore Pressures for OC Clay	γ	0.5
Small strain compressibility at load Reversal	$\varkappa_0$	0.004
Rate of Evolution of Anisotropy (rotation of bounding surface)	Ψ_0	100.0

Table 4.4: Summary of computed engineering properties for Average Gulf Clay and reconstituted NC Gulf of Mexico clay using MIT-E3 soil model

Engineering Properties	AGC	Centrifuge GoM clay
λ	0.282	0.282
G_{max}/σ'_{v0}	102	81
Su_{TC}/σ'_{v0}	0.26	0.26
ε_{af} (%)	1.5	1.5
$q(10\%)/Su_{TC}$	0.96	1.00
φ'_{TC}	25.6	26.6
Su_{TE}/σ'_{v0}	0.16	0.16
Su_{DSS}/σ'_{v0}	0.22	0.23

Table 4.5: Effect of IHPP conductor on actual bending moments with EPP model (Full Range Case)

Displacement, m	Maximum actual bending moment, MNm		
	IHPP conductor	EPP conductor	Difference, %
0.6	4.852	4.946	1.9
1.1	7.968	8.290	3.9
1.7	10.916	11.762	7.2
2.3	12.856	13.982	8.1
2.9	13.546	14.436	6.2
4	13.918	14.302	2.7
5.2	14.342	14.344	0.0
6	14.428	14.322	0.7

Table 4.6: Effect of IHPP conductor on actual bending moments with MIT-E3 model (Refined Case)

Displacement, m	**Maximum actual bending moment, MNm**		
	IHPP conductor	**EPP conductor**	**Difference, %**
0.6	5.546	5.624	1.4
1.1	8.784	9.164	4.1
1.7	11.518	12.456	7.5
2.3	12.850	13.788	6.8

Table 4.7: Effect of IHPP conductor on apparent elastic bending moments with MIT-E3 model (Refined Case)

Displacement, m	**Maximum elastic bending moment, MNm**		
	IHPP conductor	**EPP conductor**	**Difference, %**
0.6	5.870	5.765	1.8
1.1	9.840	9.375	4.7
1.7	14.300	13.275	7.2
2.3	19.086	19.630	2.9

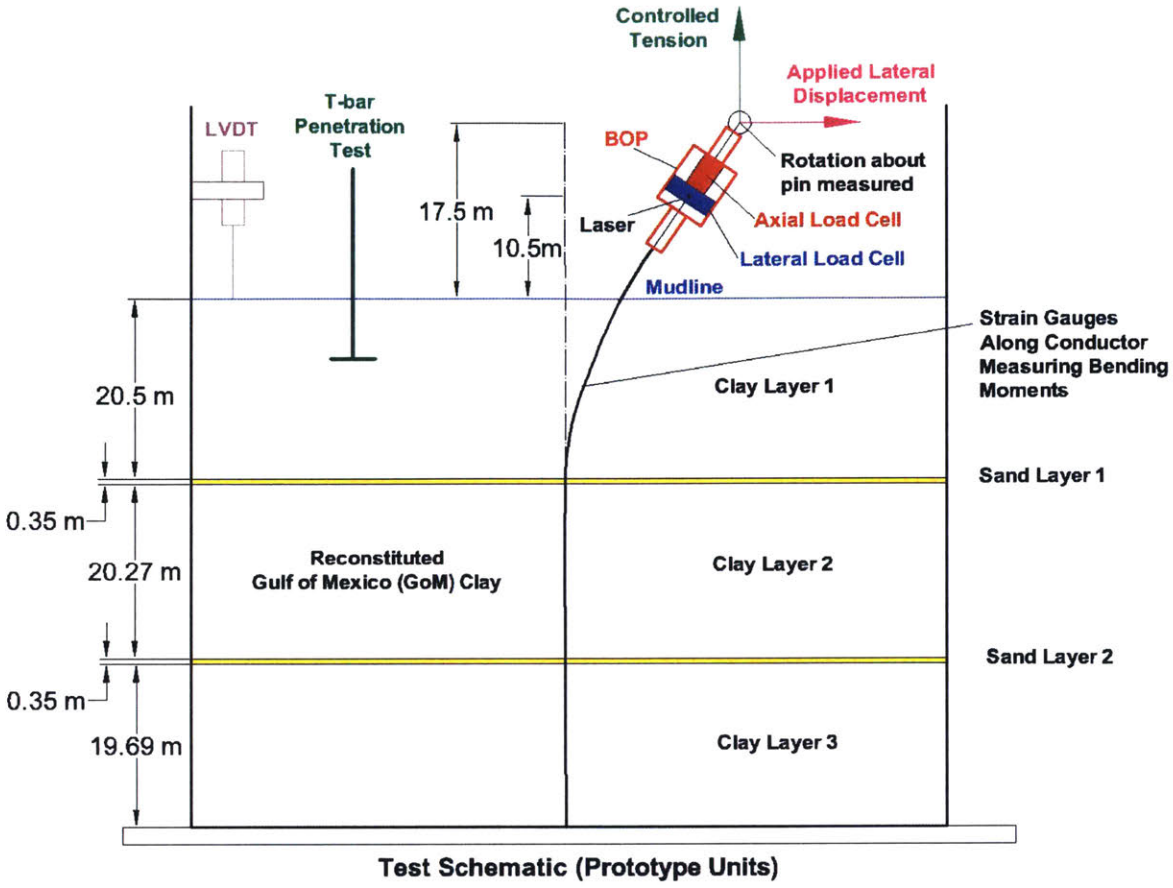

Figure 4-1: C-CORE centrifuge test schematic (prototype scale)

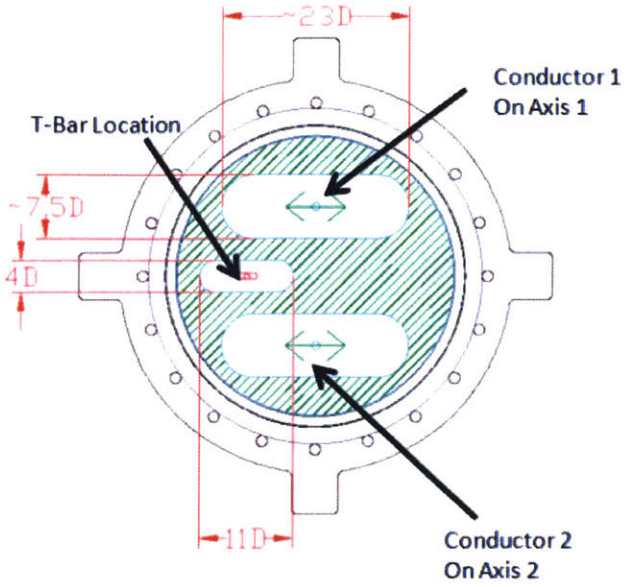

Figure 4-2: Centrifuge Test Tub (Presence of Sand Layers Marked in Green)

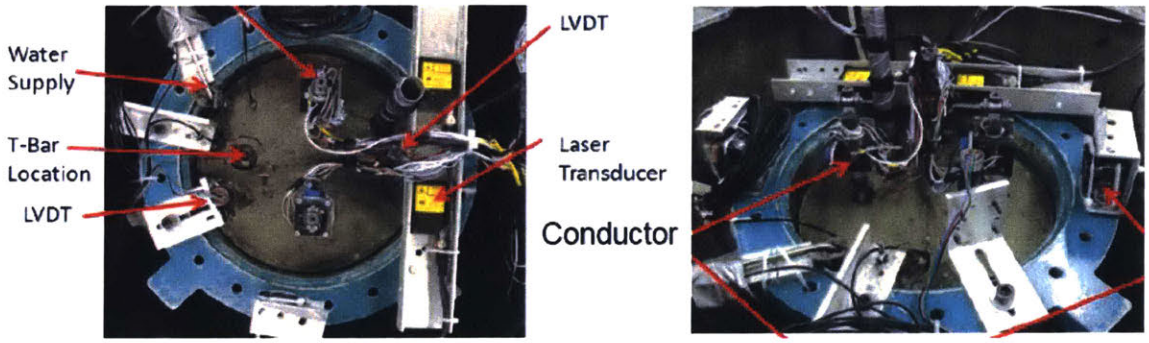

Figure 4-3: Photos of Model Conductors and Instrumentation

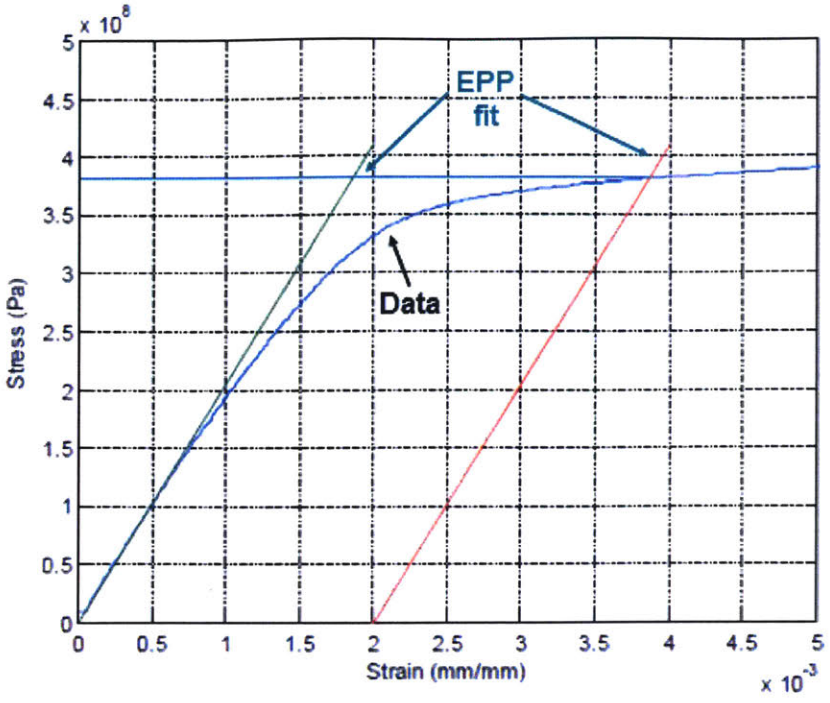

Figure 4-4: C-CORE conductor tension test data

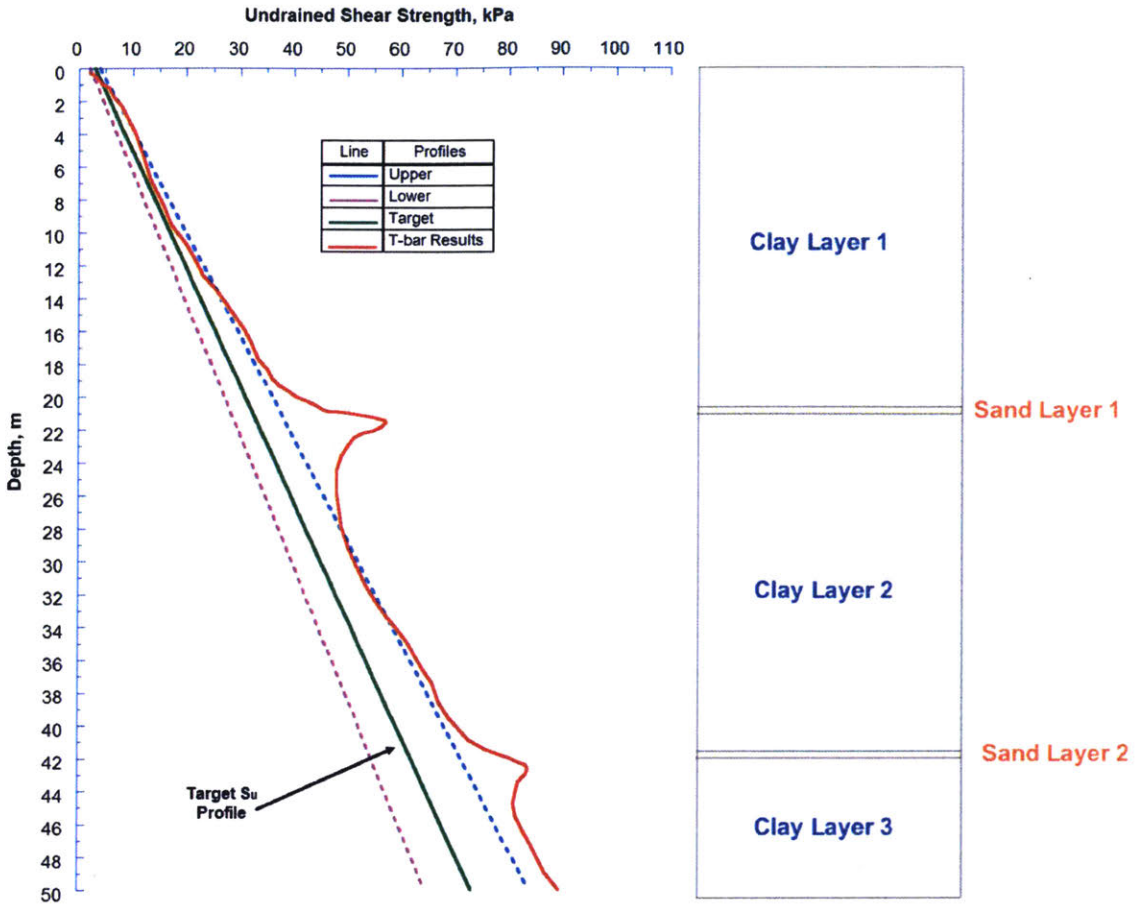

Figure 4-5: Undrained shear strength profiles

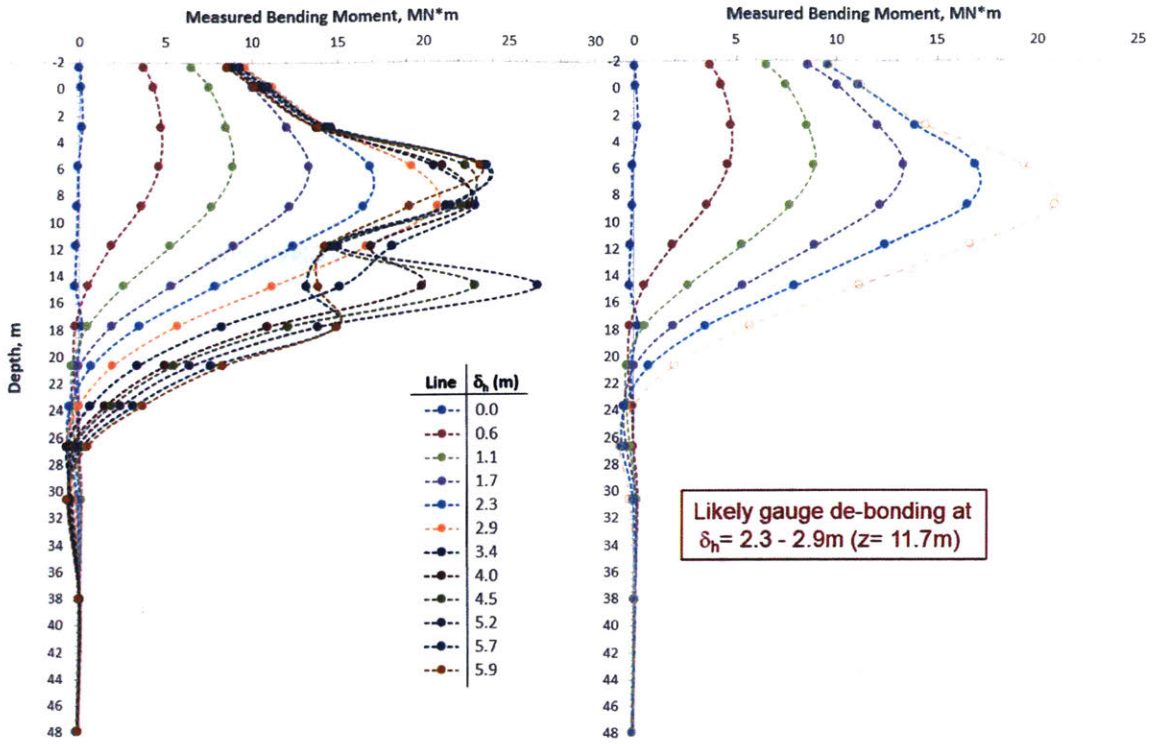

Figure 4-6: Measured bending moments from C-CORE centrifuge Model 1

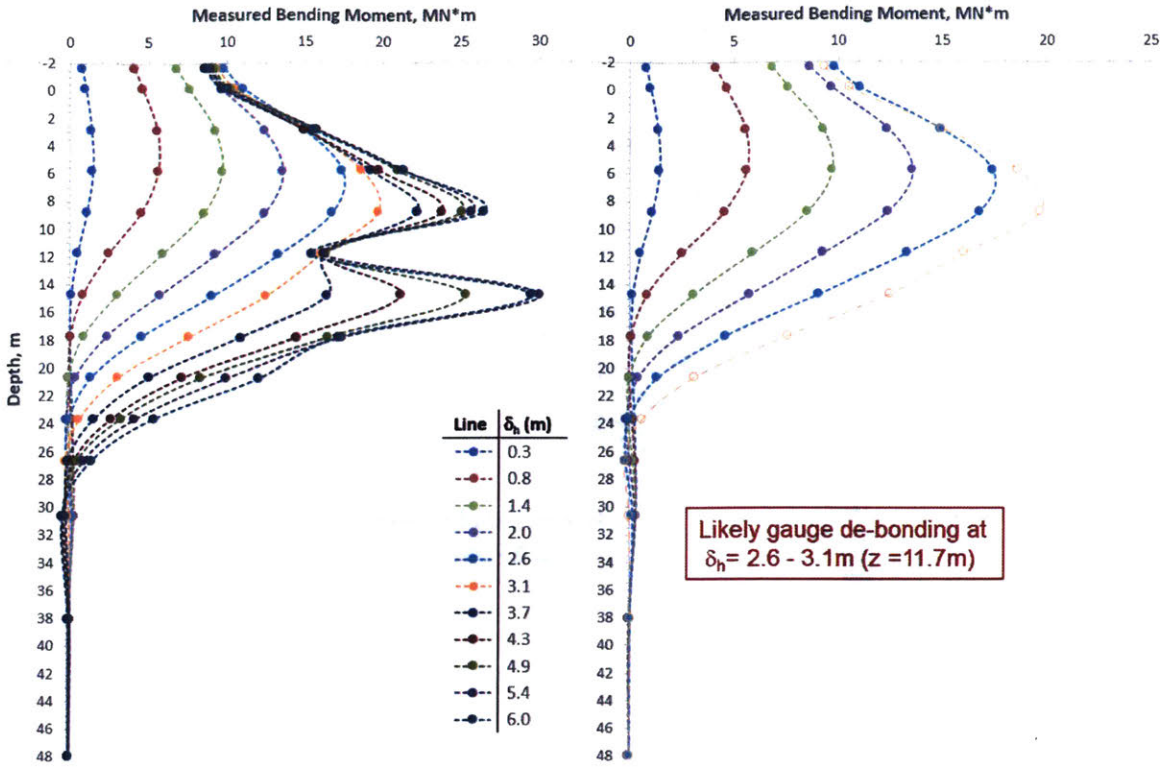

Figure 4-7: Measured bending moments from centrifuge Model 2

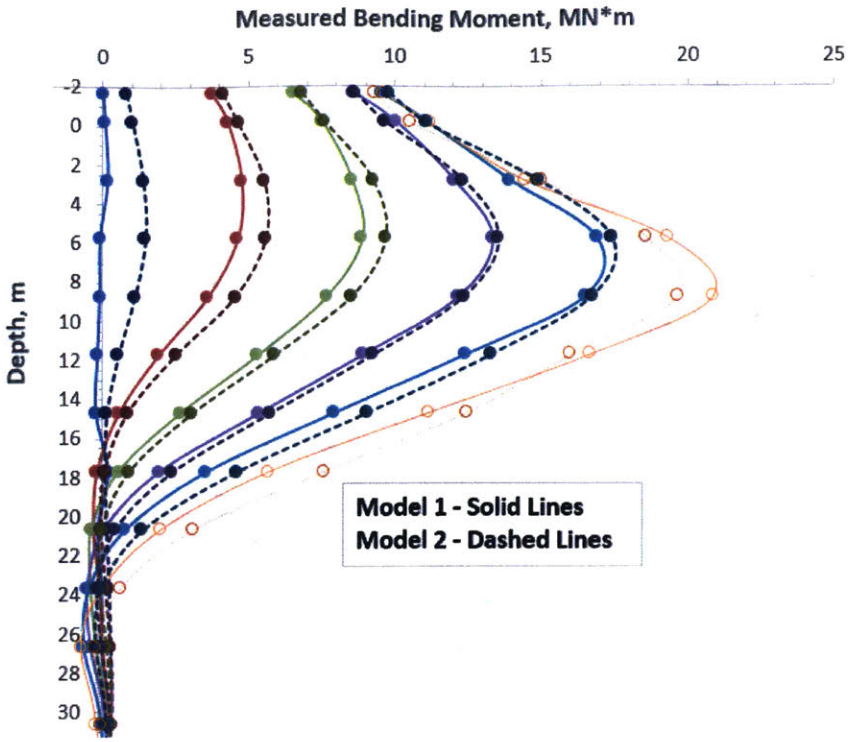

Figure 4-8: Comparison of bending moments from cenrifuge models

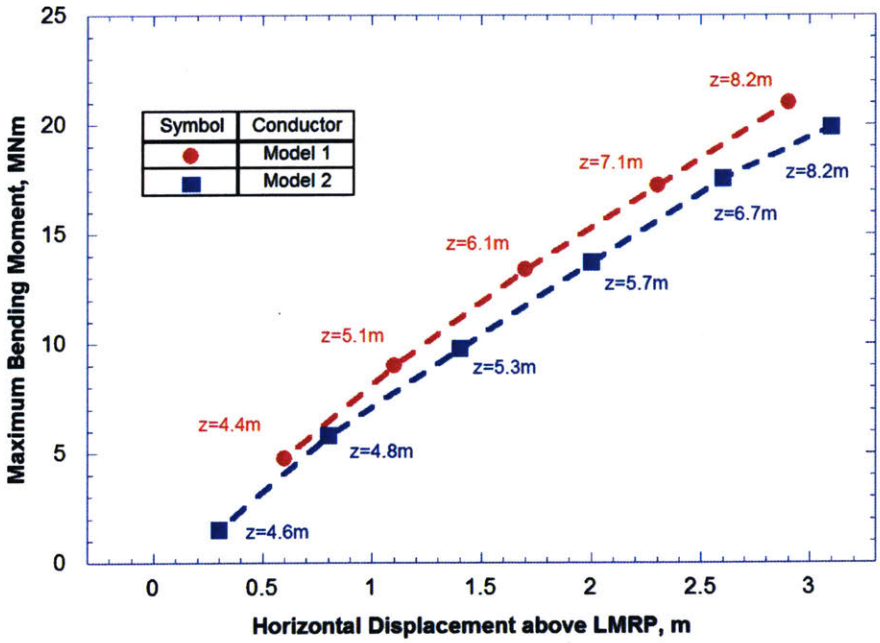

Figure 4-9: Maximum elastic bending moments from centrifuge Models 1 and 2

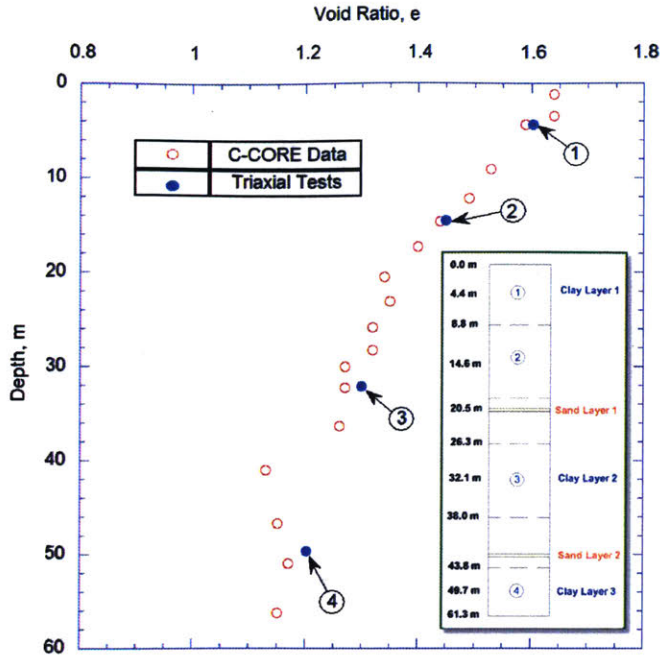

Figure 4-10: Measured void ratio of Reconstituted GoM Clay

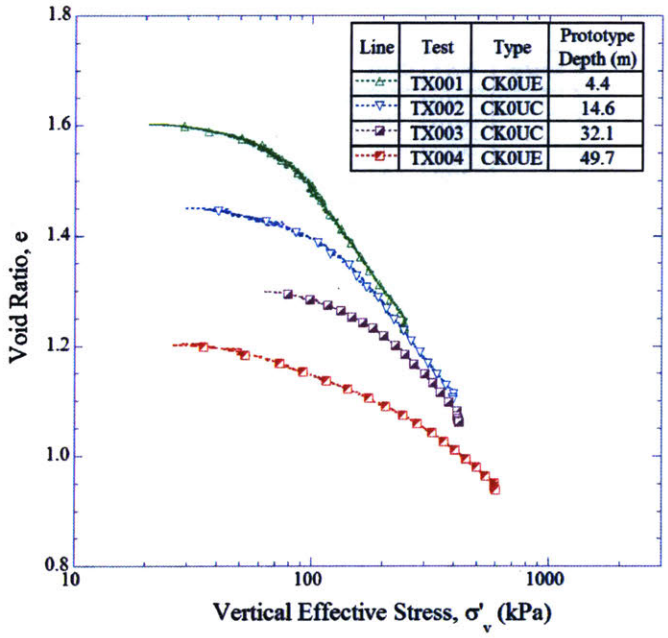

Figure 4-11: Measured 1-D consolidation behavior of Reconstituted GoM clay

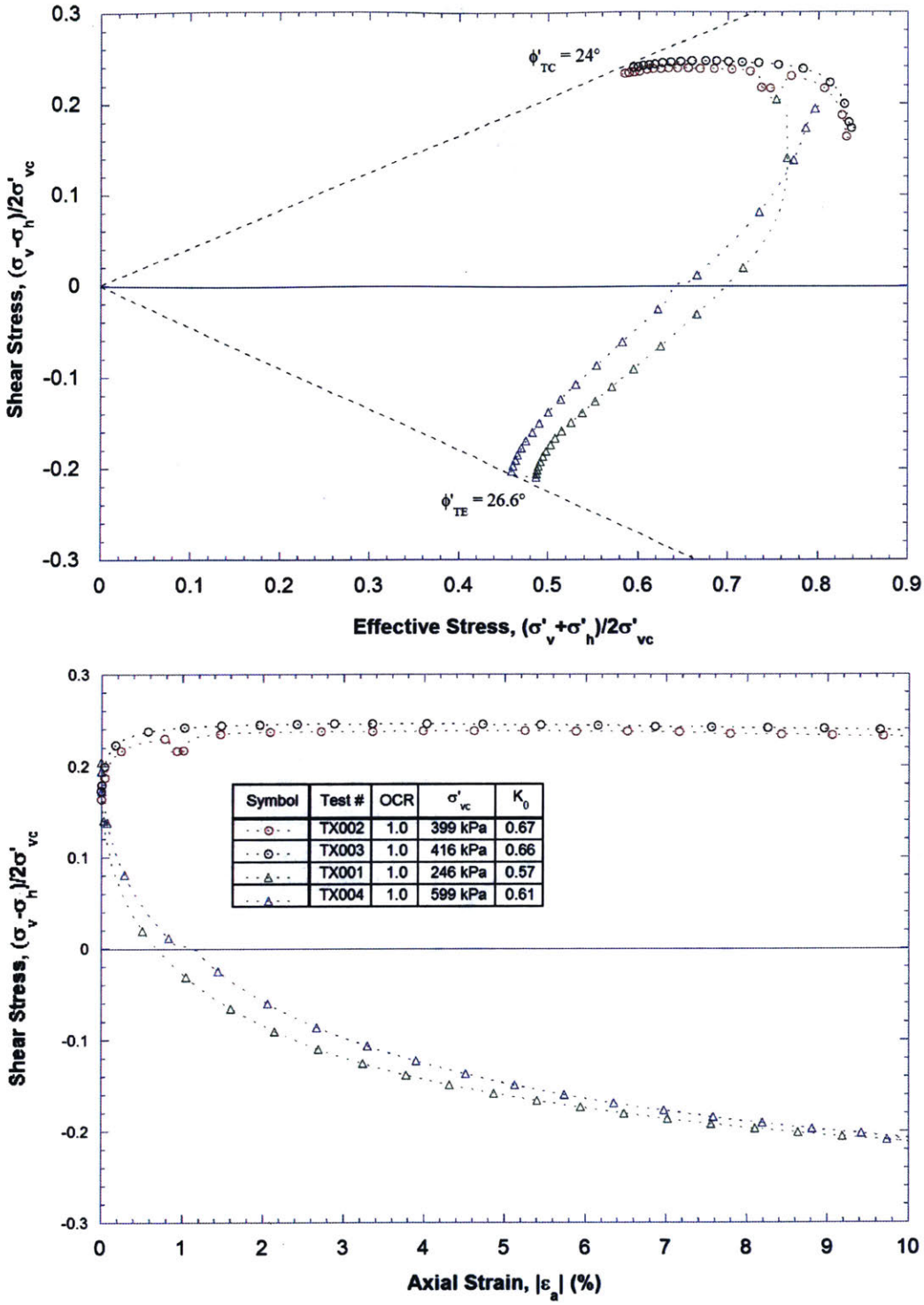

Figure 4-12: Measured triaxial shear behavior of RGoM Clay

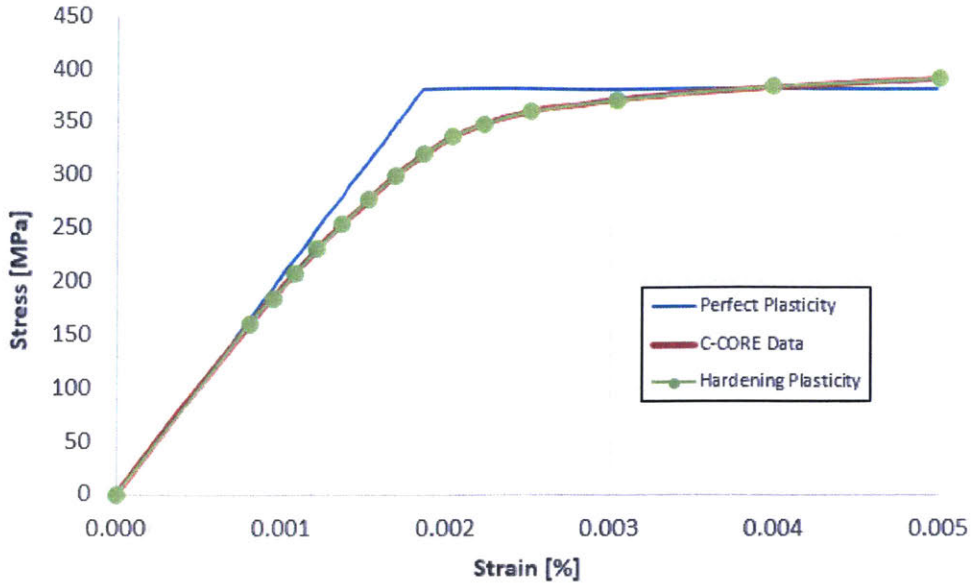

Figure 4-13: Models for conductor material – Perfect vs. hardening metal plasticity

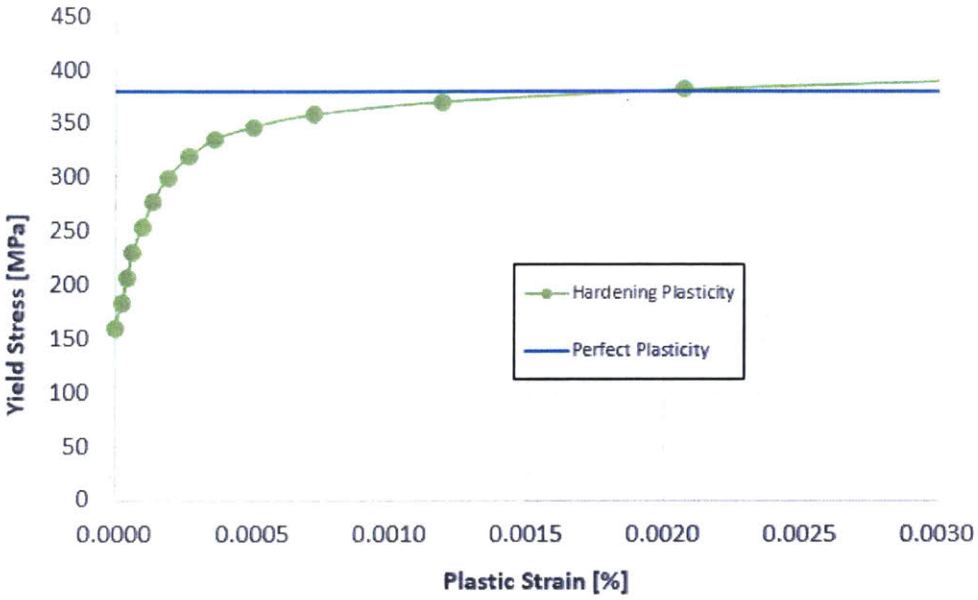

Figure 4-14: Yield Stress comparison for perfect vs. hardening metal plasticity

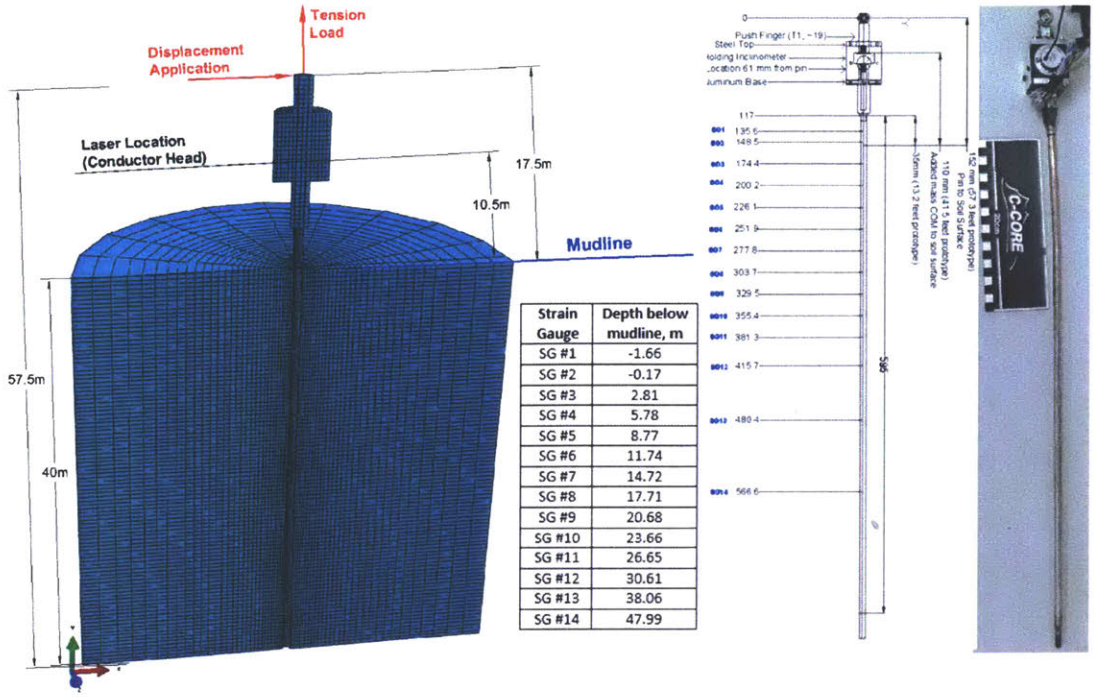

Strain Gauge	Depth below mudline, m
SG #1	-1.66
SG #2	-0.17
SG #3	2.81
SG #4	5.78
SG #5	8.77
SG #6	11.74
SG #7	14.72
SG #8	17.71
SG #9	20.68
SG #10	23.66
SG #11	26.65
SG #12	30.61
SG #13	38.06
SG #14	47.99

Figure 4-15: FE Model 1 and Conductor Model 1

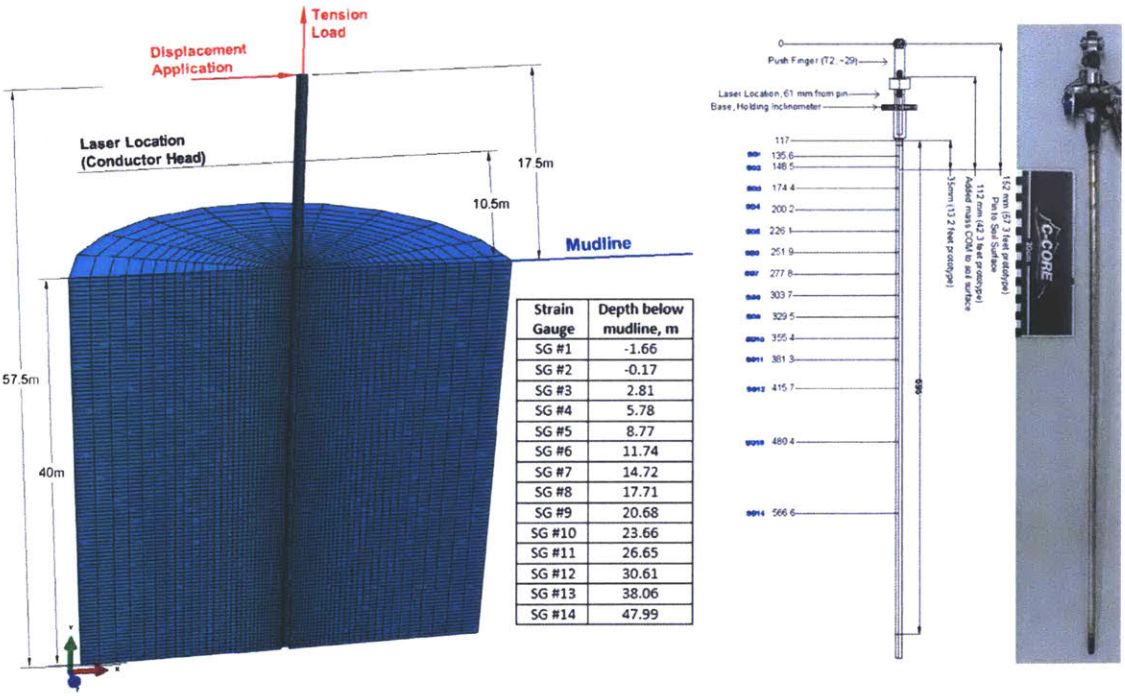

Strain Gauge	Depth below mudline, m
SG #1	-1.66
SG #2	-0.17
SG #3	2.81
SG #4	5.78
SG #5	8.77
SG #6	11.74
SG #7	14.72
SG #8	17.71
SG #9	20.68
SG #10	23.66
SG #11	26.65
SG #12	30.61
SG #13	38.06
SG #14	47.99

Figure 4-16: FE Model 2 and Conductor Model 2

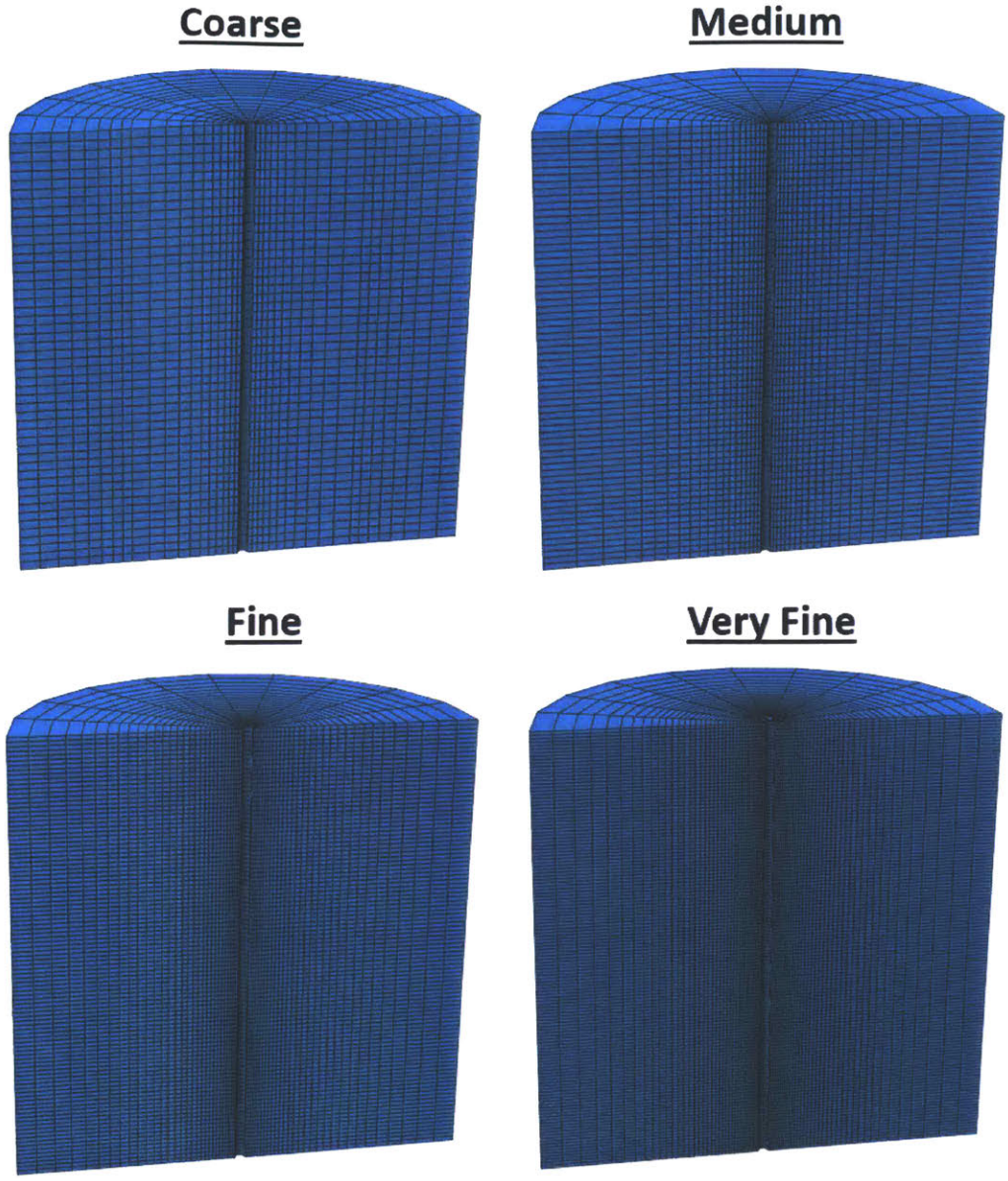

Figure 4-17: Example of different mesh sizes

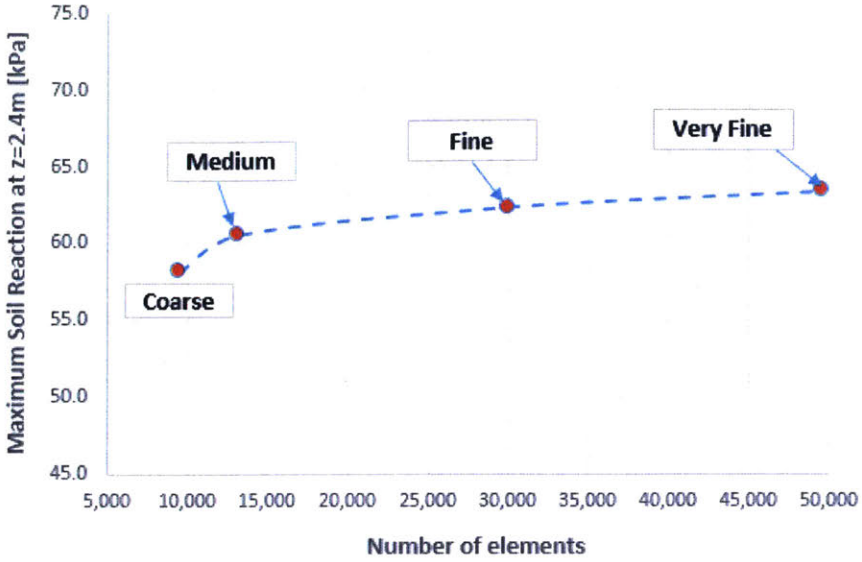

#	Mesh	Relative Seeding Scale	Number of elements	Maximum Soil Reaction (kPa) at z=2.4m
1	Coarse	2x	9500	58.1
2	Medium	1.5x	13200	60.6
3	Fine	1x	30000	62.3
4	Very Fine	0.75x	49580	63.4

Figure 4-18: Mesh sensitivity studies

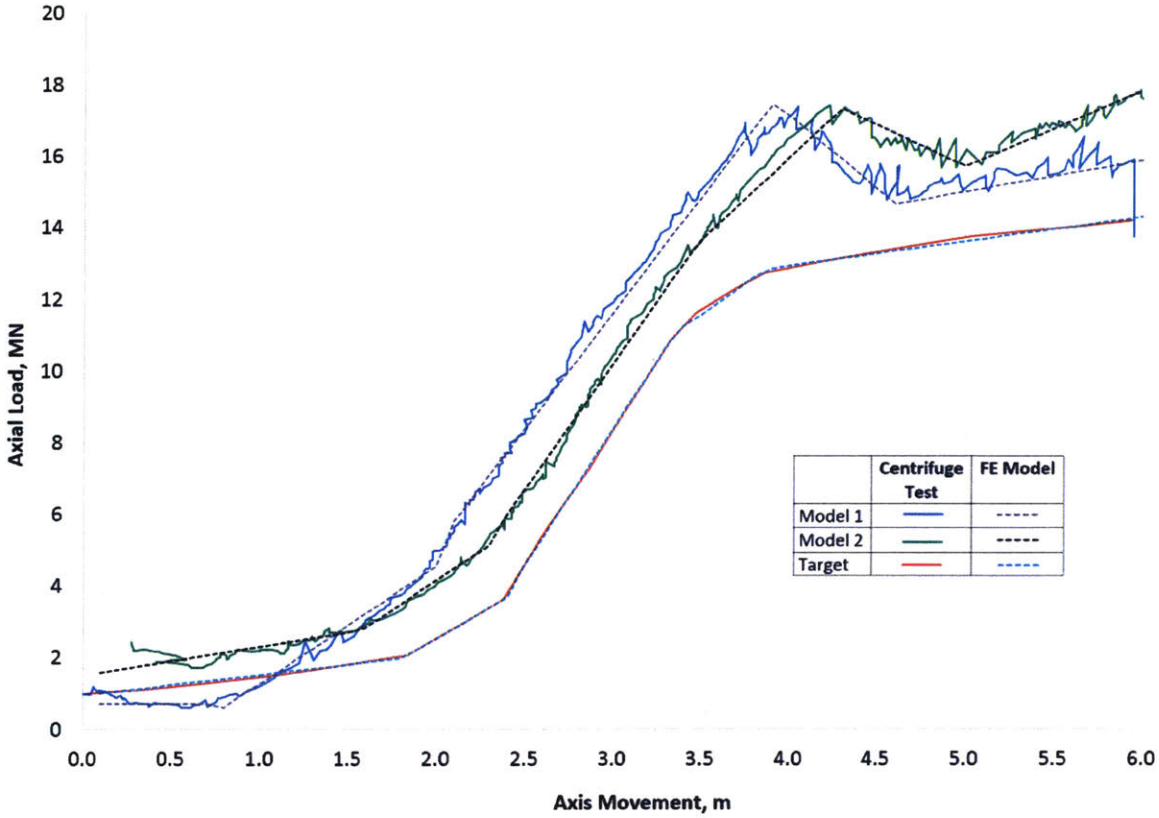

Figure 4-19: Schedule of tension loading at pinned connection above LMRP. Measured load is approximated in FE model by a multi-linear fit

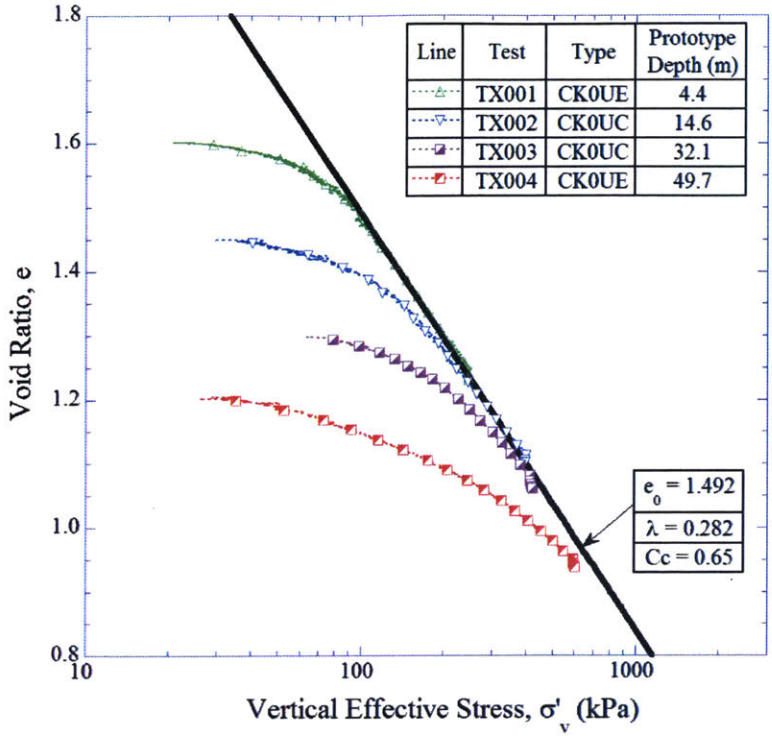

Figure 4-20: Measured and fitted 1-D consolidation behavior of Reconstituted GoM clay

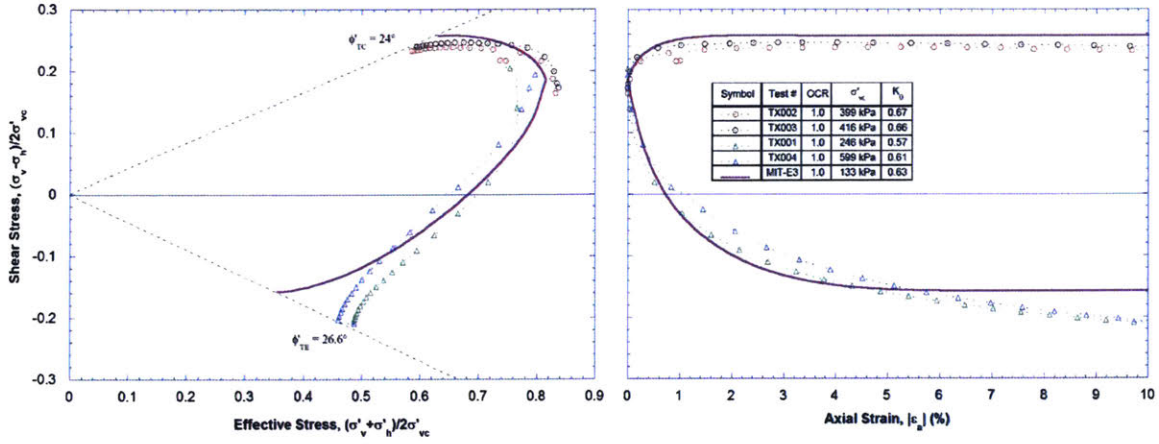

Figure 4-21: Comparison of undrained triaxial shear behavior for Reconstituted GoM Clay with MIT-E3 predictions a) Effective stress paths, b) Shear stress-strain behavior

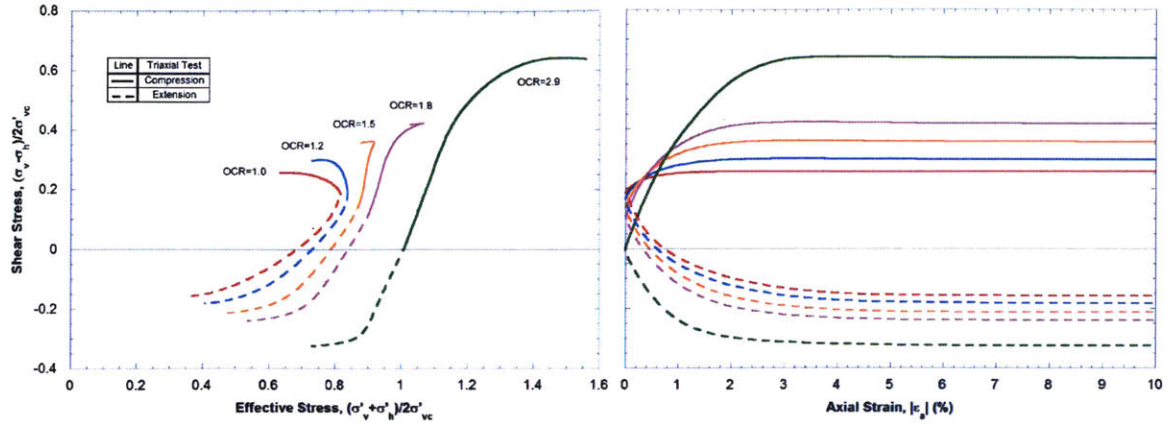

Figure 4-22: Effect of stress history on MIT-E3 predictions of undrained triaxial shear behavior (CK_0UC and CK_0UE tests) for reconstituted GoM clay

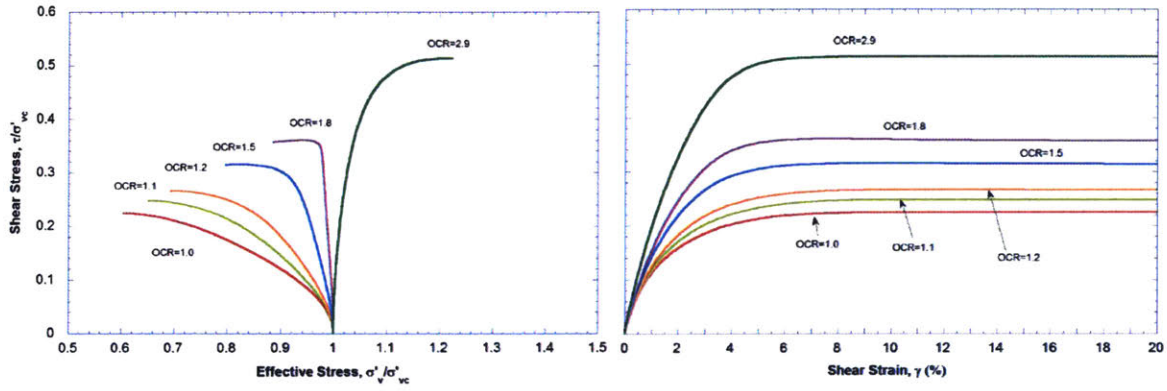

Figure 4-23: MIT-E3 predictions of undrained shear behavior Direct Simple Shear mode (CK_0UDSS tests)

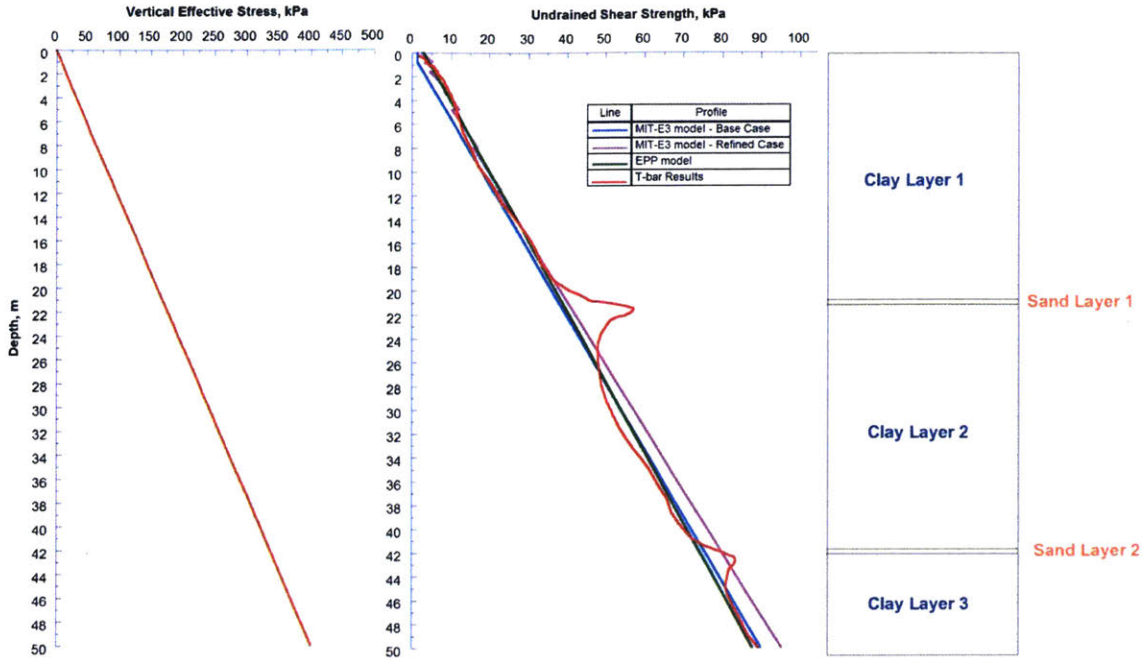

(we assume that the clay has a constant buoyant unit weight, γ_b= 8kN/m^3 such that, $\sigma'_{v0} = \gamma_b z$, where z is the depth below mudline)

Figure 4-24: Undrained shear strength profiles

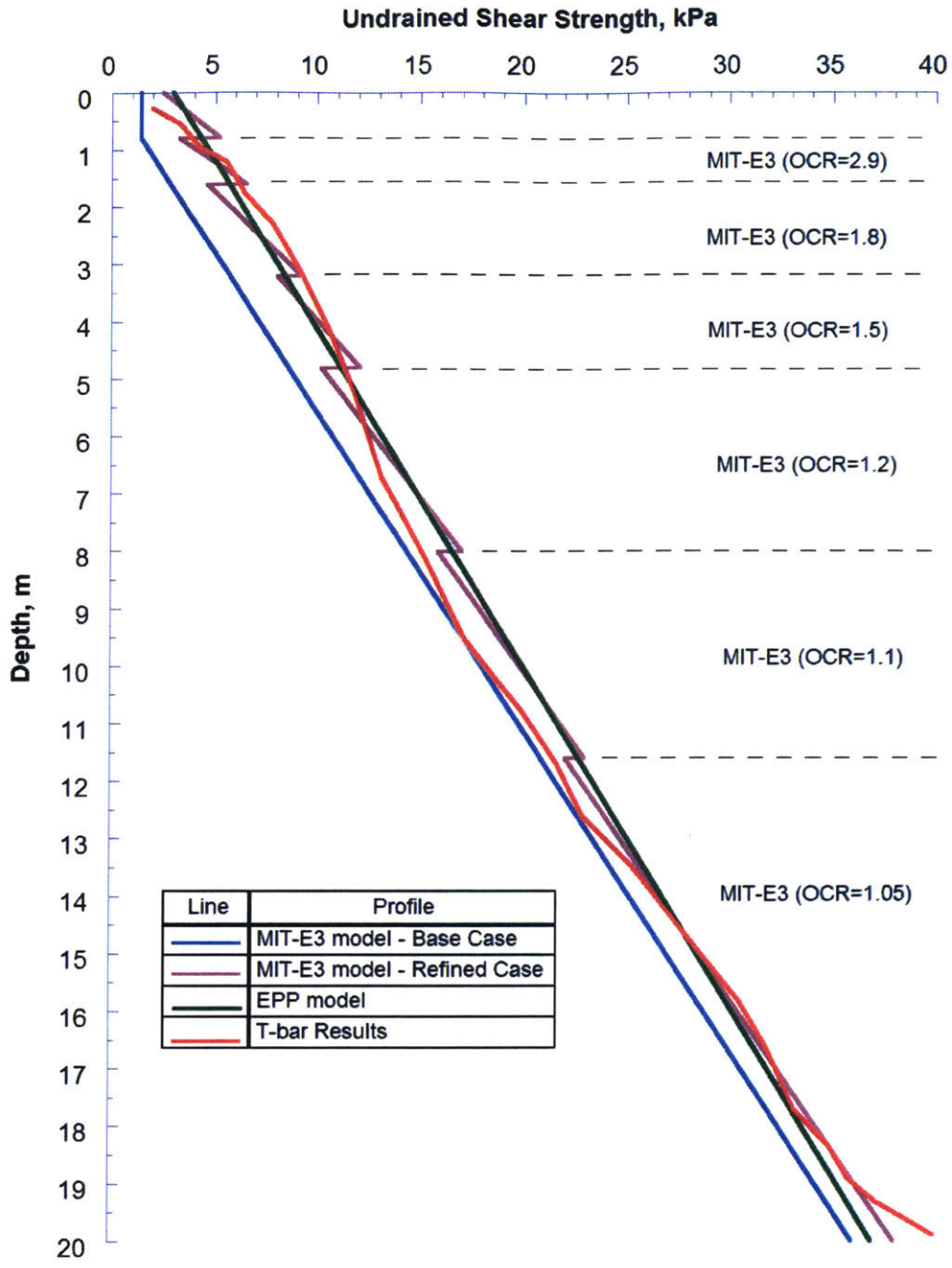

Figure 4-25: Detail of undrained strength profile in upper part of centrifuge model

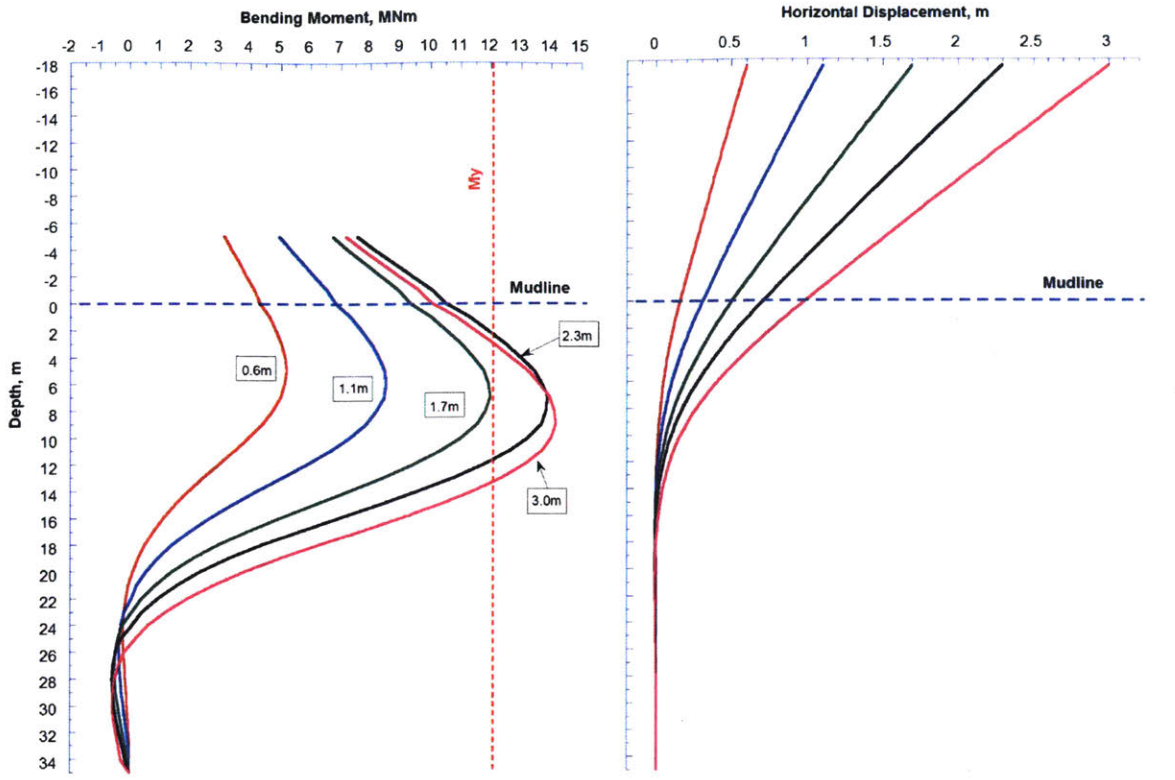

Figure 4-26: Base Case FE predictions of bending moments and conductor deflections for centrifuge Model 1

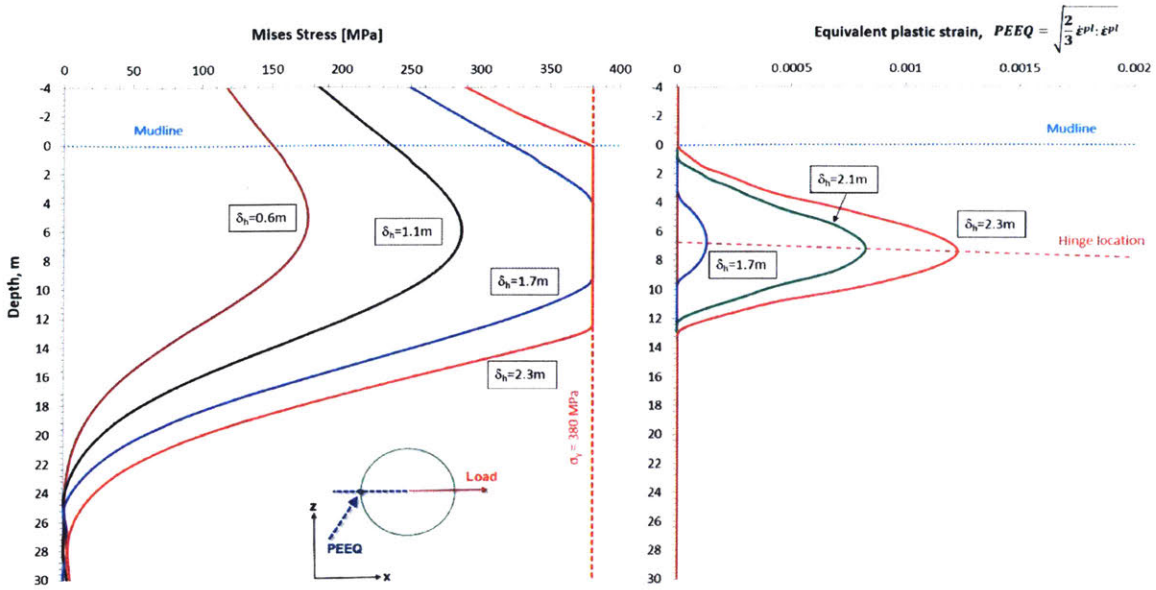

Figure 4-27: Details of plastic yielding in conductor from Base Case FE analysis

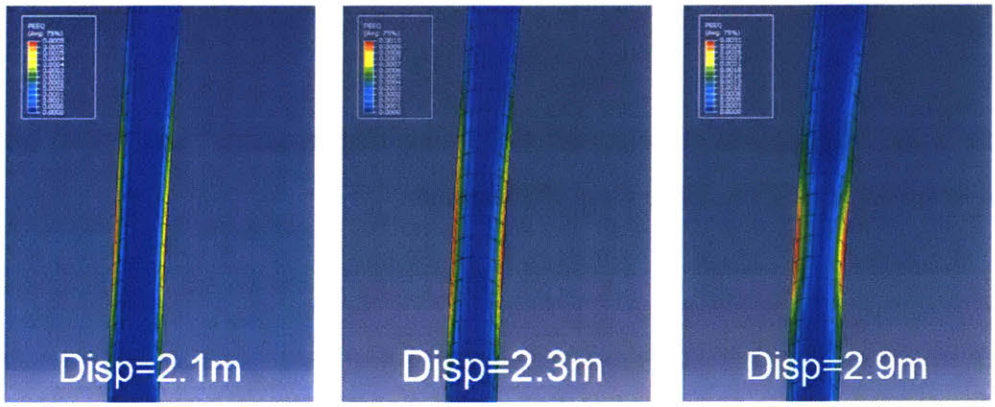

Figure 4-28: Contours of equivalent plastic strains in the conductor

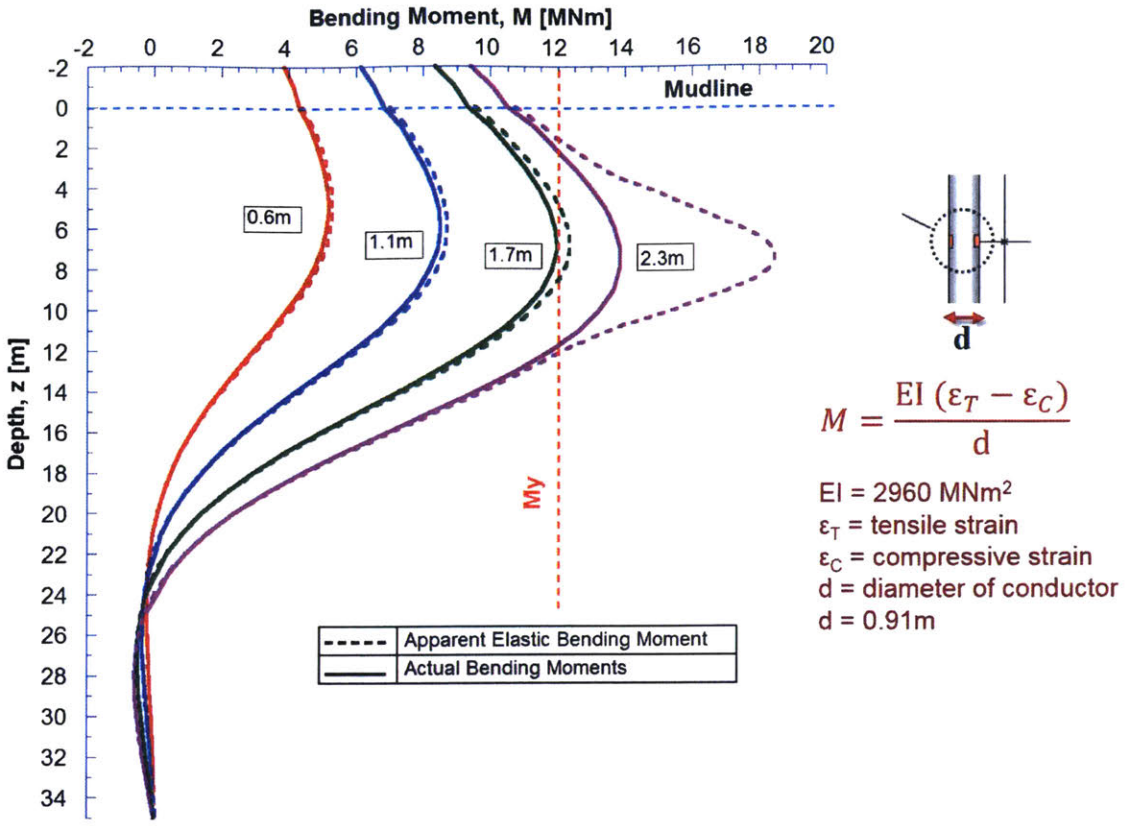

Figure 4-29: Comparison of "apparent elastic bending moments" and actual bending moments computed from Base Case FE analysis

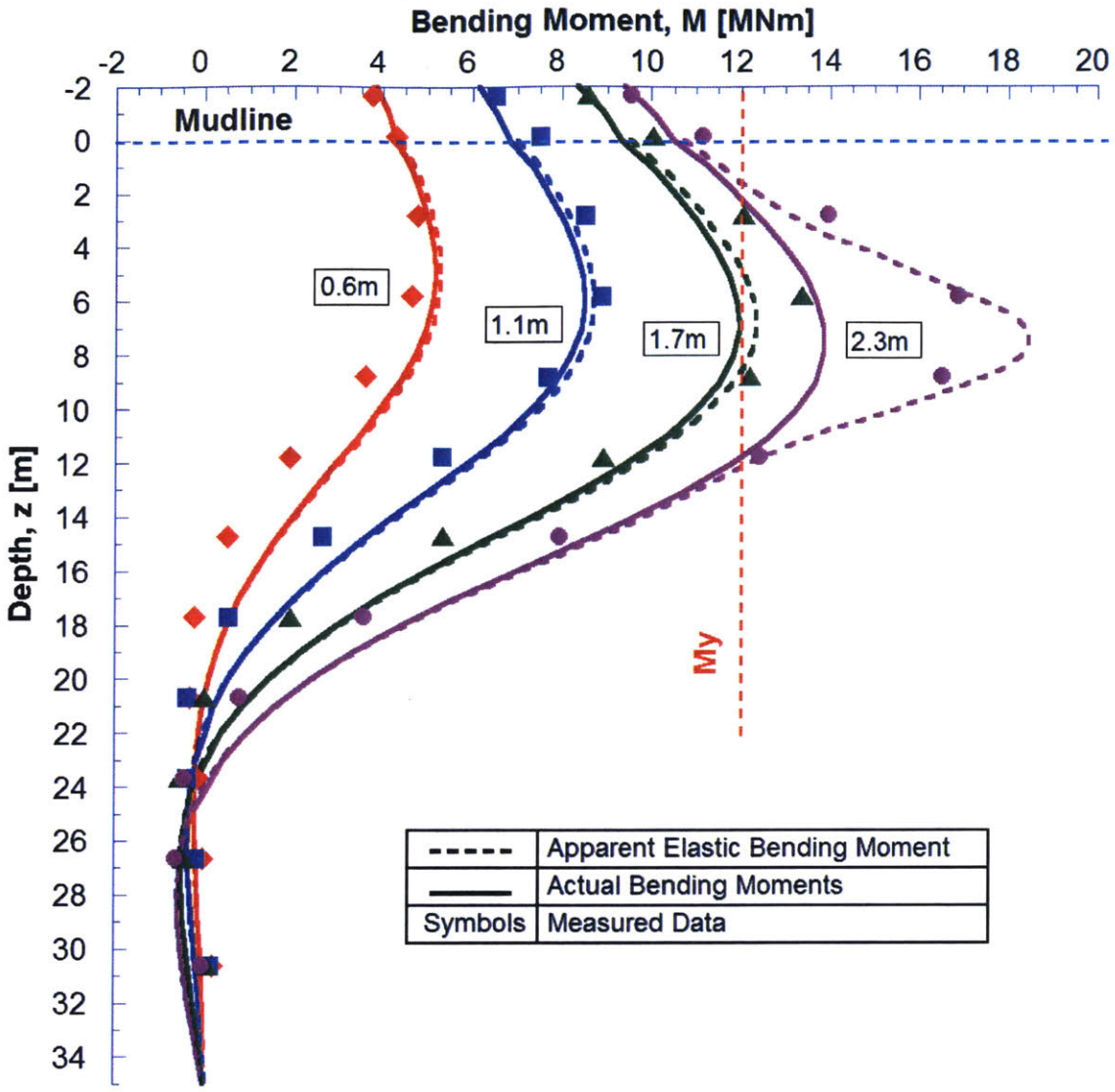

Figure 4-30: Comparison of predicted bending moments from Base Case FE analysis with measurements from centrifuge Model 1

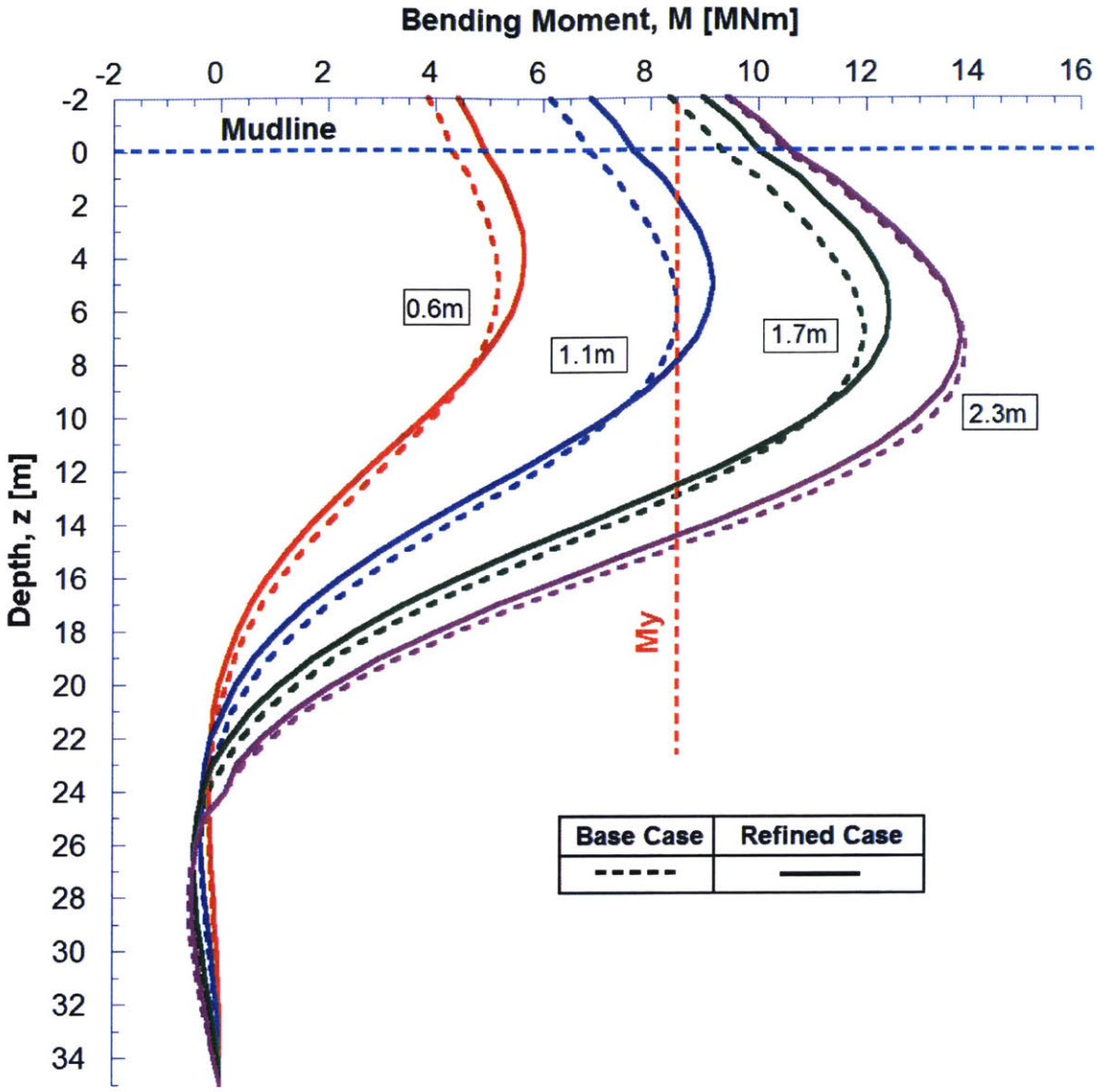

Figure 4-31: Comparison of computed bending moments for centrifuge Model 1 using Base and Refined Case FE analyses

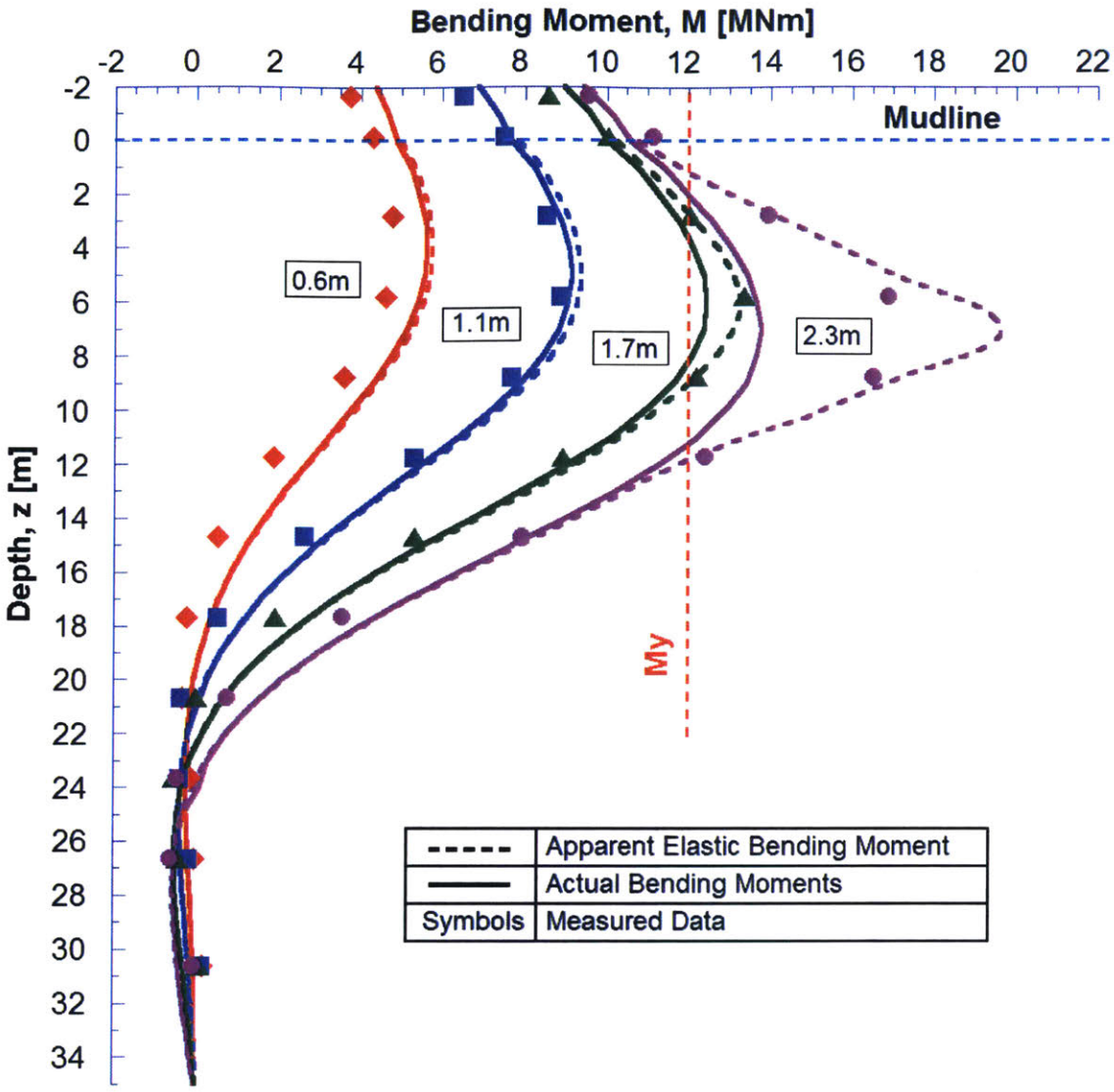

Figure 4-32: Comparison of predicted bending moments from Refined Case FE analysis with measurements from centrifuge Model 1

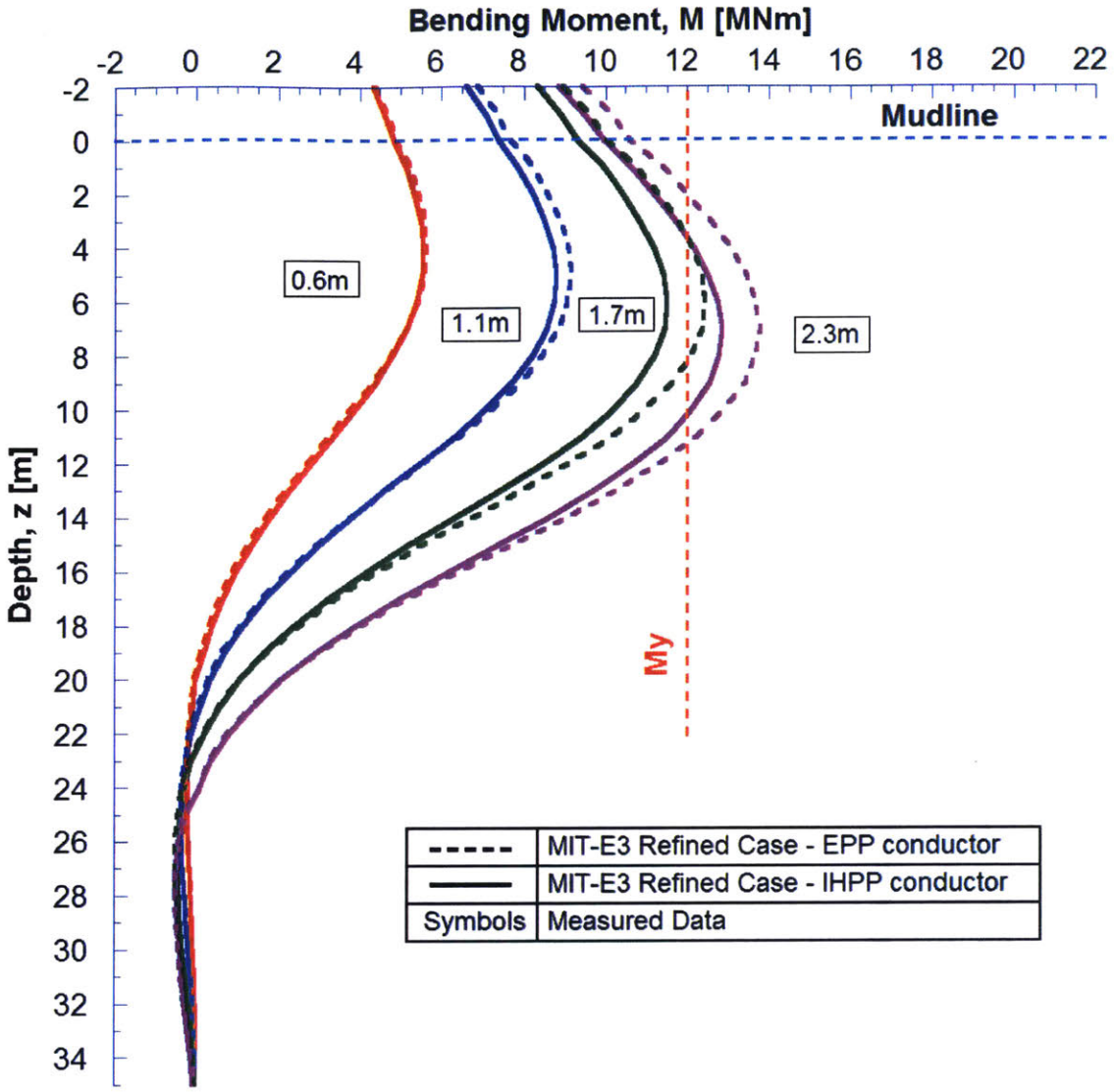

Figure 4-33: The effect of refinements in modeling plasticity of the steel conductor (EPP vs IHPP) on the computed bending moments for the Refined Case (MIT-E3)

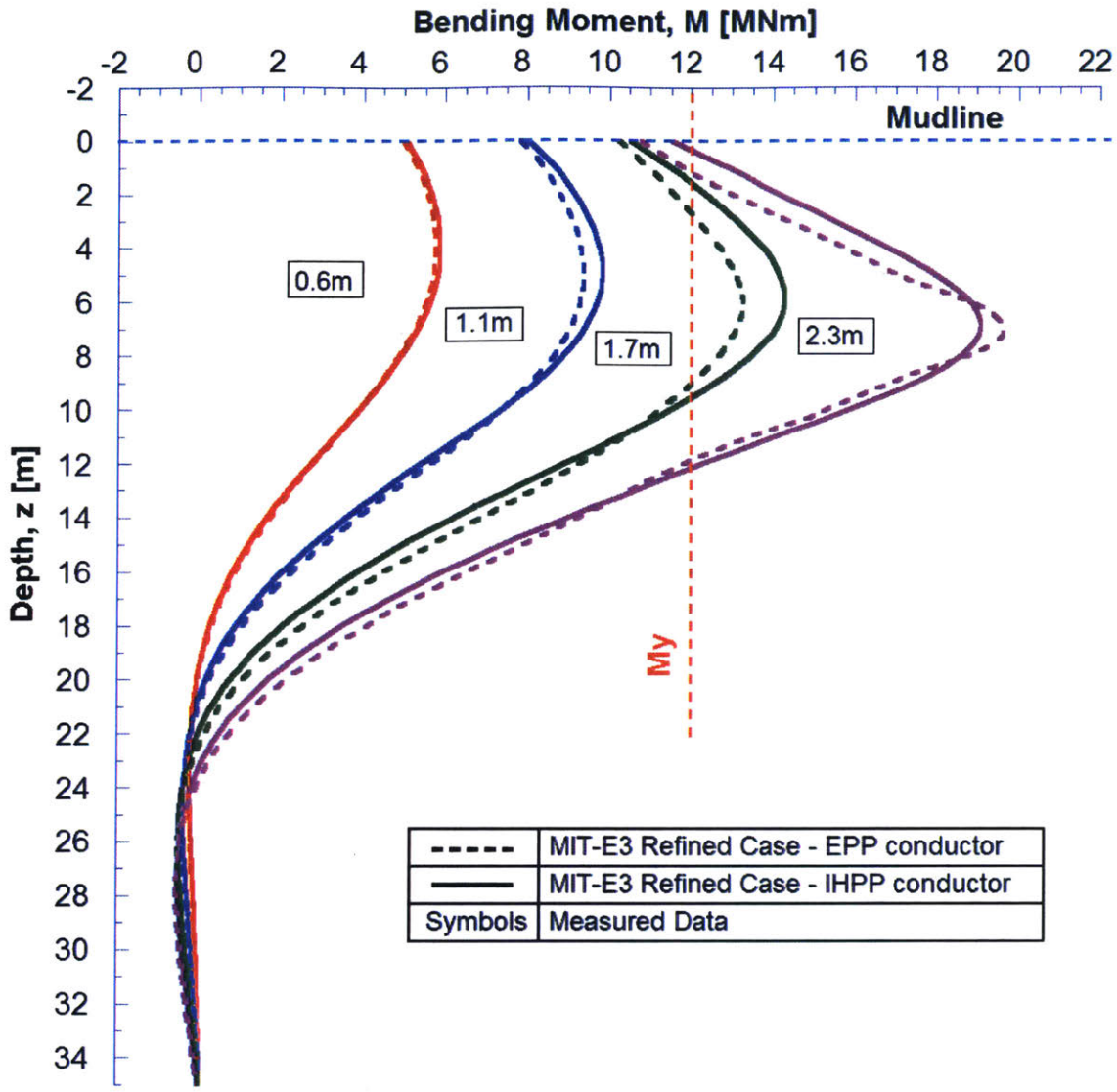

Figure 4-34: The effect of refinements in modeling plasticity of the steel conductor (EPP vs IHPP) on the computed apparent elastic bending moments for the Refined Case (MIT-E3)

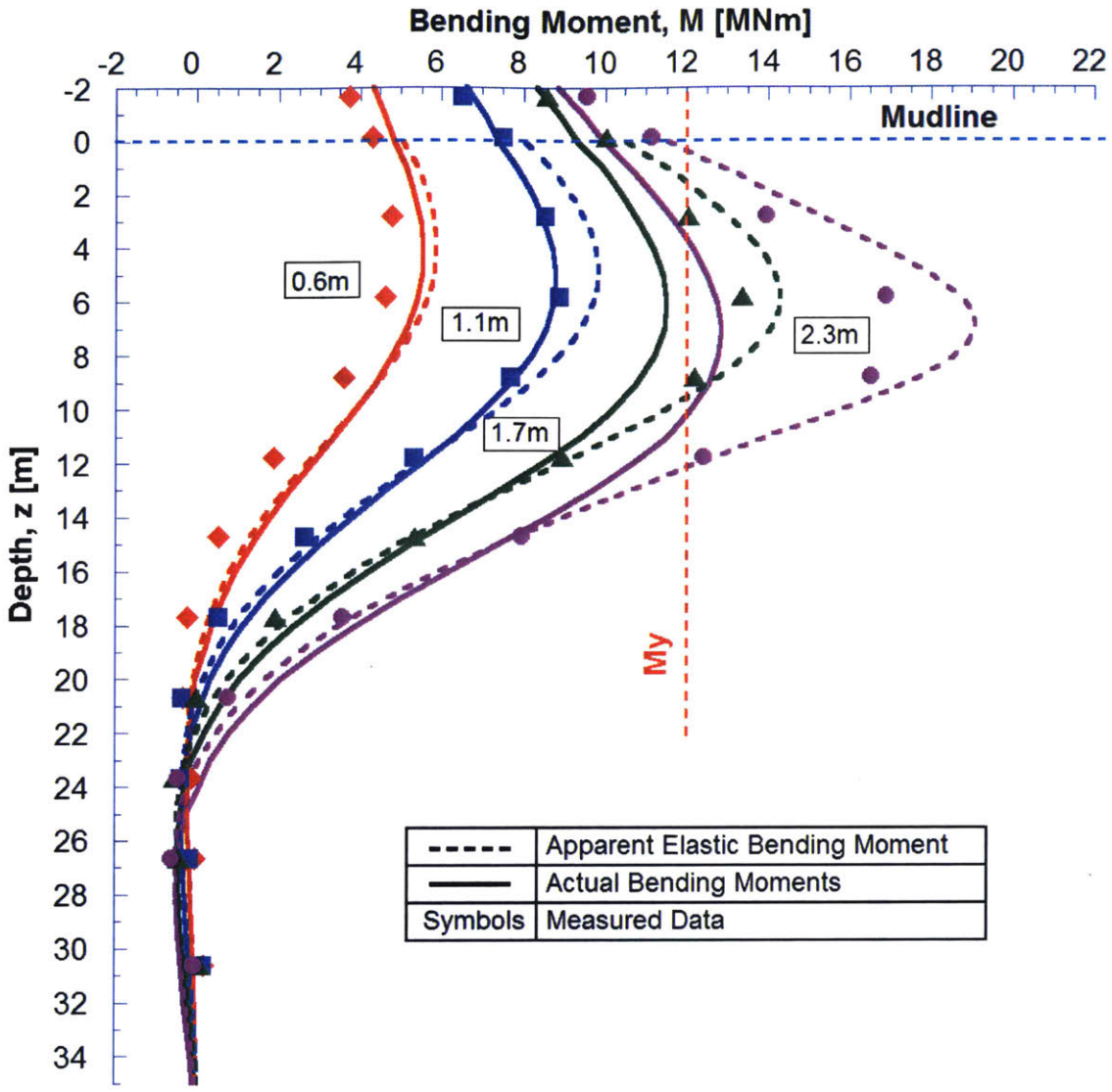

Figure 4-35: Comparison of predicted bending moments from Refined Case FEA using IHPP conductor with measurements from centrifuge Model 1

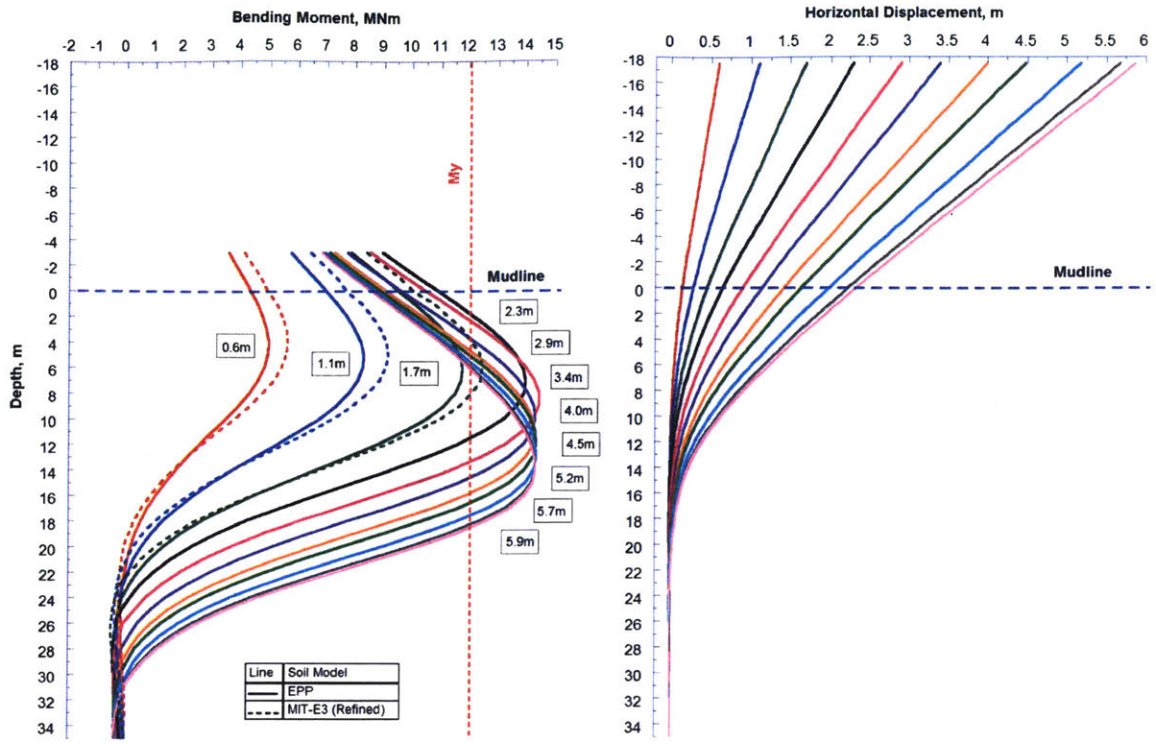

Figure 4-36: Simulation of conductor response for large pushover deformations using EPP FE analysis

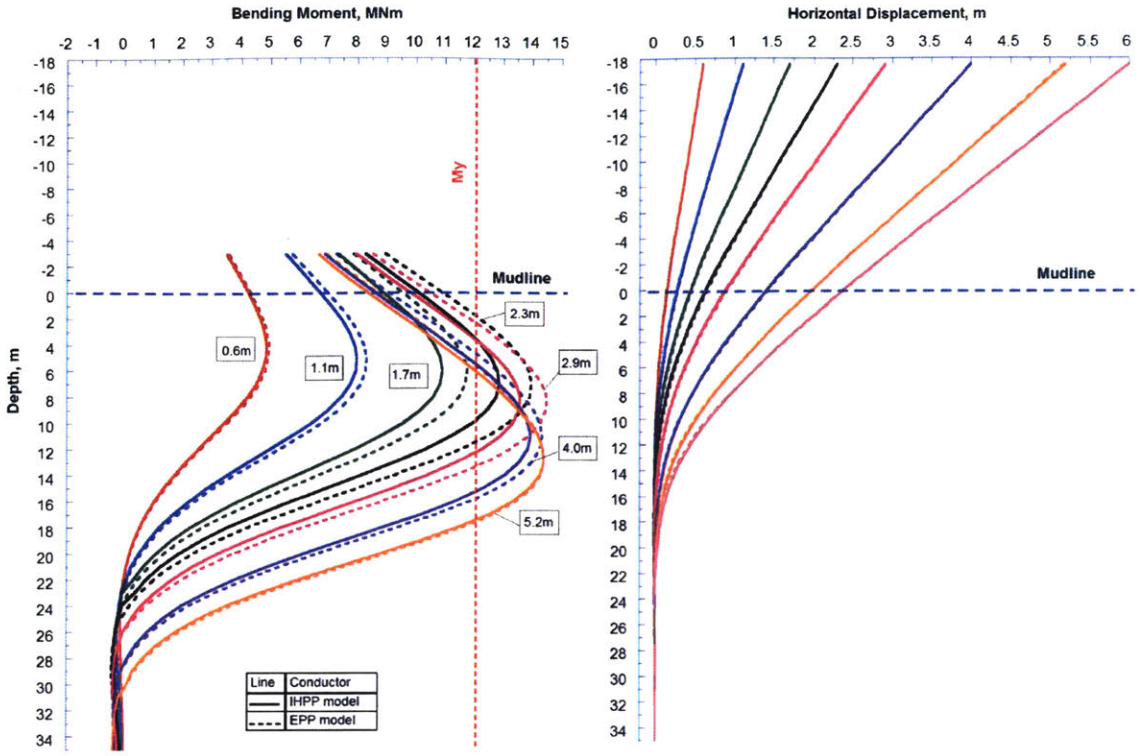

Figure 4-37: The effect of refinements in modeling plasticity of the steel conductor (EPP vs IHPP) on the computed bending moments and deformations of the conductor response for large pushover deformations using EPP FE analysis

Chapter 5

Simplified Method for Conductor-Soil Interactions

5.1 Evaluation of p-y curves

Conductor-soil interactions are conventionally represented by non-linear soil reaction-local soil displacement relations referred to as p-y curves (after Reese et al. [1974] and Matlock [1970]). These local interaction functions can be derived directly from the 3D finite element analyses by integrating the surface tractions around the perimeter of the conductor at selected depths as described in Section 3.1.2. Figure 5-1 summarizes the computed p-y curves (at 5 depths up to z = 9.2m) from the Base Case and Refined FE analyses (for pushover in Model 1 with $\delta_h = 0 - 2.3$m at the elevation of the LMRP). These results highlight that there are large differences in the derived soil reactions associated with relatively modest differences in the assumed undrained shear strength profiles (cf. Fig. 4-25). At points close to the ground surface ($z = 1.2, 2.4$m) the derived interaction curves show maximum soil reactions mobilized at relatively small lateral displacements ($y = 0.1 - 0.25$m) with very little post-peak softening (for $y \leq 0.6$m). Points further down the conductor ($z = 7.2 - 9.2$m) do not achieve full mobilization of the soil resistance at the maximum pushover displacement ($\delta_h = 2.3$m – at which point a plastic hinge is fully developed in the conductor, with $M_p = 14$MNm, Fig. 4-26).

5.2 Large deformation geometric effects

In order to understand the geometric effects associated with very large pushover events, we have performed FE analyses using the EPP model for soil behavior (analyses Case 3; with s_u profile shown in Fig. 4-5) over the full range of displacements imposed in centrifuge Model 1 (i.e., $\delta_h = 0 - 5.9$m). Figure 4-36 shows that this analysis predicts a maximum moment, $M_{max} = 14.3$MNm (corresponding to the fully plastic section) occurring at $z = 8$m at $\delta_h = 2.9$m. Further pushover of the conductor causes the point of maximum moment to migrate down the conductor to $z = 14$m at $\delta_h = 5.9$m (conductor deflections extend to a depth, $z = 19$ - 20m below mudline).

Figures 4-37a and 4-37b compare the bending moments and conductor displacement profiles for the Case 3 analyses (EPP soil model) with two different representations of conductor plasticity (EPP vs. IHPP; Fig. 4-13). When isotropic hardening of the steel conductor is simulated (IHPP) the computed maximum bending moments decrease by up to about 1.9 - 8.1% for lateral deformations up to $\delta_h = 2.9$m. However, further lateral deformations lead to convergence and almost identical bending moments at $\delta_h = 5.2$m.

Figure 5-2a compares the local conductor-soil interaction, p-y curves from the finite element analyses using EPP and MIT-E3 (Refined case) soil models for loading to $\delta_h = 2.3$m. These two analyses have very similar profiles of the reference undrained shear strength in the clay (in the reference simple shear mode of shearing, s_{uDSS}) and differ principally in the modeling of soil behavior (MIT- E3 vs. EPP). The MIT-E3 model describes more accurately the element stress-strain properties of the reconstituted GoM clay particularly in representing: i) the non-linear stress strain properties at small shear strains (EPP assumes linear elastic behavior pre-failure); and ii) the anisotropic response in different modes of undrained shearing (EPP has isotropic strength). Despite these large differences in the modeling of elemental soil properties, the two models produce qualitatively similar p-y curves with similar levels of displacement (y) to achieve maximum soil resistance. Overall, the Refined Case (MIT E3) generates higher soil resistance than EPP at each of the 5 depths reported. Figures

5-3 and 5-4 compare the mobilized lateral bearing capacity factor, N_p, from the two FE analyses. Results from the isotropic EPP model show almost unique normalized reaction curves for $z > 3.6$m ($N_p = 10$, at $y \approx 0.3$m). The anisotropic MIT-E3 model (Refined analysis) computes maximum values $N_p = 12$ - 14 and very similar normalized behavior over the same depths.

Figure 5-5 shows the p-y curves computed from the EPP analyses over the full range of pushover for centrifuge Model 1 (with maximum displacement, $\delta_h = 5.9$m). These results show significant post-peak softening of the resistance at each depth as the conductor continues to rotate and the point of maximum bending moment migrates down the conductor (cf. Fig. 4-36).

The preceding results show that differences in the modeling of elemental soil behavior have limited impacts on the computed conductor response in loading. However, much larger differences emerge when the pushover event is reversed. Figures 5-6a and 5-7 compare the computed p y curves from Refined and EPP FE analyses, respectively, for reversal of loading (i.e., conductor experiences maximum pushover to $\delta_h = 2.3$m, which is restored as the LMRP is pushed back to its original position). The unloading response computed by EPP is initially controlled by the elastic stiffness (Fig. 5-7), while the limiting soil resistance is uniquely defined by the initial undrained shear strength. In contrast, MIT-E3 predicts a much stiffer response at first reversal (controlled by non-linear small strain stiffness properties of the GoM clay) and there is a large reduction in the available shear resistance of the clay as the conductor is restored towards its original position ($z = 1.2 - 4.4$m). These effects have not been investigated in the current centrifuge tests but reflect a realistic feature of the MIT-E3 constitutive model predictions that should be included in future modeling of local conductor-soil interactions.

5.3 Simplified methods for representing conductor-soil interaction

Although nonlinear, 3D Finite Element analyses provide a comprehensive framework for modeling conductor-soil interaction problems, they involve significant computational costs and depend on the selection of appropriate constitutive laws, boundary conditions etc., as illustrated in the prior sections. The representation of conductor-soil interactions as a component in the simulation of the riser system (e.g., weak point analyses for drift/drive-off) can be accomplished more efficiently through simplified local interaction models (p-y representation) that are calibrated to the 3D finite element analyses. This section investigates the use of a simplified p y analysis framework, referred to as BWGG that was developed by Gerolymos and Gazetas [2005a] for modeling dynamic pile-soil interactions under generalized cyclic loading conditions. The BWGG framework is able to represent gapping at the pile-soil interface, radiation damping and loss of shear resistance associated with development of excess pore pressures under cyclic loading. BWGG corresponds to an extended version of the well-known Bouc-Wen model (developed for hysteretic material behavior by Bouc [1971]; and Wen [1976]; and first applied to piles by Trochanis et al. [1991]) that represents degrading hysteretic p-y behavior. We present a summary of the BWGG formulation and interpretation of model input parameters (Subsections 5.3.1 and 5.3.2) and then investigate the calibration of the BWGG model using the results from 3D finite element analyses (Section 5.3.3). The results highlight the capability of BWGG to model pile-soil interactions at large deformations, but also illustrate some limitations of the model when simulating the cyclic response of the pile.

5.3.1 Implementation and calibration of a hysteresis model

According to the general Bouc-Wen formulation, the lateral soil reaction against a deflecting pile can be expressed as the sum of elastic and hysteretic components as

follows:

$$p_s = [aKu + (1-a)\, p_y \zeta]\,(1-r) \tag{5.1}$$

where p_s is the resultant in the direction of loading of the normal and shear stresses along the perimeter of the pile of a unit thickness; u is the lateral pile deflection; K is the initial stiffness; p_y is the ultimate soil reaction, a controls the post-yield stiffness, r is a function that controls strength degradation for cyclic loading, and ζ is a dimensionless quantity that describes the non-linear response of the soil.

The latter is governed by the following differential equation:

$$d\zeta = v\left\{1 - |\zeta|^n \left[b + g\, sign\,(\zeta du)\right]\right\} \frac{du}{u_y} \tag{5.2}$$

where du is the incremental relative displacement of the pile and the displacement, $u_y = [p_y/K]$ is the displacement required to mobilize the ultimate soil reaction.

The signum function of a real number x is defined as follows:

$$sign\,(x) = \begin{cases} -1 & if\ x < 0 \\ 0 & if\ x = 0 \\ +1 & if\ x > 0 \end{cases} \tag{5.3}$$

The differential equation (eqn. 5.2) can be solved numerically in conjunction with the system of equilibrium equations for the pile-soil system using an explicit finite difference scheme (with small time steps).

The parameters n, b and g in eqn. 5.2 are dimensionless input parameters that control the hysteretic response, while ν is a function introduced by Gerolymos and Gazetas [2005a] to control stiffness degradation under cyclic loading. They propose a function which degrades stiffness over time as a function of the dissipated hysteretic energy:

$$v = \begin{cases} \frac{s_1 + a(\mu_r + 1) + s_2}{s_1 + \mu_r} & \text{for } \mu_r > s_2 \\ 1 & \text{for } \mu_r < s_2 \end{cases} \tag{5.4}$$

where $\mu_r = [u_{amp}/u_y]$ is a 'ductility index' defined in terms of the pile displacement at

the last load reversal (u_{amp}) relative to the displacement needed to mobilize the maximum soil resistance. The parameters s_1 and s_2 are used to control the degradation of stiffness at each load reversal.

Material degradation under cyclic loading is controlled by the function r (eqn. 5.1) which is related to the excess pore pressure generated around the pile:

$$r = \alpha W(t)^{\beta} \tag{5.5}$$

where a, β are constant input parameters and $W(t)$ is measure of the cumulative energy dissipated in hysteresis:

$$W(t) = (1-\alpha)\int_0^t \zeta(u,t)\,\dot{u}(t)\,dt \tag{5.6}$$

The BWGG model has been implemented in an explicit finite-difference numerical algorithm in MATLAB and in Java-program with a custom graphical user-interface (Figures 5-23 and 5-22).

5.3.2 BWGG Model Input Parameters

In its most general form, the BWGG model describes the local pile-soil interaction behavior ('p-y'; i.e., p_s vs. u, eqns. 5.1, 5.2) using three subsidiary functions (ζ, v, r) and 10 input constants. For the current applications, where there is no dilation of the clay during pile loading, the basic hysteretic response can be simulated assuming $[b+g] = 1$. In this case, the BWGG model requires 4 independent parameters to describes the initial monotonic loading response (p_y, K, a, n) and 3 independent parameters for the unload-reload behavior (b, s_1, s_2) , assuming there is minimal degradation under cyclic loading (i.e., $r = 0$ and $a = 0$; eqns. 1 and 5). More general degradation of shear resistance with cyclic loading is achieved by selecting ($a \neq 0$, β; eqn. 5.5)

Figure 5-8 illustrates BWGG simulations of local pile-soil interaction behavior ('p-y'; i.e., p_s vs. u, eqns. 5.1, 5.2) for monotonic loading. This behavior can be

characterized by 4 input parameters, p_y, K, n and a. The value of p_y defines the limiting/yield value of the soil reaction at a given depth (Fig. 5-8a), while post-yield behavior is controlled by a (hardening for $a > 0$ and softening for $a < 0$; Fig. 5-8c). The parameters K and n define the non-linear response and displacement required to reach yield conditions (Figs. 5-8b, d).

Figure 5-9 shows how values of b and s_1 affect the response of the pile in unloading and reloading, while s_2 produces a small degradation is the limiting shear resistance (Fig. 5-9c). All of these simulations show symmetry between the unloading and reloading branches and hence, conform to the general Masing conditions. Much larger degradation effects can be obtained for cases with $\alpha > 0$ (Fig. 5-9d)

5.3.3 Calibration of BWGG to 3D FE Models of Soil-Structure Interaction

In Chapter 4 we have shown a close agreement between numerical predictions and measured performance of a prototype conductor (centrifuge model test) using a Refined Case analysis (MIT-E3 with stress history profile shown in Fig. 4-5b), Figure 4-32, where the LMRP undergoes a lateral displacement $\delta_h = 2.3$m. There are also reasonable results obtained using the EPP model (Fig. 4-36), and analyses using this model have been extended to very large displacements ($\delta_h = 6$m at LMRP) to investigate effects of geometric non-linearities.

Figures 5-10 and 5-11 illustrate the matching between normalized p-y curves from the 3D FE analyses and the calibration of input parameters for the BWGG model (Table 5.2). The FE analyses show that the local pile soil interaction in monotonic loading (up to $\delta_h = 2.3$m) is well represented by a unique curve assuming:

$$p_y = N_p s_u d \tag{5.7}$$

where s_u is the undrained shear strength for the reference profile (Fig. 4-5).

For the EPP model, the back-fitted value of $N_p = 10$ (Fig. 5-10) and fits the FE computations very closely for z = 3.6 - 12.0m (somewhat lower values of N_p would

be needed for points closer to the mudline). Results for the MIT-E3 model ('Refined Case'; Fig. 5-11) also show a very good agreement between the 4 parameter BWGG model and the 3D FE computations.

Figure 5-12 summarizes the local pile-soil interaction curves from 3D FE analyses using the EPP soil model for the case where the conductor undergoes large displacements ($\delta_h = 6$m at LMRP, corresponding to the riser detachment simulated in the C-CORE centrifuge tests). The analysis simulates a complete reversal of the loading (δ_h =-6m) and reloading such that the LMRP returns to its original position. The results show clearly the pronounced post-peak softening in the soil reaction during monotonic loading, due to geometric non-linearities associated with deformations of the conductor.

The reaction curves at z = 4.8m and 7.2m reach a residual level of resistance prior to load reversal. The computed soil response after load reversal shows strain hardening, with maximum resistance occurring only at two of the selected depths (z = 8.4, 9.6m) and little post-peak softening. The magnitude of the peak soil resistance, $|p_{smax}|$ is comparable or slightly larger than that computed in first loading. The equivalent normalized soil reaction curves ($N_p = p_s/s_u d$; Fig. 5-13) show that local pile-soil is well represented by a single unique backbone function (for $z \geq 4.8$m) but with very different characteristics depending on the direction of loading. The completed computed response (across all three loading branches) is difficult to simulate using the BWGG framework. Figure 5-14 shows that the BWGG model (with no strength degradation, Table 5.3) describes a unique envelope for the maximum soil reaction that is defined by the post-yield stiffness parameter, a (Table 5.1). When this parameter is calibrated to the monotonic load behavior, it also defines a unique limit condition in the reverse loading direction. When this behavior is compared with 3D FE predictions of conductor response using the EPP model, Figure 5-15, it is apparent there are a number of pervasive discrepancies between the two models:

1. The BWGG model does not characterize the residual soil reaction observed at large deformations in the EPP simulation.

2. The BWGG model underestimates the deformations needed to mobilize maximum soil reactions (from the EPP 3D FE model) when loading is reversed and overestimates the post-peak softening.

While these features of behavior can be considered limitations of the current BWGG model, there are no measurements to endorse 3D FE computations using the EPP soil model. Indeed, by comparing the computed reloading response with the initial monotonic load behavior, it is clear that there is no degradation in the apparent soil reaction (indeed the results show a small increase in p_{smax}) assuming perfectly plastic soil behavior (a limitation of the EPP soil model).

Figures 5-16 and 5-17 summarize the local pile-soil interactions and normalized response functions from 3D FE analyses using the MIT-E3 soil model, for initial loading to $\delta_h = 2.3$m, reversal to -2.3m, and restoration of the LMRP to its original position. This simulation does not engage the post-peak geometric softening described previously (EPP model, Figure 5-12), but shows the effects of significant degradation in soil properties associated with the imposed strain history (i.e., the evolution on anisotropic properties computed by the MIT-E3 soil model). There are again no experimental data available to validate predictions in the unload-reload branches. It is apparent that the soil resistance after load-reversal is significantly reduced compared to the response in first loading.

The overall behavior (i.e., across the three phases) is reasonably described by the BWGG model by incorporating the material degradation parameters (α, β; Table 5.3), as shown in Figure 5-18. A direct comparison shows that the BWGG model tends to overestimate the stiffness in both unloading and reloading branches when compared to the MIT-E3 simulations (Figure 5-19).

Figure 5-20 shows the main screen of the developed calibration tool to simulate elemental laboratory tests using various MIT soil models. This tool is a graphical user interface developed for a previously written elemental point test solver in Fortan programming language. Multiple tests with prescribed OCR values (Figure 5-21) can be easily simulated to calibrate advanced effective stress soil models. Figure 5-22 presents the main interface of the developed tool for representing simplified conductor-

soil interactions to be used in practice. Figure 5-23 shows an example of the output based on the BWGG model previously calibrated to 3D FE simulations.

Table 5.1: The list of the general BWGG model input parameters

Parameter	Description	Loading
K	Initial tangent stiffness (kN/m^2)	Monotonic
p_y ($=N_p s_u d$)	Ultimate soil reaction (kN/m)	
a	Ratio of the post yield to initial stiffness	
n	Non-linearity in montonic loading	
b	Unloading and reloading stiffness (Note: $b + g = 1$)	Cyclic
s_1	Stiffness degradation	
s_2		
α	Strength degradation	
β		

Table 5.2: Calibrated BWGG parameters – Monotonic Loading

Parameter	Soil Model Calibration	
	EPP	MIT-E3
K (kPa)	3200	3000
p_y (kN/m)	104	100
s_u(kPa)	Fig. 4-5	
N_p	10	13
a	-0.009	0.112
n	0.48	0.5

Table 5.3: Calibrated BWGG parameters – Cyclic Response

Parameter	Soil Model Calibration	
	EPP	MIT-E3
b	0.02	0.6
s_1	3.0	1.0
s_2	5.0	10.0
α	0.0	0.9
β	--	0.4

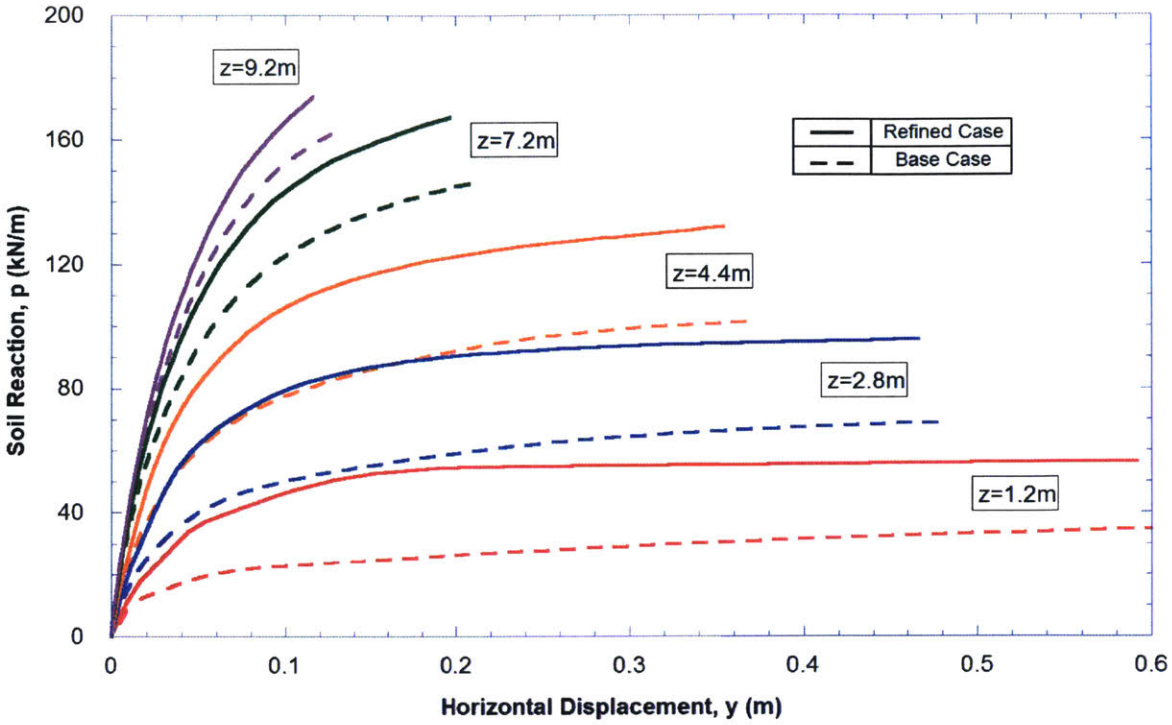

Figure 5-1: Comparison of computed p-y curves from Base Case and Refined FE analyses showing effect of stress history profile on local conductor-soil interactions

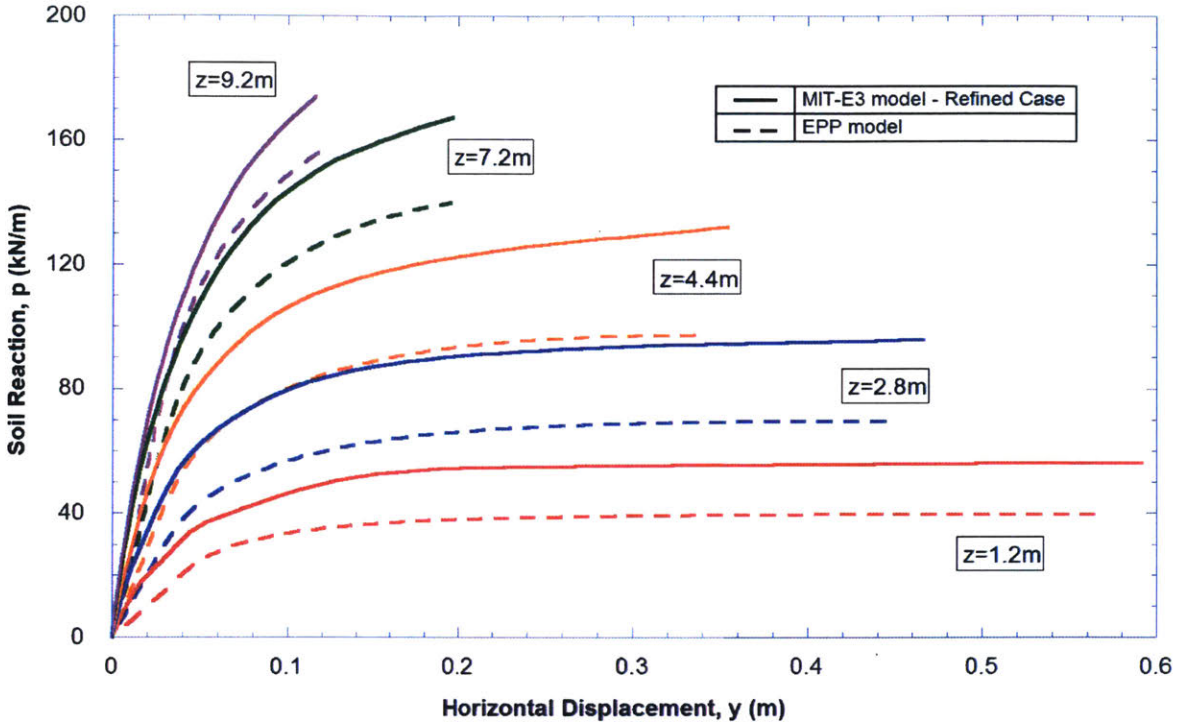

Figure 5-2: Effect of soil model on computed conductor-soil interactions from Refined (MIT-E3) and EPP FE analyses

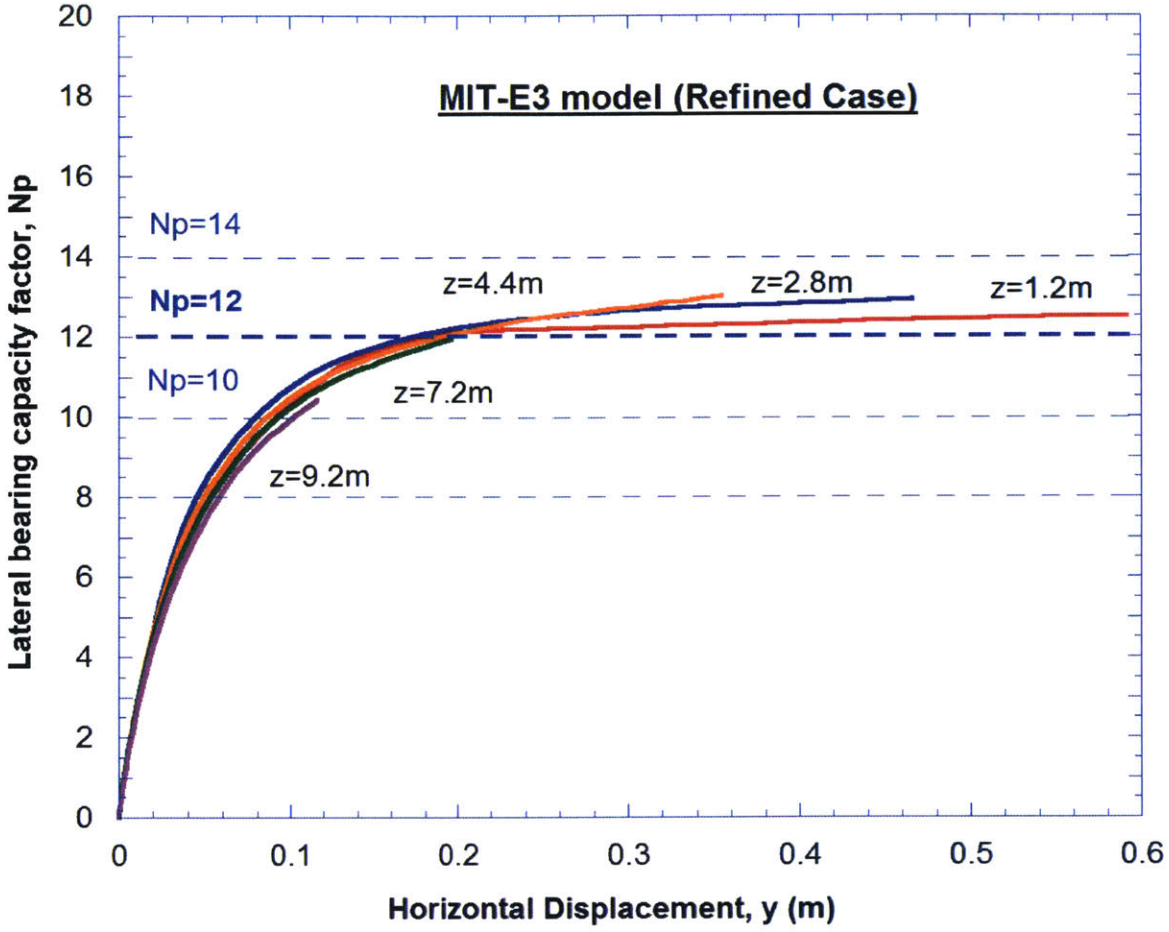

Figure 5-3: Np values from Refined (MIT-E3) Analysis

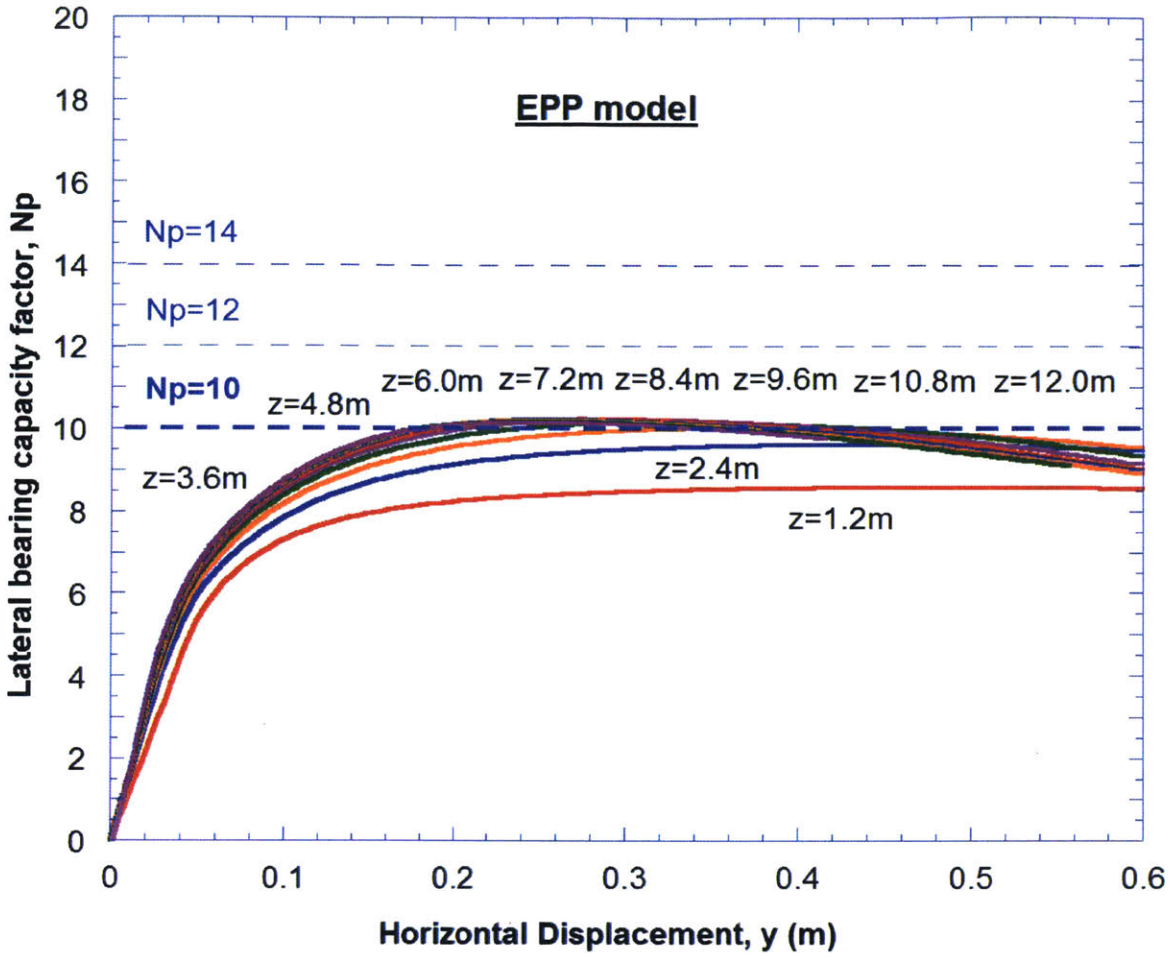

Figure 5-4: Np values from FE analysis with EPP soil model

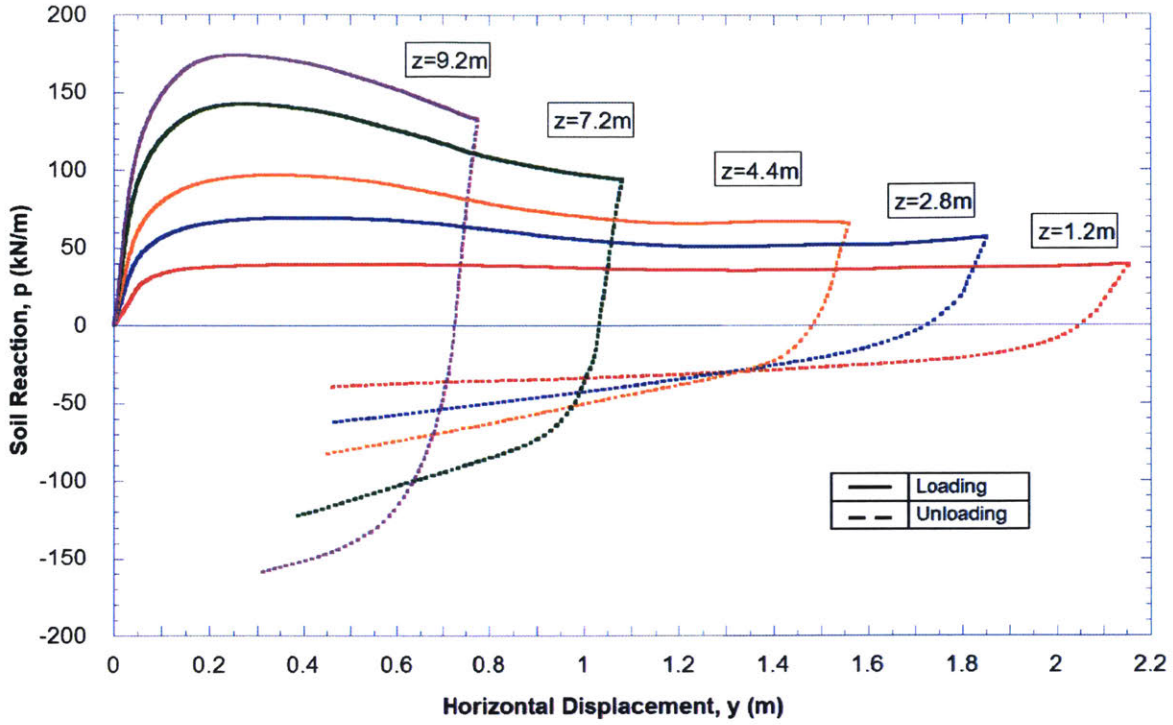

Figure 5-5: Local conductor soil interaction for large pushover events (max. $\delta_h = 5.9$m) computed from EPP FE analysis of centrifuge Model

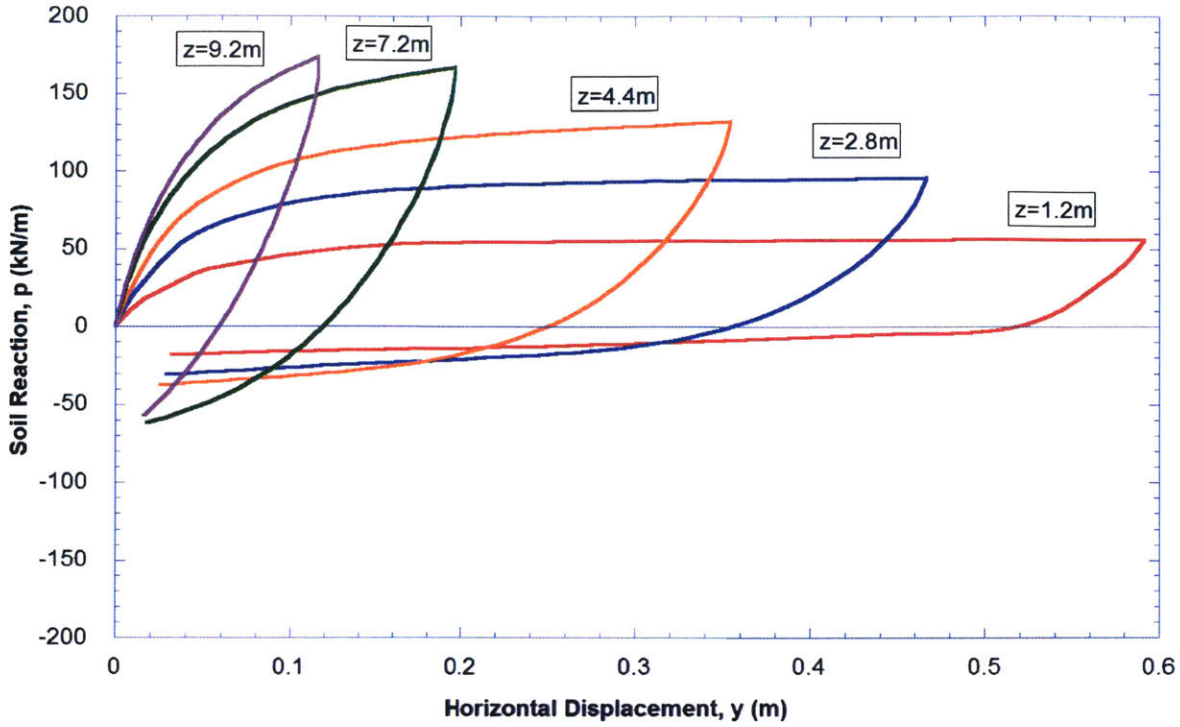

Figure 5-6: Simulation of local conductor-soil response for reversal of pushover (with maximum $\delta_h = 2.3$m) using Refined Case FE model

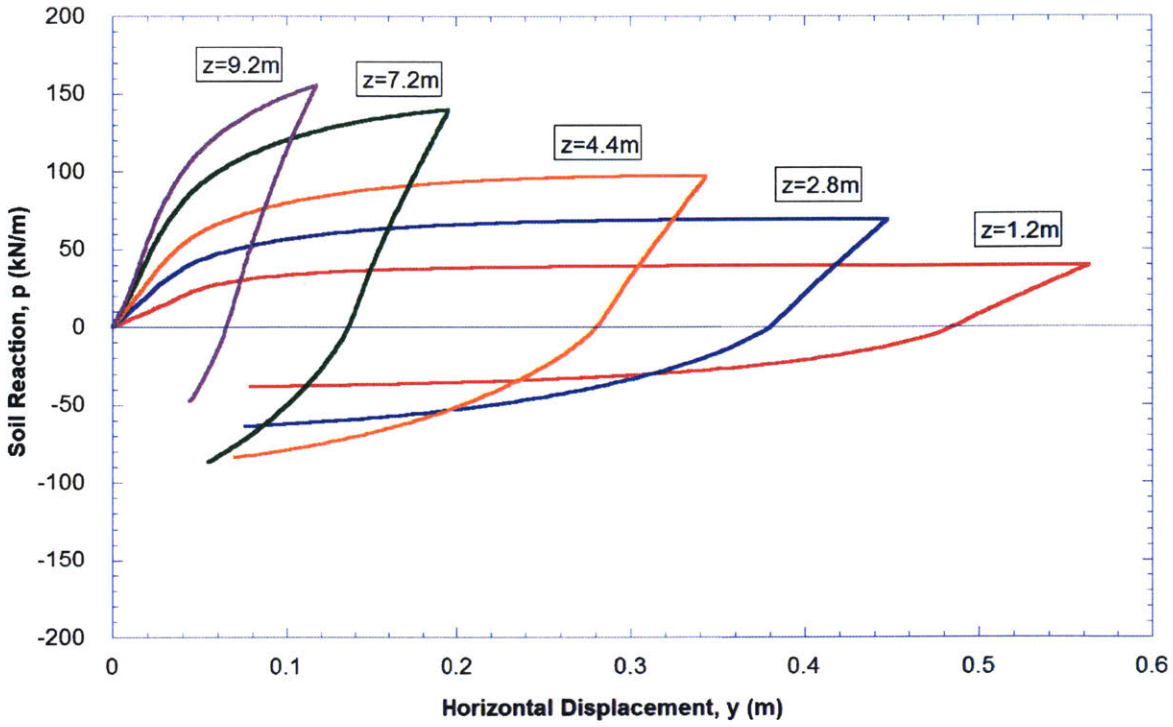

Figure 5-7: Simulation of local conductor-soil response for reversal of pushover (with maximum $\delta_h = 2.3$m) using EPP analysis

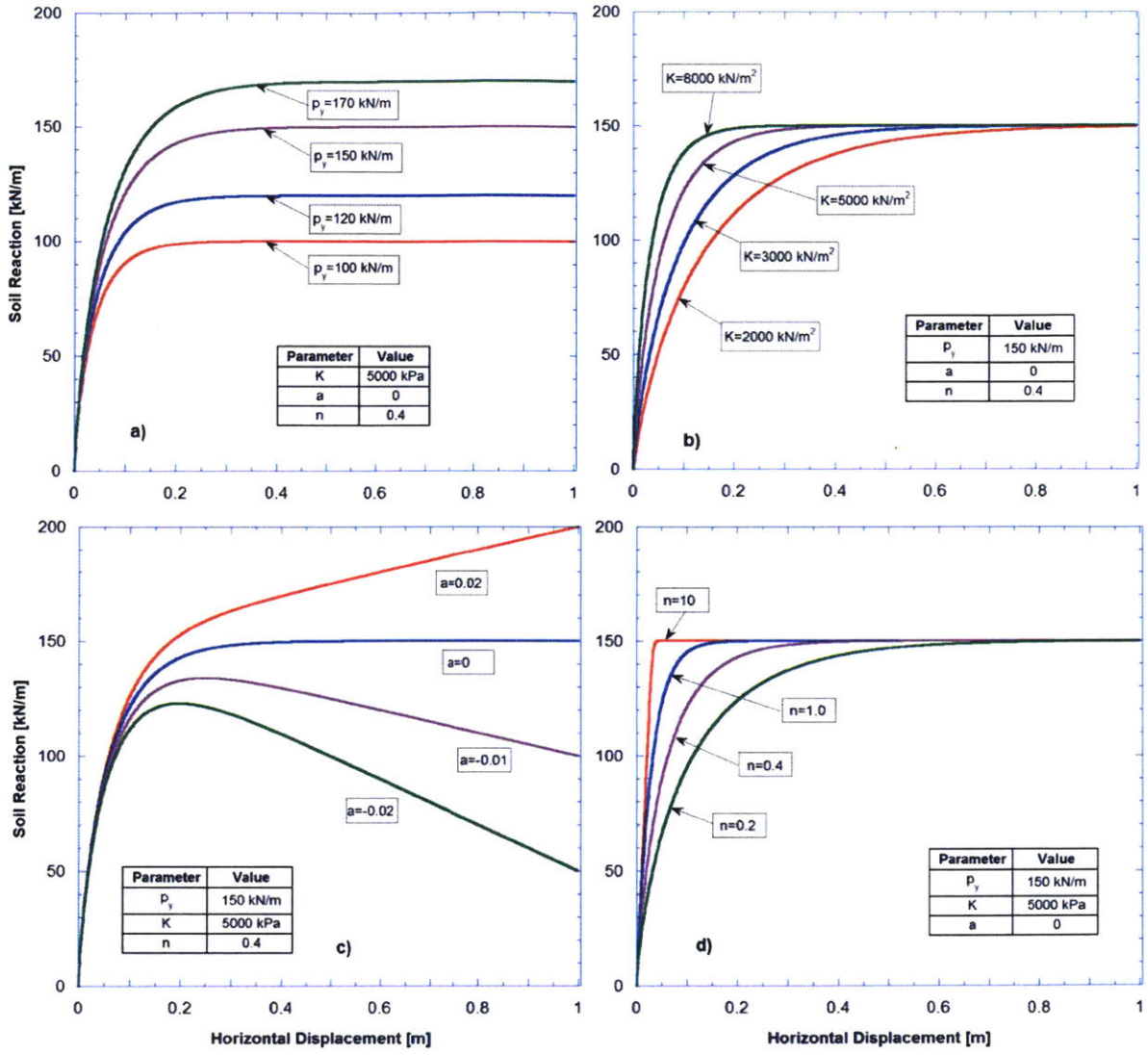

Figure 5-8: BWGG Model parameters for monotonic loading

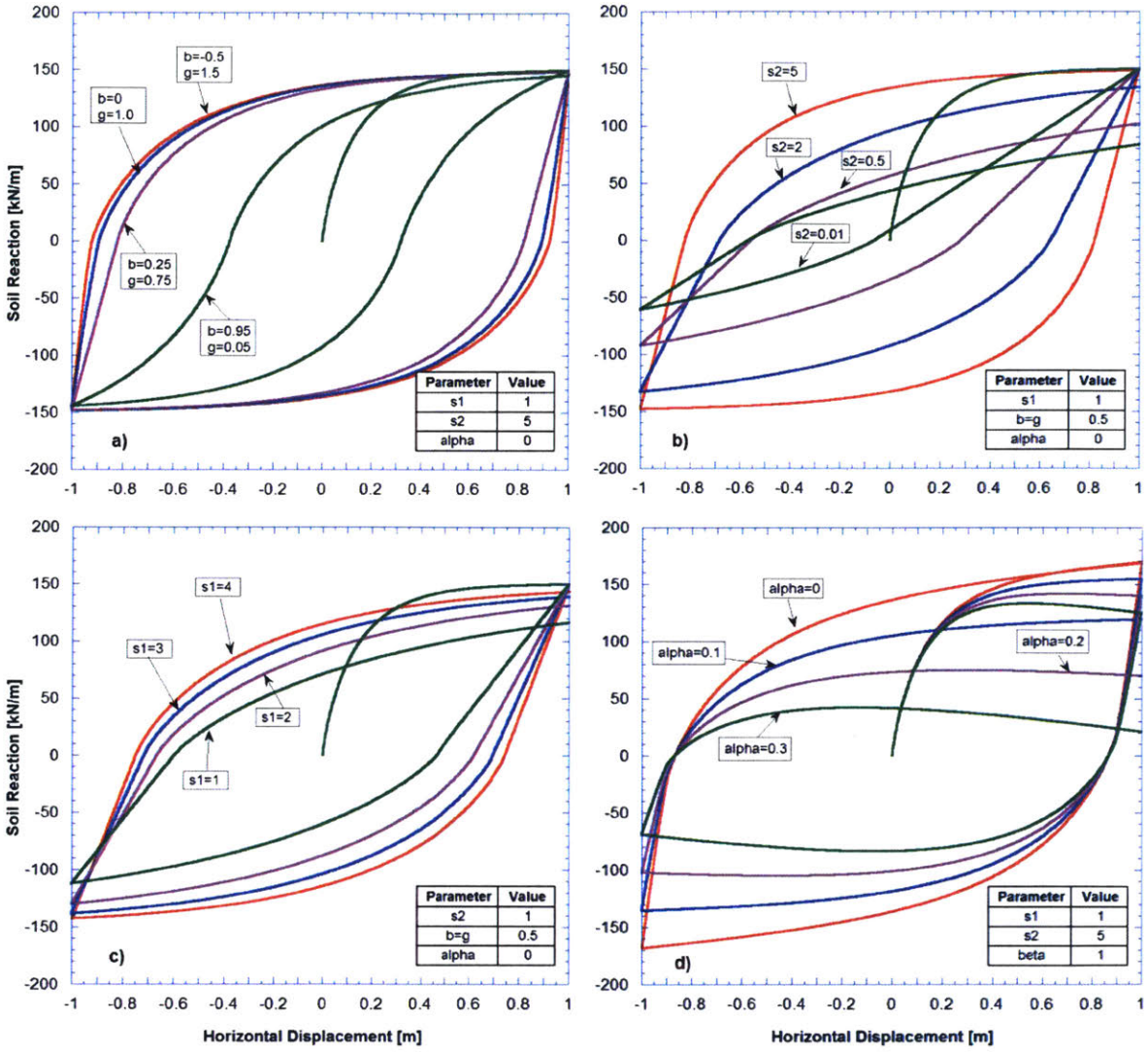

Figure 5-9: BWGG parameters for cyclic loading

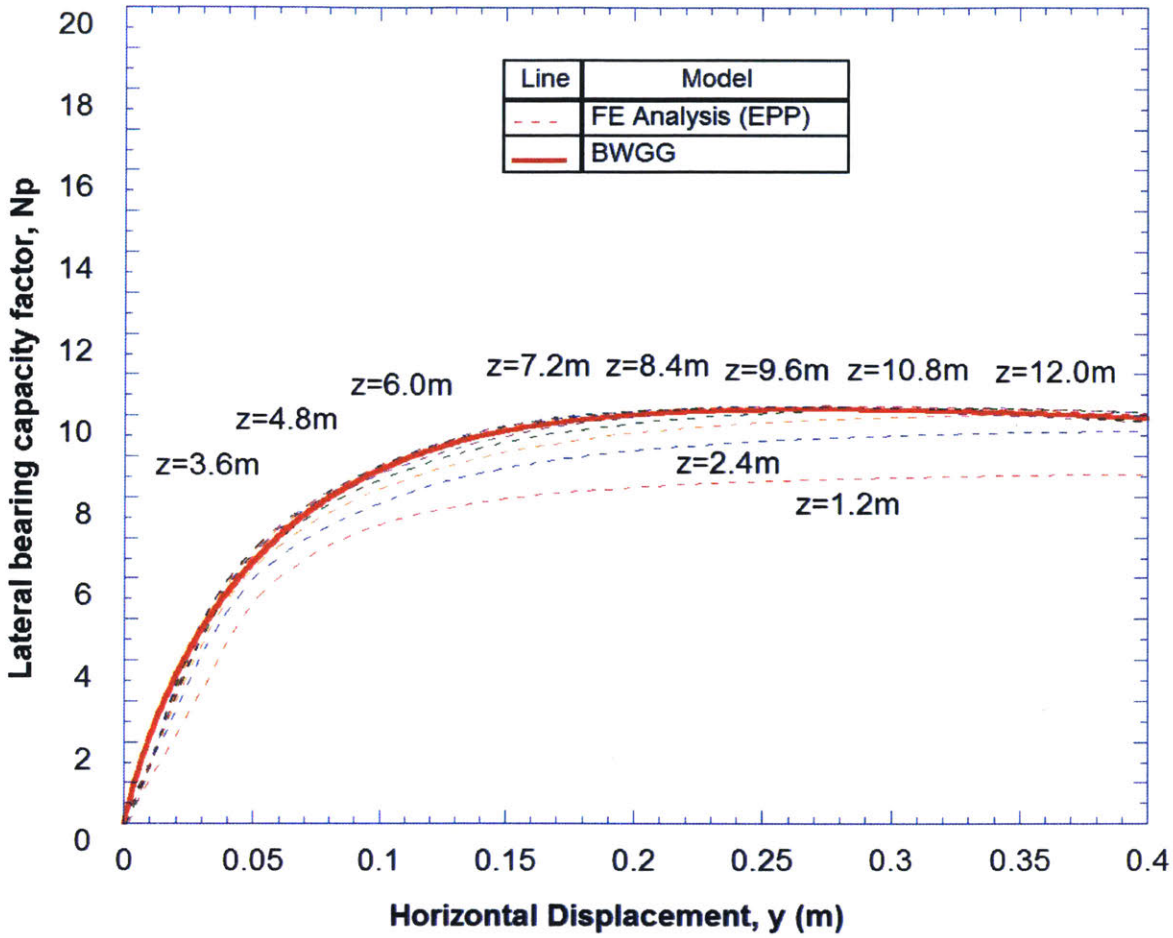

Figure 5-10: Monotonic loading – Comparison of BWGG model with 3D FE simulations using EPP model

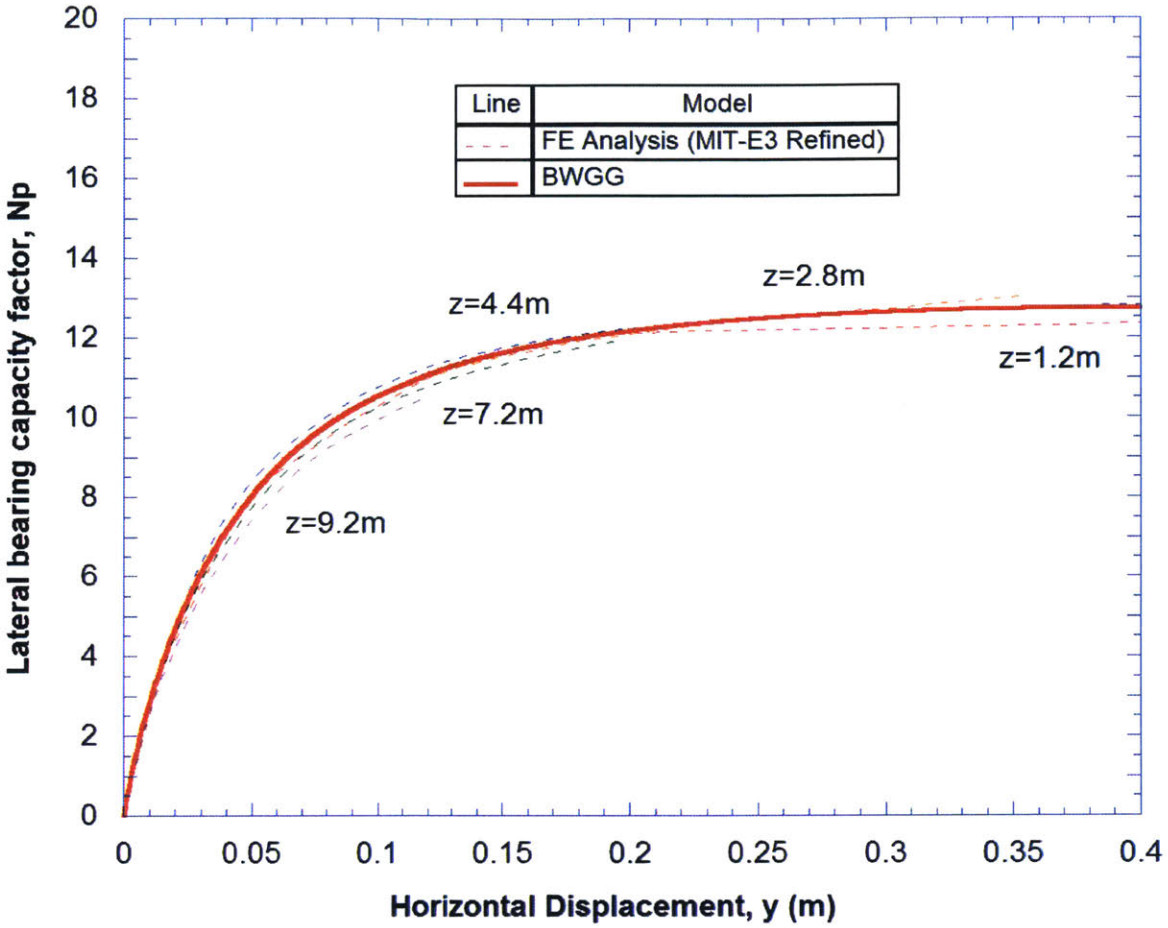

Figure 5-11: Monotonic loading – Comparison of BWGG model with 3D FE simulations using MIT-E3 model (Refined case)

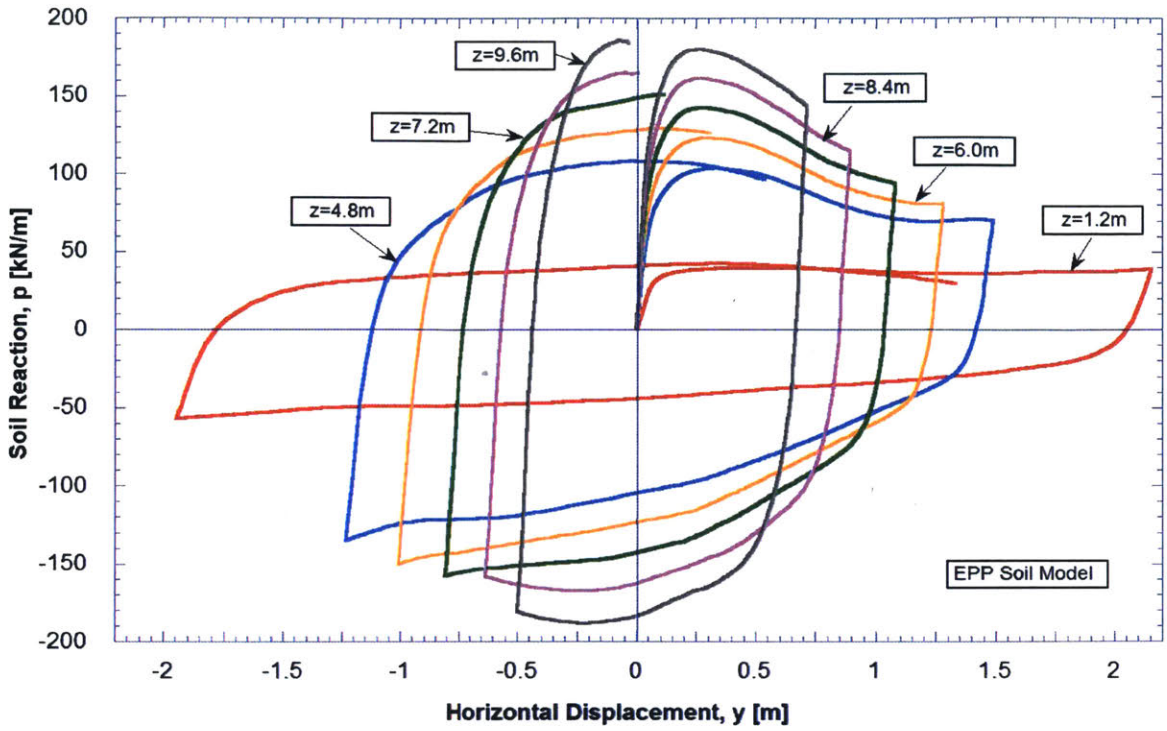

Figure 5-12: Large deformation conductor-soil interaction in cyclic loading from 3D FE analysis using EPP model

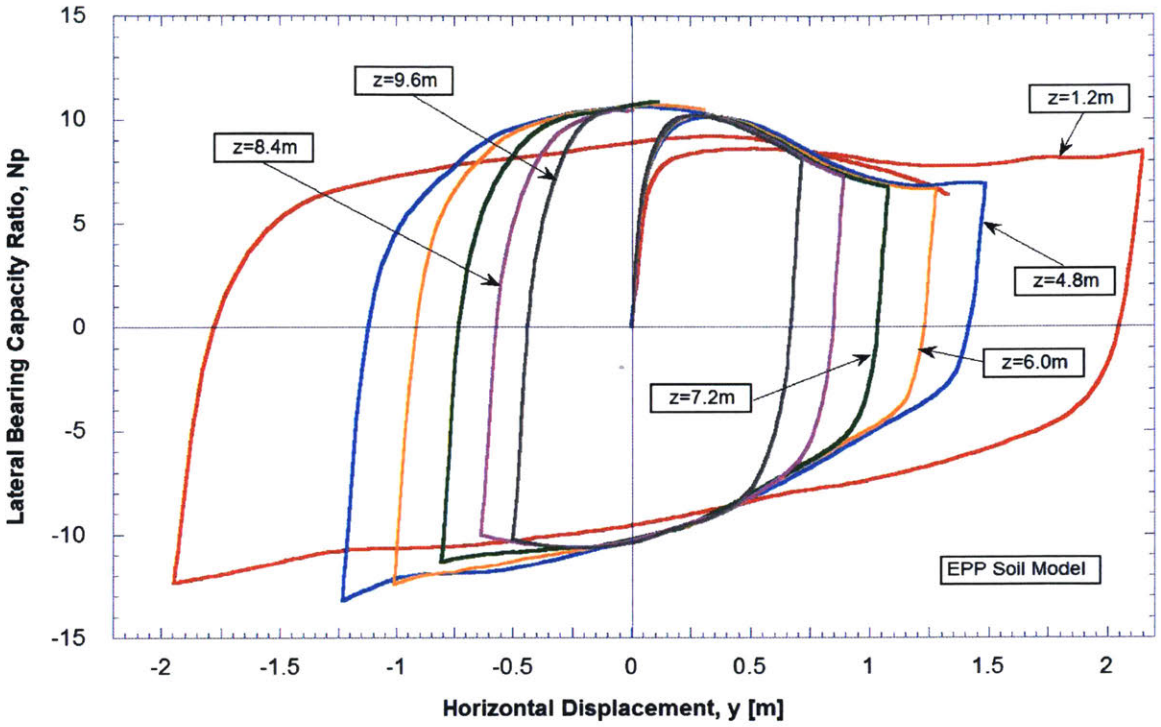

Figure 5-13: Normalized cyclic pile response functions from 3D FE analysis using EPP model with large deformations of conductor

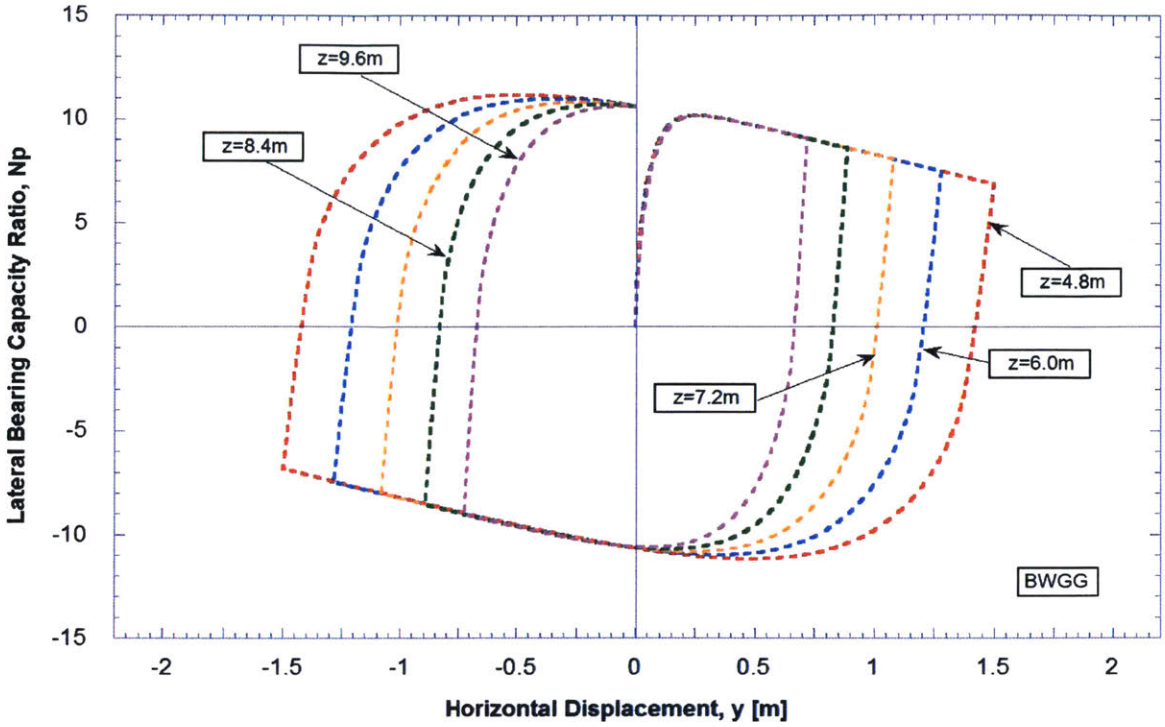

Figure 5-14: BWGG model of normalized cyclic conductor-soil interactions based on simulations using EPP soil model

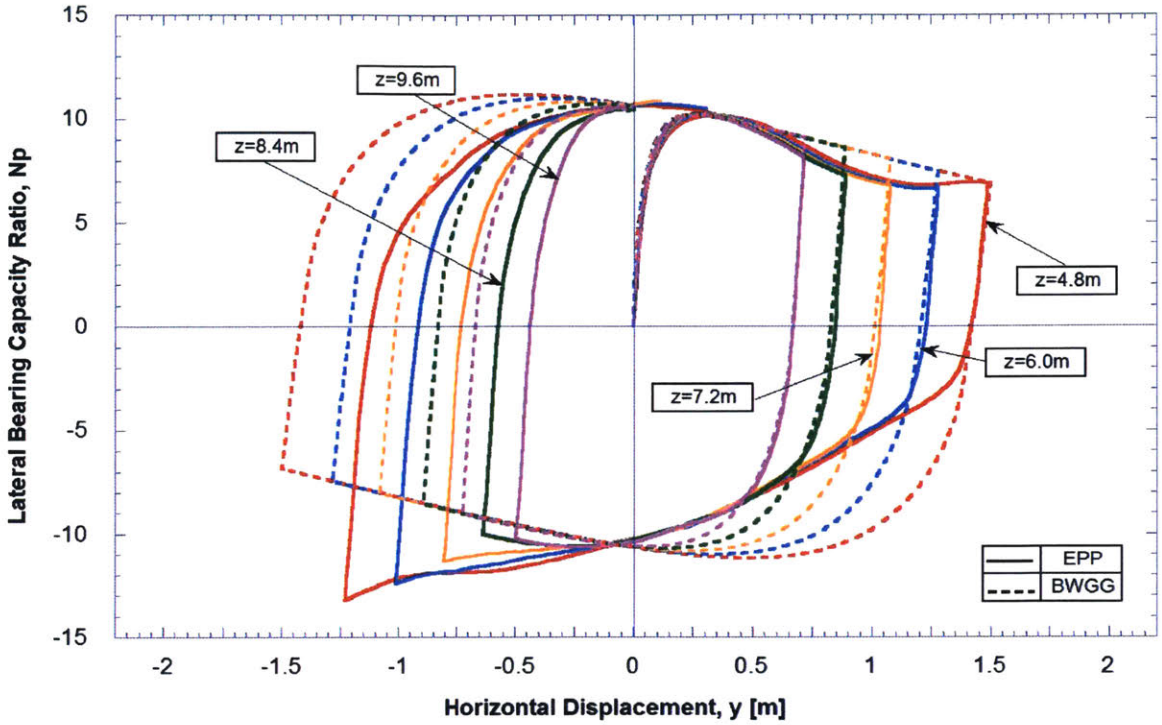

Figure 5-15: Comparison of BWGG and 3D FE models of normalized local conductor-soil interactions in cyclic loading for EPP soil model

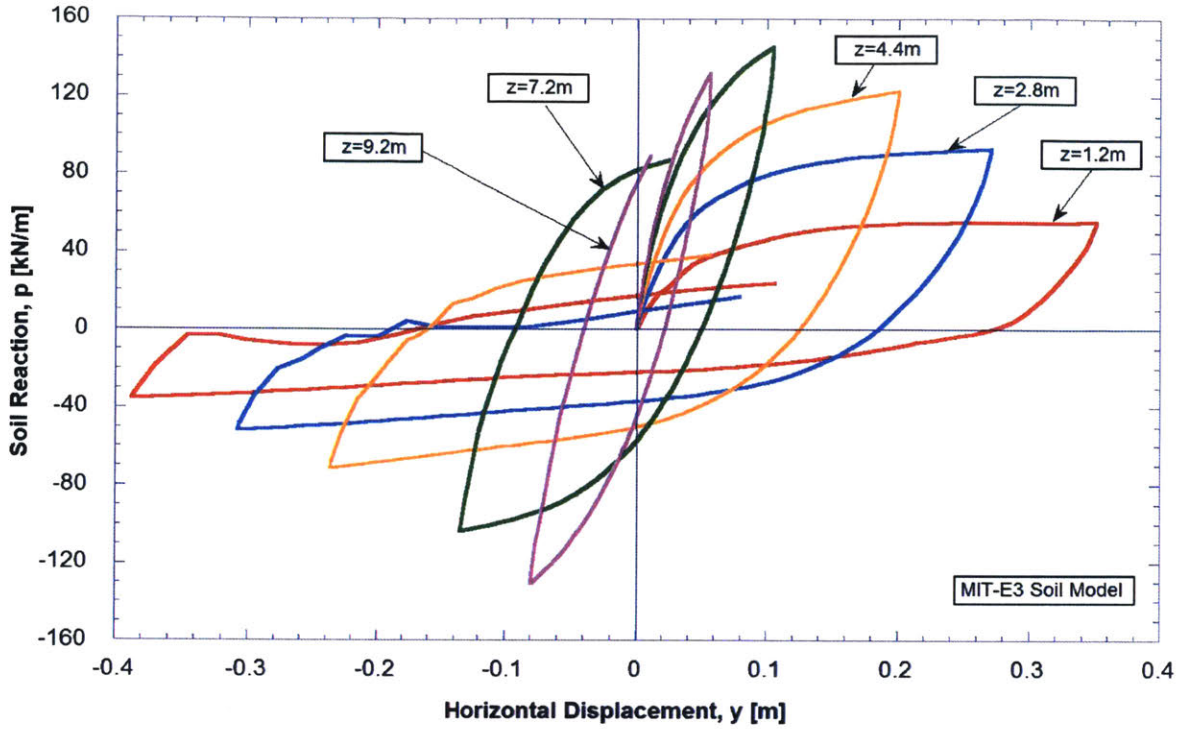

Figure 5-16: Computed local conductor-soil interactions in cyclic loading from 3D FE analysis using MIT-E3 Refined Case analysis

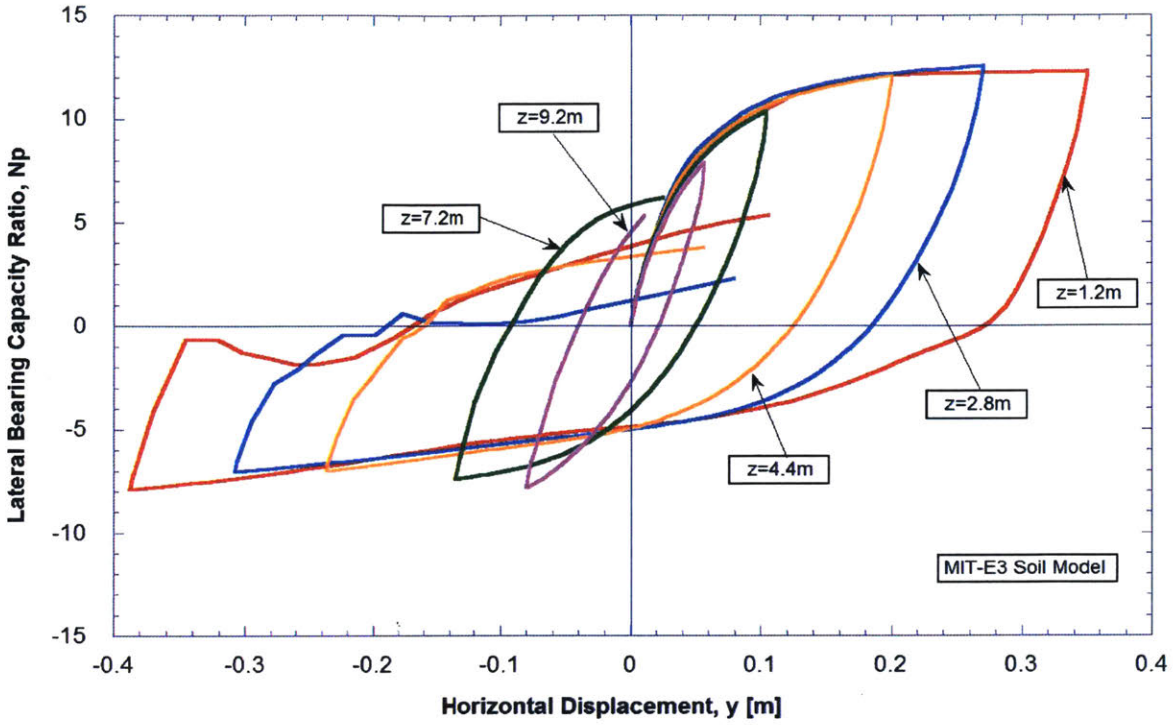

Figure 5-17: Normalized conductor-soil interactions in cyclic loading from 3D FE analysis using MIT-E3 Refined Case analysis

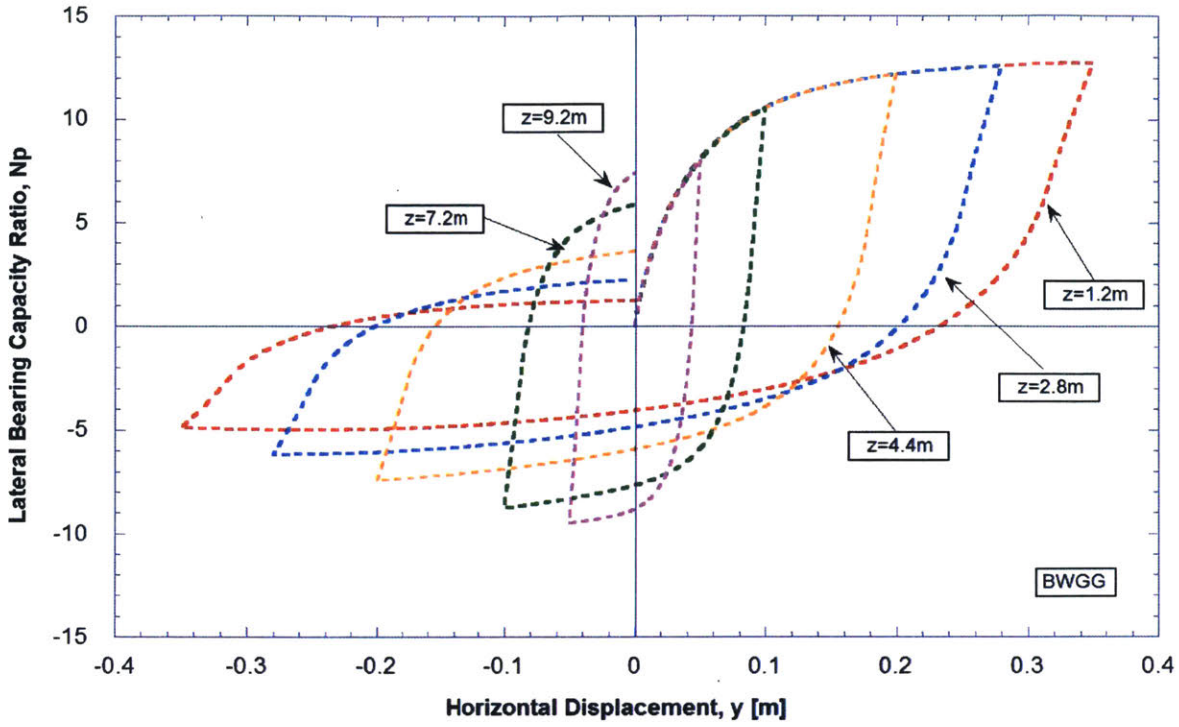

Figure 5-18: BWGG model of normalized cyclic conductor-soil interactions based on simulations using MIT-E3 Refined Case analysis

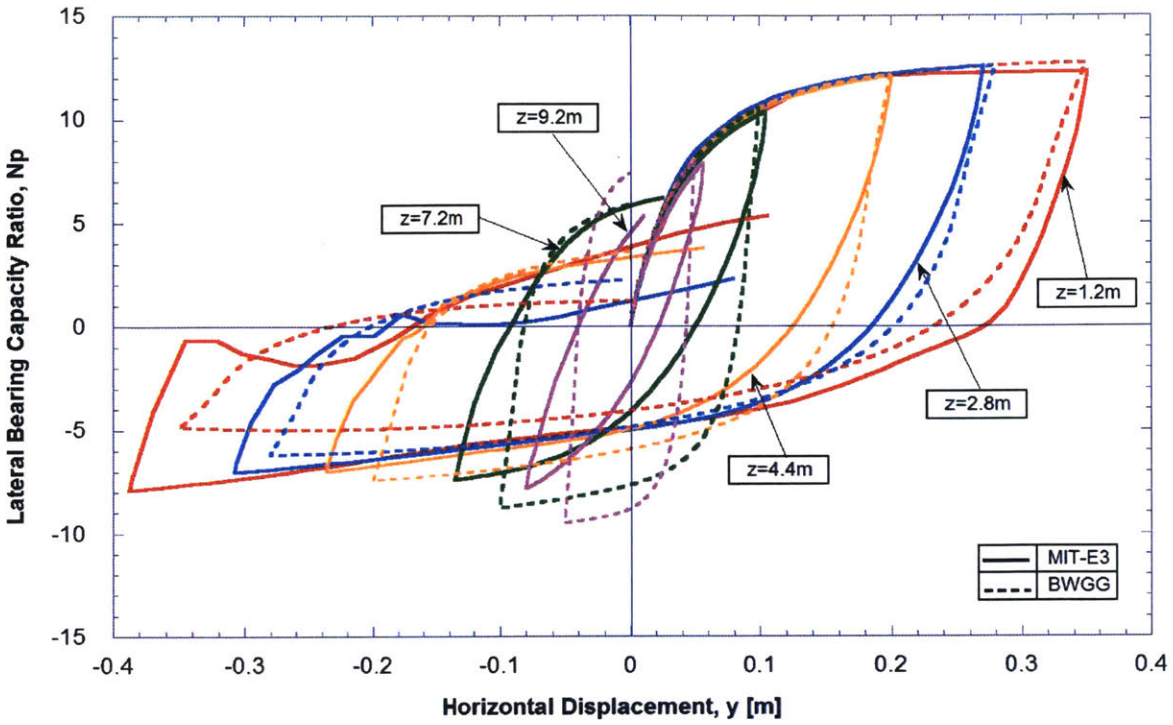

Figure 5-19: Comparison of BWGG and 3D FE models of normalized local conductor-soil interactions in cyclic loading for MIT-E3 Refined Case

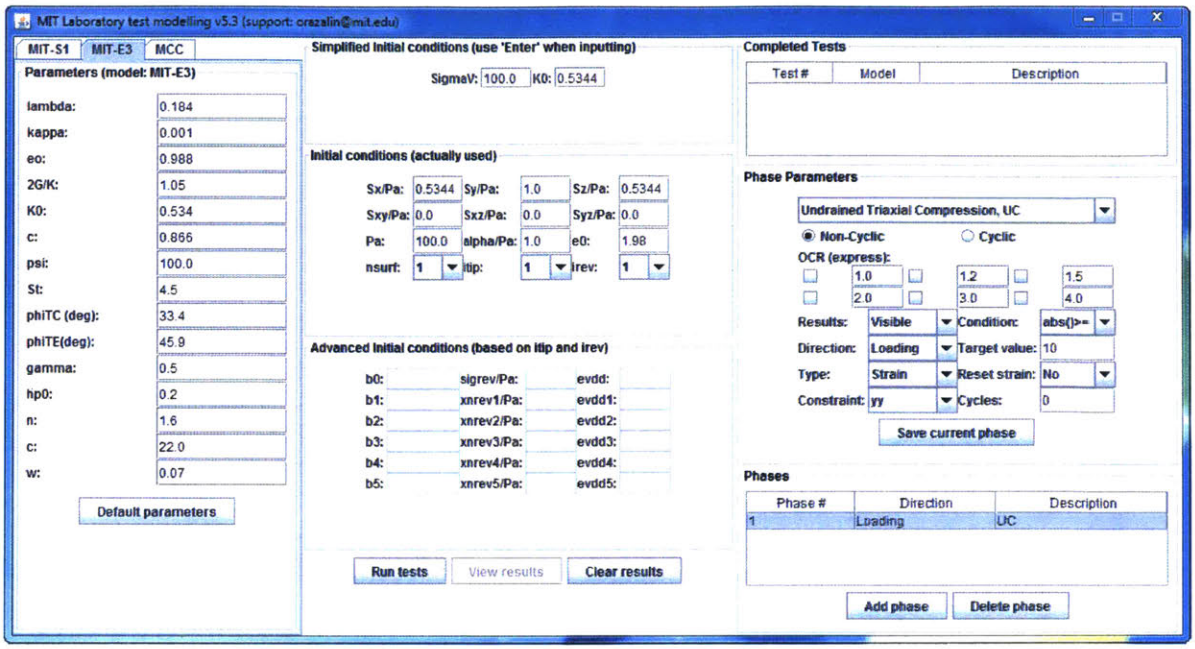

Figure 5-20: Developed calibration tool "ModelTest" - Main Interface

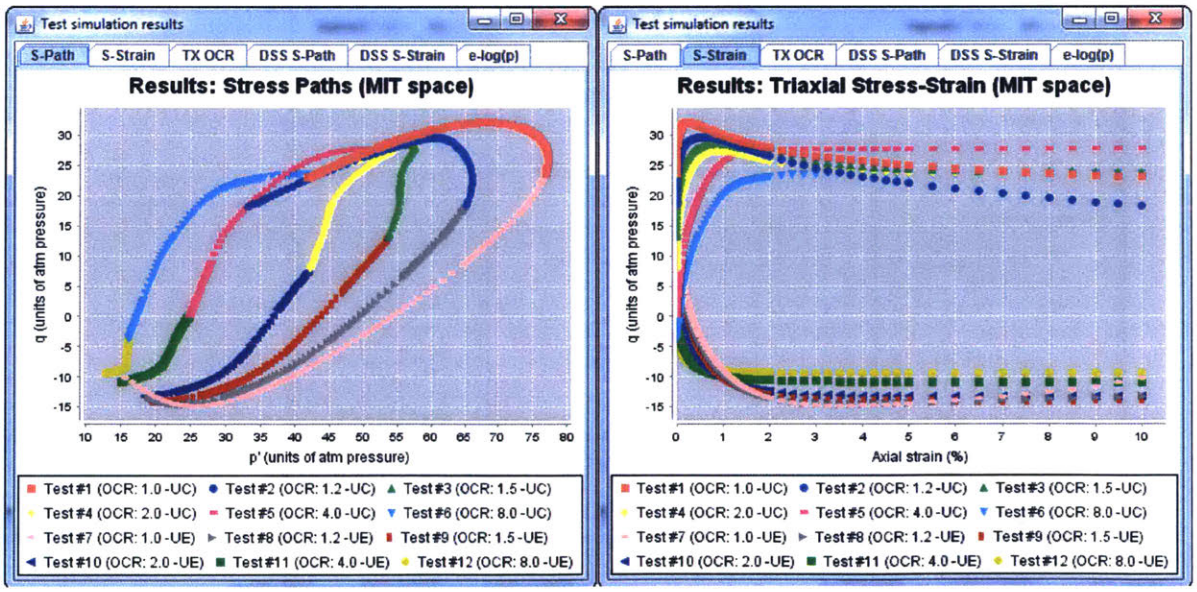

Figure 5-21: Example output of "ModelTest" program

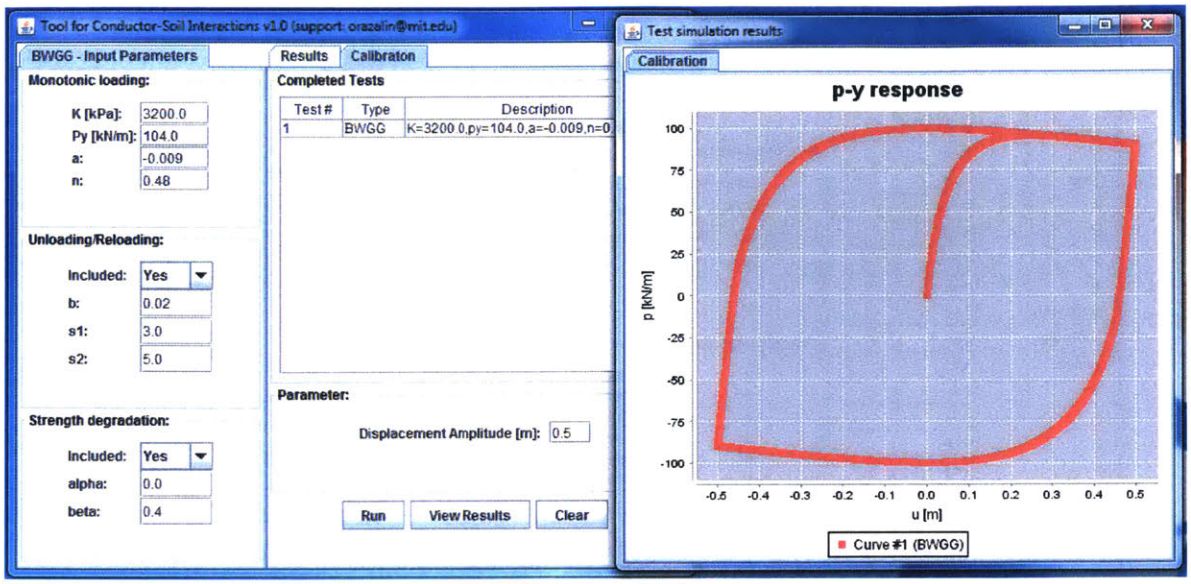

Figure 5-22: Developed tool for representing simplified conductor-soil interactions - Calibration

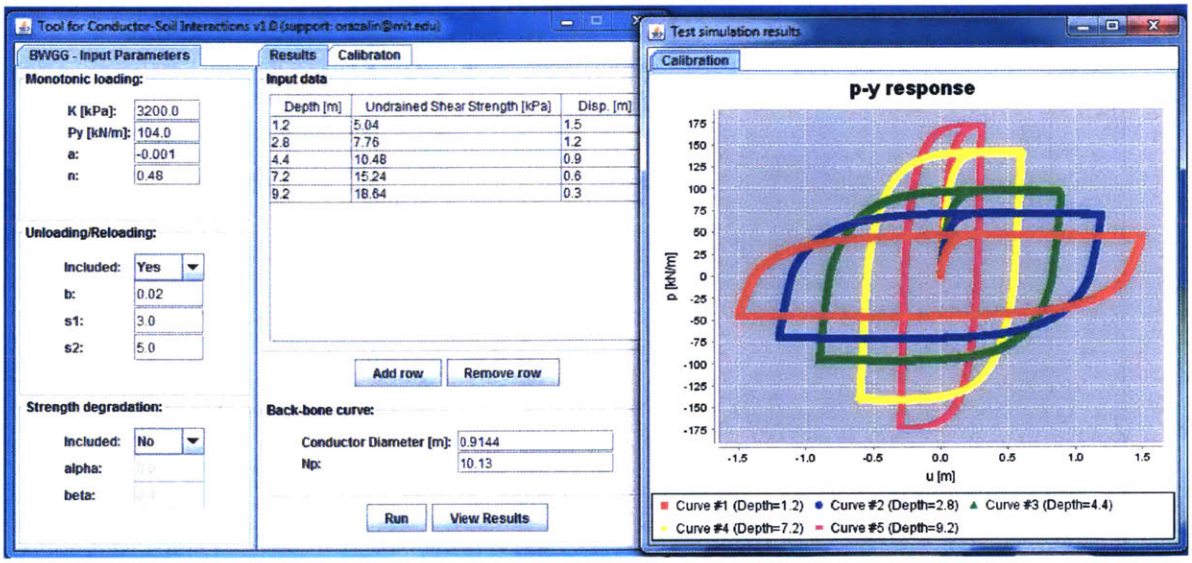

Figure 5-23: Developed tool for representing simplified conductor-soil interactions - Main Output

Chapter 6

Numerical Modeling of Cone Penetration

The chapter summarizes the details of large deformation numerical analyses based on automatic remeshing and interpolation approach (Chapter 3, Section 3.2) for the axisymmetric modeling of cone penetration in clay and presents the results from a range of effective stress soil models. The simulation results using the Modified Cam Clay (MCC; Roscoe and Burland [1968]) soil model are compared with the recently published analysis of partially drained cone penetration in reconstituted kaolin using the two-phase Material Point Method (Al-Kafaji [2013], Ceccato [2015]). The analyses using more realistic soil models that take into account complex soil behavior and penetration rate effects are also presented (MIT-E3, Whittle and Kavvadas [1994]; MIT-SR, Yuan [2016]). The deep penetration results using MCC and MIT-E3 soil models are compared with undrained steady state solutions obtained from the Strain Path Method (Baligh and Levadoux [1986], Aubeny [1992]) considering the effect of stress history. The current numerical analyses are also validated through the comparison with the results of laboratory penetration tests performed in centrifuge model tests (Schneider et al. [2007]) in kaolin and the measured piezocone field data (Aubeny [1992], Ladd [1990]) for Boston Blue Clay.

6.1 Numerical Model of Cone Penetration

As described in Chapter 2, the standard cone penetration test involves pushing a steel cone penetrometer into the soil using hydraulic jacking system at a standard rate of 2 cm/sec. This section presents the description and numerical details of the base finite element model used to simulate this entire process in soft clay.

6.1.1 Geometry and Boundary Conditions

The basic geometry of the standard piezocone cone comprises a penetrometer with the radius, R = 1.78cm, and apex angle, $\delta = 60°$. (Fig. 6-1a). Prior analyses (Baligh and Levadoux [1986]) have found that a rounded tip geometry referred to as the 'simple pile' (Fig. 6-1b) provides a close approximation of stress conditions around the piezocone in undrained steady penetration. The current analyses use a similar rounding of the conical tip shape (Fig. 6-1a) to mitigate potential numerical instabilities in the large deformations FE analyses. Soil penetration can be modeled using 2D axisymmetric finite elements and is simulated assuming a rigid penetrometer with a specified surface geometry that interacts with the soil body. The two-dimensional model parts are embedded in the X–Y plane which can be represented with the radial distance, r and the height, z in cylindrical coordinate system assuming that the revolution around the center of the cone (through the Y-axis) is specified by the polar angle, θ. Figures 6-2 and 6-3 demonstrate the base case model with two levels of mesh refinement that are specified by various biased seeding lengths (coarse and fine meshes). The seeding markers along the edges of geometry specify the target mesh density in that region. The position of the seeds is uniform along the bottom and the right edges of the base case geometry. The other edges are subdivided using biased seeding such that the mesh density increases toward one end of the edge. For example, the prescribed biased seeding range changes from 3-4 mm for the coarse mesh to 2-20 mm for the fine mesh along the top edges of the domain geometry. The seeding sizes for all edges are shown in Figures 6-2 and 6-3 for both mesh configurations. The cone penetrometer surface is modeled with a rounded surface to avoid

sharp edges (after Levadoux [1980]) and is pre-installed into the soil to the depth of about 2 cm ($y/R \approx 1$). The soil domain is a deformable media (Lagrangian Material) while the penetrometer is modeled as a rigid body (rigid shell). The soil mesh extends 0.5 m (y/R=28) both vertically and in the radial direction to minimize effects of far-field boundary conditions. The horizontal displacements are constrained at the lateral edges of the soil domain, while the bottom of the soil mesh is fully fixed. The hydraulic boundary conditions comprise impermeable hydraulic boundaries at the surface of the penetrometer, at the axis of symmetry and at the top surface, as well as fully permeable boundaries at the far lateral and at the base boundaries of the domain. The model assumes a uniform initial vertical effective stress, $\sigma'_{v0} = 100kPa$, and K_0 stress state conditions are initially prescribed, $\sigma'_{h0} = \sigma'_{v0}K_0$ based on the selected value of K_0. Since the penetrometer is pre-installed, an equilibration step with the fixed penetrometer is introduced to ensure that the initial stresses are in equilibrium. The initial excess pore pressures are assumed to be zero while the soil is assumed to be fully saturated. The penetrometer is only allowed to move vertically, and the prescribed displacement is applied at the reference point within the rigid body of the cone. The analyses simulate coupled pore fluid diffusion and deformations with a constant value of hydraulic conductivity. Hence, partial drainage can be induced by adjusting the penetration rate. For example, at a standard penetration rate, $v = 2cm/s$, and reference value of hydraulic conductivity, $k = 10^{-7}cm/s$, could approximate undrained shearing in the soil mass with large excess pore pressures around the cone. At lower penetration rates, partial drainage occurs reducing the magnitude of the excess pore pressures.

6.1.2 Contact Formulation

Abaqus™ provides multiple ways (formulations and methodologies) for defining contact interactions. The selection of the contact formulation is very important in modeling the cone penetration, so a suite of preliminary studies was conducted to define the base case model. Finite sliding and small sliding are two tracking approaches that are suitable to account for relative motion of two bodies along the surfaces in

mechanical contact. The finite sliding approach was found to be more effective for cone penetration simulation because the cone penetration process involves a relatively large sliding of one surface along the other. Based on the numerical experiments, the finite sliding was chosen as the base case contact tracking approach with the contact discretization method based on a node-to-surface formulation (Figure 6-4). The cone penetrometer was selected as the master-surface and the soil surface as the slave-surface. Smooth (i.e., frictionless) contact properties were assumed for the base case numerical model.

The finite-sliding, node-to-surface contact formulation requires that master surfaces have continuous surface normals at all points in order to avoid numerical contact convergence problems. The surface normals of element-based master surfaces used in finite-sliding node-to-surface contact simulations are automatically smoothed in Abaqus™ Standard. The degree of smoothing of the master surface in node-to-surface contact simulations can be controlled by specifying a fraction f.

For the axisymmetric deformable master surfaces:

$$f = \frac{a_1}{l_1} = \frac{a_2}{l_2} \tag{6.1}$$

where l_1 and l_2 are the lengths of the element facets that join at the surface node and $f < 0.5$. (see Figure 6-5). Abaqus™ Standard constructs either a parabolic or a cubic segment between two points at distances a_1 and a_2 from the node at which the discontinuity exists. As a result, this smoothed segment will be used in the contact calculations which will differ from the usually faceted element geometry. The default value of f is 0.2. However, it was found that for the current cone geometry the contact could not be easily established in the subsequent remeshing steps using the default values. For the automatic remeshing and interpolation approach used in the current analyses, we are using $f = 0.01$.

The adopted penetration analysis procedure is based on automatic remeshing and interpolation approach which comprise the conventional Lagrangian Finite Element Method with separate remeshing and solution mapping using the interpolation of all

the solution variables from the old mesh into the new mesh. As a result, the entire analysis consists of a series of conventional Largangian Finite Element analysis steps, followed by a complete remeshing of the domain and the interpolation of the solution variables (stresses, pore pressures, state variables, etc.) from the previous mesh. One of the requirement for remeshing a contact problem is that in a region of contact, the new mesh must conform closely to the shape of the surface from the old analysis (SIMULIA [2016]). This requirement is important because cone penetration problem involves a contact between the penetrometer and the soil. The contact algorithms may fail to converge if the surfaces defined by the new mesh are different from the surfaces in the old analysis. In the current analysis, the position of the contact surfaces is automatically configured by the developed Python scripts to remove any possible over-closures after remeshing, but Abaqus™ Standard solver can also adjust the position of the slave surface of a contact pair by specifying a small "adjustment zone" around the master surface to achieve zero gap between the penetrometer and soil surfaces before the contact establishment. The nodes on the slave surface of the initial model geometry that are within the "adjustment zone" are moved precisely onto the master surface without invoking any strain. The adjustment zone extends to a specified distance from the master surface. This distance is measured along the master surface normal that passes through the nodes of the slave surface. Figures 6-6 illustrates an example of adjusting the surfaces of contact pairs. This feature can be used within the proposed methodology for the analysis of soil-structure interaction problems involving complex contact geometry.

6.1.3 Mesh Sensitivity and Element Selection

Mesh sensitivity studies have been conducted to select an optimal mesh configuration and to determine the effect of mesh coarseness on the simulated cone resistance. The proposed automatic remeshing and interpolation approach requires a relatively fine mesh near the tip of the cone due to the high gradients of the solution variables (stresses, strains, pore pressures and constitutive model state variables). Therefore, most meshes used in the initial mesh sensitivity studies are similar to each other

(with high density around the surface of the penetrometer). Figures 6-2 and 6-3 illustrate "coarse" and "fine" mesh configurations, respectively. These two models with various mesh densities have been used to obtain the cone reaction vs. penetration displacement using the same input parameters.

In addition, we have compared two types of axisymmetric finite elements: CAX4P - 4-node bilinear displacement and pore pressure with full element stress integration, and CAX8RP - 8-node biquadratic displacement and bilinear pore pressure with reduced element stress integration.

Figure 6-7 shows the comparison between coarse and fine meshes using full integration bilinear and reduced integration biquadratic finite elements. Figure 6-7 compares the computed tip resistance as a function of the displacement for course and fine meshes and the two types of finite elements. The results show almost identical results. However, since the reduced-integration elements have only one integration (Gauss) point, these elements may potentially be subject to mesh instability issue, commonly referred to as "hourglassing" (Belytschko et al. [2013]). This instability may occur when the reduced-integration elements distort in a way that produces zero strains at the Gauss point which may lead to uncontrolled mesh distortion. In order to avoid these potential issues with mesh instability, the subsequent analyses use "fine" mesh with the full integration bilinear elements.

6.2 Simulation Results of Cone Penetration

The axisymmetric finite element model described in the previous section is considered as the Base Case. This section presents the simulation results obtained for a Base Case numerical model of cone penetration problem using the proposed automatic remeshing and interpolation method implemented for various effective stress constitutive soil models. The effect of different penetration rates modeled with two soil models and the effect of various stress history for an advanced soil model are also presented.

6.2.1 MCC Analysis

The analysis uses the Modified Cam Clay effective stress constitutive soil model with von Mises generalization of the yield function and critical state failure criterion implemented as a user-material (UMAT) in Abaqus™ (Hashash [1992]). The MCC input parameters correspond to a set of model input properties calibrated to the elemental behavior of Boston Blue Clay (Table 6.1). The initial K_0 conditions correspond to normally consolidated conditions with a uniform vertical effective stress specified as $\sigma'_{v0} = 100kPa$. The hydraulic conductivity is assumed to be constant ($k = 10^{-9}$ m/s). Figure 6-8 summarizes results from a series of simulations at penetration rates ranging from v=0.0002 cm/sec to 200 cm/sec. Each analysis involves at least 50 remeshing steps in order to achieve a total penetration of $y/R = 5$ (i.e. prescribed displacement for each remeshing step is $\Delta y/R = 0.11$). Each of the analyses show that the penetration tip resistance is converging towards a limiting steady state condition. The simulations for $v \geqslant 0.02cm/s$ showed unique results corresponding to undrained conditions. The slowest rates, $v < 0.0002cm/sec$, showed minimal excess pore pressures around the penetrometer and correspond to fully drained penetration. Figure 6-9 illustrates the steady state net tip resistance for various penetration rates as a function of the penetration rate (log scale). The results show that the normalized net tip resistance increases from $q_{s,net}/\sigma'_{v0} = 2.45$ in undrained conditions to $q_{s,net}/\sigma'_{v0} = 5.47$ in drained penetration. The transition between these two limits, which reflects partial drainage conditions, occurs for penetration rates, $v = 0.01cm/s$ and $v = 10^{-5}cm/s$. Figure 6-10 shows the contours of the excess pore pressures around the penetrometer for the base case model ($v = 2.0cm/s$). The maximum excess pore pressure $\Delta u/\sigma'_{v0} \approx 3$ occurs at the tip of the cone. Figure 6-11 presents the evolution of excess pore pressures at a fixed point 5 cm below the surface for three penetration rates $v = 4 \cdot 10^{-6}cm/s$, $v = 0.0002 - 0.002cm/s$, $v = 2cm/s$ (corresponding to drained, partially drained, and undrained). This plot is obtained automatically from each of the 50 remeshing analyses using a developed Python script listed in Appendix B. Figure 6-12 shows the excess pore pressure profiles at the penetration depth

of 6R (11 cm) in the radial and vertical directions around the cone tip. The zone of excess pores pressures extends to $r/R = 9$ laterally around the cone and to $\Delta y/R = 7$ ahead of the cone tip (small negative pore pressures extend below this zone to the base of the model). The deformed mesh is presented in Figure 6-13(deep penetration is achieved without excessive mesh distortion).

Figures 6-14 - 6-17 summarize the steady state distributions of four diagnostic stress parameters; normalized radial stress ($\frac{\sigma'_{rr}}{\sigma'_{v0}}$), normalized mean stress ($\frac{\sigma'_{mean}}{\sigma'_{v0}}$), normalized cylindrical expansion shear stress ($\frac{\sigma'_{rr}-\sigma'_{\theta\theta}}{2\sigma'_{v0}}$) , normalized shear stress ($\frac{q}{\sigma'_{v0}}$)[1]. The sign convention of Abaqus™ assumes that compressive stresses are negative, whereas tensile stresses are positive. Predictions of radial effective stresses $\sigma'_{rr}/\sigma'_{v0}$ shown in Figure 6-14 indicate the large gradients of $\sigma'_{rr}/\sigma'_{v0}$ next the base of the cone and in the immediate vicinity of the cone tip ($\sigma'_{rr}/\sigma'_{v0} = 0.22$ at the tip). The radial effective stresses reach a maximum value, $\sigma'_{rr}/\sigma'_{v0} = 0.9$ immediately adjacent to the base of the cone, and are constant along the cone shaft. Figure 6-15 presents changes in the mean effective stress, ($\sigma'_{mean}/\sigma'_{v0}$), which are controlled by the magnitude of the octahedral shear strain due to the isotropic yield behavior of the MCC model (Aubeny [1992]) and map to the zone of plasticity. The magnitude of the mean effective stress is $\sigma'_{mean}/\sigma'_{v0} = 0.693$ at K_0 conditions and $\sigma'_{mean}/\sigma'_{v0} = 0.425$ at critical state conditions. The cavity shear stress $(\sigma'_{rr} - \sigma'_{\theta\theta})/2\sigma'_{v0}$ (i.e., q_h, the maximum shear stress acting in a horizontal plane) presented in Figure 6-16 reaches a maximum value ($(\sigma'_{rr} - \sigma'_{\theta\theta})/2\sigma'_{v0} = 0.364$) close to the base of the cone and decreases at the locations above and below the cone base. Figure 6-17 shows the contours of shear stresses (q/σ'_{v0}) indicating the undrained shear strength mobilized during the cone penetration with the maximum value ($q/\sigma'_{v0} = 0.565$) around the base of the cone and below the cone tip. Figure 6-18 shows the effect of stress history (OCR values from 1.0 to 4.0) on the predictions of net tip resistance vs. penetration depth.

[1] q is equal to $\sqrt{S_1^2 + S_2^2 + S_3^2 + S_4^2 + S_5^2}$, where $S_1 ... S_5$ are the components of stress in the transformed variables.

6.2.2 MIT-SR Prediction

The MIT-SR input parameters are based on the calibration to the Resedimented Boston Blue Clay provided by Yuan [2016]. Figure 6-19 shows the results of simulation in undrained conditions for relatively fast penetration rates (0.02 cm/sec to 200 cm/sec) using the constant value of hydraulic conductivity $k = 10^{-9}$ m/s. Each analysis consists of 80 discrete remeshing and interpolation steps. The effect of interpolation after remeshing can be seen in the normalized tip resistance vs. penetration displacement plots, but due to a very fine mesh and good accuracy control, the error associated with re-equilibration of the out-of-balance forces is minimal. The computed results at each penetration rate show that the tip resistance continues to increase with penetration depth and does reach a true steady state condition within the range of penetration simulated in the FE model (proximity to the basal boundary prevent further extensions in this FE model). For current interpretation purposes we treat the final resistance (at $y/R = 6.8$) as a lower bound estimate of the true steady state condition. Figure 6-20 provides a comparison with the Base Case MCC results and MIT-SR results for the same fast penetration rates. Unlike MCC soil model in which there are no changes in the cone resistance in undrained conditions (i.e., MCC is a rate independent elasto-plastic model), the MIT-SR model showed the rate-dependency in the cone resistance. Figure 6-21 presents the contours of excess pore pressures after the penetration to the depth of 6R (11 cm). The evolution of excess pore pressures at a fixed point 4.5 cm below the surface for three fast penetration rates is shown in Figure 6-23 shows the excess pore pressure profiles at the penetration depth of 6R (11 cm) in radial and vertical directions around the cone tip. The extent of excess pore pressures at the cone base in the radial direction is $r/R = 10$ with maximum $\frac{\Delta u}{\sigma'_{v0}} = 1.5$ and in the vertical direction is $z/R = 6$ with maximum $\frac{\Delta u}{\sigma'_{v0}} \approx 2$. The maximum values of excess pore pressures at the cone base and the tip are lower compared to the analysis with the MCC soil model. The deformed mesh configuration is presented in Figure 6-24 showing that deep penetration is achieved without excessive mesh distortion. The normalized effective radial stress

$(\sigma'_{rr}/\sigma'_{v0})$ contours at the penetration level $y/R = 6$ is shown in Figure 6-25. Figure 6-26 shows the normalized mean stress contours $(\sigma'_{mean}/\sigma'_{v0})$. The magnitude of the mean effective stress is $\sigma'_{mean}/\sigma'_{v0} = 0.736$ at K_0 conditions and $\sigma'_{mean}/\sigma'_{v0} = 0.164$ at critical state. Figures 6-27 and 6-28 show the normalized cylindrical expansion shear stress contours $((\sigma'_{rr} - \sigma'_{\theta\theta})/2\sigma'_{v0})$ and normalized shear stress (q/σ'_{v0}) contours. The contours of q/σ'_{v0} indicate the undrained shear strength mobilized during the cone penetration with the maximum value $(q/\sigma'_{v0} = 0.641)$ below the cone tip. The predictions from the MIT-SR soil model are more complex than results from the MCC model reflecting anisotropic and strain rate-dependent behavior features of the MIT-SR model. The effect of stress history (OCR values from 1.0 to 2.5) on the predictions of net tip resistance vs. penetration depth is summarized in Figure 6-29. At a given OCR, the MIT-SR soil model predicts much lower values of net tip resistance compared to the MCC soil model.

6.2.3 MIT-E3 Prediction

The MIT-E3 soil model is calibrated to Boston Blue Clay elemental behavior. The soil penetration analysis conducted with the constant hydraulic conductivity $(k = 10^{-9}$ m/s) and the standard penetration rate of 2cm/s, but with various values of overconsolidation ratio (OCR=1.0, 1.5, 2.0, and 2.5). Each numerical simulation comprises 99 remeshing and interpolation steps with a fixed displacement of 0.15 cm per remeshing step. The penetration depth reached 14.85 cm or 8.25R. Figure 6-30 shows the effect of stress history (various OCR) on the cone resistance. At a given OCR, the MIT-E3 soil model predicts lower values of net tip resistance compared to the MCC soil model, but the predictions are similar to prior results obtained from the MIT-SR soil model. Figure 6-31 presents the contours of the excess pore pressures generated around the cone tip during the penetration process. Figure 6-32 shows the evolution of the excess pore pressures throughout the analyses at a fixed point located 4.5 cm below the top surface for various levels of OCR (1.0 to 2.5). The excess pore pressure profiles at the penetration depth of 6R (11 cm) in radial and vertical directions around the cone tip are presented in Figure 6-33 for the standard

penetration rate of 2 cm/s. The MIT-E3 model predicts larger zone of disturbance (excess pore pressure) around the penetrometer compared to the MCC and MIT-SR soil models. Figure 6-34 shows the deformed mesh configuration for the penetration depth of 8.25R indicating no excessive mesh distortion.

6.3 Comparison with Published Results

This section presents the comparison of cone penetration simulation results obtained using the developed approach with previously published numerical analyses and measured data for various penetration rates, drainage conditions, and stress history. A brief description of models and comparison methods are presented. The results of replicate analyses are compared with the Material Point Method (Al-Kafaji [2013], Ceccato et al. [2016]) and approximate Strain Path Method (Aubeny [1992]).

6.3.1 Material Point Method and Experimental Data

Figure 6-35 shows a set of simulation results for piezocone penetration in K_0-normally consolidated Kaolin using the MCC soil model (input parameters and initial conditions are summarized in Table 6.1) using the Material Point Method with smooth cone-soil interface (Ceccato [2015]) and the current FEM replicate simulations for various drainage conditions. In these analyses, the penetration rate is kept constant at $v = 2cm/s$, while the partial dissipation is induced by assuming the different values of hydraulic conductivity, k. Ceccato [2015] introduces a normalized penetration velocity $V = vD/c_v$ (after Finnie and Randolph [1994]) to characterize partial drainage around the penetrometer. The definition of V provides a convenient, but non-unique way of representing the non-linear consolidation process (for an elasto-plastic soil model such as MCC). The results supposedly correspond to undrained ($V = 501$), partially drained ($V = 1.2$ and $V = 12$) and drained conditions ($V = 0.01$). As reported by Ceccato et al. [2016], the numerical noise from MPM has been filtered out by running average smoothing with a bandwidth of 0.03 normalized cone displacement. The initial vertical and horizontal effective stresses are

$\sigma'_{v0} = 50kPa$ and $\sigma'_{h0} = 34kPa$. The full description of the model is given in Ceccato et al. [2016]. Based on this description and available data, a replicate FE model was developed using the proposed large deformation procedures. The MCC soil model was calibrated to the same input parameters as in the published MPM analysis. The results for undrained conditions are almost identical between the replicate analysis and the published MPM analysis. However, there is a difference in drained conditions - the replicate analysis overestimates the drained cone resistance by about 15%. Figure 6-36 presents the evolution of the excess pore pressures throughout the replicate analyses at a fixed point located 5 cm below the top surface. It shows the dissipation of the excess pore pressures for various drainage conditions that reach a steady state after deep penetration. Figure 6-37 shows the excess pore pressure profiles at the penetration depth of 6R (11 cm) in radial and vertical directions around the cone tip. The MPM simulation results for various normalized penetration rates are compared with the measured data for a smooth cone penetration in a centrifuge test[2] conducted by Schneider et al. [2007] and the results of the current replicate analysis using the proposed large deformation analysis procedure. Figure 6-38 presents the comparison of normalized excess pore pressures measured next to the cone tip for various penetration rates between MPM and Replicate analysis, as well as the comparison of normalized net cone resistance for various normalized penetration rate between the numerical analyses and the measured data. The replicate analysis shows a very good agreement with the MPM analysis in normalized excess pore pressures and the cone resistance for undrained conditions. However, it underestimates the cone resistance in drained conditions producing the ratio between the drained and undrained resistance of about 2, as opposed to 1.45 obtained from MPM. Nevertheless, this result shows a good agreement with the measured data for a smooth cone. The MPM analysis can also achieve this result using a certain friction coefficient to match the measured data closer. The possible explanations for these discrepancies are attributed to the MPM contact formulation as described by Ceccato [2015]. Further research is needed

[2]In the centrifuge experiment, the initial vertical effective stress varies from 80kPa to 100kPa, which differs from the calibration chamber assumption used in the current numerical simulations

to determine the source of these discrepancies.

6.3.2 Strain Path Method and Field Data

Aubeny [1992] has carried out extensive studies of the steady state undrained piezocone tip resistance using the approximate Strain Path Method (Baligh and Levadoux [1986]). Figure 6-39 shows the comparison between the analytical predictions of piezocone penetration using the Strain Path Method for steady state conditions and the current simulation results obtained using Finite Element Method with the proposed remeshing and interpolation approach for two soil models (MIT-E3 and MCC), as well as the results from the MIT-SR model. For varying stress history (OCR values from 1.0 to 4.0), the obtained net tip resistance is in excellent agreement for the MCC soil model. The predictions using the MIT-E3 soil model are also in good agreement with the Strain Path Method results (Aubeny [1992]). The simulation results obtained from the MIT-SR model are similar to the MIT-E3 predictions. Tables 6.4 and 6.5 summarize the normalized values of cone resistance and normalized excess pore pressures obtained from the Strain Path Method (Baligh and Levadoux [1986], Aubeny [1992]) using the MIT-E3/MCC soil models and the current axisymmetric FE analyses using the developed large deformation procedure (with the soil models calibrated to the behavior of Boston Blue Clay).

Figure 6-40 presents the direct comparison between the current Finite Element simulations using the proposed methodology and field data for Boston Blue Clay (Ladd [1990], Ladd et al. [1999]) from South Boston Special Test Program for the Central Artery/Third Harbor Tunnel (CA/T) project which was extensively studied previously at MIT (Ladd et al. [1999]). The reported field measurements are average values recorded over 1.5m intervals from the penetration records. The error bars represent maximum and minimum measured data over the same interval. The comparison shows that the MIT-E3 soil model predictions are in very good agreement with the measured data for this site in Boston Blue Clay. The MCC model predictions overestimate, while the MIT-SR model results slightly underestimate the measured net piezocone tip resistance.

Table 6.1: Input parameters for MCC soil model

Input Parameter	**Boston Blue Clay (Hashash [1992])**	**Kaolin (Ceccato [2015])**
λ	0.184	0.205
$\varkappa$	0.034	0.044
M	1.348	0.92
φ'_{TC}	33.4	23.5
2G/K	1.05	1.20
ν'	0.28	0.25
K_{0NC}	0.5344	0.68
e_0	1.12	1.41
k, cm/s	10^{-7}	-

Table 6.2: MIT-E3 Soil Model Input Parameters for BBC (Hashash [1992])

Description	**Parameter**	**Boston Blue Clay**
Reference Void Ratio on VCL	e_0	1.12
Normally Consolidated Compression	λ	0.184
Non-linear Volumetric Swelling Behavior	C	22.0
	n	1.6
Irrecoverable Plastic Strain	h	0.2
K_0 for virgin normally consolidated clay	K_{0NC}	0.543
The ratio of the tangential elastic shear modulus to the bulk modulus, which is related to the Poisson's ratio of the soil skeleton	2G/K	1.05
Critical State Friction Angles in Triaxial Compression and Extension	φ'_{TC}	33.4
	φ'_{TE}	45.9
Undrained Shear Strength (geometry of bounding surface)	c	0.86
Amount of Post-peak Strain Softening in Undrained Triaxial Compression	s_t	4.5
Non-linearity at Small Strains in Undrained Shear	ω	0.07
Shear Induced Pore Pressures for OC Clay	γ	0.5
Small strain compressibility at load Reversal	$\varkappa_0$	0.001
Rate of Evolution of Anisotropy (rotation of bounding surface)	Ψ_0	100.0
Hydraulic conductivity, cm/s	k	10^{-7}

Table 6.3: MIT-SR Soil Model Input Parameters for RBBC (Yuan [2016])

Symbols	Values	Data set used for calibration	Reference
ρ_c	0.180	log$e$ – logσ' LCC curves from triaxial tests	Casey (2014)
K_{0NC}	0.49	Stress state after K_0-consolidation	Sheahan (1991)
C_b	473	High quality small strain measurement of G_{sec}	Santagata (1998)
$2G/K$	1.13	1-D swelling σ'_v-σ'_h effective stress paths	Casey (2014) Sheahan (1991)
D	0.03	1-D swelling log$e$ – logσ' curve	
r	4.0		
w_s	30	Nonlinear small strain behavior in CK_0UC&UE tests on NC RBBC	Sheahan (1991)
ϕ'_{cs}	33.5	Critical states measured in CK_0UC tests	
ϕ'_m	24	ESPs for CK_0UC&CK_0UE at OCR=1	
m	0.6		
Ψ	10		
D_L	1.0	ESPs for CK_0UC at OCR=8	
ρ_α/ρ_c	0.02	Based on the reported values of $C_{\alpha\varepsilon}/CR$ Interpreted from 2nd compression in triaxial tests	Seah (1990) Ahmed (1990) Sheahan (1991) Casey (2014)
β	0.02	Rate-sensitivity of LCC for CRS tests using different strain rates	Force (1998) Gonzalez (2000)
$\dot{\varepsilon}_{ref}$	$2x10^{-7}$/sec	Applied strain rate in triaxial consolidation	Sheahan (1991)
β_2	6.8*	Creep behavior after unloading to different OCRs	Ng (1998)
β_3	19*		

* The β_2 and β_3 are inferred from data of Salt Lake City (SLC) clay

Table 6.4: Strain Path Method Predictions for K_0-consolidated BBC (Aubeny [1992])

Soil Model	**OCR**	**K_0**	$\frac{q_c(net)}{\sigma'_{v0}}$	$\frac{\Delta u\,(net)}{\sigma'_{v0}}$	B_q
MCC	1.0	0.48	2.5-2.6	2.0	0.77-0.80
	2.0	0.57	4.4-4.7	2.7	0.58-0.61
	4.0	0.75	7.7-8.1	3.9	0.48-0.51
MIT-E3	1.0	0.48	1.4-1.6	1.6	1.00-1.14
	2.0	0.57	2.3-2.5	2.1	0.84-0.91
	4.0	0.75	5.4-6.1	3.4	0.55-0.63

Table 6.5: Predictions using large deformation FEM for K_0-consolidated BBC

Soil Model	**OCR**	**K_0**	$\frac{q_c(net)}{\sigma'_{v0}}$	$\frac{\Delta u\,(net)}{\sigma'_{v0}}$	B_q
MCC	1.0	0.48	2.45	1.91	0.78
	1.5	0.53	3.52	2.20	0.63
	2.0	0.58	4.50	2.85	0.63
	2.5	0.63	5.46	3.05	0.56
	4.0	0.77	8.04	3.63	0.45
MIT-E3	1.0	0.53	1.75	1.69	0.97
	1.5	0.61	2.37	2.27	0.96
	2.0	0.68	2.91	2.72	0.93
	2.5	0.76	3.53	3.11	0.88
MIT-SR	1.0	0.51	1.21	1.39	1.15
	1.3	0.54	1.46	1.53	1.05
	2.0	0.61	2.17	1.79	0.82
	2.5	0.66	2.71	1.94	0.72

Note: MIT-E3 and MIT-SR results for higher OCR are not truly at steady state

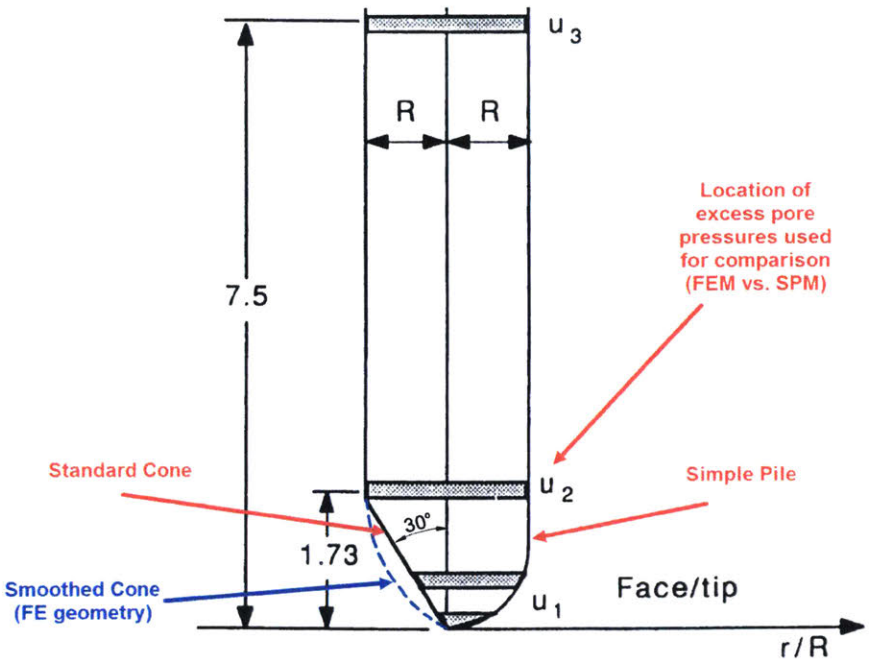

Figure 6-1: Location used to interpret predictions of piezocone pore pressures

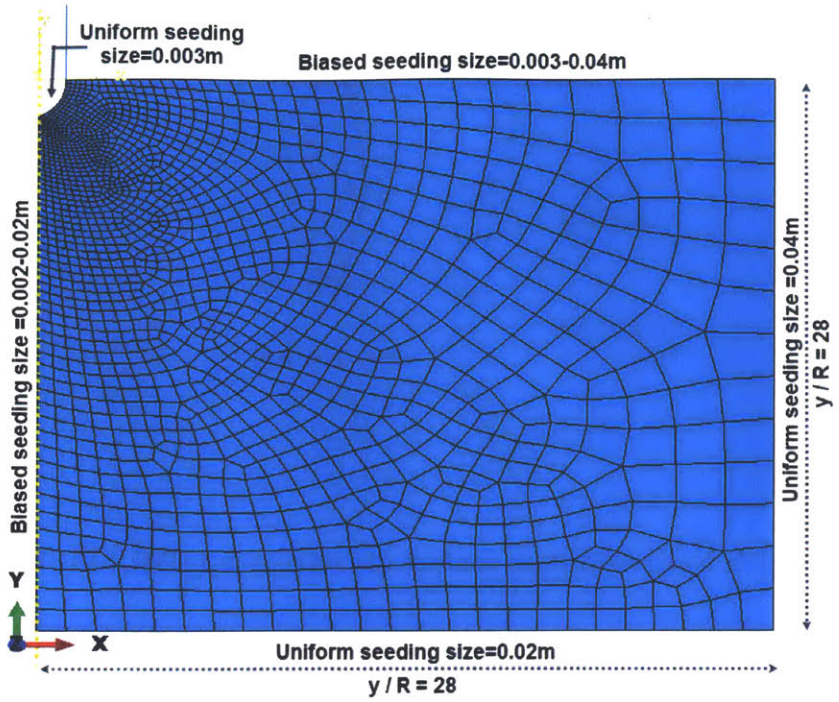

Figure 6-2: Base Case Model with Coarse Mesh

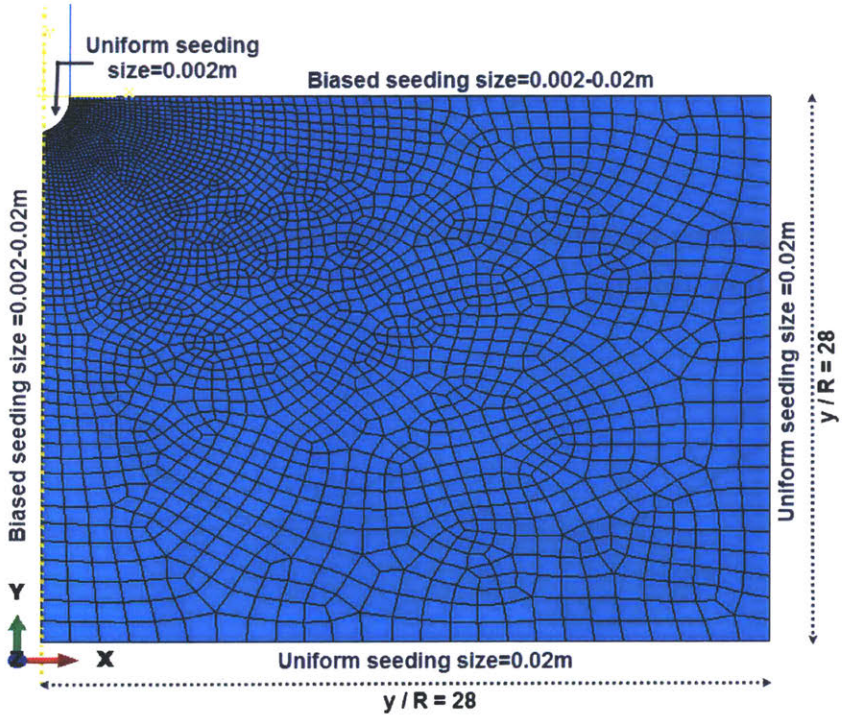

Figure 6-3: Base Case Model with Fine Mesh

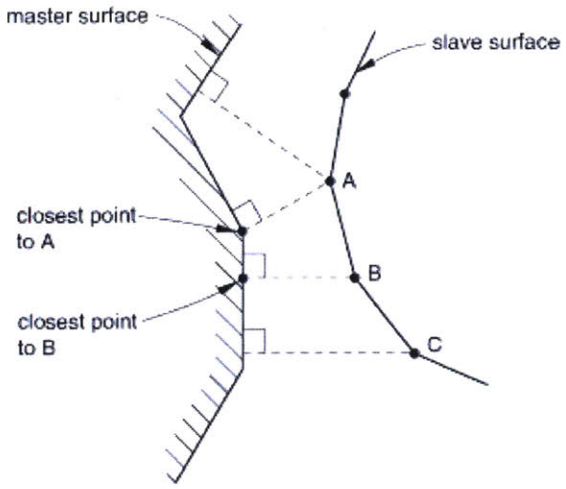

Figure 6-4: Node-to-surface contact discretization (SIMULIA [2016])

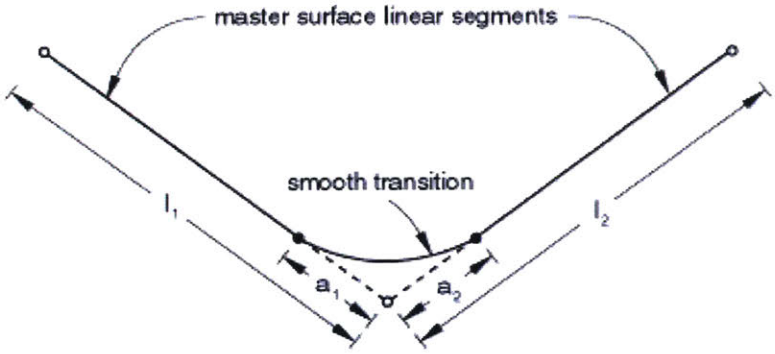

Figure 6-5: Smoothing master surfaces for finite-sliding node-to-surface contact formulation (SIMULIA [2016])

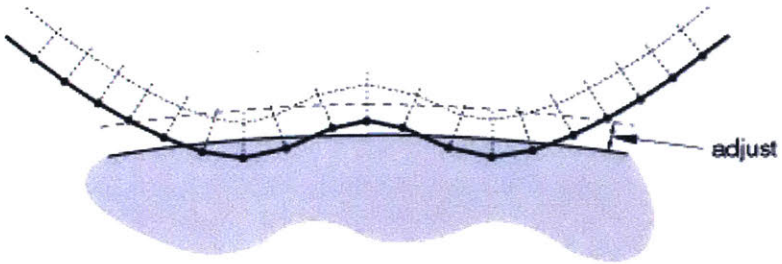

Figure 6-6: Contact surfaces and adjustment zone (SIMULIA [2016])

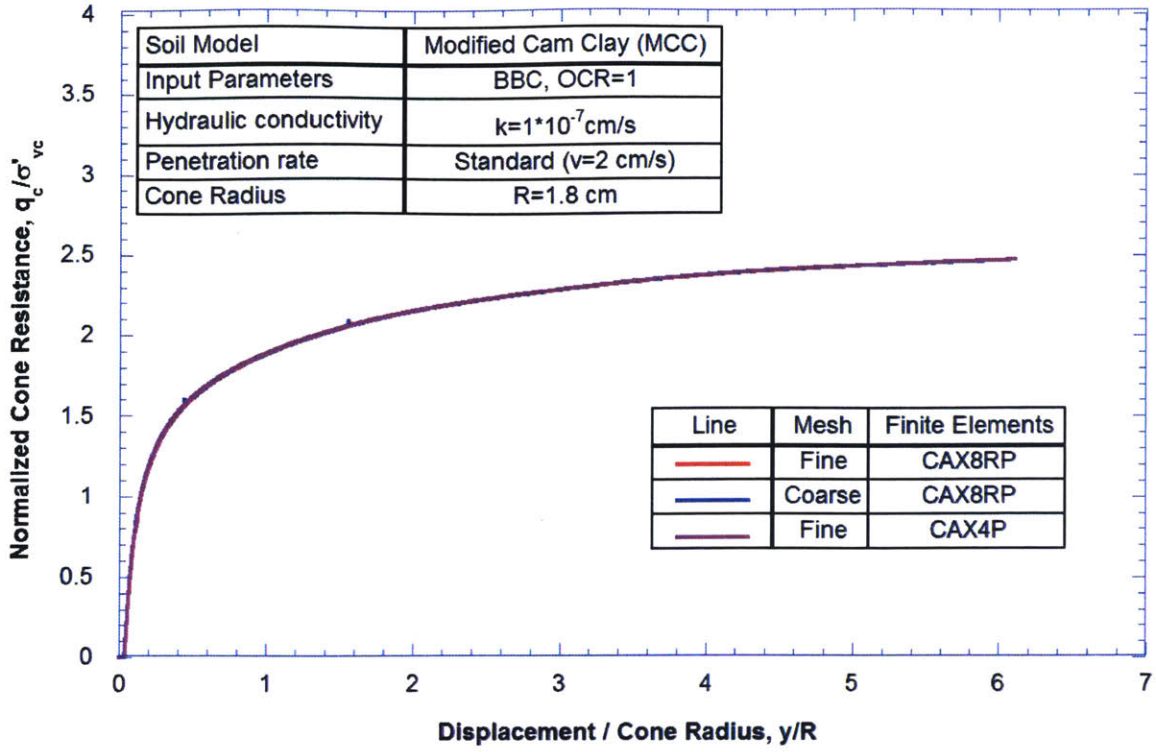

Figure 6-7: The results obtained from fine and coarse meshes using various elements

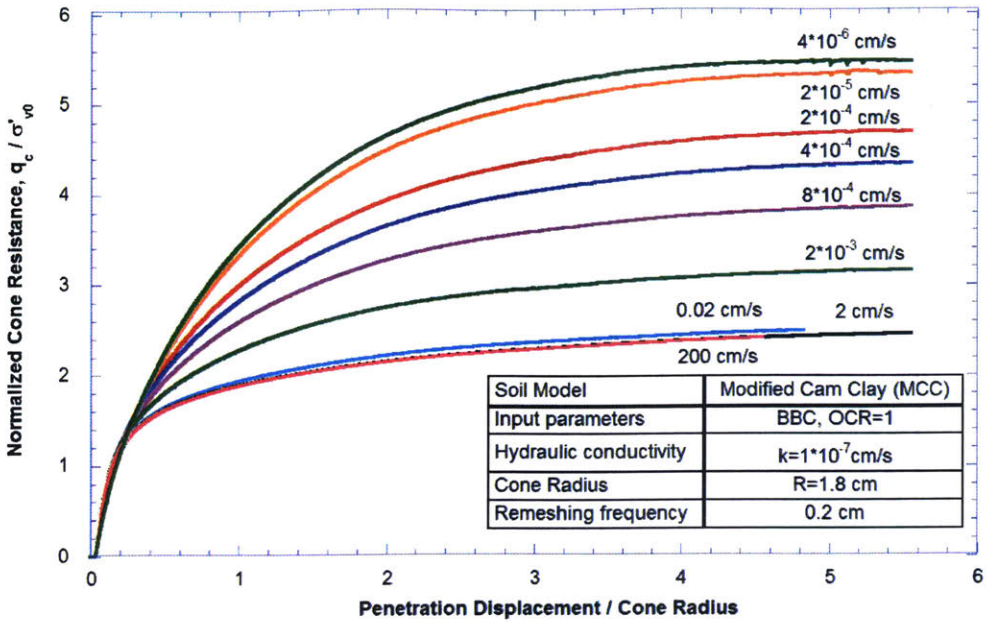

Figure 6-8: Summary of piezocone tip resistance at selected steady penetration rates using MCC soil model with input parameters for BBC

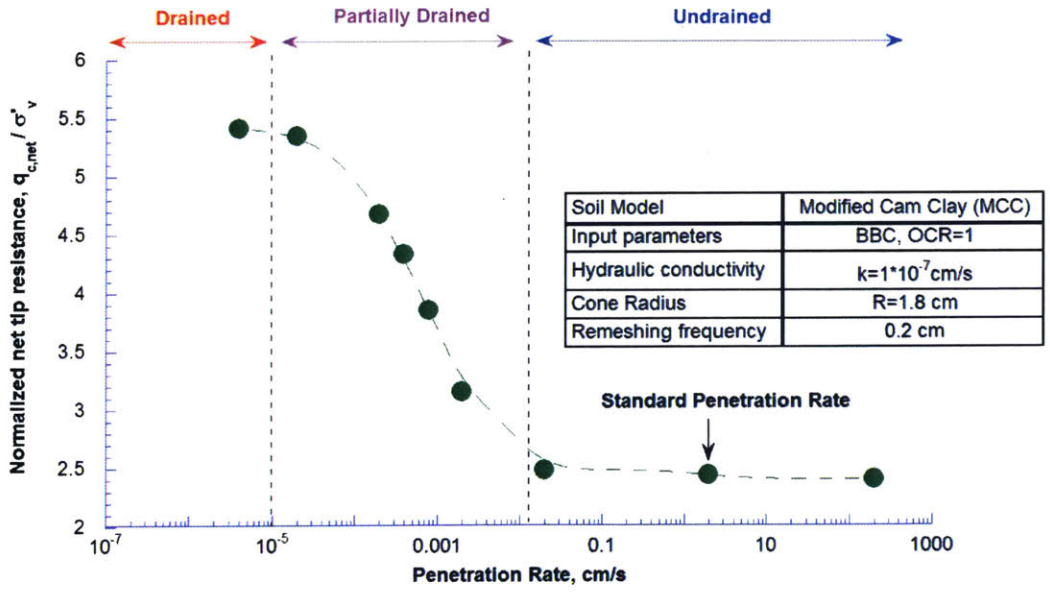

Figure 6-9: MCC soil model (BBC) analyses - net tip resistance for various penetration rates

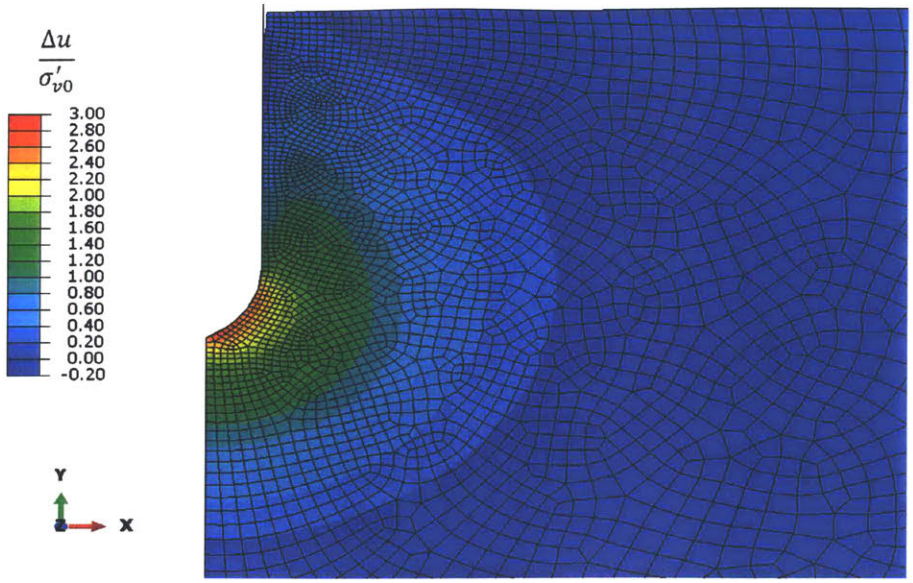

Figure 6-10: Base Case MCC Analysis - Excess pore pressures at depth of 6R (11cm)

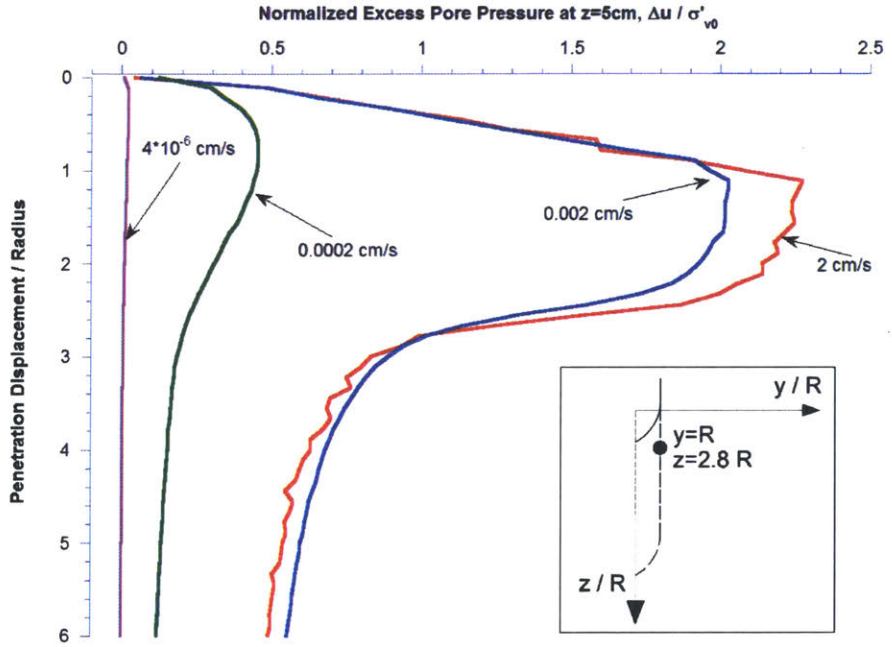

Figure 6-11: Evolution of excess pore pressures at a fixed point 5 cm below the surface

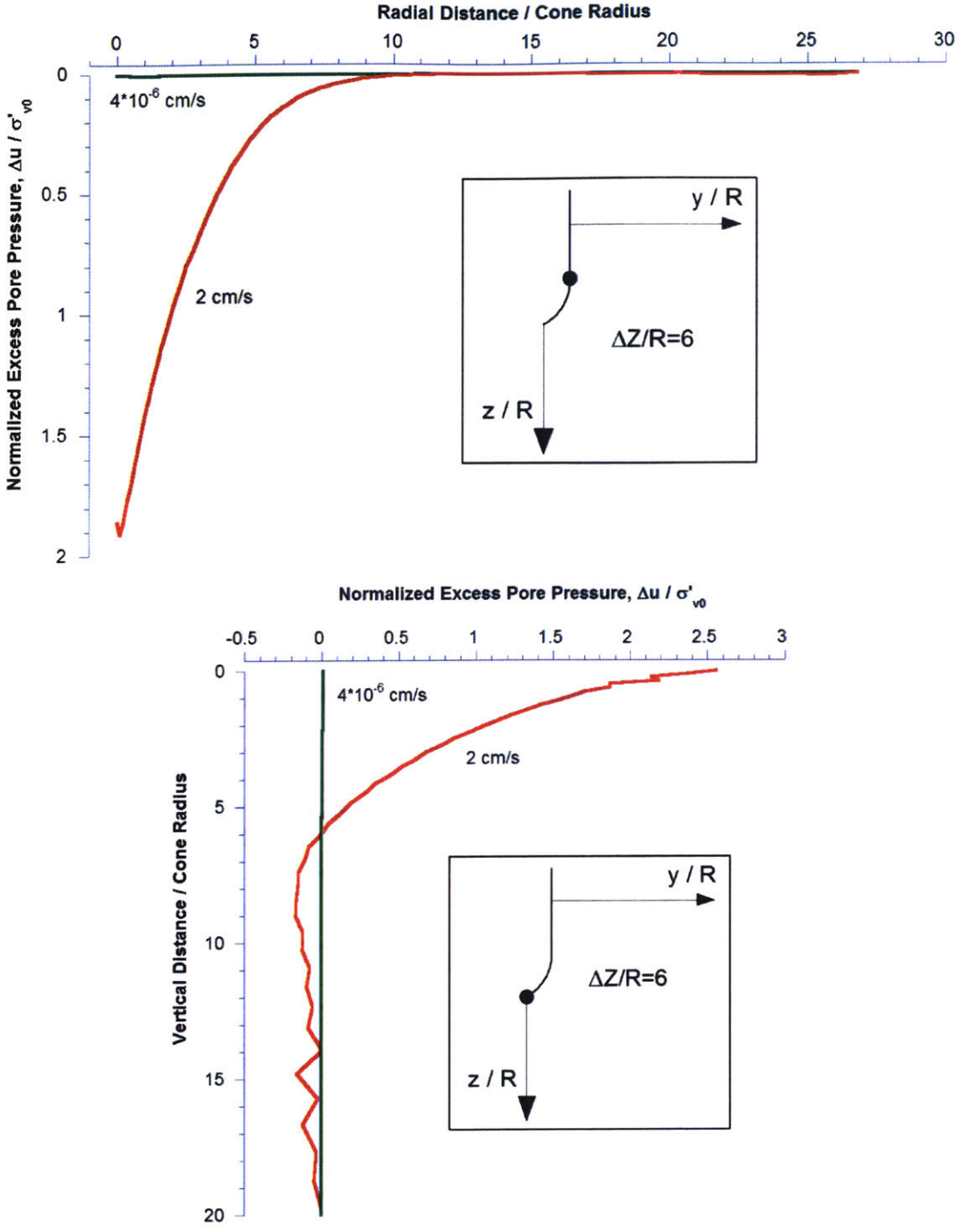

Figure 6-12: Base Case MCC Analysis - Excess pore pressure profiles at Penetration depth of 6R (11cm)

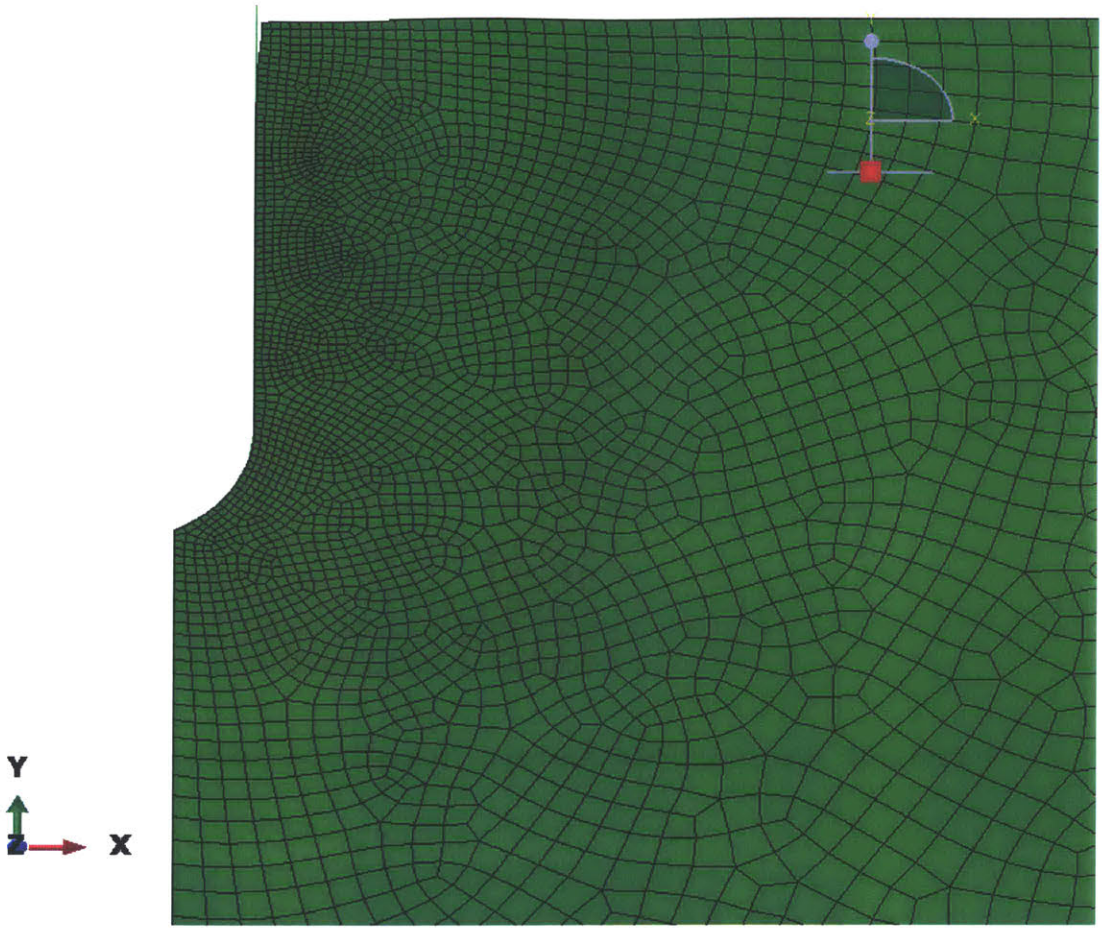

Figure 6-13: Deformed mesh configuration after deep penetration using MCC soil model (minimized distortion)

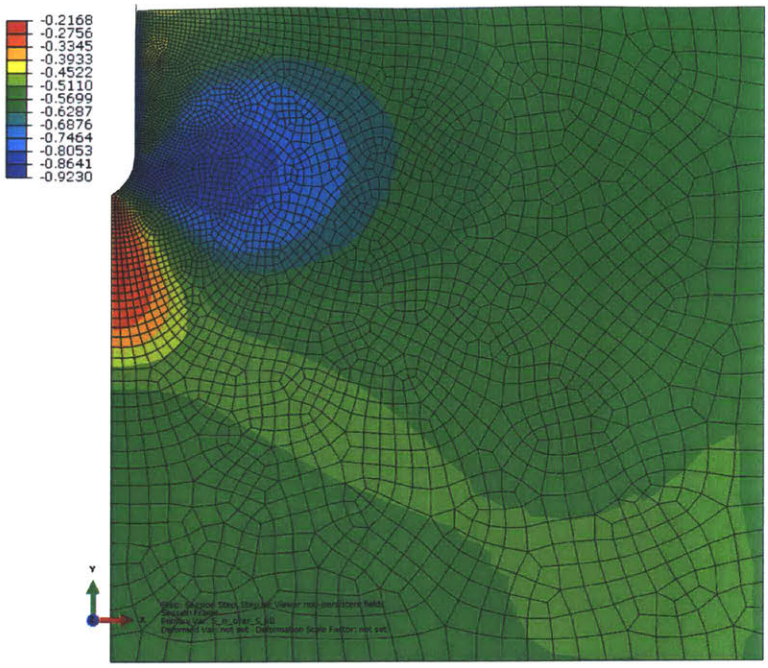

Figure 6-14: Base Case MCC Analysis - Normalized radial stress ($\frac{\sigma'_{rr}}{\sigma'_{v0}}$) contours

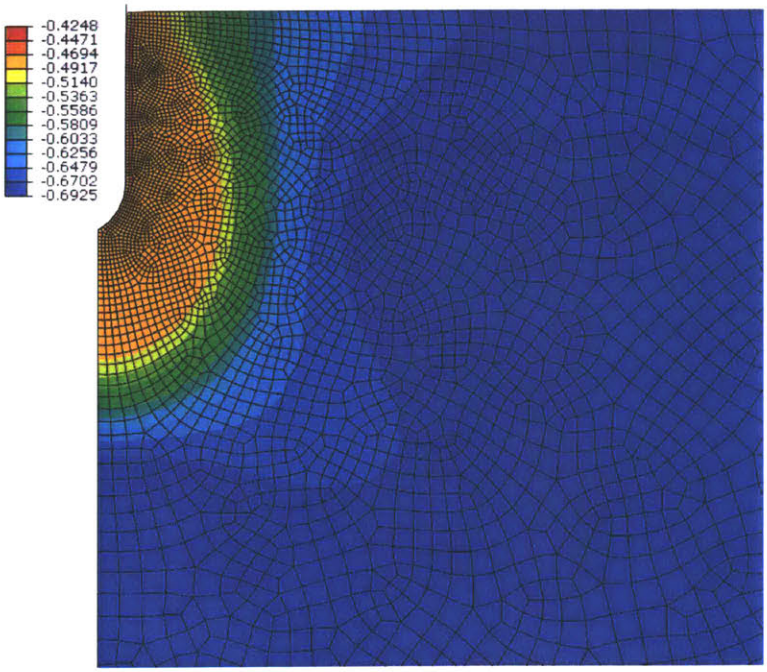

Figure 6-15: Base Case MCC Analysis - Normalized mean stress ($\frac{\sigma'_{mean}}{\sigma'_{v0}}$) contours

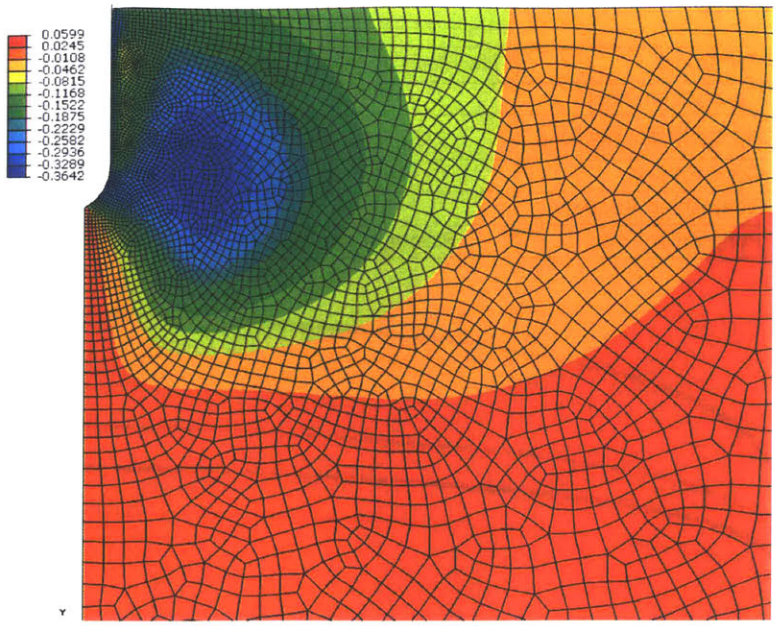

Figure 6-16: Base Case MCC Analysis - Cylindrical expansion shear stress ($\frac{\sigma'_{rr}-\sigma'_{\theta\theta}}{2\sigma'_{v0}}$) contours

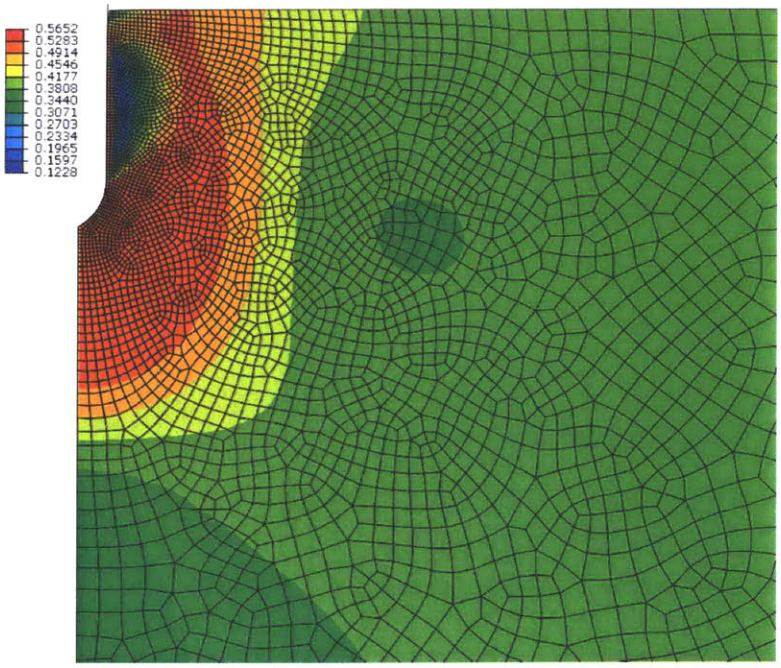

Figure 6-17: Base Case MCC Analysis - Normalized shear stress ($\frac{q}{\sigma'_{v0}}$) contours

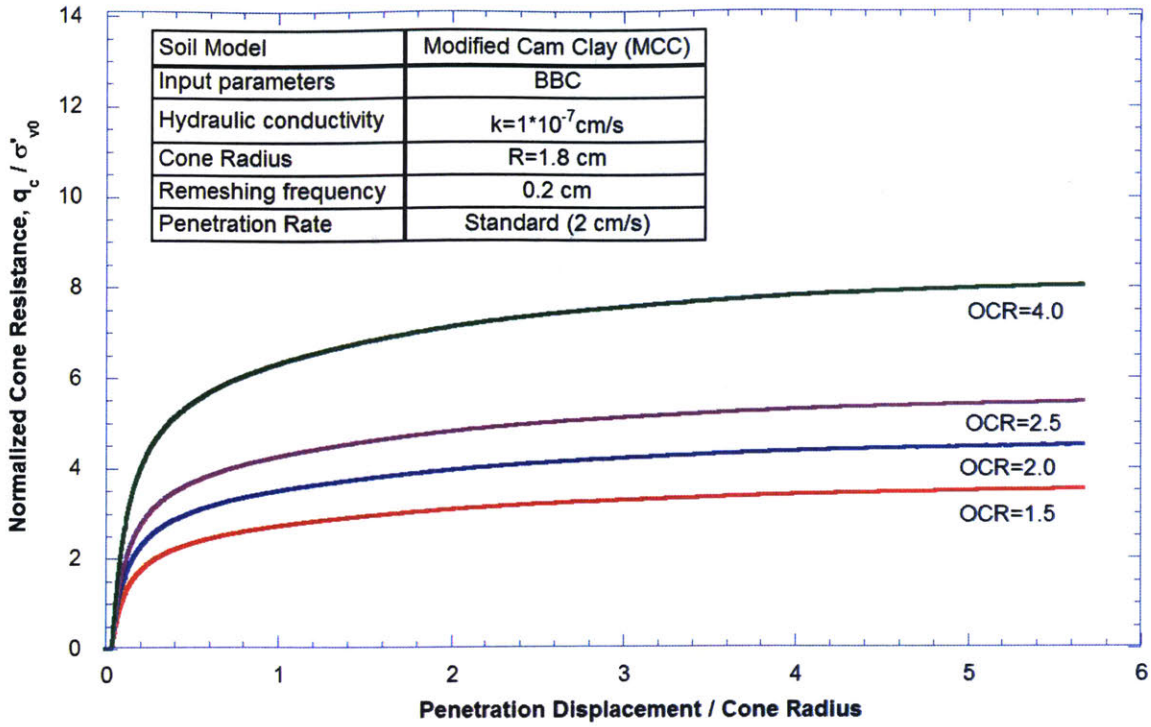

Figure 6-18: Base Case MCC Analysis - Effect of OCR on Cone Resistance

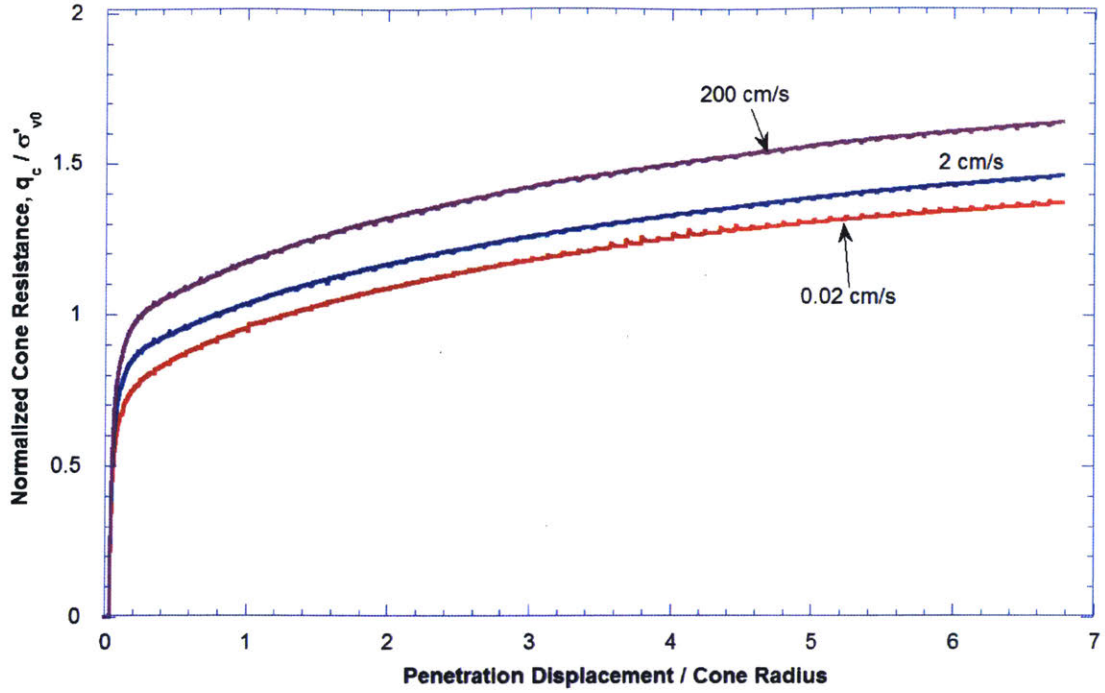

Figure 6-19: Simulations of undrained penetration+ using MIT-SR soil model (BBC)

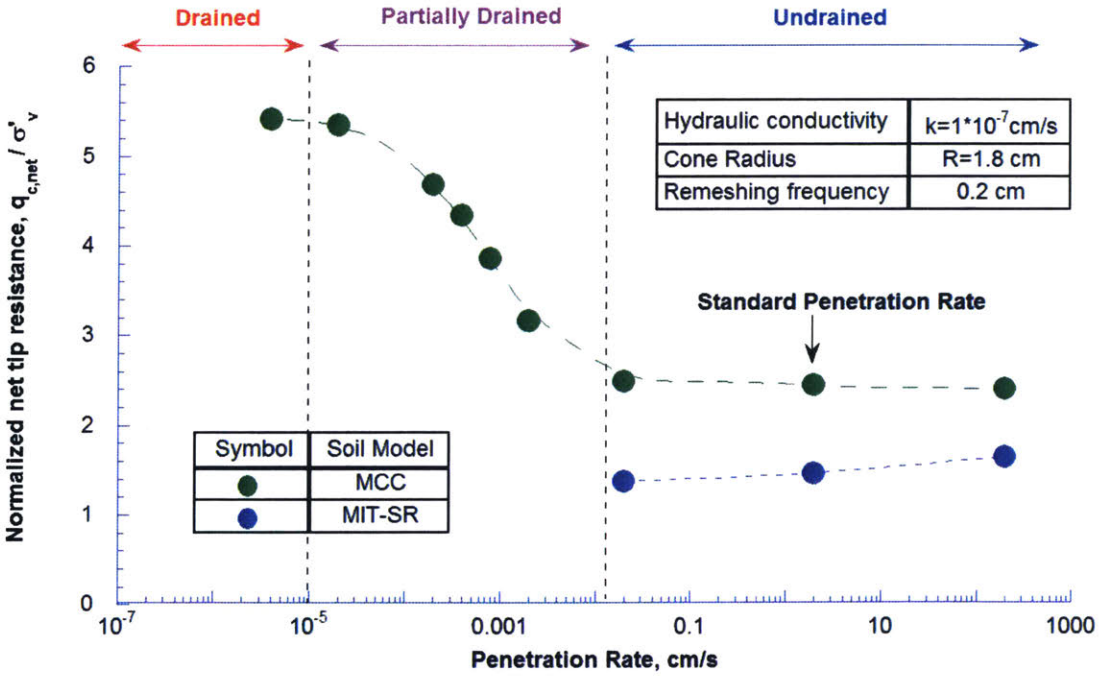

Figure 6-20: MIT-SR, MCC analyses - net tip resistance for various penetration rates

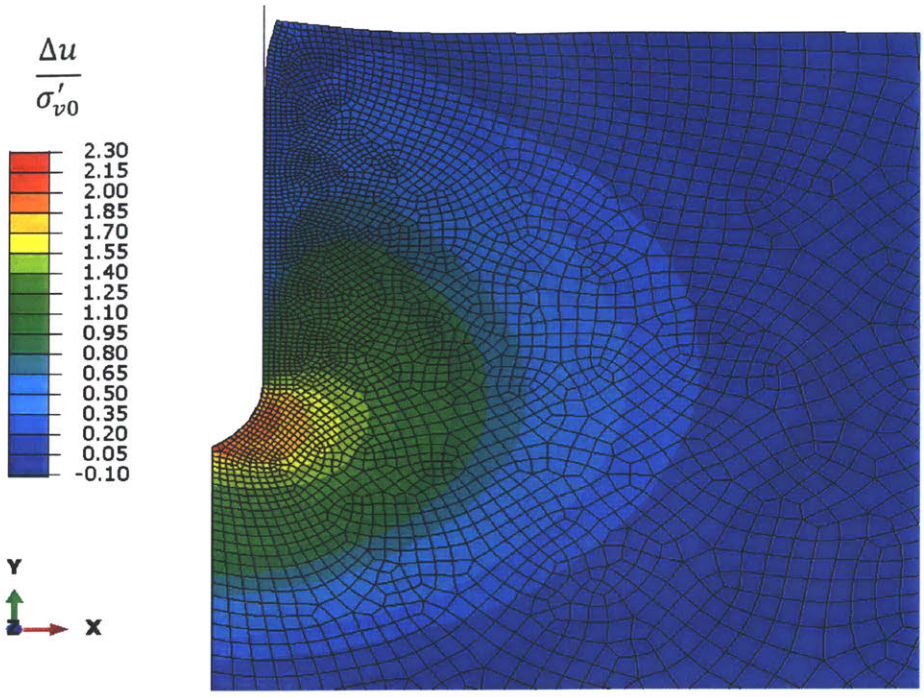

Figure 6-21: MIT-SR Analysis - Excess pore pressures at Penetration depth of 6R

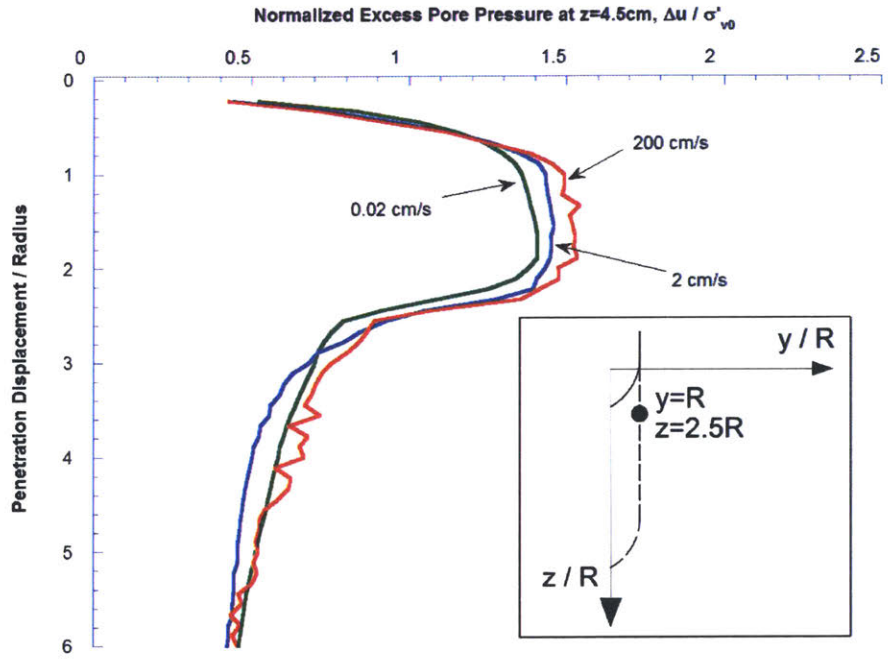

Figure 6-22: MIT-SR Analysis - Evolution of excess pore pressures at a fixed point 4.5 cm below the surface

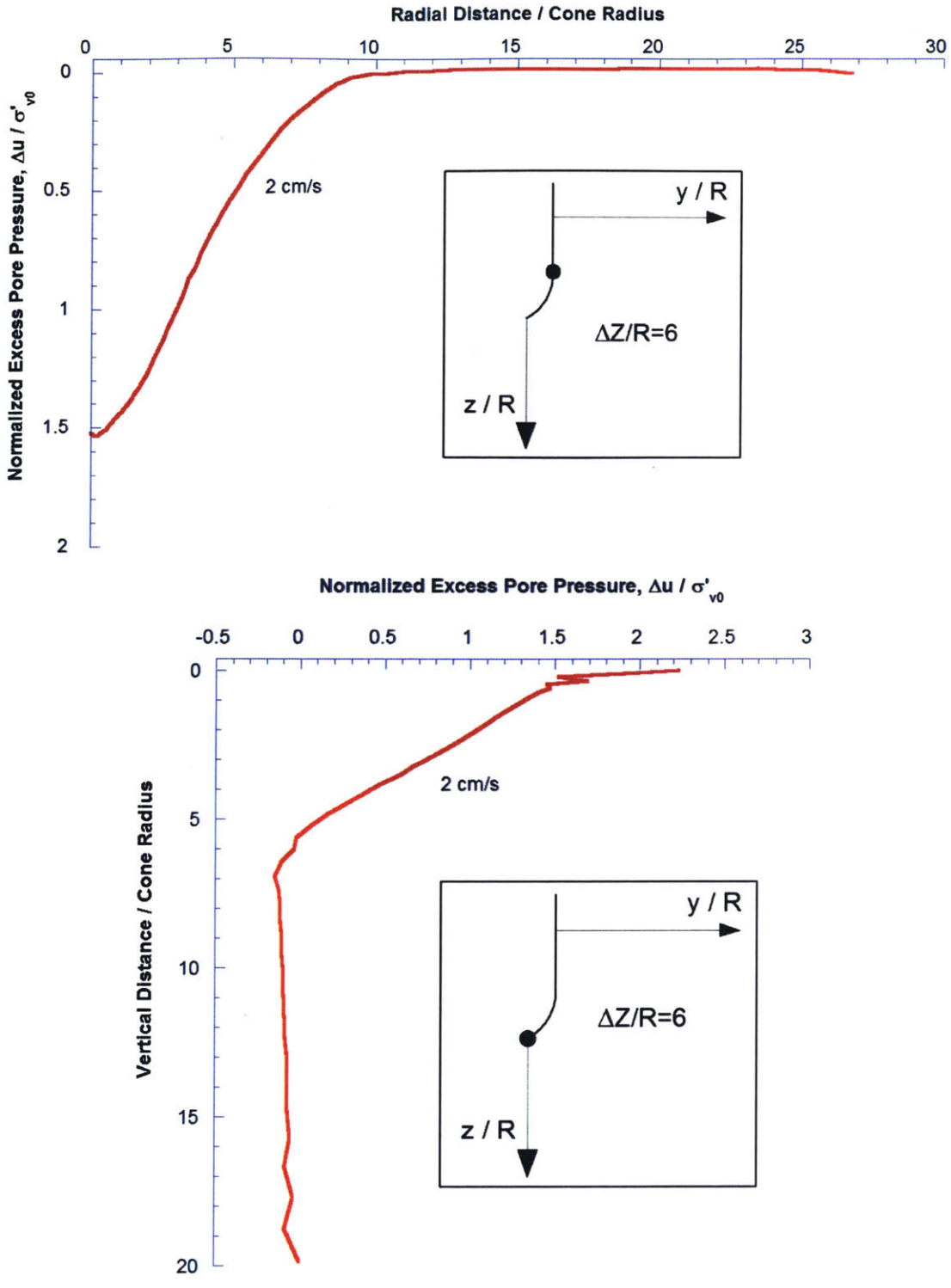

Figure 6-23: MIT-SR Analysis - Excess pore pressure profile for default penetration rate ($v = 2\,cm/s$) at penetration depth of 6R (11cm)

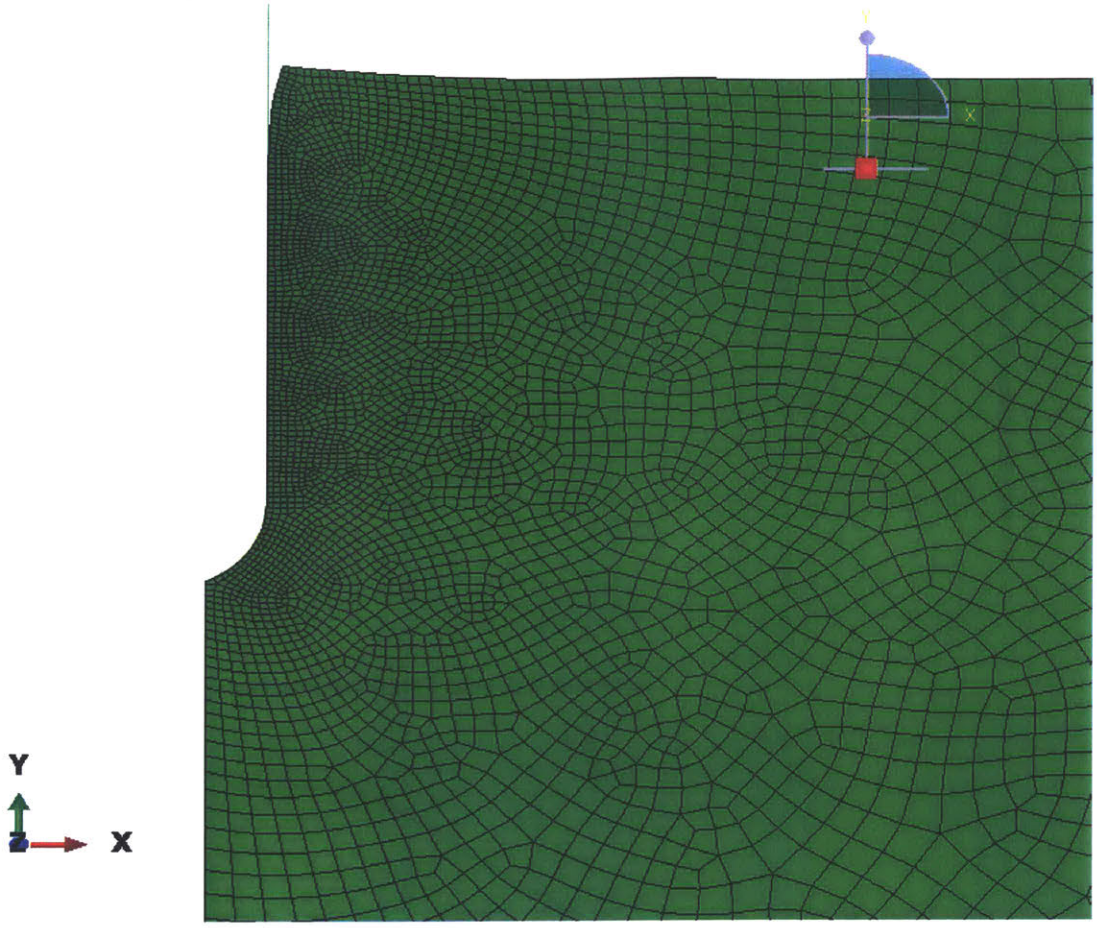

Figure 6-24: Mesh configuration obtained after deep penetration using MIT-SR soil model (minimized distortion)

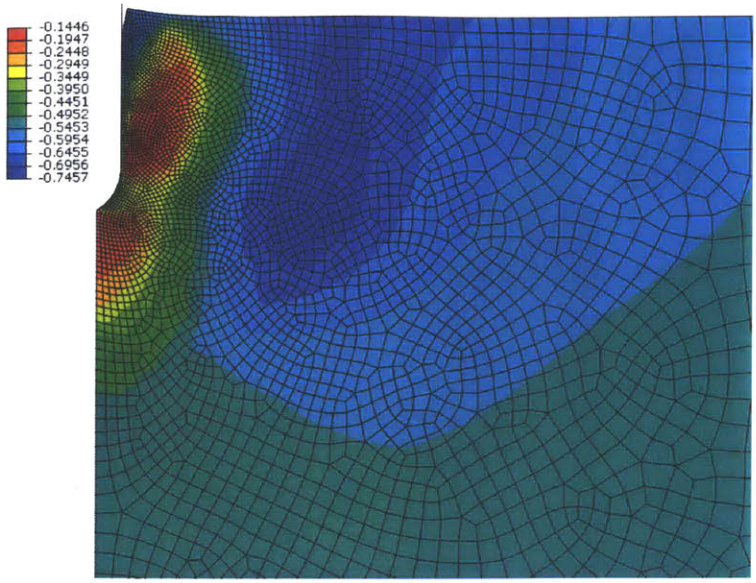

Figure 6-25: MIT-SR Analysis - Normalized radial stress ($\frac{\sigma'_{rr}}{\sigma'_{v0}}$) contours

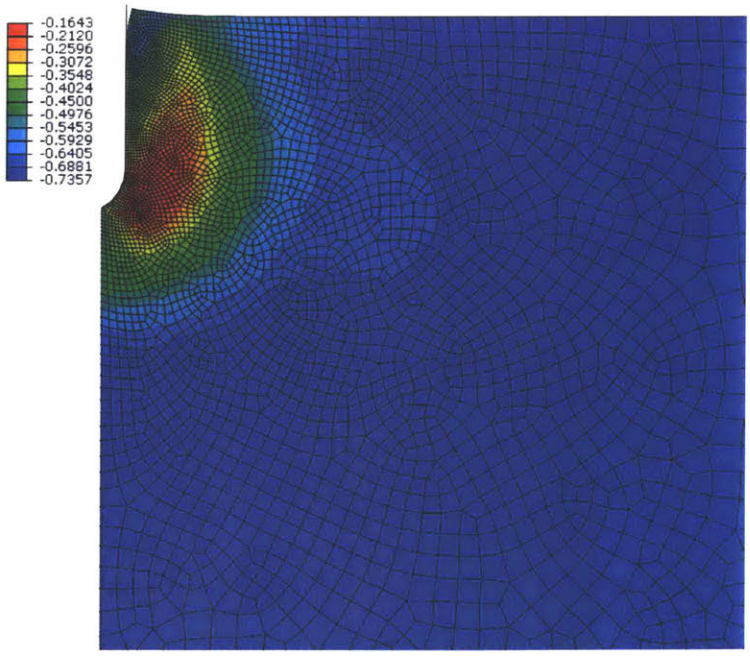

Figure 6-26: MIT-SR Analysis - Normalized mean stress ($\frac{\sigma'_{mean}}{\sigma'_{v0}}$) contours

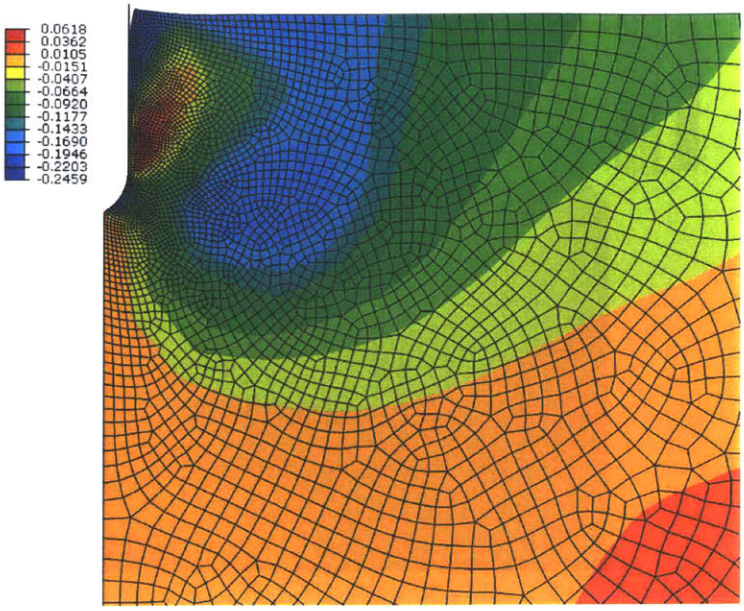

Figure 6-27: MIT-SR Analysis - Cylindrical expansion shear stress ($\frac{\sigma'_{rr}-\sigma'_{\theta\theta}}{2\sigma'_{v0}}$) contours

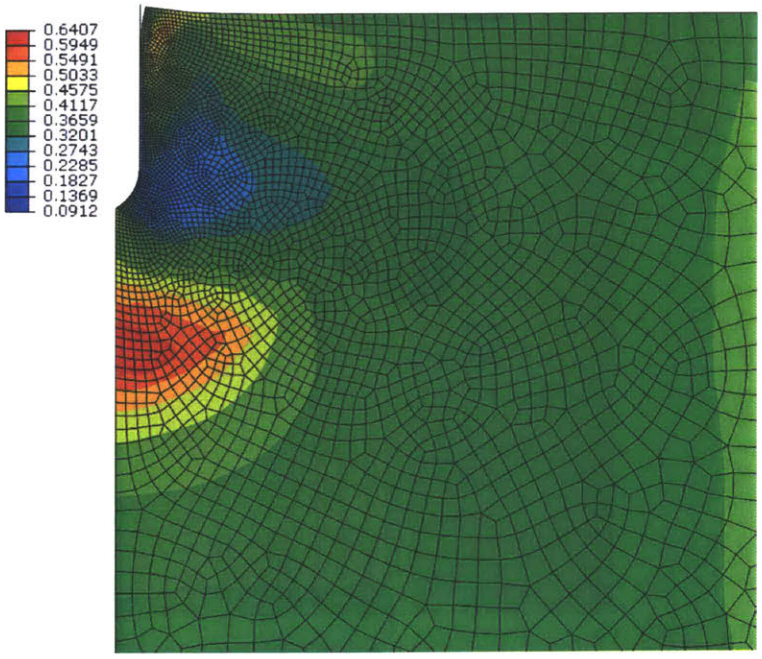

Figure 6-28: MIT-SR Analysis - Normalized shear stress ($\frac{q}{\sigma'_{v0}}$) contours

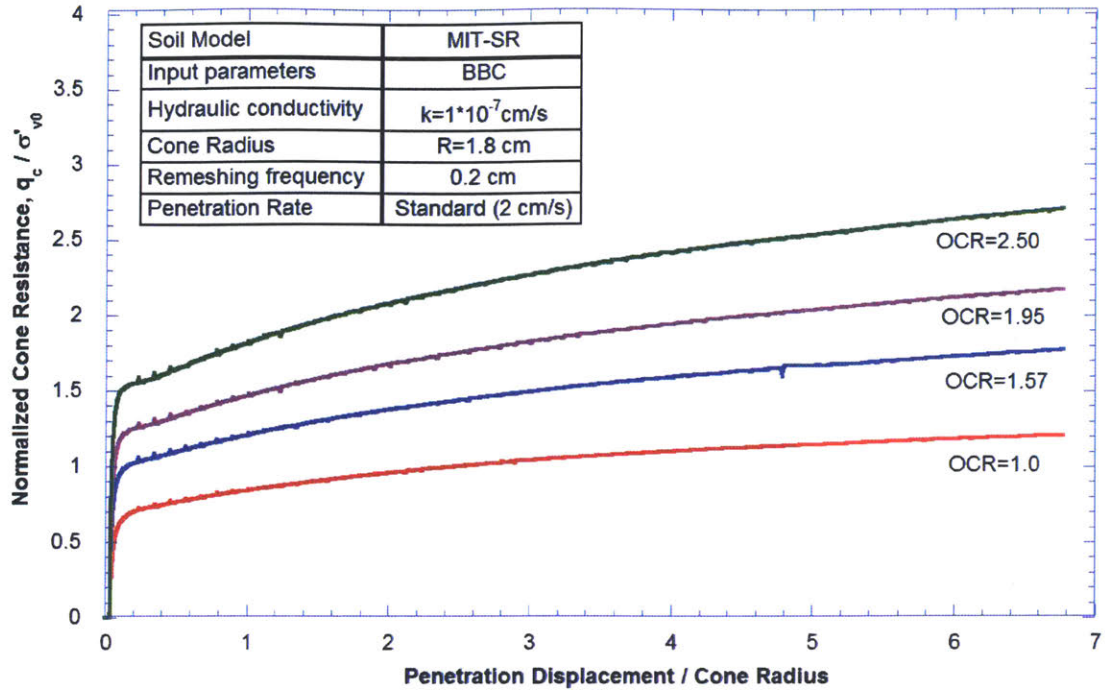

Figure 6-29: MIT-SR Analysis - Effect of OCR on Cone Resistance

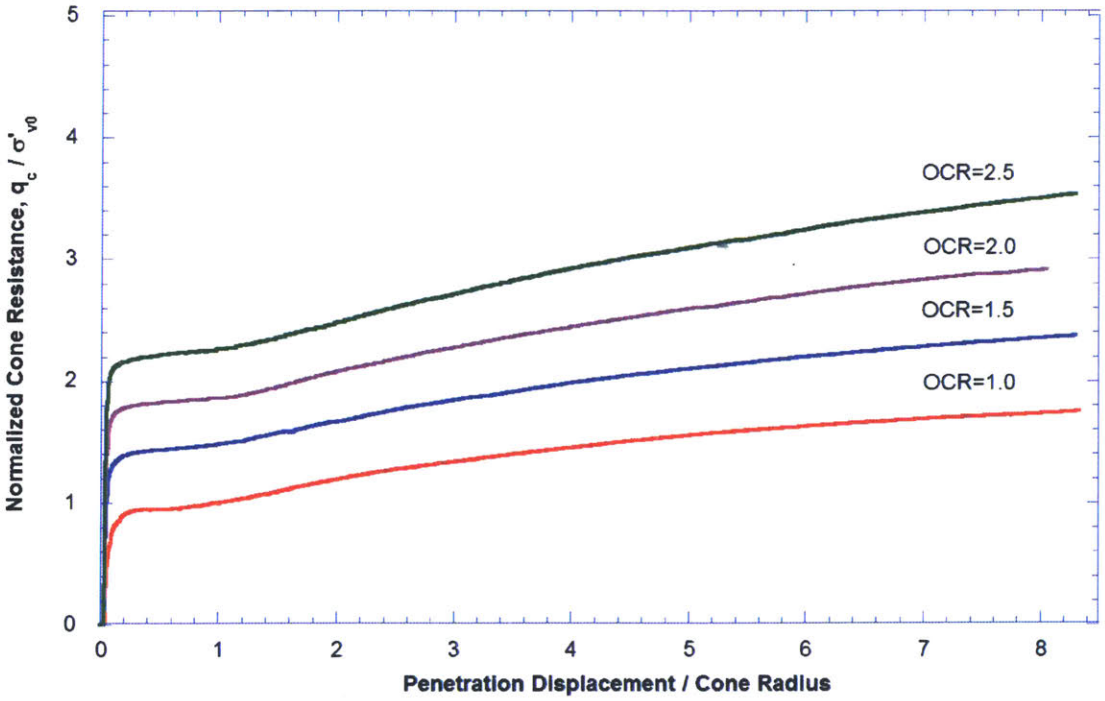

Figure 6-30: MIT-E3 Analysis - Effect of OCR on Cone Resistance

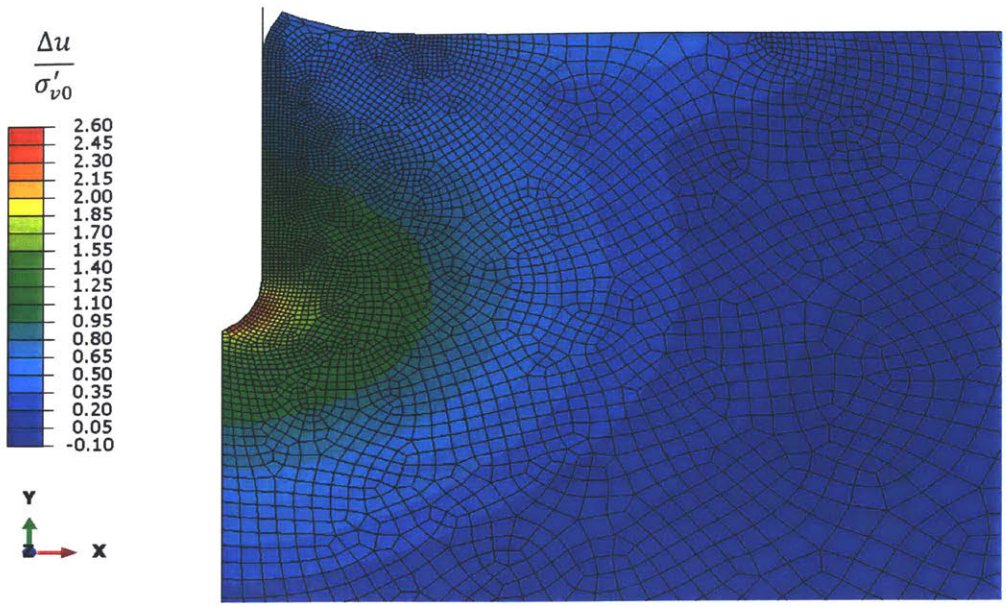

Figure 6-31: MIT-E3 Analysis - Excess pore pressures at Penetration depth of 8.3R (15cm) at OCR=1.0

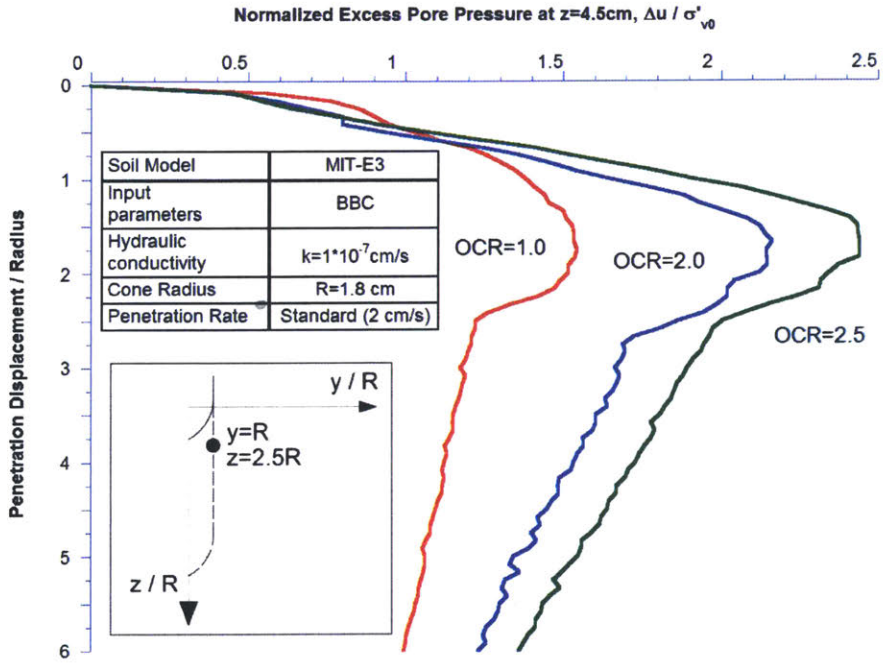

Figure 6-32: MIT-E3 Analysis - Evolution of excess pore pressure at a fixed point 5 cm below the surface

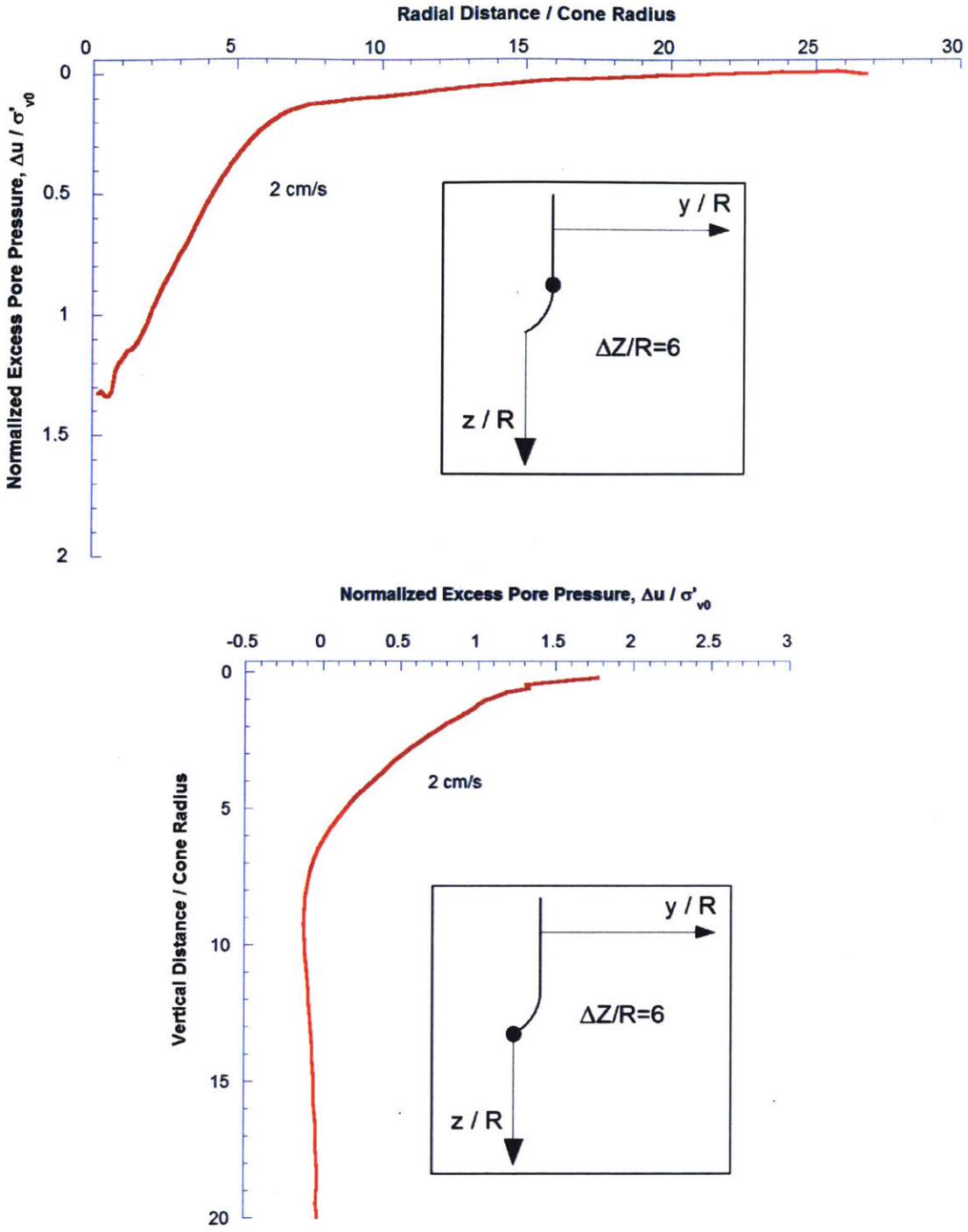

Figure 6-33: MIT-E3 Analysis - Excess pore pressure profile for default penetration rate ($v = 2\,cm/s$) at Penetration depth of 6R (12cm)

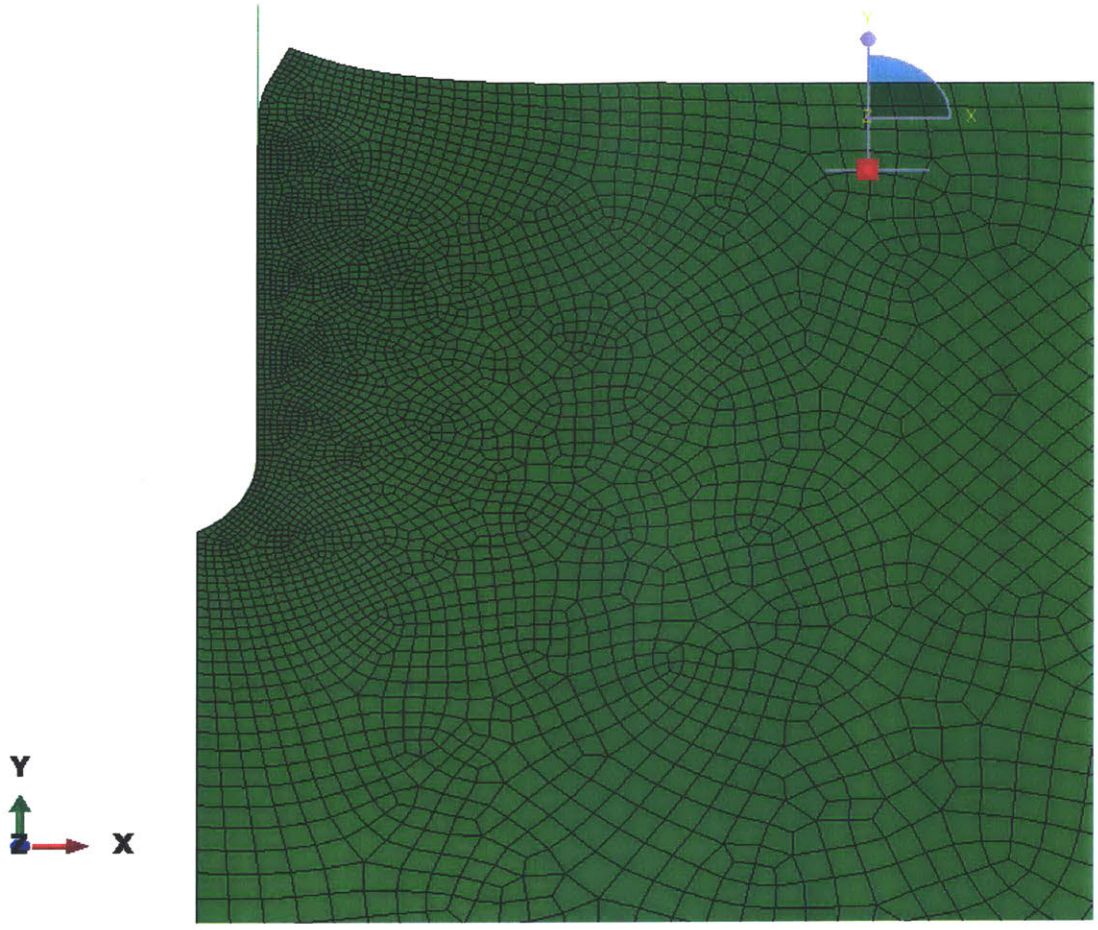

Figure 6-34: Deformed mesh quality after deep penetration using MIT-E3 soil model

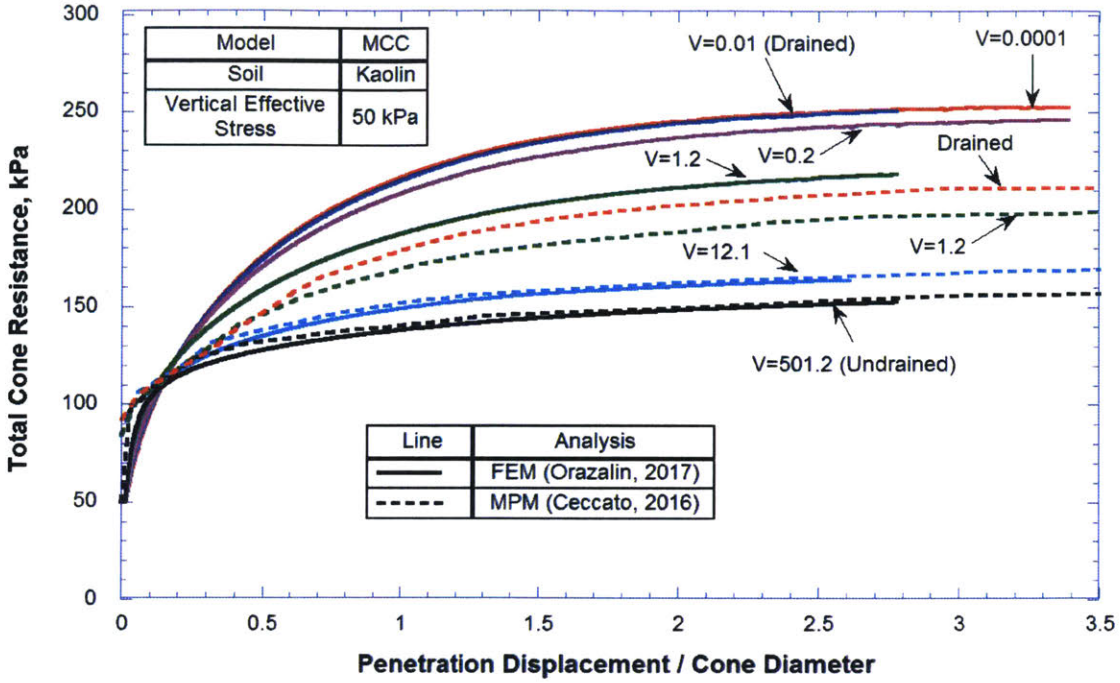

Figure 6-35: Replicate MCC (Kaolin) Analysis - Summary of penetration analyses for various drainage conditions

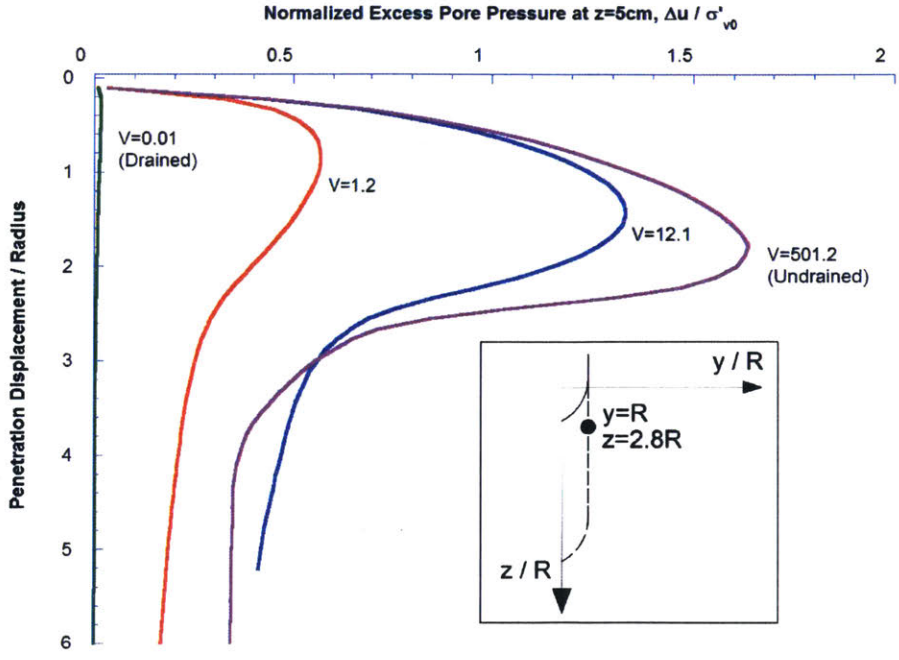

Figure 6-36: MCC Kaolin Analysis - Evolution of excess pore pressures

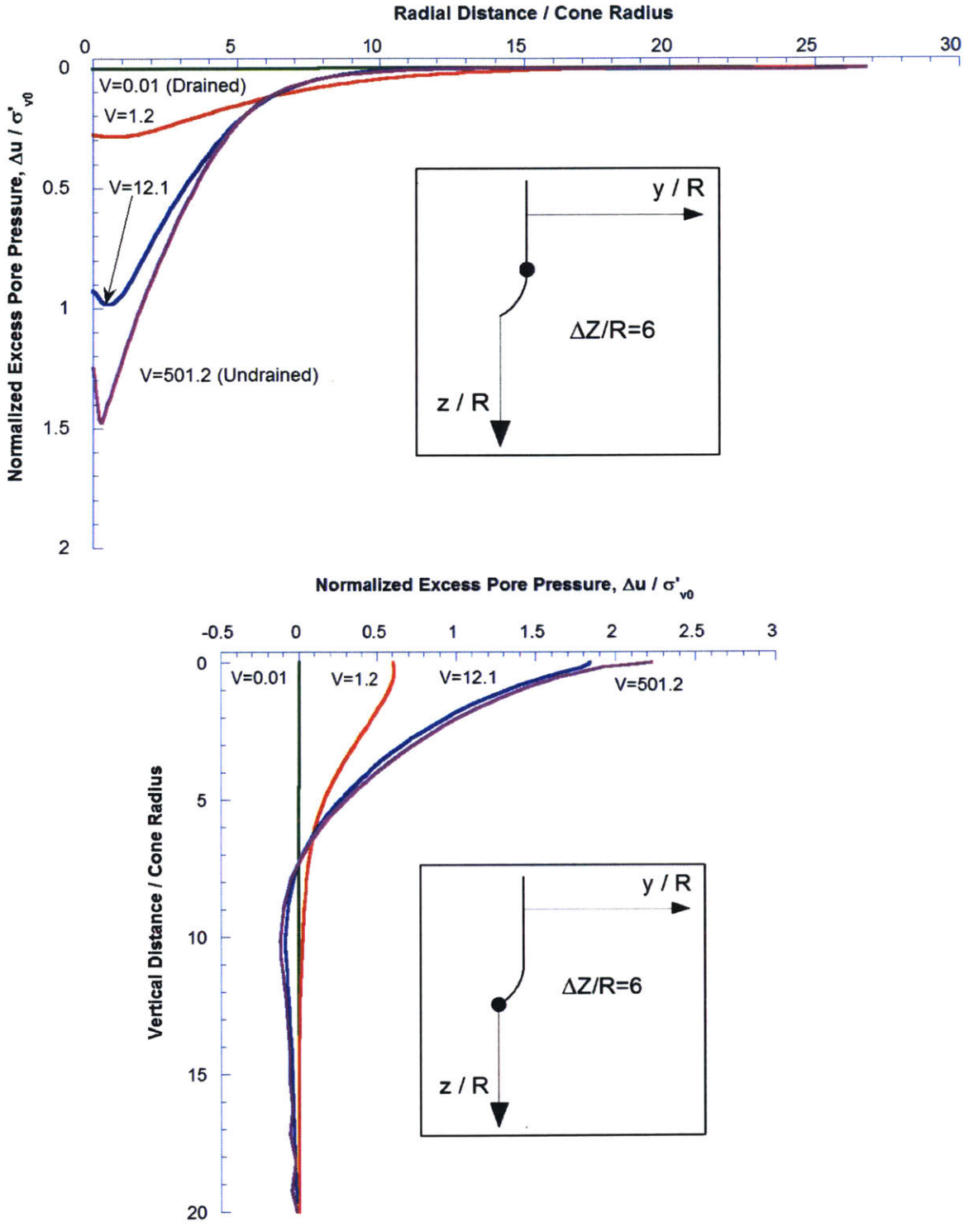

Figure 6-37: MCC Kaolin Analysis - Excess pore pressure profiles at Penetration depth of 6R (11cm)

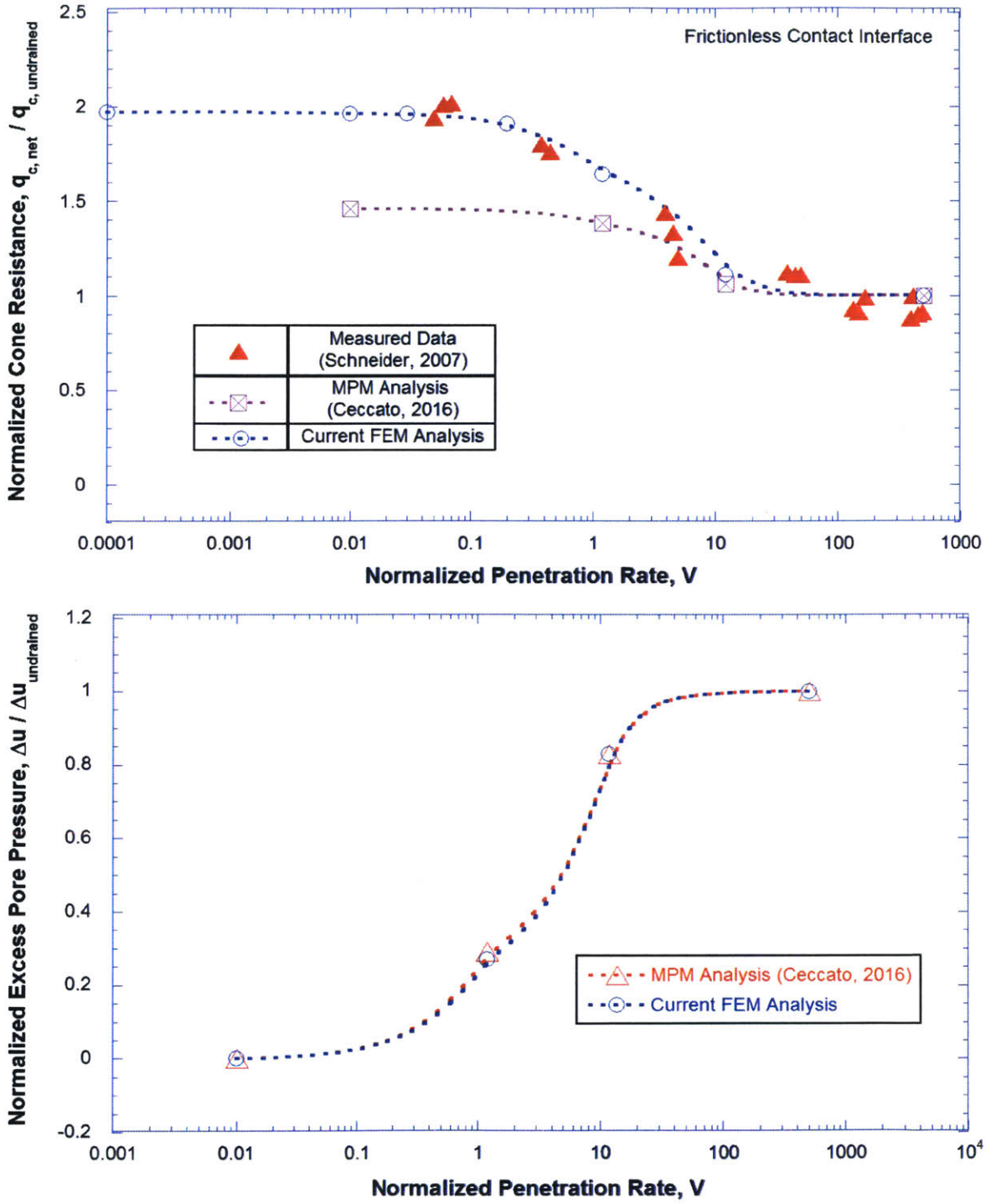

Figure 6-38: Comparison with MPM simulations (Ceccato [2015]) and Measured Data (Schneider et al. [2007])

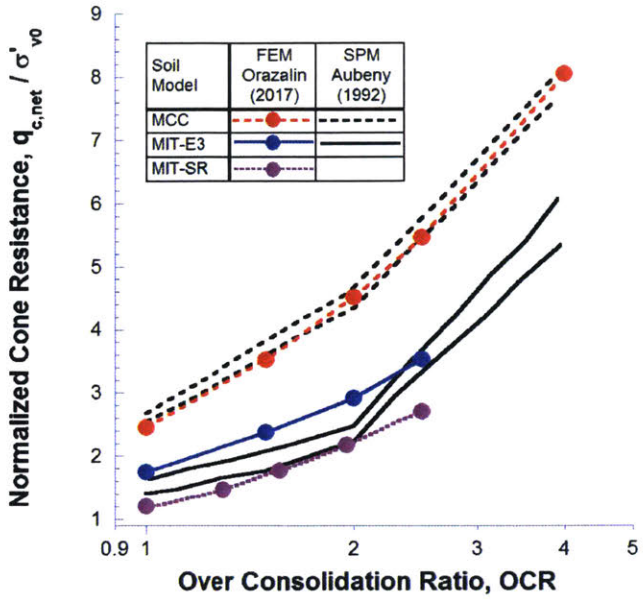

Figure 6-39: FEM Predictions vs. SPM Results for Steady State Penetration (Aubeny [1992])

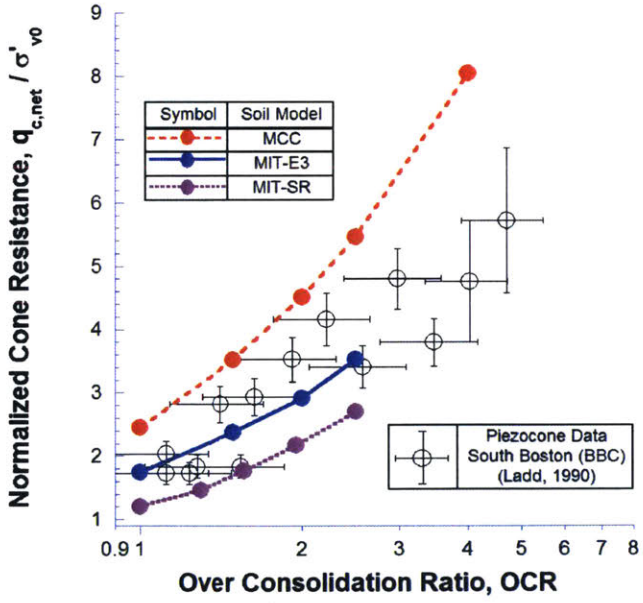

Figure 6-40: FEM Predictions vs. Measured Piezocone Data from South Boston (Ladd [1990], Aubeny [1992], Ladd et al. [1999])

Chapter 7

Summary, Conclusions and Recommendations

7.1 Summary and Conclusions

This thesis investigates two large deformation problems in soft clay and proposes a methodology for performing coupled flow and deformation analyses with advanced effective stress models.

7.1.1 Conductor-Soil Interaction

The first part of this research involved the development, validation and refinement of 3D FE models of conductor-soil interactions that address the large deformation conditions associated with drift/drive-off load events. The numerical predictions are evaluated through comparison with experimental results from centrifuge tests with a well-instrumented model conductor. The FE models simulate the prototype scale conductor soil interaction and use laboratory tests on reconstituted Gulf of Mexico Clay to calibrate constitutive model input parameters.

The centrifuge model tests[1] modeled a conductor installed in reconstituted Gulf of Mexico clay and subjected to pushover motion while under tension (the tests also

[1]Performed by C-CORE, a Canadian research and development facility located on Memorial University Campus in St. Johns, Newfoundland

simulated the quick release of the conductor after a specified pushover). The test results show little effect of the added LMRP mass while differences in axial tension have minimal effects on the bending moment obtained. Therefore, the current validation of numerical analyses has focused on results from centrifuge Model 1.

Direct comparisons with the measured bending moments provide a useful validation of the predictive capabilities of the proposed numerical analyses (but are limited by some inherent experimental issues). The 3D FE analyses also generate detailed information on local conductor-soil interactions (p-y curves). This research shows how these interactions are affected by: i) details of the undrained shear strength profile; ii) by the modeling of soil behavior (the study compare results from MIT-E3 with the much simpler, isotropic EPP model); and iii) the magnitude of lateral deformations of the riser (i.e, effects of geometric nonlinearities).

The results of three 3D FE analyses of conductor-soil interactions with undrained shearing of the clay were discussed: 1) Base Case using MIT-E3 and assuming a normally consolidated soil profile; 2) Refined Case using MIT-E3 in which the stress history (OCR) is modified to match the undrained shear strength profile of the reconstituted GoM clay (Fig. 4-25); and 3) analysis using a linearly-elastic, perfectly plastic soil model (EPP).

The measured bending moments from the centrifuge model are in a very good agreement with the results of the Refined Case FE analysis. The analysis accurately predicts the measured bending moment distribution along the length of the conductor for loading up to first yielding ($My \approx 12MNm$). Thereafter, the FE analyses predict the spread of plastic strains within the conductor (with a fully plastic moment across the section, $Mp \approx 14MNm$). Post-yield strain gauge measurements are also in good agreement with apparent elastic bending moments for the conductor but the data become unreliable at large pushover due to gauge debonding.

The analyses show that interpretations of the local conductor-soil interactions (p-y) curves are sensitive to small variations in the assumed undrained shear strength profile (Fig. 4-31). We have examined the geometric effects of large pushover events ($h = 5.9m$) using the EPP soil model. Apparent strain softening in the local p-y curves

is related to the rotation of the conductor in the clay and the migration of the plastic strains down through the conductor. Details of the elemental soil behavior have a major influence when the loading is reversed.

Efficient modeling of conductor-soil interactions within large simulations of the riser system is most conveniently carried out using macro-elements or simplified methods capable of describing conductor-soil interactions with minimized computational efforts. We have implemented the BWGG generalized p-y model (Gerolymos and Gazetas [2005a]) to provide a simplified representation of conductor-soil interactions in analyses of the overall riser system. Input parameters for the BWGG model are then calibrated to the results of the more comprehensive 3D FE analyses. A basic set of 4 input constants are needed to achieve reasonable representation of conductor-soil response in monotonic lateral loading, including softening effects associated with geometric non-linearities.

The computed hysteretic response for the reversals in the loading direction (unloading and reloading events) are strongly affected by the constitutive model used in the FE analyses. The current report shows large differences in conductor-soil interaction for the isotropic EPP model (with no material degradation) and the MIT-E3 model (where anisotropic properties evolve during first loading and there is substantial material degradation). While the generalized BWGG model can provide a reasonable representation of the cyclic response of the conductor, we have identified a number of pervasive features that may require further modification.

7.1.2 Piezocone Penetration

The second application considers the effects of partial drainage and advanced effective stress constitutive soil models for large deformation, axisymmetric quasi-static piezocone penetration in clay. As discussed in Chapter 2, the excessive mesh distortion problem restricts the usage of the pure Lagrangian Finite Element Method to analyze problems with extremely large deformations such as steady state cone penetration in soft clay. In order to analyze these problems, a suitable large-deformation analysis method is needed to overcome the issue of excessive mesh distortion. Chapter

2 presents an overview of the existing large deformation analysis methods that have been applied to geotechnical problems previously. Most of the published analyses use relatively simple isotropic constitutive soil models and drainage conditions (the soil is usually assumed to be a single phase material). In many cases, this is due to the fact that these large-deformation methods incorporate the convection of the soil relative to the mesh within the finite element governing equations (a difficult task for complex soil models). In this thesis, the proposed procedure for large deformation cone penetration analysis using advanced effective stress soil model is based on the RITSS procedures described by Hu and Randolph [1998a] and is independently implemented for the widely-used commercially available finite element program Abaqus™ using a set of custom Python scripts. This approach comprise i) conventional Lagrangian Finite Element Method , and ii) separate remeshing and solution mapping using the interpolation of all the solution variables from the old mesh into the new mesh (without the ALE convection equations). The main principle is that each remeshing step makes up a new analysis with the appropriate initial conditions (geometry, solution variables, loads and boundary conditions) that reflect the preceding sequence of analysis steps. The main advantage of this approach is that it can be used in the effective stress analysis with advanced soil models and without requiring complex reformulation of the constitutive equations as long as the solution variables are properly interpolated from one mesh to another. The developed methodology for performing large deformation effective stress geotechnical analyses is described in detail in this thesis and can be used by other researchers in a commercial FEA solver using the provided source codes.

Using the described methodology, we have analyzed the penetration resistance for a piezocone device using two elasto-plastic soil models (MCC, MIT-E3) and the recent elasto-viscoplastic MIT-SR soil model (Yuan [2016]) over a range of steady penetration velocities. Predictions of piezocone penetration using the proposed FE analyses were evaluated through comparison with undrained steady state analytical solutions obtained from the Strain Path Method (Aubeny [1992]) and field measurements in South Boston (Ladd et al. [1999]). The deep penetration FE results using the

advanced MIT-E3 soil model considering the effect of stress history are in good agreement with the measured data in Boston Blue Clay. The MCC predictions are also in very good agreement with laboratory measurements of tip resistance and penetration pore pressures measured in centrifuge model tests in reconstituted Kaolin (Schneider et al. [2007]). The results from more advanced soil models illustrate the impacts of anisotropic, rate dependent soil behavior on penetration tests in natural clays and are within the range of empirical measurements. The proposed analyses provide a complete framework that can now be used to investigate effects of partial drainage that occurs in piezocone tests for soils (such as silts) of intermediate permeability.

7.2 Recommendations for Future Work

The proposed methodology and the discussed results of the large deformation offshore geotechnical FE analyses may suggest several future research directions and projects:

1. The centrifuge tests of the conductor subjected to large deformations under tension are unique. Further experimental data are needed to further improve and assess the predictive capabilities of advanced 3D FE numerical models. The available centrifuge model tests of drift/drive-off loading events also simulated the quick release of the conductor after a specified pushover. The next step would be to perform the dynamic analysis of the problem and consider the dynamic response of the system following parting of the riser using an advanced constitutive model capable of modeling dynamic cyclic loading.

2. The current 3D FE model of the conductor-soil interaction assumed tied interface connections between soil and conductor (no slip was allowed at the conductor-soil interface). A general contact algorithm can be employed to further refine the model and consider the possibility of a gap formation between the soil and conductor, as well as the effect of conductor roughness. A more advanced contact model could be developed to refine the conductor-soil interface.

These enhancements could further improve the capabilities of the numerical model for various loading and boundary conditions.

3. The current study implemented and evaluated the capabilities and limitations of the BWGG framework (Gerolymos & Gazetas, 2005) to represent the p-y response computed by the 3D FE analyses. While the current implementation of the generalized BWGG model can provide a reasonable representation of the cyclic response of the conductor, we have identified a number of pervasive features that may require further modification. For example, there are several discrepancies between 3D FE predictions of conductor response using the EPP soil model and a simplified framework including: i) current BWGG model implementation does not characterize the residual soil reaction observed at large deformations in the EPP simulation; ii) BWGG model underestimates the deformations needed to mobilize maximum soil reactions (from the EPP 3D FE model) when loading is reversed and overestimates the post-peak softening. An immediate next task is to obtain experimental data to assess the predictive accuracy of the 3D FE analyses for these loading scenarios.

4. Currently, the developed methodology for large deformation analysis with automatic remeshing and interpolation relies on the Abaqus in-built "MAP solution" procedure for solution mapping algorithm. A custom implementation using Python scripts can also be used to have more control over the solution mapping process for complex cases and advanced elasto-plastic constitutive soil models. This will provide a complete set of debugging tools for reducing the frequency of necessary remeshing improving the efficiency of the analyses.

5. Application of the developed automated remeshing and solution mapping methodology to 3D problems of soil-structure interaction that involves large deformations. These problems include lateral spreading beneath piled bridge abutments, lateral buckling of pipelines, penetration of spudcan foundations for mobile jack-up rigs, and many others.

6. Further analyses of cone penetration tests using the available in-situ and laboratory data. The undrained shear response of clays is dependent on the shear strain rate, but this is not usually considered directly in most available rate-independent simple soil models that have been used in the previously published penetration analyses. In this study, the realistic modeling of penetration rate effects was achieved using MIT-SR model capable of modeling rate-dependent behavior of clays. The MIT-SR model showed the effect of rate-dependency in the cone resistance that changed with the penetration rate. The proposed methodology shows that the MIT-SR model allows more realistic predictions of rate-dependent penetration processes. Therefore, more analyses are recommended to establish better interpretations of the in-situ cone penetration tests. The consideration of other factors such as the effects of the cone roughness on the tip resistance can also be helpful.

Bibliography

S.A. Akl. *Wellbore instability mechanisms in clays.* PhD thesis, Massachusetts Institute of Technology, 2010.

I.K.J. Al-Kafaji. *Formulation of a Dynamic Material Point Method (MPM) for Geomechanical Problems.* PhD thesis, University of Struttgart,, 2013.

J.B. Anderson, A. Rodriguez, K.C. Abdulah, R.H. Fillon, L.A. Banfield, H.A. Mckeown, and J.S. Wellner. Late Quaternary stratigraphic evolution of the northern Gulf of Mexico margin: a synthesis. 2004.

API. *Recommended Practice for Planning, Designing and Constructing Fixed Offshore Platforms - Working Stress Design, RP 2A-WSD*, 2000.

C.P. Aubeny. *Rational interpretation of in-situ tests in cohesive soils.* PhD thesis, Massachusetts Institute of Technology, 1992.

M.M. Baligh and J. Levadoux. Consolidation after undrained piezocone penetration. II: Interpretation. *Journal of geotechnical engineering*, 112(7):727–745, 1986.

T. Belytschko, W. K. Liu, B. Moran, and K. Elkhodary. *Nonlinear finite elements for continua and structures.* John Wiley & Sons, 2013.

D. Benson. An efficient, accurate, simple ale method for nonlinear finite element programs. *Computer Methods in Applied Mechanics and Engineering*, 72:305–350, March 1989.

B. Boroomand and O.C. Zienkiewicz. An improved REP recovery and the effectivity robustness test. *International Journal for numerical methods in engineering*, 40 (17), 1997.

H. Borouchaki, P. Laug, and P. George. Parametric surface meshing using a combined advancing-front generalized Delaunay approach. *International Journal for Numerical Methods in Engineering*, 49(1-2), 2000.

R. Bouc. A mathematical model for hysteresis (in French). *Acustica*, 21:16–25, 1971.

A. Bowyer. Computing dirichlet tessellations. *The computer journal*, 24(2):162–166, 1981.

H.H. Bui, K. Sako, R. Fukagawa, and J.C. Wells. SPH-based numerical simulations for large deformation of geomaterial considering soil-structure interaction. In *The 12th International Conference of International Association for Computer Methods and Advances in Geomechanics (IACMAG)*, volume 1, pages 570–578, 2008.

C-CORE. C-CORE Report R-14-012-1106, Revision 2.0. 2014.

J.P. Carter and N.P. Balaam. *AFENA Users Manual*, 1995.

J.C. Cavendish, D.A. Field, and W.H. Frey. An apporach to automatic three-dimensional finite element mesh generation. *International journal for numerical methods in engineering*, 21(2):329–347, 1985.

F. Ceccato. *Study of large deformation geomechanical problems with the Material Point Method.* PhD thesis, University of Padova, 2015.

F. Ceccato and P. Simonini. Numerical study of partially drained penetration and pore pressure dissipation in piezocone test. *Acta Geotechnica*, pages 1–15, 2016.

F. Ceccato, L. Beuth, and P. Simonini. Analysis of Piezocone Penetration under Different Drainage Conditions with the Two-Phase Material Point Method. *Journal of Geotechnical and Geoenvironmental Engineering*, 2016.

S. Chatterjee, D.J. White, and M.F. Randolph. Numerical simulations of pipe-soil interaction during large lateral movements on clay. *Geotechnique*, 62(8):693–705, 2012.

H. Chen, T. Moan, and H. Verhoeven. Safety of dynamic positioning operations on mobile offshore drilling units. *Reliability Engineering & System Safety*, 93(7): 1072–1090, 2008.

J.Y. Cheon. *Analysis of Spatial Variability in Geotechnical Data for Offshore Foundations.* PhD thesis, University of Texas at Austin, 2010.

G.A. Corral. *Methodology for updating numerical predictions of excavation performance.* PhD thesis, Massachusetts Institute of Technology, 2013.

Y. Di, J. Yang, and T. Sato. An operator-split ALE model for large deformation analysis of geomaterials. *International Journal for Numerical and Analytical Methods in Geomechanics*, 31(12):1375–1399, 2007.

J. Donea, A. Huerta, J.-Ph. Ponthot, and A. RodrÃguez-Ferran. *Arbitrary Lagrangian-Eulerian Methods.* John Wiley & Sons, Ltd, 2004. ISBN 9780470091357.

B. Dugan and J.T. Germaine. Near-seafloor overpressure in the deepwater Mississippi Canyon, northern Gulf of Mexico. *Geophysical Research Letters*, 35(2), 2008.

H.H. Einstein. Uncertainty in rock mechanics and rock engineering-Then and now. In *10th ISRM Congress.* International Society for Rock Mechanics, 2003.

C. Fan and J. Long. Assessment of existing methods for predicting soil response of laterally loaded piles in sand. *Computers and Geotechnics*, 32(4):274 – 289, 2005.

I.M.S. Finnie and M.F. Randolph. Punch-through and liquefaction induced failure of shallow foundations on calcareous sediments. In *Proceedings of International Conference on Behaviour of Offshore Structures, Boston, MA*, pages 217–230, 1994.

P.J. Frey and P. George. *Mesh generation: application to finite elements.* ISTE, 2007.

P.J. Frey and P. George. *A Comprehensive Survey of Mesh Generation Methods*, pages 95–131. ISTE, 2010.

M.S. Gadala and J. Wang. ALE formulation and its application in solid mechanics. *Computer Methods in Applied Mechanics and Engineering*, 167(1):33–55, 1998.

J.T. Germaine and C.C. Ladd. State-of-the-art paper: Triaxial testing of saturated cohesive soils. In *Advanced triaxial testing of soil and rock*. ASTM International, 1988.

N. Gerolymos and G. Gazetas. Constitutive model for 1-D cyclic soil behaviour applied to seismic analysis of layered deposits. *Soils and Foundations*, 45(3):147–159, 2005a.

N. Gerolymos and G. Gazetas. Phenomenological model applied to inelastic response of soil-pile interaction systems. *Soils and Foundations*, 45(4):119–132, 2005b.

B.C. Gerwick. Construction of marine and offshore structures, 2007.

R.A. Gingold and J.J. Monaghan. Smoothed particle hydrodynamics: theory and application to non-spherical stars. *Monthly notices of the royal astronomical society*, 181(3):375–389, 1977.

C. Han, D. Wang, C. Gaudin, C.D. O'Loughlin, and M.J. Cassidy. Behaviour of vertically loaded plate anchors under sustained uplift. *Géotechnique*, 66(8):681–693, 2016.

F.H. Harlow. The particle-in-cell computing method for fluid dynamics. *Methods in computational physics*, 3(3):319–343, 1964.

Y.M.A. Hashash. *Analysis of deep excavations in clay*. PhD thesis, Massachusetts Institute of Technology, 1992.

K. Ho-Le. Finite element mesh generation methods: a review and classification. *Computer-Aided Design*, 20(1), 1988.

M.S. Hossain and M.F. Randolph. Deep-penetrating spudcan foundations on layered clays: Numerical analysis. *Geotechnique*, 60(3):171–184, 2010.

M.S. Hossain, Y. Hu, M.F. Randolph, and D.J. White. Limiting cavity depth for spudcan foundations penetrating clay. *Geotechnique*, 55(9):679–690, 2005.

Y. Hu and M.F. Randolph. A practical numerical approach for large deformation problems in soil. *International Journal for Numerical and Analytical Methods in Geomechanics*, 22(5), 1998a.

Y. Hu and M.F. Randolph. H-adaptive FE analysis of elasto-plastic non-homogeneous soil with large deformation. *Computers and Geotechnics*, 23(1):61–83, 1998b.

T. Hueckel and R. Nova. Some hysteresis effects of the behaviour of geologic media. *International Journal of Solids and Structures*, 15(8), 1979.

T.J.R. Hughes, W.K. Liu, and T.K. Zimmermann. Lagrangian-Eulerian finite element formulation for incompressible viscous flows. *Computer Methods in Applied Mechanics and Engineering*, 29(3):329–349, 1981.

P. Jeanjean. Re-Assessment of P-Y Curves for Soft Clays from Centrifuge Testing and Finite Element Modeling. In *Offshore Technology Conference*, number Vm, pages 1–23. Offshore Technology Conference, 2009.

L.C. Jen. *The design and performance of deep excavations in clay.* PhD thesis, Massachusetts Institute of Technology, 1998.

Y.M. Jiang and M. Liu. Granular Solid Hydrodynamic. *Granular Matter*, 2009.

B.P. Johnston and J.M. Sullivan. Fully automatic two dimensional mesh generation using normal offsetting. *International journal for numerical methods in engineering*, 33(2):425–442, 1992.

P. Josefsson and S. Dincal. Improved DP system failure simulation for drilling riser emergency disconnect. In *Proceedings of the 19th Offshore Symposium.* Texas Section of the Society of Naval Architects and Marine Engineers, February 2014.

E. Kausel. Early history of soil-structure interaction. *Soil Dynamics and Earthquake Engineering*, 30(9):822–832, 2010.

M. Kavvadas. *Non-linear consolidation around driven piles in clays.* PhD thesis, Massachusetts Institute of Technology, 1982.

C.C. Ladd. Results of CA/T Special Test Program at South Boston. Presentation to Haley & Aldrich and Bechtel / Parsons Brincherhoff, Oct., 1990.

C.C. Ladd and Edgers L. Consolidated undrained direct simple shear tests on saturated clays. Technical report, Research Report R72-82, Cambridge: Dept. of Civil & Engin., Massachussettes Institute of Technology, 1972.

C.C. Ladd, G.A. Young, S.R. Kraemer, and D.M. Burke. Engineering properties of Boston Blue Clay from Special Testing Program. In *Proceedings, Special Geotechnical Testing: Central Artery/Tunnel Project in Boston, Massachusetts, GSP 91, GeoCongress 98, ASCE National Convention, Boston*, pages 1–24, 1999.

J. Levadoux. *Pore pressure generated during cone penetration.* PhD thesis, Ph. D. thesis, Department of Civil Engineering, MIT, Cambridge, Massachusetts, 1980.

D.S. Lo. *Finite element mesh generation.* CRC Press, 2014.

S.H. Lo. A new mesh generation scheme for arbitrary planar domains. *International Journal for Numerical Methods in Engineering*, 21(8):1403–1426, 1985.

R. Löhner and P. Parikh. Generation of three-dimensional unstructured grids by the advancing-front method. *International Journal for Numerical Methods in Fluids*, 8 (10):1135–1149, 1988.

Q. Lu, M.F. Randolph, Y. Hu, and I.C. Bugarski. A numerical study of cone penetration in clay. *Géotechnique*, 54(4):257–267, 2004.

L.B. Lucy. A numerical approach to the testing of the fission hypothesis. *The astronomical journal*, 82:1013–1024, 1977.

S. Ma and X.M. Zhang, X.and Qiu. Comparison study of MPM and SPH in modeling hypervelocity impact problems. *International Journal of Impact Engineering*, 36(2): 272–282, 2009.

H. Matlock. Correlations for design of laterally loaded piles in soft clay. In *2nd Annual Offshore Technologie Conference*, volume 1, pages pp. 577–594. Offshore Technology Conference, 1970.

W.O. McCarron. *Deepwater foundations and pipeline geomechanics.* J. Ross Publishing, 2011.

V. Mehra, C.D. Sijoy, V. Mishra, and S. Chaturvedi. Tensile instability and artificial stresses in impact problems in SPH. In *Journal of Physics: Conference Series*, volume 377, 2012.

J. K. Mitchell, K. Soga, et al. *Fundamentals of soil behavior.* John Wiley & Sons Hoboken, NJ, 2005.

MMS. *Gulf of Mexico Deepwater Operations and Activities. Environmental Assessment. U.S. Department of the Interior, Minerals Management Service, Gulf of Mexico OCS Region, New Orleans*, 2000.

P. Möller and P. Hansbo. On advancing front mesh generation in three dimensions. *International Journal for Numerical Methods in Engineering*, 38(21):3551–3569, 1995.

J.J. Monaghan. Smoothed particle hydrodynamics and its diverse applications. *Annual Review of Fluid Mechanics*, 44:323–346, 2012.

M. Nazem, D. Sheng, and J. P. Carter. Stress integration and mesh refinement for large deformation in geomechanics. *International Journal for Numerical Methods in Engineering*, 65(7):1002–1027, 2006.

Z.Y. Orazalin, A.J. Whittle, and Olsen M.B. Three-Dimensional Analyses of Excavation Support System for the Stata Center Basement on the MIT Campus. *Journal of Geotechnical and Geoenvironmental Engineering*, 141(7), 2015.

S.J. Owen. A survey of unstructured mesh generation technology. In *IMR*, pages 239–267, 1998.

K. Pan, R.H.A. IJzermans, B.D. Jones, A. Thyagarajan, B.W.H. van Beest, and J.R. Williams. Application of the SPH method to solitary wave impact on an offshore platform. *Computational Particle Mechanics*, 3(2), 2016.

M.A. Pando. Analyses of Lateral Loaded Piles with P-Y Curves - Observations on the Effect of Pile Flexural Stiffness and Cyclic Loading. NCDOT 7th Geo3, April 2013.

A. Panteghini and R. Lagioia. A fully convex reformulation of the original Matsuoka-Nakai failure criterion and its implicit numerically efficient integration algorithm. *International Journal for Numerical and Analytical Methods in Geomechanics*, 2014.

J. Peraire, Morgan V., K. Morgan, and O.C. Zienkiewicz. Adaptive remeshing for compressible flow computations. *Journal of computational physics*, 72(2):449–466, 1987.

G. Qiu, S. Henke, and J. Grabe. Application of a Coupled Eulerian-Lagrangian approach on geomechanical problems involving large deformations. *Computers and Geotechnics*, 38(1):30–39, 2011.

R. Ragni, B. Britta, D. Wang, D. Mašín, and M.J. Cassidy. Numerical modelling of the effects of consolidation on the undrained spudcan capacity under combined loading in silty clay. *Computers and Geotechnics*, 86, 2017.

M. Randolph and S. Gourvenec. *Offshore geotechnical engineering.* CRC Press, 2011.

M. Randolph, M. Cassidy, S. Gourvenec, and C. Erbrich. Challenges of offshore geotechnical engineering. In *Proceedings of the international conference on soil mechanics and geotechnical engineering*, volume 16, page 123, 2005.

M.F. Randolph and G.T. Houlsby. The limiting pressure on a circular pile loaded laterally in cohesive soil. *Geotechnique*, 34(4):613–623, 1984.

M.F. Randolph, D. Wang, H. Zhou, M.S. Hossain, and Y. Hu. Large deformation finite element analysis for offshore applications. In *Proceedings of the12th International Conference of International Association for Computer Methods and Advances in Geomechanics, Goa, India*, pages 1–6, 2008.

L.C. Reese, W.R. Cox, and F.D. Koop. Analysis of Laterally Loaded Piles in Sand. In *Offshore Technology Conference*, pages 473–483. Offshore Technology Conference, 1974.

K.H. Roscoe and J.B. Burland. On the Generalized Stress-Strain Behavior of 'Wet' Clay. *Engineering Plasticity, Cambridge University Press*, pages 535–609, 1968.

S.A. Savidis, D. Aubram, and F. Rackwitz. Arbitrary Lagrangian-Eulerian finite element formulation for geotechnical construction processes. *Journal of Theoretical and Applied Mechanics*, 38(1-2):165–194, 2008.

J.A. Schneider, B.M. Lehane, and F. Schnaid. Velocity effects on piezocone measurements in normally and over consolidated clays. *International Journal of Physical Modelling in Geotechnics*, 7(2):23–34, 2007.

T.C. Sheahan. *An experimental study of the time-dependent undrained shear behavior of resedimented clay using automated stress path triaxial equipment.* PhD thesis, Massachusetts Institute of Technology, 1991.

SIMULIA. *Abaqus Documentation (2016), SIMULIA by Dassault Systemes*, 2016.

Z. Song, Y. Hu, and M.F. Randolph. Numerical simulation of vertical pullout of plate anchors in clay. *Journal of Geotechnical and Geoenvironmental Engineering*, 134 (6):866–875, 2008.

M.G. Sottile. Implementation and evaluation of a recently developed rate-dependent effective stress soil model MIT-SR. Master's thesis, Massachusetts Institute of Technology, 2016.

D.P. Stewart and M.F. Randolph. T-Bar Penetration Testing in Soft Clay. *Journal of Geotechnical Engineering*, 120(12):2230–2235, 1994.

L. Suklje. The analysis of the consolidation process by the isotaches method. In *Proceedings of the 4th International Conference on Soil Mechanics and Foundation Engineering*, 1957.

D. Sulsky, Z. Chen, and H.L. Schreyer. A particle method for history-dependent materials. *Computer methods in applied mechanics and engineering*, 118(1-2):179–196, 1994.

E. Susila and R.D. Hryciw. Large displacement FEM modelling of the cone penetration test (CPT) in normally consolidated sand. *Int. J. Numer. Anal. Meth. Geomech.*, 2003.

T. Sutabutr. *Analyses and interpretation of tapered piezoprobe and application to offshore pile design.* PhD thesis, Massachusetts Institute of Technology, 1999.

A.M. Tartakovsky, N. Trask, K. Pan, B. Jones, W. Pan, and J.R. Williams. Smoothed particle hydrodynamics and its applications for multiphase flow and reactive transport in porous media. *Computational Geosciences*, 20(4), 2016.

J.S. Templeton. Finite Element Analysis of Conductor/Seafloor Interaction. In *Offshore Technology Conference*. Offshore Technology Conference, 2009.

Y. Tian, M.J. Cassidy, M.F. Randolph, D. Wang, and C. Gaudin. A simple implementation of RITSS and its application in large deformation analysis. *Computers and Geotechnics*, 56, 2014.

Y. Tian, C. Gaudin, M.F. Randolph, and M.J. Cassidy. Influence of padeye offset on bearing capacity of three-dimensional plate anchors. *Canadian Geotechnical Journal*, 52(6):682–693, 2015.

A.M. Trochanis, J. Bielak, and P. Christiano. Simplified Model for Analysis of One or Two Piles. *Journal of Geotechnical Engineering*, 117(3):448–466, 1991.

P. van den Berg. *Analysis of soil penetration.* PhD thesis, Delft University of Technology, 1994.

G. Van Rossum and F. L. Drake. *Python language reference manual.* Network Theory, 2003.

C. Wang, Y. Wang, C. Peng, and X. Meng. Smoothed Particle Hydrodynamics Simulation of Water-Soil Mixture Flows. *Journal of Hydraulic Engineering*, 142 (10), 2016.

D. Wang, Y. Hu, and M. F. Randolph. Three-dimensional large deformation finite-element analysis of plate anchors in uniform clay. *Journal of Geotechnical and Geoenvironmental Engineering*, 136(2):355–365, 2009.

D. Wang, D.J. White, and M.F. Randolph. Large-deformation finite element analysis of pipe penetration and large-amplitude lateral displacement. *Canadian Geotechnical Journal*, 47(8):842–856, 2010.

D.F. Watson. Computing the n-dimensional Delaunay tessellation with application to Voronoi polytopes. *The computer journal*, 24(2):167–172, 1981.

Y. Wen. Method for random vibration of hysteretic systems. *Journal of Engineering Mechanics*, 102(2):249–263, 1976.

A.J. Whittle. *A constitutive model for overconsolidated clays with application to the cyclic loading of friction piles.* PhD thesis, Massachusetts Institute of Technology, 1987.

A.J. Whittle. *Assessment of an effective stress analysis for predicting the performance of driven piles in clays*, volume 28, pages 607–607. Springer Netherlands, 1993a.

A.J. Whittle. Evaluation of a constitutive model for overconsolidated clays. *Geotechnique*, 43(2), 1993b.

A.J. Whittle. Discussion: Evaluation of a constitutive model for overconsolidated clays. *Geotechnique*, 45(1):169–173, 1995.

A.J. Whittle and M.J. Kavvadas. Formulation of MIT-E3 Constitutive Model for Overconsolidated Clays. *Journal of Geotechnical Engineering*, 120(1):173–198, 1994.

A.J. Whittle and T. Sutabutr. Parameters for average Gulf Clay and Prediction of Pile Set-up in the Gulf of Mexico. *Geo-Frontiers Congress 2005*, pages 440–458, 2005.

A.J. Whittle, M.M. Baligh, A.S. Azzouz, and A.M. Malek. A model for predicting the performance of TLP piles in clay. *Proceedings 5th International Conference on Behavior of Offshore Structures*, 1988.

A.J. Whittle, T. Sutabutr, J.T. Germaine, and A. Varney. Prediction and interpretation of pore pressure dissipation for a tapered piezoprobe. *Geotechnique*, 51(7): 601–617, 2001.

L. Yu, Y. Hu, J. Liu, M.F. Randolph, and X. Kong. Numerical study of spudcan penetration in loose sand overlying clay. *Computers and Geotechnics*, 46:1–12, 2012.

Y. Yuan. *A New Elasto-Viscoplastic Model For Ratedependent Behavior Of Clays.* PhD thesis, Ph. D. thesis, Department of Civil Engineering, MIT, Cambridge, Massachusetts, 2016.

A. Zakeri, E. Clukey, B. Kebadze, P. Jeanjean, D. Walker, G. Piercey, J. Templeton, L. Connelly, C. Aubeny, et al. Recent advances in soil response modeling for well conductor fatigue analysis and development of new approaches. In *Offshore Technology Conference*. Offshore Technology Conference, 2015.

H. Zhou and M.F. Randolph. Resistance of full-flow penetrometers in rate-dependent and strain-softening clay. *Geotechnique*, 59(2):79–86, 2009.

O.C. Zienkiewicz and J.Z. Zhu. Adaptivity and mesh generation. *International Journal for Numerical Methods in Engineering*, 32(4):783–810, 1991.

O.C. Zienkiewicz and J.Z. Zhu. The superconvergent patch recovery and a posteriori error estimates. Part 1: The recovery technique. *International Journal for Numerical Methods in Engineering*, 33(7):1331–1364, 1992.

Appendix A

Summary of Triaxial Test Results

Table A.1: Summary of Performed Triaxial Undrained Tests on RGoM Clay

Specimen Location		Specimen Data	Consolidation Results				Shearing Results				Remarks
			General		Pre-shear		At Max Shear		At Max Obliquity		
Test #	Depth	ω_n	e_0	Cc	ε_a	σ'_{vc}	ε_a	q/σ'_{vc}	ε_a	q/σ'_{vc}	
Boring		γ_t	ε_a/hr	λ	ε_{vol}	OCR		p'/σ'_{vc}		p'/σ'_{vc}	
Sample		G_s			K_0	e_{final}				ϕ'	
TX001	4.4	56.0	1.6	0.55	14.3	246	16.7	0.198	16.7	0.198	CK_0UE
		16.4	0.1	0.231	14.3	1.0		0.465		0.465	
C-CORE		2.65			0.57	1.23				25.15°	
TX002	14.6	51.7	1.45	0.60	14.3	399	2.1	0.237	15.0	0.221	CK_0UC
		16.3	0.1	0.257	14.6	1.0		0.704		0.552	
C-CORE		2.65			0.67	1.1				23.67°	
TX003	32.1	47.3	1.3	0.45	10.4	416	2.1	0.245	16.4	0.216	CK_0UC
		17.3	0.1	0.178	10.7	1.0		0.711		0.554	
C-CORE		2.65			0.66	n/a				23.02°	
TX004	49.7	40.7	1.203	0.41	12.1	599	14.9	0.231	14.9	0.231	CK_0UE
		17.8	0.1	0.157	12.5	1.0		0.455		0.455	
C-CORE		2.65			0.61	0.94				27.34°	

a) Unit weight in kN/m^3
b) Stresses in kPa
c) 1 kPa = 47.88 ksf
d) Depth in meters (Prototype scale)
e) Water content and strain in %

Appendix B

Numerical Settings and Procedures

Table B.1: Project files for cone penetration analysis in Abaqus™ Standard

#	File name	Description
1	CPT_CAX4P.cae	Initial CAE (Complete Abaqus™ Environment) file for cone penetration model in Abaqus™ Standard. The initial input file "CPT_CAX4P_00.inp" is generated, where "00" indicates the remeshing step number, N.
2	Automated_Run.py	Main Python script that governs the automated analysis process and calls all the other scripts
3	First.py	Python script for the first fully automated step
4	Continue.py	This Python script creates the next model based on the previous step (for N>1). The main script is subdivided into multiple files for the possibility of manual execution from the Abaqus™ Environment
5	Sets_and_Surfaces.py	The script applies the necessary sets and surfaces to the geometry obtained from the deformed mesh
6	Meshing.py	Remeshing of the domain and creation of the new input files for the Abaqus™ solver invoking map solution

Table B.2: Description of procedures as implemented in Python code for automated remeshing and interpolation analysis

#	**Procedure**	**Description**
1	Initial script configuration	The analysis settings such as desired mesh density, remeshing frequency, system paths, etc. are prescribed in the Python scripts between the sections marked as "==CONFIGURATION==" at the beginning and "==/CONFIGURATION==" at the end.
2	Initial FE analysis	The first FE model must be created manually or created using the Python script "InitialModel.py" (provided in the package). The initial analysis (step "00") must be completed before invoking the scripts.
3	Import of the deformed orphan mesh and geometry conversion	A new model based on the previous step is created. The deformed mesh from the previous analysis is imported into the new model. The deformed mesh is converted into geometry.
4	Application of virtual topology	The obtained geometry from the deformed mesh is improved using the virtual topology in Abaqus™ to eliminate extra edges and points.
5	Creation of sets and surfaces	The geometrical sets and surfaces are redefined for boundary conditions and contact interactions.
6	Remeshing	The previously deformed geometry is re-discretized.
7	Solution mapping and analysis continuation	A new input file is created and submitted to the Abaqus™ solver using "MAP solution" feature that automatically interpolates the solution variables

Table B.3: Numerical settings for initial cone penetration FE model

#	**Numerical setting in Abaqus™ Standard**	**Selected Value**
1	Finite Element Solver	Direct
2	Matrix storage	Unsymmetric
3	Solution technique	Full Newton
4	Default load variation with time	Instantaneous
5	Pore fluid response	Transient consolidation
6	Contact interaction	Surface-to-surface contact
7	Sliding formulation	Finite sliding
8	Discretization method	Node to surface
9	Degree of smoothing for master surface	0.01
10	Use supplementary contact points	Always
11	Unbalanced stress in MAP Solution	STEP (resolve the stress unbalance in the first increment of the step)
12	Time Incrementation in General Solution Controls	Discontinuous analysis

Appendix C

Source Code Listings

All project files listed in Table B.1 are available for download at:

http://www.orazalin.com/thesis/.

The example source code of the Python script for the first automated step is presented below.

Listing C.1: File "First.py"

```
#################################################################
# Zhandos Orazalin, MIT.
# May, 2017
# Full package at: http://www.orazalin.com/thesis/
#################################################################

from abaqus import *
from abaqusConstants import *
import __main__
import section
import regionToolset
import displayGroupMdbToolset as dgm
import part
import material
```

```
import assembly
import step
import interaction
import load
import mesh
import optimization
import job
import sketch
import visualization
import xyPlot
import displayGroupOdbToolset as dgo
import connectorBehavior

# SIMULIA code (Abaqus Manual)
def GetBlockPosition(modelName, blockPrefix):
    if blockPrefix == '':
        return len(mdb.models[modelName].keywordBlock.
            sieBlocks)-1
    pos = 0
    for block in mdb.models[modelName].keywordBlock.sieBlocks
        :
        if block[0:len(blockPrefix)].lower()==blockPrefix.
            lower():
            return pos
        pos=pos+1
    return -1
# /SIMULIA code

#============================CONFIGURATION============================
umatname='UMAT.for'
```

```
displacement=-0.002
nextdisplacement=-0.002
elements_type='CAX4P' # CAX4P, CAX8RP or other
mesh_type='Fine' # Coarse or Fine
map_solution_string='*MAP_SOLUTION, _UNBALANCED_STRESS=STEP'
load_amplitude=STEP # RAMP or STEP
cpus='1'
local_temp_path='C:/Temp/'
system_temp_path='C:\\Temp\\'
fortran_path='C:\\Progra~2\\Intel\\Composer_XE_2013_SP1\\bin
    \\ifortvars.bat'
abaqus_path='C:\\SIMULIA\\Commands\\abq2016'
umat_path='C:\\Projects\\SoilModels\\UMAT\\'
#==============/CONFIGURATION=========================

LastModelNameFull=str(mdb.models.keys()[-1])
yourmodelname=LastModelNameFull[:-2]

oldmodel=str(mdb.models.keys()[-1])
currentnumber=int(oldmodel[-2:])

print 'Current_number:_'+str(currentnumber)
if currentnumber < 9 :
    newmodel=yourmodelname+'0'+str(currentnumber+1)
else:
    newmodel=yourmodelname+str(currentnumber+1)

soilInstance = 'SOIL-1'          # Deformed instance name.
deformedShape = DEFORMED         # Shape.
angle = 0.1
```

```
mdb.Model(name=newmodel, objectToCopy=mdb.models[oldmodel])
del mdb.models[newmodel].parts['SOIL']
session.openOdb(local_temp_path+oldmodel+'.odb')
odb = session.odbs[local_temp_path+oldmodel+'.odb']

orphanSoil=mdb.models[newmodel].PartFromOdb(name='meshSOIL',
    fileName=oldmodel+'.odb', instance=soilInstance, shape=
    deformedShape, step=-1, frame=-1)

del mdb.models[newmodel].parts['meshSOIL'].sets['_TOP_S1']
del mdb.models[newmodel].parts['meshSOIL'].sets['BOTTOM_PP_']
del mdb.models[newmodel].parts['meshSOIL'].sets['RIGHT_PP_']

mdb.models[newmodel].Part2DGeomFrom2DMesh(name='SOIL', part=
    orphanSoil, featureAngle=angle)
mdb.models[newmodel].steps.changeKey(fromName='Geostatic',
    toName='Equilibrium')
mdb.models[newmodel].SoilsStep(name='Equilibrium',
    previous='Initial', maintainAttributes=True, timePeriod
        =0.001,
    maxNumInc=5000, creep=OFF, timeIncrementationMethod=FIXED
        ,
    initialInc=0.001, end=None, utol=None, cetol=None,
        matrixSolver=DIRECT,
    matrixStorage=UNSYMMETRIC, extrapolation=NONE, nlgeom=ON,
    convertSDI=CONVERT_SDI_OFF)
p1 = mdb.models[newmodel].parts['meshSOIL']
p = mdb.models[newmodel].parts['meshSOIL']
region = p.sets['ALL']
p = mdb.models[newmodel].parts['meshSOIL']
```

```
p.SectionAssignment(region=region, sectionName='SOIL', offset
    =0.0,
     offsetType=MIDDLE_SURFACE, offsetField='',
     thicknessAssignment=FROM_SECTION)

del mdb.models[newmodel].predefinedFields['STRESS']

mdb.models[newmodel].boundaryConditions['REFERENCE'].
    setValuesInStep(
     stepName='Equilibrium', u1=0, u2=0, ur3=0)
a = mdb.models[newmodel].rootAssembly
a.translate(instanceList=('CONE-1', ), vector=(0.0,
    displacement, 0.0))
mdb.models[newmodel].boundaryConditions['REFERENCE'].
    setValuesInStep(
     stepName='Loading', u2=nextdisplacement)

p = mdb.models[newmodel].parts['SOIL']
f = p.faces
pickedRegions = f.getSequenceFromMask(mask=('[#1 ]', ), )
p.setMeshControls(regions=pickedRegions, elemShape=QUAD)

if elements_type=='CAX8RP':
    elemType1 = mesh.ElemType(elemCode=CAX8RP, elemLibrary=
        STANDARD)
    elemType2 = mesh.ElemType(elemCode=CAX6MP, elemLibrary=
        STANDARD)
elif elements_type=='CAX8P':
    elemType1 = mesh.ElemType(elemCode=CAX8P, elemLibrary=
```

```
        STANDARD)
    elemType2 = mesh.ElemType(elemCode=CAX6MP, elemLibrary=
        STANDARD)
elif elements_type=='CAX4RP':
    elemType1 = mesh.ElemType(elemCode=CAX4RP, elemLibrary=
        STANDARD,
          hourglassStiffness=1000.0)
    elemType2 = mesh.ElemType(elemCode=UNKNOWN_TRI,
        elemLibrary=STANDARD)
elif elements_type=='CAX4P':
    elemType1 = mesh.ElemType(elemCode=CAX4P, elemLibrary=
        STANDARD)
    elemType2 = mesh.ElemType(elemCode=UNKNOWN_TRI,
        elemLibrary=STANDARD)

p = mdb.models[newmodel].parts['SOIL']
f = p.faces
faces = f.getSequenceFromMask(mask=('[#1 ]', ), )
pickedRegions =(faces, )

p.setElementType(regions=pickedRegions, elemTypes=(elemType1,
    elemType2))

p = mdb.models[newmodel].parts['SOIL']
f = p.faces
faces = f.getSequenceFromMask(mask=('[#1 ]', ), )
p.Set(faces=faces, name='ALL')
region = p.sets['ALL']

p = mdb.models[newmodel].parts['SOIL']
```

```
p.SectionAssignment(region=region, sectionName='SOIL', offset
    =0.0,
     offsetType=MIDDLE_SURFACE, offsetField='',
     thicknessAssignment=FROM_SECTION)

vert_coords = []
horiz_coords = []

SoilNodes=mdb.models[newmodel].parts['meshSOIL'].nodes

for i in range(len(SoilNodes)):
     vert_coords.append(SoilNodes[i].coordinates[1])
     horiz_coords.append(SoilNodes[i].coordinates[0])
max_vert_coord=max(vert_coords)
min_vert_coord=min(vert_coords)
max_horiz_coord=max(horiz_coords)

selected_horiz_coord=mdb.models[newmodel].parts['meshSOIL'].
    sets['POINT'].nodes[-1].coordinates[0]
selected_vert_coord=mdb.models[newmodel].parts['meshSOIL'].
    sets['POINT'].nodes[-1].coordinates[1]

print 'Obtaining coordinates from the previous set "POINT"...
    '


verts = mdb.models[newmodel].parts['SOIL'].vertices.findAt(((
    selected_horiz_coord, selected_vert_coord, 0), ))
p.Set(vertices=verts, name='POINT')

print 'Obtaining coordinates from the previous set "POINT" '
```

```
    was successful!'

LeftNodes=mdb.models[newmodel].parts['meshSOIL'].sets['LEFT'
    ].nodes
left_vert_coords = []
left_horiz_coords = []

for i in range(len(LeftNodes)):
    left_horiz_coords.append(LeftNodes[i].coordinates[0])
    left_vert_coords.append(LeftNodes[i].coordinates[1])
max_left_vert_coord=max(left_vert_coords)
select_left_horiz_coord=left_horiz_coords[left_vert_coords.
    index(max_left_vert_coord)]

# VIRTUAL TOPOLOGY - TOP #1 - horizontal
p = mdb.models[newmodel].parts['SOIL']
v = p.vertices
verts = v.getByBoundingBox(selected_horiz_coord+0.0001,
    selected_vert_coord-0.01, 0, max_horiz_coord-0.01,
    max_vert_coord+0.01, 0,)
pickedEntities =(verts, )
p.ignoreEntity(entities=pickedEntities)

# VIRTUAL TOPOLOGY - TOP #2 - vertical
p = mdb.models[newmodel].parts['SOIL']
v = p.vertices
verts = v.getByBoundingBox(select_left_horiz_coord,
    max_left_vert_coord+0.0001, 0, selected_horiz_coord+0.01,
    selected_vert_coord-0.0001, 0)
pickedEntities =(verts, )
```

```
p.ignoreEntity(entities=pickedEntities)

# VIRTUAL TOPOLOGY - LEFT
p = mdb.models[newmodel].parts['SOIL']
v = p.vertices
verts = v.getByBoundingBox(-0.0001, min_vert_coord+0.01, 0,
    0.0001, max_left_vert_coord-0.0001)
pickedEntities =(verts, )
p.ignoreEntity(entities=pickedEntities)

# VIRTUAL TOPOLOGY - RIGHT
p = mdb.models[newmodel].parts['SOIL']
v = p.vertices
verts = v.getByBoundingBox(max_horiz_coord-0.01,
    min_vert_coord+0.01, 0, max_horiz_coord+0.01, -0.02, 0)
pickedEntities =(verts, )
p.ignoreEntity(entities=pickedEntities)

# VIRTUAL TOPOLOGY - BOTTOM
p = mdb.models[newmodel].parts['SOIL']
v = p.vertices
verts = v.getByBoundingBox(0.0001, min_vert_coord-0.01, 0,
    max_horiz_coord-0.01, min_vert_coord+0.01, 0)
pickedEntities =(verts, )
p.ignoreEntity(entities=pickedEntities)

p = mdb.models[newmodel].parts['SOIL']
e = p.edges
edges = e.findAt(((0, min_vert_coord+0.01, 0), ))
p.Set(edges=edges, name='LEFT')
```

```
p = mdb.models[newmodel].parts['SOIL']
e = p.edges
edges = e.getByBoundingBox(max_horiz_coord-0.01,
    min_vert_coord-0.01, 0, max_horiz_coord+0.01, 0.1, 0)
p.Set(edges=edges, name='RIGHT')

p = mdb.models[newmodel].parts['SOIL']
e = p.edges
edges = e.findAt(((0.2, min_vert_coord, 0), ))
p.Set(edges=edges, name='BOTTOM')

p = mdb.models[newmodel].parts['SOIL']
s = p.edges
side1Edges = s.getByBoundingBox(max_horiz_coord-0.01,
    min_vert_coord-0.01, 0, max_horiz_coord+0.01, 0.1, 0)
p.Surface(side1Edges=side1Edges, name='RIGHT')

# TOP
p = mdb.models[newmodel].parts['SOIL']
s = p.edges
side1Edges = s.getByBoundingBox(-0.1, min_vert_coord+0.01, 0,
    max_horiz_coord+0.01, 0.2, 0)
p.Surface(side1Edges=side1Edges, name='TOP')

del mdb.models[newmodel].parts['meshSOIL']

# TOP #2 - vertical
p = mdb.models[newmodel].parts['SOIL']
e = p.edges
```

```
pickedEdges = e.getByBoundingBox(select_left_horiz_coord
    -0.01, max_left_vert_coord-0.01, 0, selected_horiz_coord
    +0.01, selected_vert_coord+0.01, 0)

if mesh_type=='Coarse':
    p.seedEdgeBySize(edges=pickedEdges, size=0.003,
        deviationFactor=0.1,
        constraint=FINER)
else:
    p.seedEdgeBySize(edges=pickedEdges, size=0.002,
        deviationFactor=0.1,
        constraint=FINER)


# TOP #1 - horizontal
p = mdb.models[newmodel].parts['SOIL']
e = p.edges
pickedEdges2 = e.getByBoundingBox(selected_horiz_coord
    -0.0001, -0.01, 0, max_horiz_coord+0.01, max_vert_coord
    +0.01, 0)

if mesh_type=='Coarse':
    p.seedEdgeByBias(biasMethod=SINGLE, end2Edges=
        pickedEdges2, minSize=0.003,
        maxSize=0.04, constraint=FINER)
else:
    p.seedEdgeByBias(biasMethod=SINGLE, end2Edges=
        pickedEdges2, minSize=0.002,
        maxSize=0.02, constraint=FINER)
```

```
# LEFT
p = mdb.models[newmodel].parts['SOIL']
e = p.edges
pickedEdges1 = e.findAt(((0, min_vert_coord+0.01, 0), ))
p.seedEdgeByBias(biasMethod=SINGLE, end1Edges=pickedEdges1,
    minSize=0.002,
     maxSize=0.02, constraint=FINER)

# BOTTOM
p = mdb.models[newmodel].parts['SOIL']
e = p.edges
pickedEdges = e.findAt(((0.2, min_vert_coord, 0), ))
p.seedEdgeBySize(edges=pickedEdges, size=0.02,
    deviationFactor=0.1,
     constraint=FINER)

# RIGHT
p = mdb.models[newmodel].parts['SOIL']
e = p.edges
pickedEdges = e.getByBoundingBox(max_horiz_coord-0.01,
    min_vert_coord-0.01, 0, max_horiz_coord+0.01, 0.1, 0)

if mesh_type=='Coarse':
     p.seedEdgeBySize(edges=pickedEdges, size=0.04,
         deviationFactor=0.1,
          constraint=FIXED)
else:
     p.seedEdgeBySize(edges=pickedEdges, size=0.02,
         deviationFactor=0.1,
          constraint=FIXED)
```

```
p = mdb.models[newmodel].parts['SOIL']
p.generateMesh()

a = mdb.models[newmodel].rootAssembly
a.regenerate()
session.viewports['Viewport: 1'].setValues(displayedObject=a)

del mdb.models[newmodel].boundaryConditions['TOPLEFT']
a = mdb.models[newmodel].rootAssembly
region = a.instances['SOIL-1'].surfaces['TOP']
mdb.models[newmodel].loads['TOP'].setValues(region=region)

a = mdb.models[newmodel].rootAssembly
session.viewports['Viewport: 1'].setValues(displayedObject=a)
session.viewports['Viewport: 1'].assemblyDisplay.setValues(
    step='Equilibrium')
session.viewports['Viewport: 1'].assemblyDisplay.setValues(
     adaptiveMeshConstraints=ON)

mdb.models[newmodel].fieldOutputRequests['F-Output-1'].move(
     'Equilibrium', 'Loading')
mdb.models[newmodel].historyOutputRequests['H-Output-1'].move
    (
     'Equilibrium', 'Loading')

mdb.models[newmodel].loads['RIGHT'].move('Equilibrium', '
    Loading')

mdb.models[newmodel].loads['TOP'].move('Equilibrium', '
```

```
    Loading')

del mdb.models[newmodel].steps['Equilibrium']

mdb.models[newmodel].steps['Loading'].setValues(
    utol=1000.0, matrixSolver=DIRECT, matrixStorage=
        SOLVER_DEFAULT,
    amplitude=load_amplitude, response=CONSOLIDATION, end=
        None, cetol=None)

mdb.models[newmodel].steps['Loading'].control.setValues(
    allowPropagation=OFF, resetDefaultValues=OFF,
        discontinuous=ON)

mdb.models[newmodel].steps['Loading'].control.setValues(
    displacementField=(0.005, 0.05, 0.0, 0.0, 0.02, 1e-05,
        0.001, 1e-08,
    1.0, 1e-05, 1e-08), hydrostaticFluidPressureField=(0.005,
         0.05, 0.0,
    0.0, 0.02, 1e-05, 0.001, 1e-08, 1.0, 1e-05),
        poreFluidPressureField=(
    0.005, 0.05, 0.0, 0.0, 0.02, 1e-05, 0.001, 1e-08, 1.0, 1e
        -05),
    rotationField=(0.005, 0.05, 0.0, 0.0, 0.02, 1e-05, 0.001,
         1e-08, 1.0,
    1e-05))

input_file_string='**␣
    ------------------------------------------------------------\
    n**␣\n**␣STEP:␣Loading\n**␣'
```

```
mdb.models[newmodel].keywordBlock.synchVersions()
mdb.models[newmodel].keywordBlock.insert(GetBlockPosition(
    newmodel, input_file_string)-1, map_solution_string)

odb.close()

# PREPARE THE INPUT BAT FILE FOR THE ABAQUS SOLVER
mdb.Job(name=newmodel, model=newmodel,
      description='', type=ANALYSIS, atTime=None, waitMinutes
         =0, waitHours=0,
      queue=None, memory=90, memoryUnits=PERCENTAGE,
      getMemoryFromAnalysis=True, explicitPrecision=SINGLE,
      nodalOutputPrecision=SINGLE, echoPrint=OFF, modelPrint=
         OFF,
      contactPrint=OFF, historyPrint=OFF, userSubroutine='',
         scratch='',
      resultsFormat=ODB, multiprocessingMode=DEFAULT, numCpus
         =1, numGPUs=0)
with open(system_temp_path+newmodel+'.bat', 'w') as batfile:
      batstring='@call "'+fortran_path+'" intel64\n'
      batstring=batstring+abaqus_path+' analysis job='+newmodel
         +' oldjob='+oldmodel+' user='+umat_path+umatname+'
         cpus='+cpus
      batfile.write(batstring)
mdb.jobs[newmodel].writeInput(consistencyChecking=OFF)

# END OF THE SCRIPT
# BAT FILES ARE EXECUTED FROM THE MAIN PROGRAM:
# "Automated_Run.py"
```